UNIVERSITY OF SOUTHAMPTON
Faculty of Engineering and the Environment

Development of a Multi-Physics Modelling Framework to Characterise the Interactions of Skin and Wet Shaving Products

by Maria Fabiola Leyva Mendivil

Thesis for the degree of Doctor of Philosophy

April 27, 2016

UNIVERSITY OF SOUTHAMPTON

ABSTRACT

FACULTY OF ENGINEERING AND THE ENVIRONMENT
national Centre for Advanced Tribology at Southampton (nCATS)/Bioengineering

Doctor of Philosophy

Development of a Multi-Physics Modelling Framework to Characterise the Interactions of Skin and Wet Shaving Products

by Maria Fabiola Leyva Mendivil

This PhD project comprised the development of a state-of-the-art multi-physic modelling framework for the characterisation of wet shaving interactions in a coupled Eulerian-Lagrangian finite element environment. The experimental characterisation of shave prep fluids required the development of sound methodologies to capture the viscous and adhesive properties of the shave prep fluids. The process required step by step modelling approach for the verification of the fluid viscous response and the analysis of the contact interactions and its implications in the behavioural response and simulation run-time performance. The final product resulted in a modular finite element framework, for its application in the analysis of wet-shaving lubrication phenomena, for the assessment of new products designs.

Going beyond the original purposes of the project, an state-of-the-art anatomical skin model was developed with the use of image-based modelling techniques, capturing the skin microstructure with high geometrical fidelity. This model was applied for the investigation of the role of the skin microstructure on the macroscopic response to deformation and contact interactions, revealing a complex non-linear interplay between the geometry and mechanical characteristics of the skin layers. In extension/compression, the skin topography reassembles a 'hinge-like' mechanism for dissipation of strains in the epidermis, where highest levels of strains were observed at the skin furrows, and lowest at the crests. In contact interactions simulations, the topographic features of the skin appear to dominate the global friction response. The study revealed that the *stratum corneum* plays a crucial role in the peripheral deformation and propagation of stress, further away from the area of contact. The high concentration of shear stresses derived from the multi-asperity contact summed to the high concentration of strains in the skin furrows, highlighted the importance of the skin microstructure on the mechano-biological implications of shear stress and strain distribution within the skin layers.

To all of those who I've missed so much on this journey...

Contents

List of Figures

List of Tables

List of Symbols

Declaration of Authorship

I, **Maria Fabiola Leyva-Mendivil**, declare that this thesis and the work presented in it are my own and has been generated by me as the result of my own original research.

Development of a Multi-Physics Modelling Framework to Characterise the Interactions of Skin and Wet Shaving Products

I confirm that:

1. This work was done wholly or mainly while in candidature for a research degree at this University;
2. Where any part of this thesis has previously been submitted for a degree or any other qualification at this University or any other institution, this has been clearly stated;
3. Where I have consulted the published work of others, this is always clearly attributed;
4. Where I have quoted from the work of others, the source is always given. With the exception of such quotations, this thesis is entirely my own work;
5. I have acknowledged all main sources of help;
6. Where the thesis is based on work done by myself jointly with others, I have made clear exactly what was done by others and what I have contributed myself;
7. Either none of this work has been published before submission, or parts of this work have been published as:

   Chapter 6:

   Leyva-Mendivil, Maria F. and Page, Anton and Bressloff, Neil W. and Limbert, Georges. "A mechanistic insight into the mechanical role of the stratum corneum during stretching and compression of the skin". *Journal of the Mechanical Behavior of Biomedical Materials*. 49:197-219, 2015. ISSN: 17516161. doi: 10.1016/j.jmbbm.2015.05.010.

Signed: _____ Date: _____

Acknowledgements

Thanks to the Mexican Council of Science and Technology (CONACyT), Procter & Gamble (P&G) and the University of Southampton for the sponsorship of this programme. Thanks as well to the supervisory team, my academic supervisors Prof. Georges Limbert and Prof. Neil Bressloff, and my industrial supervisor from P&G, Dr. David O'Callaghan for the guidance and support on the project matters. I am also grateful to the staff at the Great London Innovation Centres in Reading (GLIC-R) and Egham (GLIC-E), in the United Kingdom, the Biomedical Imaging Unit in the Southampton General Hospital, and the University of Southampton Electrochemistry department for support, training and advice on the experimental techniques used in this project. I'd like to acknowledge the technical support from Dr. Ross Cotton from Simpleware Ltd, Exeter, UK and Dr. Jakub Lengiewicz, from the Polish Academy of Sciences, Warsaw.

Personally, I deeply thank all of those who supported me in this journey. My family and friends who've hold on across the distance, my 'Southampton family', and those who beyond their supervisory 'role' in this project offered their advice as colleagues and became my friends. My most sincere thanks to you all.

Notation

Throughout this thesis, two types of notation have been used:

Scalar notation:

All the scalars are indicated in mathematical form as $a, b, c \ldots$. For scalars, a subindex or superindex might be indicated as part of the scalar to identify an specific case of a value. For example, a local coefficient of friction μ_l might be distinguished from a global one μ_g with the indication a subindex as part of the scalar symbol.

Tensor notation:

All tensors of order one or two are indicated in bold case. Most of the first order tensors are indicated in lowercase as $\mathbf{a}, \mathbf{b}, \mathbf{c}, \ldots$ and second order ones with upper case as $\mathbf{A}, \mathbf{B}, \mathbf{C} \ldots$ Some exceptions to this notation are the Cauchy stress $\boldsymbol{\sigma}$ and the left Cauchy-Green deformation tensor $\mathbf{B}$, which are second order tensors, and the material coordinates $\mathbf{X}$, which is a first order tensor.
Third order tensors are indicated in uppercase form as $\mathcal{A}, \mathcal{B}, \mathcal{C}, \ldots$, and fourth order tensors as $\mathbb{A}, \mathbb{B}, \mathbb{C}, \ldots$

Indicial notation:

Vectors (first order tensors) are also indicated with indicial notation as $a_i, b_i, c_i \ldots$ Likewise, second order tensors can be indicated in this notation as $A_{ij}, B_{ij}, C_{ij} \ldots$ In the case that a tensor is described with a symbol including a subindex, the indicial notation is indicated with a comma, as $b_{c,i}$.

Acronyms

Abbreviations

2D	Two-dimensional
3D	Three-dimensional
AMP	Anti-microbial peptides
BIU	Biomedical Imaging Unit
CAD	Computer-aid design
CEL	Coupled Eulerian-Lagrangian
CFD	Computational fluid dynamics
CMC	Critical micelle concentration
DE	Dermis
DEJ	Dermal-epidermal junction
DoE	Design of experiment
ED	Epidermis
FCC	Face centred cubic
FE	Finite element
FEA	Finite element analysis
FSI	Fluid-structure interactions
GLIC-E	Great London Innovation Centre - Egham
GLIC-R	Great London Innovation Centre - Reading
GMS	Global median strain
GRM	Generalised relaxation mode
HD	Hypodermis
IQR	Interquartile range
LMS	Local median strain
PEG	Polyethylene glycol
PEO	Polyethylene oxide
PVR	Peak value range
RH	Relative humidity
SA	Sensitivity analysis
SC	*Stratum corneum*
SCF	Sub-cartridge force
SPH	Smoothed particle hydrodynamics
VE	Viable epidermis
WCT	Wall clock time
xSA	Extended sensitivity analysis

Finite element models

DRS	Dermis-rigid solid
DS	Droplet sliding
LF	Laminar flow
SG	Skin-guard
SGS	Skin-guard-shave prep
SRS	Solid-rigid skin-shave prep
TCF	Taylor-Couette flow

Chapter 1

Introduction

The modelling of the wet shaving process requires a multi-physics approach that gathers together mechanical behaviour of the materials in the razor cartridge, its parts and mechanisms, the non-linear behaviour of the human skin and the non-Newtonian behaviour of the shave preps. The consumer shaving style defines the dynamic conditions of the shaving process. Setting the outlines for the development of a multi-physics modelling framework to characterise the interaction of skin and wet shaving products, this chapter provides the objective of this thesis project, the followed methodology and the project outputs. The outline of the chapter's contents describes the work flow of the project, delivering a full image of the integration of the different phenomena involved in wet shaving.

The human skin is subject to a wide range of tribological interactions on a daily basis. This is the case of wet shaving, where the skin interacts with shaving devices in a hydrated low friction environment (provided by the shave prep —any foam, gel or cream used to ease the gliding of a razor cartridge over the skin surface) during a shaving stroke. This activity involves complex coupled multi-scale physical phenomena such as non-linear deformation, surface physics, shear rate dependent fluid viscosity and fluid-structure interactions. The aim of the project was to characterise and unravel some of the key multi-physics interactions taking place between the skin, shave prep (gel/-foam) and razor. This was achieved by developing a modelling environment based on multi-physics finite element techniques using the experimental framework developed by the industrial sponsor, Procter and Gamble (P&G), for skin deformation as a starting point.

1.1 Objective

The objective of the project was the development of a multi-physics modelling framework that characterises the interactions between the skin, razor and shave preps in

shaving stroke simulations. This computational modelling platform was developed for P&G for its use in the design process of new high performance shaving systems. Its implementation allowed the assessment of the shave prep behaviour during the shaving stroke and how it is affected by the cartridge design, providing advantages in the performance evaluation prior to production, and reducing the prototyping costs. Further contributions were achieved by the development of a micro-mechanical model of the human skin. This model was developed with the support to the Biomedical Imaging Unit, at the Southampton General Hospital, for the evaluation of effect of the skin topography and its mechanical properties on the distribution of strain and stress across the skin, during deformation and contact interactions involved in skin tribology.

1.2 Methods

The development of the modelling framework for the characterisation of wet shaving interactions involved the fluid-structure interactions (FSI) of the components: skin, razor cartridge, and the shave prep (shaving foam/gel). These components were first characterised individually, accounting for their mechanical properties and/or geometrical parameters. Given the experimental framework provided by P&G for the characterisation of the skin and the razor cartridge, a critical aspect of the development of this project involved the experimental characterisation of the shave prep viscous and adhesive behaviours, its implementation in a finite element environment, and the optimisation of the computational models so that runtimes are kept to a minimum. The experimental tribological characterisation of the shave preps was performed at the facilities of P&G at the Great London Innovation Centres in Reading (GLIC-R) and Egham (GLIC-E), in the United Kingdom. The adhesive behaviour of the shave prep was captured by the use of the contact angle measuring facilities in the electrochemistry laboratory at the University of Southampton. The development of the image-based micromechanical antomical model of the human skin involved the acquisition and preparation of a human skin sample into histological slides, digitalisation of the slides and image processing for the construction of a finite element mesh. The individual skin layers were represented according to the literature parameters and tested under in-plane deformation and indentation.

The modelling of single components was followed by the modelling of two-component interactions, prior to the integration of the three component in the multi-physics modelling framework. The interactions of the shave prep with the skin and cartridge were captured in the coupled Eulerian-Lagrangian (CEL) finite element environment provided by Abaqus 6.14 (Simulia, Dassault Systèmes, Providence, RI, USA) which features advanced constitutive models and multi-physics solvers. Supercomputing capabilities of P&G Research and Development centre in Cincinnati, OH, USA were used for the multi-physics simulations.

1.3 Project outputs

The developed modelling framework provides several benefits to the sponsoring company, P&G. The short terms benefits include:

- **In-depth knowledge of the effects of the model parameters on the behavioural and simulation runtime performance.** These effects were evaluated through a series of sensitivity analyses.
- **Fluid adhesion characterisation.** The model captured the spreading and adhesive behaviour of the shave preps on different surfaces, showing a realistic distribution under different shearing conditions.
- **Effects of skin surface topographic features (microscopic scale) on the macroscopic response to deformation and tribological interactions.** Based on an anatomical model, the influence of these features were studied in terms of skin stress/strain, for further application in the study of the protection layer formation under the blades.

In the long term, the expected outputs are:

- **Faster performance analysis.** The performance analysis will require only the manipulation of the parameters defining the characteristics of the model (i.e. shave prep properties and shave stroke dynamics), substitution of newly designed cartridge parts, and the use of the computational resources available.
- **Reduction in the need of experiments.** Experiments required will be reduced to the verification of the model and the acquisition of the shave preps parameters required for the model.
- **Consumer perception identification.** The consumer perception is recorded in P&G facilities in terms of ease of sliding, noise produced at shaving, quality of shaving, general comfort, among others. The computational model of the products used by the consumer will provide virtual measurements that are to be connected to consumer perception.
- **Forward design.** Once the comfort parameters are identified, the composition of the shave prep and the cartridge material and geometry can be manipulated to improve the performance of the foam and razor. As part of the design process, this will mean that (instead of a design-prototype-test loop prior to fabrication) the process would require a design-evaluation loop prior to verification followed by product production.

1.4 Outline

Following the project work flow diagram (**Figure 1.1**), it can be visualised how the wet shaving components (skin, shaving foam, cartridge) and consumer preferences are linked together in the development of the multi-physics modelling framework, contributing with the sponsoring company in the search of increasing the customer satisfaction.

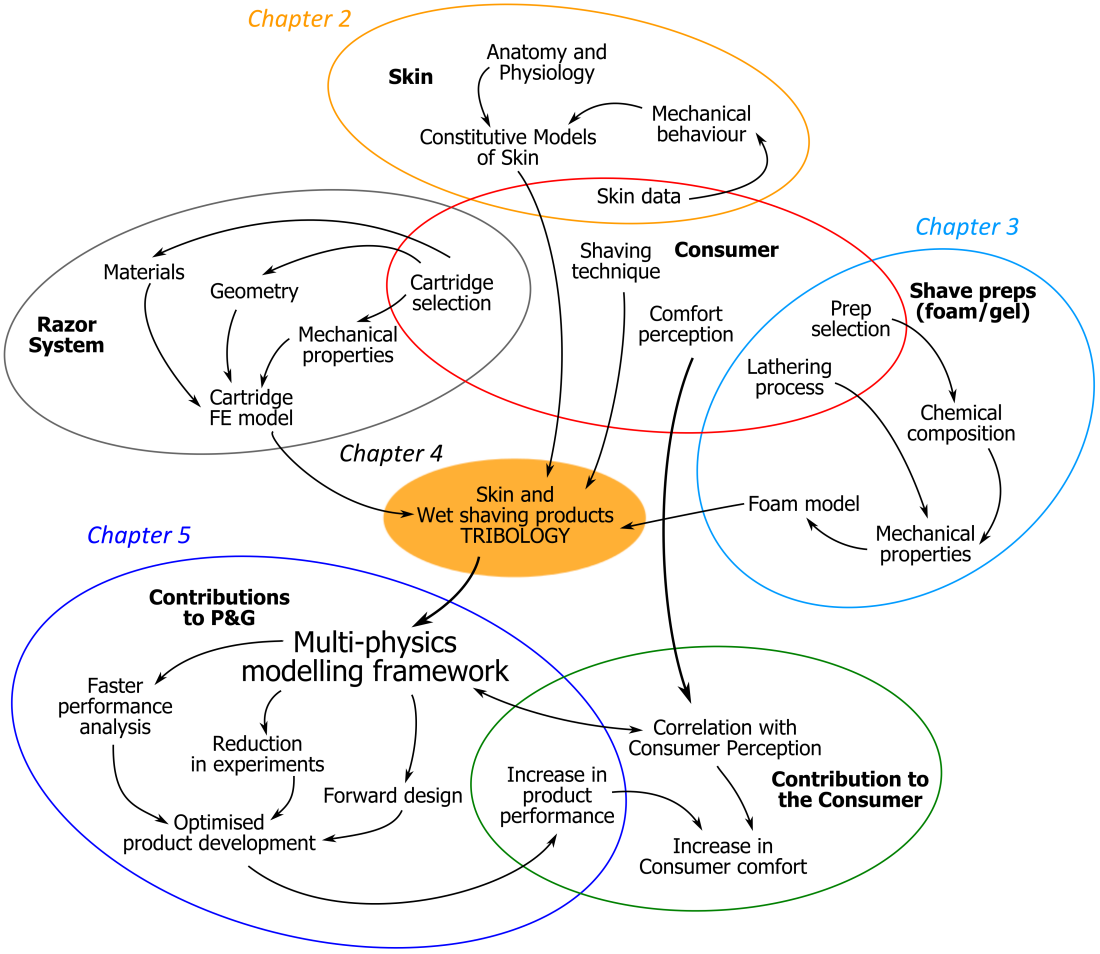

Figure 1.1: Work flow diagram of the development of the skin and wet shaving products interaction multi-physics modelling framework, including the project contribution to the sponsoring company and the consumer.

Figure 1.2 shows the three wet shaving components represented by a coloured oval (blue for the shave prep, yellow for the skin and grey for the razor cartridge); the information available (literature/experimental background) of each component is shown inside the ovals, where no overlap between the components is observed. The contributions made to each component during the development of this project are indicated with the inwards arrows, and the outcomes from the analyses with the outwards ones. The overlapping areas show how the two-component interactions are characterised and how they 'feed' the multi-physics modelling framework.

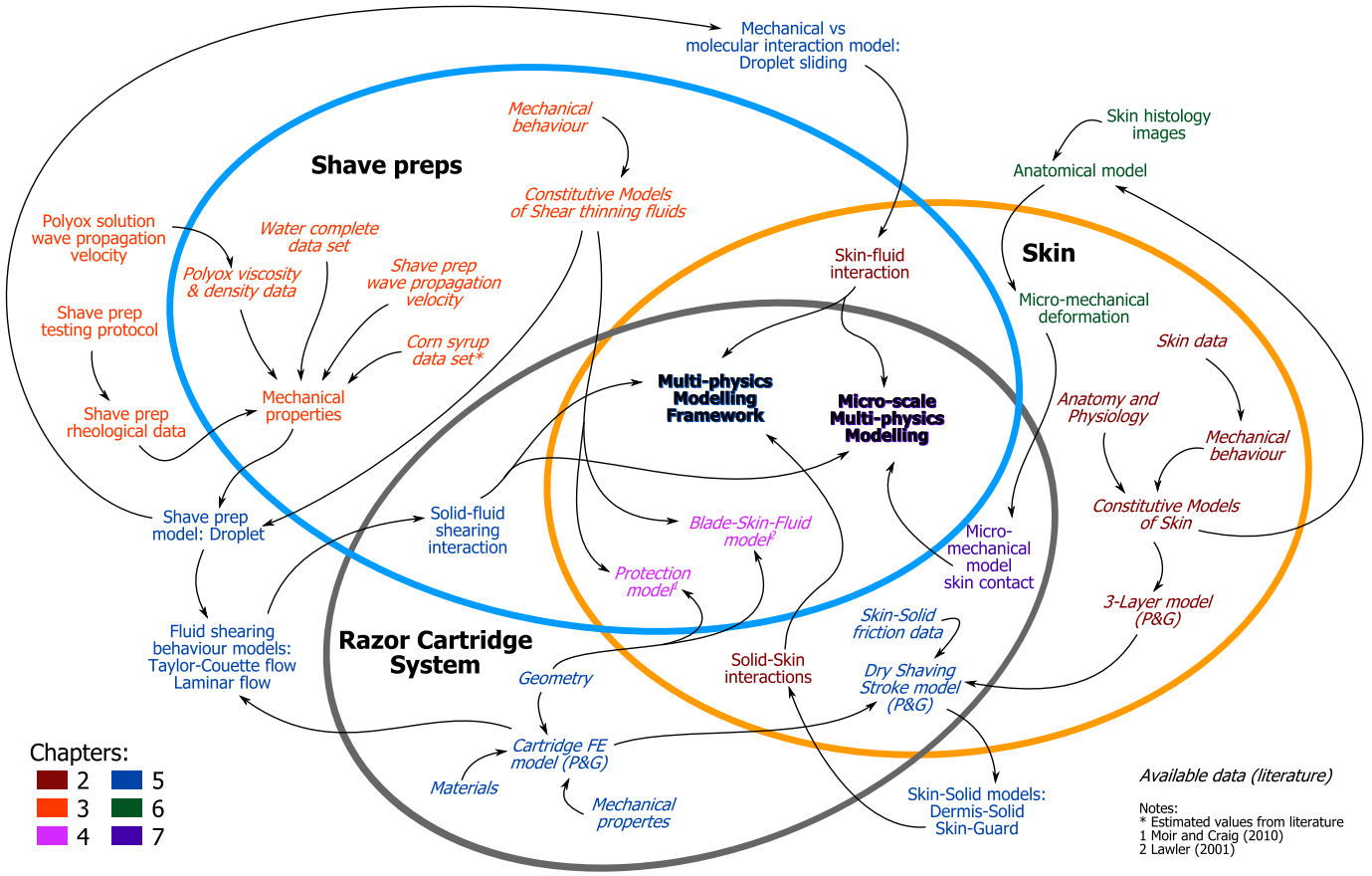

Figure 1.2: Contents diagram. The ovals representing the three shaving stroke components (skin - yellow, shave prep - light blue, and razor cartridge system - grey), intersect each other at the different 2-components interactions (skin-fluid, solid-skin, and solid-fluid). In the centre, where the three components interact, the multi-physics modelling frameworks (macro and micro-scale) are located. The data available from the literature is shown in italics. The contributions to the project located outside the ovals, either take some of the available data to explore the individual 2-component interactions or show the identified requirements to complete the required data for the characterisation of those interactions. The arrows show which subjects have been taken to complete the contributions (arrow towards the contribution) and the subject they contribute with (arrow leaving the contribution). Each subject and contribution are coloured to represent the chapter where they are described or discussed.

The contents in **Figure 1.2** are colour coded with the aim to provide a visual index of the chapter contents. The anatomy and physiology of skin are described in **Chapter 2**. As a multi-layer composite, each skin layer is described and further related with their role in the overall mechanical behaviour of skin. In this chapter, it is included the description of the commonly used constitutive models adopted in this project to represent the skin elastic and viscoelastic behaviour. A brief description of the frictional behaviour of skin is also provided.

The physics behind the shave preps, both as foams and interstitial fluid, are described in **Chapter 3**, going from the bubble formation to the viscous behaviour of shave preps (either as foam or interstitial fluid). A review of the constitutive models adopted in this project to represent shear thinning fluids is included, a long to the description of the most common testing method to characterise the shave preps. A brief description of the molecular contact parameters that describe the fluid-solid interactions is also included. The experimental procedures adopted for the rheological characterisation of the shave prep viscous response and its contact interactions with the cartridge materials are explained later in **Section 3.7**. As precedents of this project, the description of the existing shaving stroke models and a discussion of their limitations is provided in **Chapter 4**.

Chapter 5 covers the theory behind the fluid-structure interactions and the process to develop the multi-physics modelling framework. It involves the computational characterisation of the shaving prep, skin and razor cartridge, and the characterisation of the interactions between each shaving stroke component under adhesive and shearing conditions. These interactions were incorporated in a simple version integrating the three shaving stroke components, providing the bases for the full cartridge multi-physics modelling framework. **Chapter 6** describes the development of a skin anatomical model and its application for the assessment of the effects of the skin topography and the effect of humidity during in-plane deformation at a microscopic scale. **Chapter 7** describes the application of this micro-mechanical model to tribological interactions of the skin. The conclusions of this project can be found in **Chapter 8**, where the outcomes of the project and its further application are discussed.

Chapter 2

Anatomy, physiology, mechanics and constitutive models of human skin

The skin is a multi-layered composite material, acting as the main physical barrier between the exterior and interior of the human body. In this chapter, a review of the skin anatomy and physiology is presented, explaining the link between the mechanical properties and structure/composition of each skin layer. As part of the review, an analysis of the most common constitutive models used to represent the non-linear mechanical behaviour of this tissue is also provided. The applicability of these models to specific physical conditions is examined for the selection of the most appropriate constitutive models to represent the skin behaviour in the ***multi-physics modelling framework*** *and the* ***anatomical skin model*** *developed in this PhD project. Of high relevance for the tribological interaction of the skin with wet shaving devices, this chapter also includes the basic information on frictional response of human skin, and the lubricating action provided by the shave prep.*

The skin is a complex multi-layer tissue, consisting of three main layers: the hypodermis, dermis and epidermis, from the inside out. Within these layers, various appendices (to be subsequently detailed) connected to the nervous system provide sensory mechanisms to sample the external environmental conditions, particularly when these conditions represent a potential hazard to the skin (Burns et al., 2004; Shimizu, 2007). The structural, mechanical and biochemical properties of the skin layers and the various sensory cells make the skin a highly multi-functional biophysical interface which provide mechanical protection as well as thermoregulatory functions. This will be detailed in the next sections.

Mechanical protection involves the three skin layers, the sensory-receptors providing the sense of touch and the presence of hair. The hypodermis provides damping of impact forces; the dermis and hypodermis control the levels of in-plane deformation;

the epidermis forms a thin strong layer of dead cells on the skin surface that acts as a mechanical barrier from the environment. This outer layer, the *stratum corneum*, is covered in a layer of fatty acids that controls the water loss in the skin. The sense of touch is provided by mechano-receptors specialised for the detection of tactile sensation, pressure and vibration at low deformation (such as the Merkel cells, and the Pacinian and Meissner corpuscles), and nociceptors (free nerve ending) specialised for the detection of potential skin damage at high deformation (e.g. puncture, cuts) (Shimizu, 2007).

Finally, hair provides mechanical protection by two means: on the one hand, high concentration of neural terminals at the base of the hair follicles allows the detection of slight movement of hair, providing high sensitivity to low forces acting on the skin (e.g. wind, insects); on the other hand, hair also provides mechanical cushioning and reduction of skin-skin friction (Veijgen et al., 2013c) (e.g. armpits, pubis).

The skin barrier function is confined to the epidermis, which provides an impermeable layer preventing water loss with high strength to prevent penetration of harmful substances (Hendriks et al., 2006; Pedersen and Jemec, 2006). In the *stratum corneum*, **chemical protection** is provided in the first instance by deposition of the sebaceous and sweat glands secretions, which allow to maintain stable internal conditions underneath the skin surface. The sebum produced by the sebaceous glands forms the fatty acids coating on the skin surface, that, with pH levels between 4 and 6, acts as a bactericide (Shimizu, 2007). Sweat also contains small amounts of anti-microbial peptides (AMP), aminoacids that increase the chemical protection at the skin surface against a broad spectrum of pathogenic microorganisms (Burns et al., 2004). In case of skin rupture, other bacteria and pathogens can enter the skin, for which case the keratinocytes forming the epidermis increase the AMPs production (Burns et al., 2004). For further protection, immune system cells (e.g. phagocytes, lymphocytes) constantly patrol the different skin layers in search of pathogens, and triggering the primary immune response when necessary (Burns et al., 2004).

Being the interface between the body and the external environment, the skin plays an important role in the regulation of body temperature. Preserving a constant temperature is advantageous for the well functioning of the body, so the environmental conditions do not interfere with the metabolic processes (Burns et al., 2004). However, the temperature in the body can be affected by intense activity (e.g. sports), emotional stimulus, immune response (e.g. fever, infammation), or environmental conditions.

The fat tissue in the hypodermis provides **thermal insulation**, but for **thermal regulation**, the skin involves hair, peripheral blood vessels, and sweat glands, which react to physical stimuli sensed by the cutaneous thermo-receptors. The normal or "physiological" temperature in the human skin is about 34°C, and specific cold and warmth

receptors are 'activated' at abnormal thermal conditions. Cold receptors detect temperatures between 14-30°C (1-20°C lower than the normal skin temperature), while higher temperatures of 32-45°C are detected by warmth receptors. Thermal sensation depends on the rate and degree of temperature change, and according to the sensed conditions, the thermo-receptors send signals to the hypothalamus to activate the thermal regulation response (Burns et al., 2004). In case of low temperatures, shivering is stimulated for elevating the body temperature, and contraction of the peripheral blood vessels prevents diffusion of heat through the skin surface. Furthermore, the activation of the *arrector pili* muscles attached to the hair root sheath, moves the hair to a position where more air is trapped at the skin surface (i.e. goose bumps), providing an enhanced thermal insulation (Burns et al., 2004; Shimizu, 2007). In the case of high temperatures, the skin response involves the endocrine system which activates the sweat glands so the body is cooled down by perspiration. Conversely, high temperatures induce dilatation of the peripheral blood vessels so that heat is brought to the skin surface for thermal diffusion through sweat evaporation and radiation (Burns et al., 2004). It is worth mentioning that thermal pain is triggered when either damage or noxious stimuli is caused at cold temperatures, or when the skin temperature is above 45°C (in this later case, the signal is produced by nociceptors rather than warmth receptors) (Burns et al., 2004). With such stimuli, the withdrawal reflex is triggered, activating muscular response to remove the skin from the heat source and prevent further damage to the skin tissue (Pur, 2001).

All together, the skin structure and its appendices, provide great protection to the human body from the external environment. Being of high relevance for this project, the next section describes in detail the structure, function and mechanical behaviour of the skin layers. For further information about the integumentary system involving the skin and its appendices the reader is referred to Burns et al. (2004); Shimizu (2007), and Marieb and Hoehn (2010).

2.1 Skin anatomy and physiology

The hypodermis, dermis and epidermis layers are distinguished by their own particular constitution. The simpler structure is observed in the hypodermis, while the composition of the dermis and epidermis shows higher structural complexity, as schematically represented in **Figure 2.1**.

The **hypodermis** is mainly constituted of fat cells grouped in fat lobules, that give a granular appearance to this layer. Its thickness is largely variable across the body and between individuals, being particularly thicker at the cheeks, tights, palms and soles (Kong et al., 2011; Shai et al., 2009; Shimizu, 2007). As already mentioned, it provides impact and thermal protection to internal organs and the muscles. Furthermore,

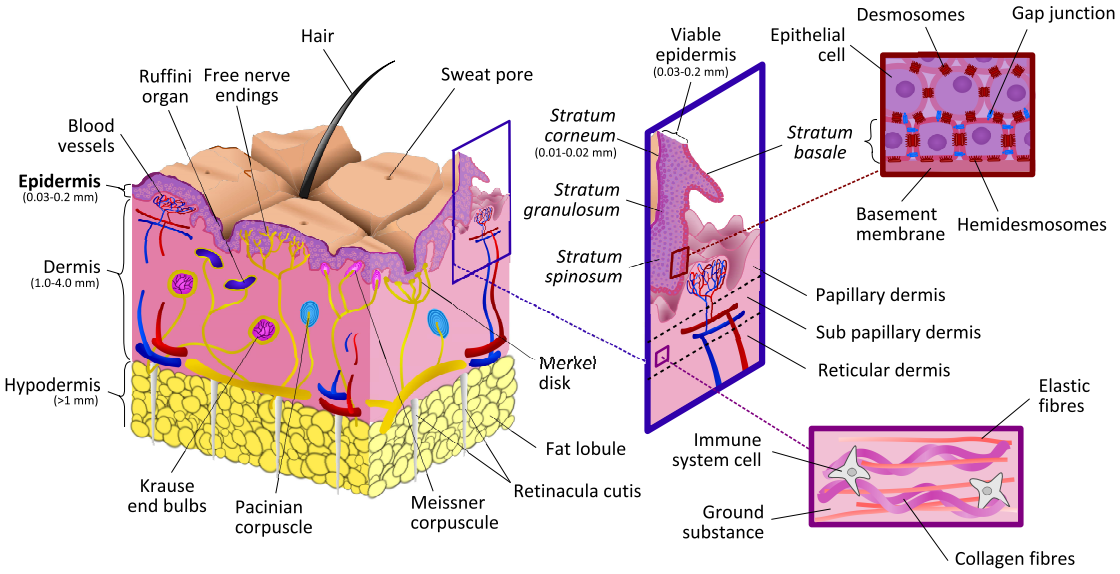

Figure 2.1: Simplified structure representation of the skin anatomy, featuring the epidermis, dermis and hypodermis. The deepest layer, the hypodermis, is formed by fat lobules. Across this layer, the *retinacula cutis* fibres provide an anchoring structure between the dermis and the muscular fascia. The dermis is formed by collagen and elastin fibres, embedded in a ground substance matrix. These components are arranged differently through the depth of this layer: in the reticular dermis, above the hypodermis, the collagen and elastin fibres are packed in dense bundles; while closer to the epidermis, these fibres are loose allowing patrolling of the immune system cells in the subpapillary and papillary dermis. The papillary dermis has a characteristic egg-crate shape formed by dermal papillae in which the capillary blood vessels loops are embedded. The epidermis is formed by epithelial cells. Through the dermal-epidermal junction, the blood vessels provide nutrients and oxygen to the basal epidermal layer. This, the *stratum basale*, contains 'mother cells' that constantly replicate to form and renew the epidermis. As the epithelial cells replicate and migrate towards the surface and away from the source of nutrition, their structure changes, forming the *stratum spinosum* and *stratum granulosum* before they keratinise to form the strongest epidermal layer called *stratum corneum*. Due to the different mechanical properties of the *basale*, *spinosum*, and *granulosum* strata with respect to the *stratum corneum*, these softer layers are commonly referred as the viable epidermis. The sensory receptors of pressure, vibration and deformation (Ruffini organs, Krause end bulbs, Pacinian and Meissner corpuscules and Merkel disks) are distributed trhoughout the dermis, but the pain receptors (free nerve endings) are located in the viable epidermis.

it eases the sliding of skin on top of the muscles during deformation. Excess of sliding is prevented by fibre bundles (*retinacula cutis*) that connect the hypodermis to the dermis with the deeper tissue (e.g. the *fascia* covering the muscles) (Burns et al., 2004; Shimizu, 2007).

The **dermis** is mainly constituted of type I/III collagen and elastic fibres embedded in a "viscous gel-like" matrix formed of polysaccharides and proteoglycans, known as *ground substance* (Burns et al., 2004). The dermis thickness varies between 1.0 and 4.0 mm according to body location. Through its depth, it can be classified in three sublayers according to their fibre-matrix arrangement, into reticular, subpapillary and papillary dermis, from the inside out (Geerligs, 2010; Shimizu, 2007). The reticular dermis, forming 90% of the dermis (Wu, 2006), is characterised by soft elastic fibres bundles oriented parallel to the skin surface, and dense bundles of stiffer collagen fibres, that together induce the stretch-stiffening elastic response of skin on tension (Shimizu, 2007). The elastic fibres are highly elastic, and help to maintain the skin

natural residual tension and are key in providing the skin with its elastic recoil ability (Bischoff et al., 2000; Boyer et al., 2009; Humbert et al., 2012; Tran et al., 2007). The collagen fibres, representing 70% of the dermis dry mass, are composed of tropocollagen molecules forming 'wormlike' fibres (Kuhl et al., 2005; Shimizu, 2007) arranged in a preferred orientation along the body. The *Langer lines*, describing the skin natural tension lines (Langer, 1861), are associated with such preferred orientation of the collagen fibres bundles (Ní Annaidh et al., 2012a), providing different tensile responses to the skin for particular stretch directions on the skin surface (Flynn et al., 2011b; Kuhl et al., 2005; Liang et al., 2010; Marieb and Hoehn, 2010; Shimizu, 2007; Vexler et al., 1999; Wu et al., 2006b). Above the reticular layer, in the subpapillary and papillary dermis, the collagen and elastic fibres are loose and tortuous, allowing immune system cells to navigate in the ground substance, looking for infiltrated bacteria (Marieb and Hoehn, 2010). The dermis is anchored to the dermal-epidermal junction (DEJ) through type VII collagen fibrils and fibrillin-rich microfibril bundles (Naylor et al., 2011).

Most of the skin appendices, such as the oil and sweat glands, hair roots, sensory receptors and blood vessels, are contained within the dermis. The sensory receptors distributed through the dermis and epidermis are connected to a network of nerves that transfers the sensory information to the central nervous system (Burns et al., 2004; Goldstein, 2008). While the thermo and mechano-receptors (detecting pressure, vibration and deformation) are located at the dermis, the free nerve terminals or nociceptors (detecting high deformation, extreme temperatures and chemical irritation, providing the 'pain' sensation) are located in the viable epidermis (Goldstein, 2008). Veins and arteries are contained within the dermis, forming a network of vessels in the deeper dermis (*subcutaneous plexus*) that ascend to form a secondary network within the subpapillary dermis (*subpapillary plexus*) (Shimizu, 2007). The capillary vessels extend up to the dermal papillae, from where they provide with nutrients and oxygen to the epidermis through the DEJ (Burns et al., 2004; Shimizu, 2007).

The **epidermis** is made of epithelial cells, of which 95% are *keratinocytes* that are kept together via specialised cell adhesion complexes called *desmosomes* (Burns et al., 2004). This layer, varies between 0.03 and 0.2 mm in thickness across the body (Jachowicz et al., 2007; Shimizu, 2007). It goes through a continuous regeneration process to maintain and repair its barrier function. The epidermal layer originates at the *stratum basale*, a one-cell-thick layer of stem cells attached by hemidesmosomes to a basement membrane rich in type IV collagen, located at over the DEJ where they are able to receive the nutrients from the capillaries located in the dermal papillae. These cells constantly replicate and renew the epidermis, pushing the older cells towards the surface. As they get farther from the source of nutrition, the cells go though a transformation process from keratinocytes to corneocytes that desquamate at the skin surface (Burns

et al., 2004). In this migration process, taking place over a period of 13-18 days (Epstein and Maibach, 1965), the cells experience structural changes which lead to the identification of four sub-layers (five in the case of palmo-plantar skin).

Above the *stratum basale*, larger keratinocytes are grouped in the thickest layer of the epidermis, the *stratum spinosum*, where the desmosomes keeping the cells together give this layer a prickled appearance. Nearer to the surface, the cells start dying due to the lack of nutrients and the glycolipids contained in the cells are released into the inter-cellular space. In this layer, the *stratum granulosum*, the cells become flatter and the lamellar granules contained in the cells become more evident; at this stage, the keratinisation process begins. In palms and soles, a layer of nucleated flat cells characterises the *stratum lucidum* (Burns et al., 2004). In the outermost layer, the *stratum corneum*, the cells complete the transformation into corenocytes: they have lost their nuclei and become fully keratinised, providing a strong mechanical barrier for the skin (Burns et al., 2004; Shimizu, 2007). The integrity of the outer layer is provided by the glycolipid content in the inter-cellular space and the strength of the desmosomes (Wu et al., 2006a). The extreme contrast in mechanical properties between the keratinocytes and corneocytes allows the epidermis to be divided into two layers: the viable epidermis (also known as living epidermis), and the *stratum corneum*. Final degradation of the desmosomes leads to desquamation of the skin surface.

At its exterior surface, the skin is characterised by topographic features (i.e. skin furrows and crests) visible to the naked eye. Depth and orientation of the topographic features vary according to body location and age. These features, often referred as "microrelief" (Asserin et al., 2000; Lévêque and Audoly, 2013; Piérard et al., 2003), redirect the stresses in the skin surface as they unfold (Geerligs, 2010; Geerligs et al., 2011a; Leyva-Mendivil et al., 2015; Pedersen and Jemec, 2006). In this PhD project, it was demonstrated through 2D finite element simulations that the topographic features of the skin can modulate the macroscopic strains taken in the *stratum corneum* during in plane deformation (Leyva-Mendivil et al. (2015), **Chapter 6**).

Each of the components of the skin layers contribute in one form or another to the overall mechanical response of the skin. However, such response is affected by the structural arrangement of the skin elements (e.g. geometry, fibre orientation), providing a complex anisotropic mechanical behaviour. In the following section, the link between the skin structural components and the mechanical response of the skin is reviewed.

2.2 Mechanical behaviour of skin

The mechanical properties of the human skin, which are highly dependent on a relatively large number of intrinsic and extrinsic factors, can vary according to body location, individuals, age, sex, race, hormonal status, hydration conditions (Burns et al., 2004; Flynn et al., 2011b; Marieb and Hoehn, 2010; Shimizu, 2007; Vexler et al., 1999). In addition, the exposition to environmental conditions (e.g. humidity, UV radiation, temperatures) and chemicals (e.g. topical medication, skin care products), can modify temporarily or permanently the skin mechanical behaviour (Geerligs et al., 2011a; Jachowicz et al., 2007). All these variability factors, added to the intrinsic structural complexity of the tissue and its anisotropic mechanical response, make it impossible to characterise with a single experimental test the full mechanical behaviour of the skin.

From a macroscopic point of view, the skin mechanical behaviour can be described as anisotropic, stretch-stiffening and viscoelastic. These characteristics are distributed in different proportions through the skin, according to the physical characteristics of each layer, but are not necessarily present in every skin layer. The skin **anisotropy** is conditioned by its stratified structure, fibre direction in the dermis, and the geometry of the skin layers interfaces and its surface topography; the **stretch-stiffening elasticity** is due to the combined response of the elastic and collagen fibres in the dermis and *retinacula cutis* in the hypodermis; and the **viscoelasticity**, by the combination of viscous effects provided by the fat tissue in the hypodermis, the ground substance in the dermis, the glycolipids in the epidermis, and the time-dependent structural rearrangements (e.g. fibre uncrimping and realignment in the dermis). Following the approach for the description of the anatomy and physiology, the distribution of the mechanical characteristics of the human skin is explained next for each skin layer, from the inside out.

2.2.1 Mechanical behaviour of the hypodermis

The **hypodermis** is partially responsible for the skin viscoelastic response (Geerligs et al., 2008; Marieb and Hoehn, 2010). Its main contribution is observed in the overall skin mechanical response, under indentation. Loads applied normal to the skin surface cause the displacement of the fat tissue in between the upper skin layers and muscle. This motion attenuates and disperses the applied forces and provides a delayed response to deformation (Geerligs, 2010; Geerligs et al., 2008; Marieb and Hoehn, 2010). In tension, the high compliance of the hypodermis allows the sliding of the skin (Delalleau, 2007), thus reducing the shear of the tissue at low deformation. The *retinacula cutis* fibres, form a strong collagen network that connects the dermis to the muscular fascia (Burns et al., 2004), preventing excessive displacement of the skin over the bony structures. It is probable that these fibres play an important role in the

mechanical behaviour of the skin (Geerligs, 2010), as they provide with a high non-linear mechanical response to the hypodermis (Sommer et al., 2013). However, these structures are often ignored in the skin computational models.

2.2.2 Mechanical behaviour of the dermis

In the dermis, the anisotropic, stretch-stiffening elastic and viscoelastic effects are simultaneously observed. The anisotropic elastic response in this layer is determined by the fibre-reinforcement nature of the tissue: in tension, the strength is provided by the collagen and elastic fibres; in compression, the mechanical response depends mostly on the nearly incompressible ground substance matrix. In addition, the orientation of the collagen fibre bundles along the Langer lines, provide further in-plane anisotropy in tension.

The stretch-stiffening elasticity is provided by the combined response of the collagen and elastic fibres (Delalleau, 2007; Pedersen and Jemec, 2006). As mentioned in **Section 2.1**, the elastic fibres are highly elastic, for which at small deformation they provide low resistance to tensional forces. The undulated shape of the collagen fibres do not provide any resistance to deformation until fully stretched. The gradual mechanical 'activation' of these fibres shifts the strain-stress curve of the skin from a low stiffness and toe region at smalls strains, to a high stiffness region at large ones (Bischoff et al., 2000; Burns et al., 2004; Delalleau, 2007; Gu et al., 2010; Hendriks, 2005; Hendriks et al., 2004; Huang et al., 2010; Hung et al., 2009; Moir and Craig, 2010; Ní Annaidh et al., 2012b). The preferred orientation of the collagen fibres plays a crucial role in the skin anisotropy, in which the skin tensile stiffness is dependent on the loading direction . Ní Annaidh et al. (2012a) showed that the skin is stiffer when loaded parallel to the Langer lines, whose direction is correlated with collagen fibres preferred orientation. This behaviour has been widely reported in the literature , and is characteristic of most soft tissues in many mammalian species (Flynn et al., 2011b; Kuhl et al., 2005; Liang et al., 2010; Marieb and Hoehn, 2010; Shimizu, 2007; Vexler et al., 1999; Wu et al., 2006b).

The ground substance provides a significant contribution to the skin viscoelasticity because of its inherent water content (Delalleau, 2007; Derler and Gerhardt, 2012; Hendriks, 2005). Loading of the skin modifies the space where the ground substance is contained, forcing the fluid to flow through the porous structure formed by the collagen and elastic fibres, providing a delayed response to deformation (Gerhardt et al., 2008; Kumagai et al., 2011; Zahouani et al., 2011). By unloading the skin, the ground substance flows back in place and the skin recovers its original shape. Depending on the intensity and time of the applied load, the recovery can take a few seconds or up to a several minutes. A good example of this delayed response involve pressure marks

made by wearing tight clothing. Intrinsic and extrinsic ageing causes significant alterations to these viscoelastic effects (Zahouani et al., 2011).

2.2.3 Mechanical behaviour of the epidermis

The main function of the epidermis is to provide a direct mechanical barrier for the protection of skin (Pedersen and Jemec, 2006). Although the epidermis contribution to the tensile mechanical response of the skin is lower than that of the dermis, it plays an important role in the preservation of such barrier. Due to its stratified and multiphasic structure, the epidermis features anisotropic and viscoelastic characteristics.

The anisotropy of the epidermis is provided by the variation in properties with cell keratinisation and degradation as a function of depth. In the viable epidermis, the strength is provided by the desmosomes and cytoskeleton of the keratinocytes; in the *stratum corneum*, the thicker wall of the corneocytes, and their respective desmosomes, provide this outer layer with higher stiffness than that in the viable epidermis (Geerligs, 2010). Albeit homogeneous properties are expected at each sublayer of the epidermis, the non-linear elastic response of the epidermis is influenced by the intricate complexity of its geometry (i.e. the undulating shape of the dermal-epidermal junction and the surface topographic features) that produces an uneven distribution of strains across this skin layer (Leyva-Mendivil et al., 2015).

In the epidermis, providing that the *stratum corneum* is not in its softest state (e.g. under high humidity conditions, or after full water intake), mechanical stresses concentrate into the stiffer *stratum corneum* as the skin furrows fold/unfold during extension and compression (Geerligs, 2010). This 'folding' can be viewed as a 'hinge' mechanism where the strains are concentrated in the deeper area of the furrows, while minimum strains are experienced in the crests (Leyva-Mendivil et al., 2015). With such mechanism, the topographic features of the skin reduce the overall strains experienced by the outer layers of the skin, in comparison of the total applied deformation (Leyva-Mendivil et al., 2015).

Minor viscoelastic effects are also attributable to the flow of glycolipids in the intercellular space, as highlighted by Crichton et al. (2011). With an intercellular space of 2% in volume in the viable epidermis, this effect is more obvious in the *stratum corneum* where intercellular spaces are larger (about 0.1-0.3 μm) (Geerligs, 2010). However, this fluid can be easily washed out and/or replaced by water or moisturising creams that modify the epidermis' mechanical response (Bhushan, 2012; Hendriks et al., 2004; Jemec and Na, 2002; Vexler et al., 1999; Wu et al., 2006b), as explained in **Section 2.3**.

The macroscopic or gross mechanical response of the skin is a direct result of the mechanical properties of its individual structural components and to the way they are assembled together. The next section explains the structural mechanisms that condition the macroscopic skin response.

2.2.4 Description of the overall skin mechanical response to deformation

The skin is subject to deformation on a daily basis. With simple body motion, it experiences in-plane compression, extension, shear, and any combination of these different types of load. When interacting with other objects or itself, the skin can also experience out-of-plane deformation. Contact interactions such as those resulting from self contact, sitting on a chair or shaving, generates out-of-plane compressive deformation. Through adhesive forces (such as plaster stripping) or pinching of the skin, tensile forces can generate tensile out-of-plane deformation of the skin.

When the skin is subject to **in-plane extension**, high elasticity is provided by the elastic fibres at low deformation. The gradual activation of the collagen fibres provides a stiffening response at larger deformation. The epidermis applies little resistance to deformation as the skin furrows open in a 'hinge-like' response, and the crests displace as the skin extends. Releasing the in-plane tension allows the skin to recover its original shape; however, a delayed response is observed, caused by the flow of the interstitial fluid in it and the various structural damping mechanisms (such as the ground substance between the collagen and elastin fibres). See **Figure 2.2**.

In-plane compression of skin induces buckling of the collagen and elastic fibres in the dermis and bulging/wrinkling of the epidermis, as the skin slides on the hypodermis. The latter effect is expressed as compression and extension zones at the bulging surface, which are a direct result of the geometrical instabilities provided by the topographic features. Compressive stresses are taken by the bulk material of the fibres and the ground substance. As a result of the increment in pressure, the ground substance is eventually displaced from the area of compression. Due to the continuity of the skin (connected throughout the body surface), in-plane compression of the skin is typically accompanied by stretch in the surrounding areas, and *vice versa*, with the mechanical response mentioned above. Like for in-plane extension, releasing the compressive force allows the skin to recover its original shape with a viscoelastic response caused by the flow of the ground substance between the collagen and elastic fibres. See **Figure 2.3**.

By the application of **out-of-plane extension** (e.g. stripping of a plaster), the skin is displaced on top of the hypodermis and is subject to tensile forces. In the epidermis, the top part of the skin unfolds, opening the skin furrows, and it is the collagen fibres that provide major resistance to deformation, as observed with in-plane extension. The ground substance flows into the pulled area, by the negative pressure caused by the

skin displacement; likewise, some fat lobules could be also drawn to this region. As the skin is pulled out, further displacements that could put the skin at risk of damage are prevented by the action of the *retinacula cutis* in the hypodermis, maintaining the attachment of the skin to the muscular fascia. See **Figure 2.4**. The ground substance and fat tissue will provide a delay in the skin recovery as the forces are released, as explained above.

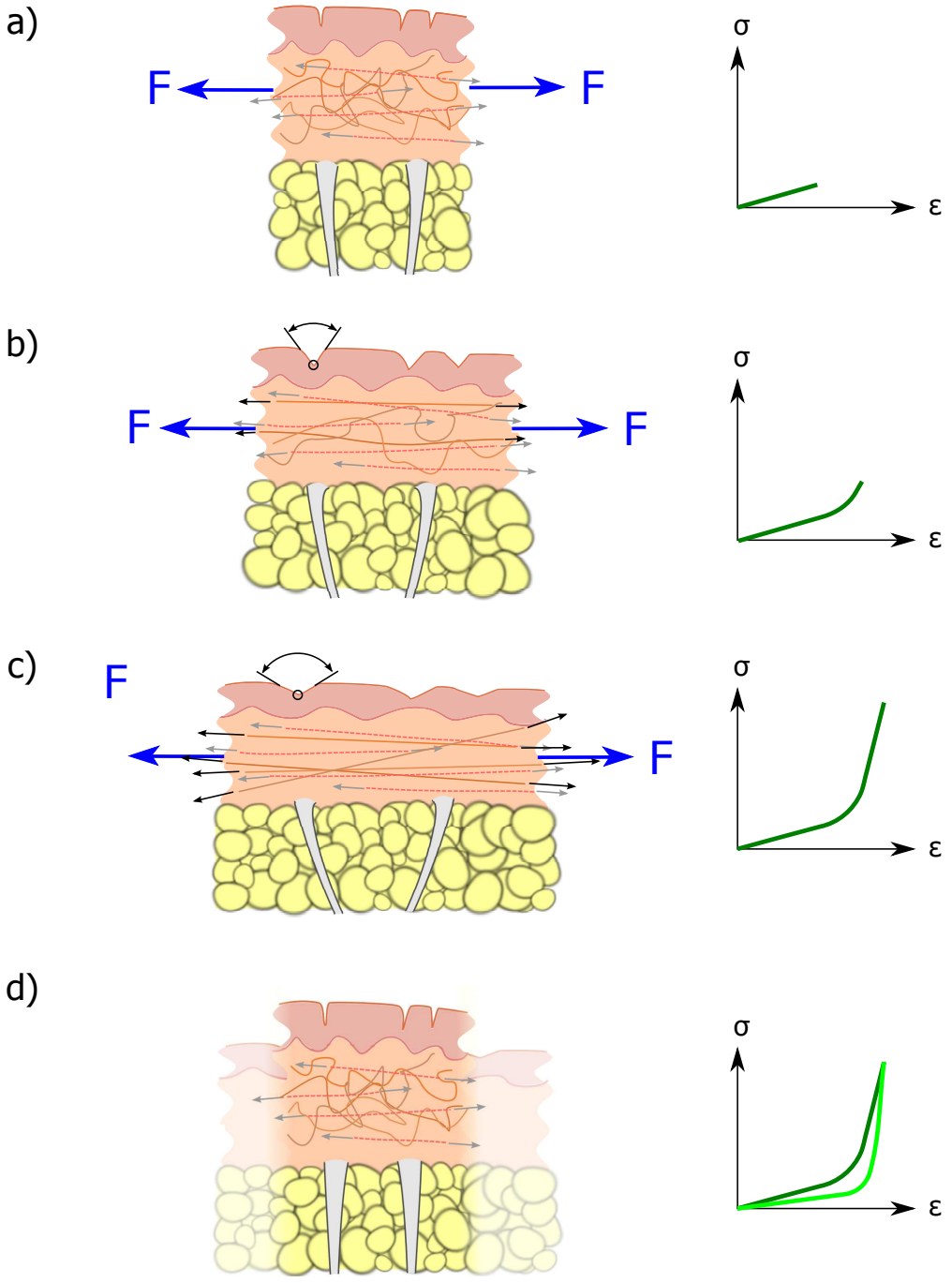

Figure 2.2: Skin subject to in-plane tension forces. *a*) A small force of magnitude F is applied and taken mostly by the elastic fibres (dotted pink lines, forces represented by the small grey arrows). The skin shows linear behaviour in the stress-strain curve. As the force increases, *b*) the skin gradually stiffens as the collagen bundles (solid lines) start stretching (black arrows); at the dermis, the skin furrows open up exhibiting a 'hinge-like' response. At higher forces, *c*) all the tension is distributed among all the elastic and collagen fibres showing a linear but much stiffer behaviour (Huang et al., 2010). *d*) Once the force is withdrawn, the skin takes its original shape, preserving the natural pre-tension in the elastic fibres, with a delayed (viscoelastic) response due to the interstitial fluid in the skin and various structural damping mechanisms. In all cases, the skin slides on top of the hypodermis; the *retinacula cutis* (white bundles) activate at large displacement of the skin, preventing damaging tension in the tissue. The uni-directional stress-strain diagram for each case is shown on the right.

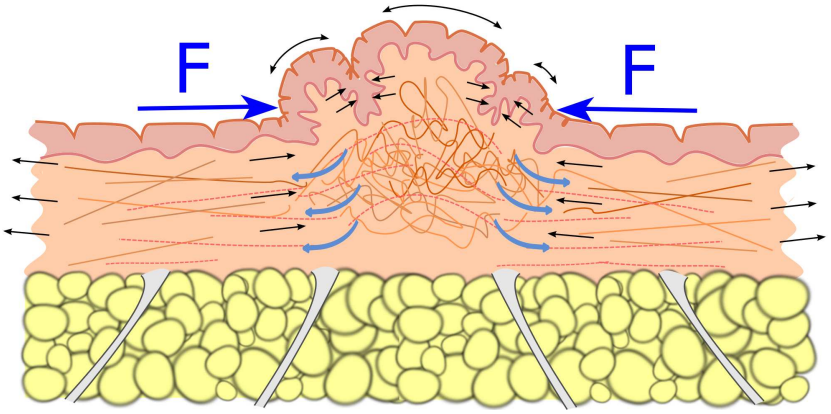

Figure 2.3: In-plane compression of the skin. With the application of a compressive force of magnitude F in-plane, the skin slides on the hypodermis into a compression area where buckling of the collagen and elastic fibres and bulging of the epidermis are observed. Such bulging, influenced by the skin topographic features, causes compression and extension zones in the epidermis. The applied pressure causes the ground substance to leave the compression area (light blue arrows). As a reaction to the in-plane compression, tensile effects are observed outside the compression region (black arrows).

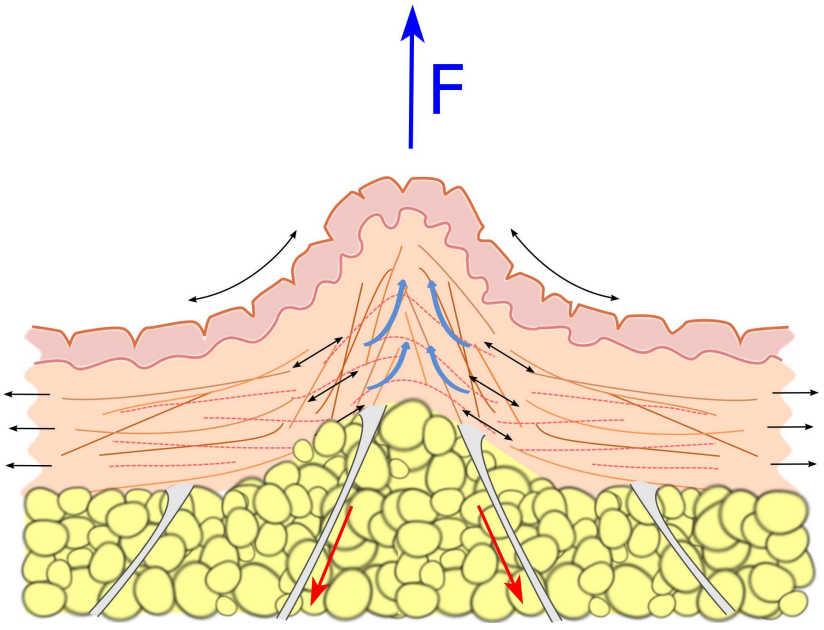

Figure 2.4: Skin subject to out-of-plane tension forces. As the skin is pulled out with a force of magnitude F, the skin ridges open due to bending of the epidermis. In the dermis, tensile resistance is provided by the collagen and elastic fibres. Although the skin is allowed to displace on top of the hypodermis, further resistance (red arrows) is provided by the *reticula cutis* to avoid excessive deformation of the skin.

Out-of-plane compression consists on a the application of a compressive force that presses the skin against the underlying tissue (e.g. shaving, sitting on a chair). Under this action, the surface of the skin adapts to the contact surface, where often the topographic features of the skin condition the real contact area, which is smaller than the apparent one. In the dermis, the collagen and elastic fibres are unable to bear any significant load, unless bending of the skin structure occurs, causing tensile effects in the reticular dermis. The applied pressure is then borne by the bulk material of the fibres and the dermal matrix, causing the ground substance to flow away from the deformed area. Likewise, the fat lobules are displaced out of the area of high indenting pressure. The magnitude and duration of the applied force have a direct influence on the time necessary for the skin to recover its original shape. See **Figure 2.5**.

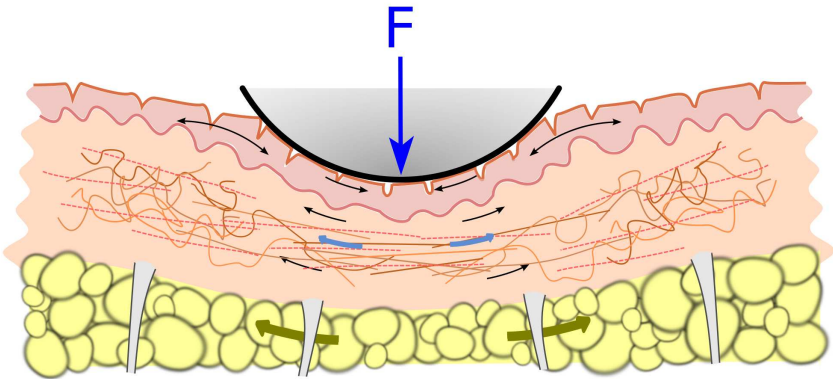

Figure 2.5: Out-of-plane skin compression. Under indentation load of magnitude F, the skin surface adapts to the indenting surface (although gaps at the location of the skin ridges are expected), and most of the pressure is taken by the epithelial cells in the epidermis and the bulk tissue and ground substance matrix in the dermis. If bending occurs in the dermis, the collagen and elastic fibres can provide tensile resistance. The applied pressure causes the displacement of the ground substance (light blue arrows) and the fat lobules (dark yellow arrows) towards the outside of the area under pressure.

Due to the skin structural complexity (stratified intricate geometry with different mechanical properties at each layer), the characterisation of the mechanical response of this tissue as a single layer is highly complex. As reviewed in this section, each the skin layers provide a different response depending on the loading conditions. For this reason, the load-dependency (magnitude and direction) of the skin mechanical response needs to be taken into account for its experimental characterisation, as discussed in the next section.

2.2.5 Experimental characterisation of the skin mechanical properties

Numerous experimental techniques have been applied to characterise the mechanical behaviour of the human skin. However, due to the complex structure of this tissue, the type of data obtained through a single experimental test is dependent on the specific loading conditions applied. This is reflected in the great dispersion of values found in

the literature to describe the skin mechanical behaviour (e.g. Young's modulus). This variability in the results depends not only on the inter/intra subject variability, but also on the nature of the experimental techniques used to analysed the tissue. The dimensions and magnitude of the test parameters determine which of the skin layers or zones are mechanically stimulated and for which the mechanical response is captured. Further variability is expected if the test is performed *in vivo* or *ex vivo*, and with different environmental conditions, as explained next for the most common techniques applied for the experimental characterisation the human skin mechanical response.

The characteristics of the load is an important factor as it can be used to measure specific anisotropic properties or to provide a general response of the skin tissue. The in-plane anisotropy of the skin elastic response can be measured by the application of tensile forces at along different directions, either applying a single tensile load at the time as in the case of **uniaxial** and **extensometry** tests (Wan Abas and Barbenel, 1982), or multiple simultaneous forces as in the case of **biaxial** and **multiaxial** tensile tests (Kvistedal and Nielsen, 2004; Payne, 1991). Other techniques measure the in-plane anisotropy by means of **shear wave propagation**, taking measurements along specific directions (Vexler et al., 1999; Xing Liang and Boppart, 2010). From a different perspective, (Flynn et al., 2010) developed a technique for testing the elastic response of the skin for multiple directions, in and out of plane. Axisymmetric loading can be applied to the skin for the characterisation of the general in-plane elastic response, as it occurs for **suction** (Hendriks et al., 2006; Payne, 1991) and **torsion** (Delalleau, 2007) tests, or for the characterisation of the out-of-plane elastic response, as in the case of **indentation** tests (Delalleau et al., 2006; Flynn et al., 2011b; Geerligs et al., 2011b; Payne, 1991). In many cases, the measurements of the skin mechanical properties are performed in pre-conditioned skin or with quasi-static loading conditions, reducing short-time dynamic effects from the measurements (Shames and Cozzarelli, 1997); however, the experimental techniques mentioned above can be adapted to account for the time-dependent response characterising the skin viscoelasticity (Boyer et al., 2009; Crichton et al., 2011; Gerhardt et al., 2009a; Jee and Komvopoulos, 2014; Khatyr et al., 2006; Vexler et al., 1999).

With the complex skin microstructure, where each layer have different mechanical characteristics, capturing the mechanical response of the skin is a complicated procedure. In many cases, the measurements are highly dependent in the number of layers loaded in the experimental tests. Two examples of this high sensitivity to the scale of the experiment are **suction** and **indentation** tests. In suction tests, the dimension of the suction cup is related with the depth of the tissue for which the mechanical properties are obtained; while a 2 mm diameter cup captures the response of the tissue up to maximum 0.2 mm depth, a 6 mm diameter cup can capture up to 1 mm depth (Boyer et al., 2009; Hendriks et al., 2006; Khatyr et al., 2006). For indentation tests, good practice in indentation test involves a material 15 times larger and 10 times thicker

than the indenter radius, and a maximum indentation depth of 1/5 of the material thickness, to avoid boundary effects (Karduna et al., 1997). So, the indenting probe diameter and the applied normal load (or indenter displacement) are to be selected according to the number of layers to be analysed.

Further source of variation in the measurements of the skin mechanical properties can be observed in *in vivo* and *ex vivo* testing. *In vivo* testing has the advantage of providing a mechanical response of skin under 'working conditions' such as natural pretension, body temperature and blood flow in the capillaries (Delalleau, 2007). Although skin is often pre-conditioned to obtain consistent results (Flynn et al., 2013; Hendriks et al., 2006), skin is able to recover its normal conditions allowing re-testing of its mechanical properties at different conditions (e.g. relative humidity, application of moisturising creams). Furthermore, *in vivo* testing allows to capture the skin mechanical response over time: the skin mechanical properties can change due to different cream treatments, UV damage, scaring and ageing, and *in vivo* test can be used to trace these changes as they develop (Jemec and Na, 2002). These advantages come at the cost of not being able to test single inner skin layers, for which its mechanical properties have to be indirectly estimated from the skin surface deformation. *Ex vivo* testing allows to excise the skin to separate its layers for their individual testing (Crichton et al., 2011; Geerligs, 2010; Ní Annaidh et al., 2012b). Although the natural conditions of the skin are lost, *ex vivo* testing allows the mechanical characterisation of individual skin components, even beyond the limits of skin recovery (for which pain would be an ethical limitation to *in vivo* testing) (Ní Annaidh et al., 2012b; Wu et al., 2006a). Nevertheless, some concerns on *ex vivo* testing involve the loss of blood and ground substance from the dermis, as well as the loss of integrity of the sample during its preparation (Delalleau, 2007; Geerligs, 2010).

Many of these experimental techniques are sensitive enough to capture the changes in mechanical properties of the skin when subject to specific varying environmental conditions that alter the structure and mechanical properties of the *stratum corneum* (e.g. moisture). Changes in the material properties of this outer layer can modify the mechanical response of the epidermis, and thus the response of the whole skin tissue. The factors responsible for the sensitivity of the *stratum corneum* mechanical properties to environmental conditions are explained in the next section.

2.3 Sensitivity of the mechanical properties of the *stratum corneum* to environmental conditions

The mechanical response of the *stratum corneum* is highly sensitive to environmental conditions such as relative humidity (hydration) and the presence of a lubricant (e.g. body lotion, shave prep) (Jemec and Na, 2002; Papir et al., 1975; Park, 1972).

Water or other liquid substances can affect the cohesion of the corneocytes as they penetrate into the inter-cellular space or are absorbed by the keratinised cells, resulting into the modification of its mechanical and contact interaction properties (Burns et al., 2004; Delalleau, 2007; Jachowicz et al., 2007; Jemec and Na, 2002; Moir and Craig, 2010; Pedersen and Jemec, 2006; Vexler et al., 1999; Wu et al., 2006b; Zhai and Maibach, 2002). Excessive absorption of water into on the *stratum corneum* can result in swelling up to five times its volume after one hour of soaking in water (Zhai and Maibach, 2002), creating inter-cellular cisternae that modify the structure of the corneocytes arrangement (Warner et al., 2003). These structural alterations are translated into a significant reduction of stiffness in the skin outer layer (Geerligs et al., 2011a; Wu et al., 2006b). The lipidisation (hydration with an oily substance) of the *stratum corneum*, does not affect the barrier properties nor the overall mechanical properties of the skin, but major effects are observed in the plasticity of the skin (i. e. affecting the *stratum corneum*'s stiffness) (Jemec and Wulf, 1999; Jemec and Na, 2002). These changes in mechanical properties of the *stratum corneum* can have a great effect on the distribution of strains in the subjacent layers as demonstrated in a recent computational study (Leyva-Mendivil et al., 2015), explained in **Chapter 6**.

The skin hydration or lipidisation can also either increase or reduce the coefficient of friction of the skin. In the presence of water, an increase in skin friction with various materials is attributed to the softening of the skin that increases the contact area and higher work of adhesion caused by the absorption of moisture in the contact area; the saturation of the *stratum corneum* with water allows the formation of a fluid film at its surface that reduces the friction as hydrodynamic lubrication takes place (Derler and Gerhardt, 2012; Pailler-Mattéi and Zahouani, 2004). As the skin dries out, the coefficient of friction observed in the original dry conditions is recovered (Sivamani et al., 2003). An inverse effect is observed in the presence of oily substances such as cosmetic products, where the coefficient of friction is immediately reduced, followed by an increase in coefficient of friction after $\sim$ 25 minutes (Koudine et al., 2000; Sivamani et al., 2003).

Changes in the biophysical properties of the *stratum corneum* with environmental conditions are of high relevance for many applications, especially those involving tribological interactions. It high humidity conditions, the *stratum corneum* stiffness is reduced, resulting in lower shear strength on the skin surface (Gefen, 2011). Furthermore, a higher coefficient of friction between the skin and a contacting object can result in higher shear stresses within the skin, leading to skin damage in the form of pressure ulcers and friction blisters (Guerra and Schwartz, 2011; Kirkham et al., 2014; Sopher and Gefen, 2011; Zhong et al., 2006).

2.4 Constitutive models of skin

The mechanical behaviour of the human skin can be represented through a variety of constitutive models that are able to capture certain aspects of the skin complex mechanical response to deformation. The skin can be represented as a single or a multilayer structure, accounting or not for its anisotropic and viscoelastic response. The skin elastic response can be represented by linear elasticity at low deformation, or nonlinear elasticity (this includes a variety of hyperelastic modes) at moderate to large deformations. Entropic formulations capture the behaviour of the dermis, where the collagen fibre network plays an important role in the anisotropy of the skin. Viscoelastic effects can be incorporated to the elastic response implementing formulations that represent combinations of dashpot and spring elements or as through biphasic (poroelastic) constitutive models. These constitutive models are explained as follows.

2.4.1 Linear isotropic elasticity

In a linear elastic material stress is a linear function of the current strain; if load is removed, the material is able to recover its original shape (Belytschko et al., 2000). Many materials that behave linearly at low deformation reach a plastic region at which larger stresses induce permanent residual deformations. The full linear isotropic elastic model can be described with two elastic constants, the Young's modulus E and the Poisson's ration υ, as explained next. From these two constants, the first Lamé's parameter λ, and the shear modulus or second Lamé's parameter G are obtained as:

$$\lambda = \frac{E\upsilon}{(1+\upsilon)(1-2\upsilon)} \tag{2.1}$$

and

$$G = \frac{E}{2(1+\upsilon)} \tag{2.2}$$

The linear elasticity tensor $\mathbb{C}$ is defined as:

$$\mathbb{C} = \lambda \mathbf{I} \otimes \mathbf{I} + 2G\mathbb{I} \tag{2.3}$$

where $\mathbf{I} = \delta_{ij}\boldsymbol{e}_i \otimes \boldsymbol{e}_j$ is the second order identity tensor, and $\mathbb{I} = \frac{1}{2}\left[\delta_{ik}\delta_{jl} + \delta_{il}\delta_{jk}\right]\boldsymbol{e}_i \otimes \boldsymbol{e}_j \otimes \boldsymbol{e}_k \otimes \boldsymbol{e}_l$ is the fourth order symmetric identity tensor.

With the strain tensor $\boldsymbol{\varepsilon}$ accounting for change of length and orientation, the Cauchy stress tensor $\boldsymbol{\sigma}$ is given by:

$$\boldsymbol{\sigma} = \mathbb{C} : \boldsymbol{\varepsilon} \tag{2.4}$$

Many experimental tests characterising the skin elastic behaviour report its Young's modulus, but not its Poisson's ratio. A commonly accepted assumption for soft tissues

is a Poisson's ratio $0.3 < \upsilon < 0.5$ (Delalleau, 2007; Gu et al., 2010; Khatyr et al., 2006; Pailler-Mattei et al., 2008). The selection of a Poisson's ratio value of 0.5 is justified under the assumption that the skin is mainly made of water (i.e. fully incompressible) (Bhushan, 2012; Jachowicz et al., 2007; Limbert, 2011; Sokolov and Woodworth, 2005; Xing Liang and Boppart, 2010), while lower values for this parameter are selected under consideration of the compressibility effects provided by other components of the skin (i.e. quasi-incompressible) (Adams et al., 2007; Delalleau, 2007; Derler and Gerhardt, 2012; Geerligs, 2010; Hendriks and Franklin, 2010; Lapeer et al., 2011; Makhsous et al., 2007; Sokolov and Woodworth, 2005; Sopher and Gefen, 2011; Wagner et al., 2008). The assumption of quasi-incompressibility is often taken in the computational modelling of skin for the prevention of computational singularities in finite element analysis (FEA) calculations (Diridollou et al., 2001).

The linear elastic formulation is valid for small deformations only (Aba, 2014c; Delalleau, 2007; Taylor and Zienkiewicz, 2005). Thus, as skin deformation is large with small loads, a better approach is to consider the skin as an hyperelastic material.

2.4.2 Hyperelasticity

Hyperelasticity describes non linear elastic behaviour by means of a strain energy function, Ψ, which represents the energy per volumetric unit stored in the material upon deformation. Hyperelastic models are conservative, which implies that elastic deformations are fully recovered upon unloading. Hyperelastic formulations provide a better fit to the stretch stiffening response of skin, as registered in experimental tests. Furthermore, they can be extended to represent the skin viscoelasticity (Taylor and Zienkiewicz, 2005).

The deformation gradient $\mathbf{F}$, also known as the 'Jacobian matrix of deformation' (Belytschko et al., 2000), represents the deformation in non linear continuum mechanics as:

$$\mathbf{F} = \frac{\partial \mathbf{x}}{\partial \mathbf{X}}; \qquad F_{ij} = \frac{\partial x_i}{\partial X_j} \tag{2.5}$$

where $\mathbf{x}$ represents the spatial position of a material point in the current configuration and $\mathbf{X}$ its spatial position in the initial one (these terms and their application in finite element analyses are later explained in **Chapter 5.1**). The right and left Cauchy-Green deformation tensors, $\mathbf{C}$ and $\mathbf{b}$, respectively, are defined as:

$$\mathbf{C} = \mathbf{F}^T \cdot \mathbf{F} \tag{2.6}$$

and

$$\mathbf{b} = \mathbf{F} \cdot \mathbf{F}^T \tag{2.7}$$

Then, for hyperelastic materials, the principal deformation invariants can be defined as (Belytschko et al., 2000; Holzapfel, 2004):

$$I_1(\mathbf{C}) = \mathbf{I} : \mathbf{C}; \qquad I_1(\mathbf{b}) = \mathbf{I} : \mathbf{b} \tag{2.8}$$

and

$$I_2(\mathbf{C}) = \frac{1}{2}\left(\mathbf{I} : \mathbf{C} - \mathbf{I} : (\mathbf{C} \cdot \mathbf{C})\right); \qquad I_2(\mathbf{b}) = \frac{1}{2}\left(\mathbf{I} : \mathbf{b} - \mathbf{I} : (\mathbf{b} \cdot \mathbf{b})\right) \tag{2.9}$$

If λ_i $(i = 1, 2, 3)$ are the principal stretches (i.e. eigenvalues of $\mathbf{F}$), the principal invariants can be written in terms of principal stretches as:

$$I_1 = \lambda_1^2 + \lambda_2^2 + \lambda_3^2 \tag{2.10}$$

and

$$I_2 = \frac{1}{2}\left(\lambda_1^2\lambda_2^2 + \lambda_1^2\lambda_3^2 + \lambda_2^2\lambda_3^2\right) \tag{2.11}$$

The volume ratio J term is introduced, as:

$$J = \det(\mathbf{F}) = \lambda_1\lambda_2\lambda_3 \tag{2.12}$$

Hyperelastic models can be represented as a strain energy function of the principal deformation invariants and the volume ratio as $\Psi(I_1, I_2, J)$ or the principal stretches $\Psi(\lambda_1, \lambda_2, \lambda_3)$. In order to separate the effects of shape changes (induced by shear) and change of volume (induced by hydrostatic pressure), the deformation gradient can be separated into a *deviatoric* (i.e. distortional) and a *volumetric* terms through a multiplicative decomposition (Belytschko et al., 2000):

$$\mathbf{F} = \mathbf{F}_d \cdot \mathbf{F}_v, \qquad \text{where} \quad \mathbf{F}_d = J^{-1/3}\mathbf{F}, \quad \mathbf{F}_v = J^{1/3}\mathbf{I} \tag{2.13}$$

With this approach, the deviatoric term of the strain energy function is a function of the invariants derived from the deviatoric deformation gradient (identified by the 'bar' symbol as $\bar{I}_1, \bar{I}_2$), and the volumetric term is a function of the volume ratio:

$$\Psi = \Psi_d\left(\bar{I}_1, \bar{I}_2\right) + \Psi_v(J) \tag{2.14}$$

A common approach in the field of rubbers modelling is to represent the *deviatoric* term of the strain energy function for isotropic hyperelastic materials in the **general polynomial** form (Samani and Plewes, 2004):

$$\Psi_d\left(\bar{I}_1, \bar{I}_2\right) = \sum_{i+j=1}^{m} C_{ij}\left(\bar{I}_1 - 3\right)^i\left(\bar{I}_2 - 3\right)^j \tag{2.15}$$

where m is the polynomial order and C_{ij} is a material parameter. The most common formulations for Ψ_d derived from **Equation 2.15** are explained in **Table 2.1**.

Table 2.1: Hyperelastic formulations derived from the general polynomial form (**Equation 2.15**), with order $m = 1, 2, 3$.

m	Deviatoric strain energy function	Formulation
1	$\Psi_d = C_{10}\left(\bar{I}_1 - 3\right)$	Neo-Hookean
	$\Psi_d = C_{10}\left(\bar{I}_1 - 3\right) + C_{01}\left(\bar{I}_2 - 3\right)$	Mooney-Rivlin
2	$\Psi_d = C_{10}\left(\bar{I}_1 - 3\right) + C_{11}\left(\bar{I}_1 - 3\right)\left(\bar{I}_2 - 3\right)$	Extended Mooney
3	$\Psi_d = C_{10}\left(\bar{I}_1 - 3\right) + C_{01}\left(\bar{I}_2 - 3\right) + C_{11}\left(\bar{I}_1 - 3\right)\left(\bar{I}_2 - 3\right) + C_{20}\left(\bar{I}_1 - 3\right)^2 + C_{30}\left(\bar{I}_1 - 3\right)^3$	Jamus-Green-Simpson
	$\Psi_d = C_{10}\left(\bar{I}_1 - 3\right) + C_{20}\left(\bar{I}_1 - 3\right)^2 + C_{30}\left(\bar{I}_1 - 3\right)^3$	Yeoh

These formulations have been widely used in the literature to model the behaviour of the human skin under different mechanical loading conditions. The **neo-Hookean** formulation has been applied to define the skin (single layer) and hypodermis to assess pressure-induced muscle pain sensitivity by Finocchietti et al. (2011); analyses of micro-needle insertion in the skin (Kong et al., 2011); to study the relative contribution of the different skin layers to mechanical response in suction tests (Hendriks et al., 2006); and for studying the effect of wrinkles and micro-climate on skin lesions (Sopher and Gefen, 2011). The **Jamus-Green-Simpson** formulation has been applied in the analysis of the heel mechanical response by Luo et al. (2011); however, the constants C_{01}, C_{20} and C_{30} were set to zero in their study, resulting in the **extended Mooney** model. Flynn and McCormack (2010) have combined the use of different constitutive models for the study of ageing effects on wrinkling in a multi-layer skin model, representing the *stratum corneum* as a neo-Hookean material, the dermis as an orthotropic hyperelastic tissue, and the hypodermis as a **Yeoh** material.

Another formulation used for the respresentation of the skin behaviour is the **Ogden formulation**, whose deviatoric strain energy term is defined by:

$$\Psi_d = \sum_{i=1}^{m} \frac{2\mu_i}{\alpha_i^2}\left(\bar{\lambda}_1^{\alpha_i} + \bar{\lambda}_2^{\alpha_i} + \bar{\lambda}_3^{\alpha_i} - 3\right) \tag{2.16}$$

where α_i, μ_i are the Ogden parameters, and the initial shear modulus is defined by $\mu_0 = \sum_{i=1}^{m} \mu_i$. Although the principal deviatoric strains depend on the deviatoric deformation invariants $(\bar{I}_1, \bar{I}_2)$, the Ogden's strain energy function cannot be written in these terms (Aba, 2014c). The neo-Hookean and Mooney-Rivlin models are special cases of the Ogden model; they can be recovered by setting $m = 1$ and $\alpha_1 = 2$, and $m = 2$, $\alpha_1 = 2$ and $\alpha_2 = -2$, respectively (Aba, 2014c; Holzapfel, 2004).

The **Ogden model** provided a close fit to experimental data in the deformation of facial skin (Flynn et al., 2013); and it proved useful for the assessment of the heel skin

stiffness effect in foot biomechanics (Gu et al., 2010) and evaluation of pressure ulcer formation risk (Luboz et al., 2014; Oomens et al., 2013).

The *volumetric term* of the strain energy function, defined to provide mathematical simplicity to the calculations, is related to the volumetric deformation. In this term, the incompressibility constraint $J = 1$ is enforced by defining it in the form of $p\,(J-1)$ (Holzapfel, 2004). Other approaches define this term in relation with the material bulk modulus:

$$\kappa_0 = E/\,(1-2\upsilon) \tag{2.17}$$

as a parameter to account for the hydrostatic pressure p in the material (Horgan and Murphy, 2009). With this decomposed finite element method, the volume ratio field is incorporated and treated as an independent variable, thus discretised independently, leading to stable numerical solutions (Aba, 2014c; Holzapfel, 2004). The volumetric term is defined in different forms as shown on **Table 2.2**. Equation d) is typically implemented in many commercial finite element codes such as Abaqus (Simulia, Dassault Systèmes, Providence, RI, USA), used in this research project.

Table 2.2: Versions of the volumetric term for the strain energy function Ψ_d.

Volumetric strain energy function	References
a) $\Psi_v = -\frac{1}{2}p\,(J-1)$	Lapeer et al. (2011)
b) $\Psi_v = p\,(J-1)$	Hung et al. (2009)
c) $\Psi_v = \sum_{i=1}^{m} \frac{\kappa_0}{2}\,(J-1)^i$	Delalleau et al. (2011); Tran et al. (2007); Flynn and McCormack (2010)
d) $\Psi_v = \sum_{i=1}^{m} \frac{\kappa_0}{2}\,(J-1)^{2i}$	Aba (2014c); Flynn and McCormack (2010); Makhsous et al. (2007)
e) $\Psi_v = \frac{\kappa_0}{2}\left(\frac{J^2-1}{2} - \ln J\right)$	Aba (2014c); O'Callaghan and Cowley (2010)

Hyperelastic models present a series of advantages and limitations. Often, they capture only a portion of the mechanical response. For this reason, the computational characterisation of soft connective tissue is subject to an appropriate fit of the constitutive models to the experimental results (Delalleau, 2007; Hendriks, 2005). For example, the neo-Hookean formulation is able to represent the skin mechanical behaviour, when defined as linear elastic, for relatively small strains only. However, for the fitting of experimental data involving larger deformation, a higher order polynomial is required (Hendriks, 2005). Some models, like the Mooney-Rivlin, are viable for characterisations of strains up to 100% (Ans, 2010); but, in certain cases, the identification the model parameters is ill-defined (Delalleau, 2007).

In the study of skin-razor interactions, it is important to capture the appropriate deformation of the skin under the razor cartridge. For the development of a finite element skin model for these interactions, O'Callaghan and Cowley (2010) performed *in vivo*

testing of facial skin, combining indentation and extensometry techniques, for the experimental characterisation of the hyperelastic and viscoelastic properties of this tissue. Further details about the level of deformation captured in this model can be consulted in their **published patent** O'Callaghan and Cowley (2010). A key requirement in the experimental test was the ability to capture skin bulging between the blades, for which the indentation test was adapted to capture this mechanical response with the use of a slotted indenting die. Several hyperelastic models were explored for the fitting to the experimental data. However, the **van der Waals** hyperelastic formulation was the only model able to capture the experimentally observed skin deformation, including skin bulging at the die slot (O'Callaghan and Cowley, 2010) —this particular response was not observed with the use of other hyperelastic constitutive models.

The **van der Waals** model, which is analogous to equations of state based on entropic approaches (consideration of changes in the system organisation, molecular friction and statistical variations) applied for real gases (Aba, 2014c), is defined as:

$$\Psi = G_0 \left\{ -\left(\lambda_m^2 - 3\right)\left[\ln\left(1-\gamma\right)+\gamma\right] - \frac{2}{3}\vartheta\left(\frac{\tilde{I}-3}{2}\right)^{\frac{3}{2}} \right\} + \frac{\kappa_0}{2}\left(\frac{J^2-1}{2} - \ln J\right) \quad (2.18)$$

where λ_m is linked to the locking stretch, at which asymptotic behaviour is observed, and G_0 the initial shear modulus; the variables $\tilde{I}$ and γ are defined by:

$$\tilde{I} = (1-\beta)\,\bar{I}_1 + \beta \bar{I}_2; \qquad \gamma = \sqrt{\frac{\tilde{I}-3}{\lambda_m^2 - 3}}$$

and the global dimensionless interaction parameter ϑ, accounting for the molecular chains interaction, is defined as

$$\vartheta = \frac{2C_{01}}{3G_0} + \frac{\lambda_m^2}{\lambda_m^3 - 1}$$

where C_{01} is the second Mooney-Rivlin parameter (the Mooney-Rivlin model is derived from the first order general polynomial, **Equation 2.15**, $m = 1$). The linear mixture parameter β varies between 0 and 1, and captures the respective contributions of deformation modes associated with the deviatoric invariants $\bar{I}_1$ and $\bar{I}_2$.

This model has been applied for the modelling of rubbers at large deformations by Pathak (2010), using the Gaussian theory described in **Section 2.4.3** to describe the mechanics of polymer chain networks (which behave similarly to the collagen fibre networks).

With the different hyperelastic models reviewed, the strain energy function Ψ is obtained. Then, the second Piola-Kirchhoff stress tensor $\mathbf{S}$ is obtained by differentiation

of the strain energy function with respect to the right Cauchy-Green deformation tensor or the Green-Lagrange strain tensor $\mathbf{E} = \frac{1}{2}(\mathbf{C} - \mathbf{I})$ as:

$$\mathbf{S} = 2\frac{d\Psi}{d\mathbf{C}} = \frac{d\Psi}{d\mathbf{E}} = \frac{\partial\Psi}{\partial I_i}\frac{\partial I_i}{\partial \mathbf{C}} \tag{2.19}$$

and the Kirchhoff stress is obtained by the push forward operation (or Piola tranformation) (Holzapfel, 2004):

$$\boldsymbol{\tau} = \mathbf{F}\cdot\mathbf{S}\cdot\mathbf{F}^T = J\boldsymbol{\sigma} \tag{2.20}$$

2.4.3 Entropic-based formulations

Like rubbers, many soft biological tissues (e.g. skin dermis) are composed of complex three-dimensional networks of polymer chains assembled into more complex multi-scale structures (Kuhl et al., 2005). These polymer chains can be in equilibrium in a virtually unlimited number of configurations. Perturbation of the chain configuration by the application of thermal fluctuating forces (see **Figure 2.6**) results in the generation of entropic reaction forces. Due to the large amount of possible chain configurations, it would be too complex to describe every molecular chain individually, thus a statistical approach is taken (Holzapfel, 2004; Kuhl et al., 2005).

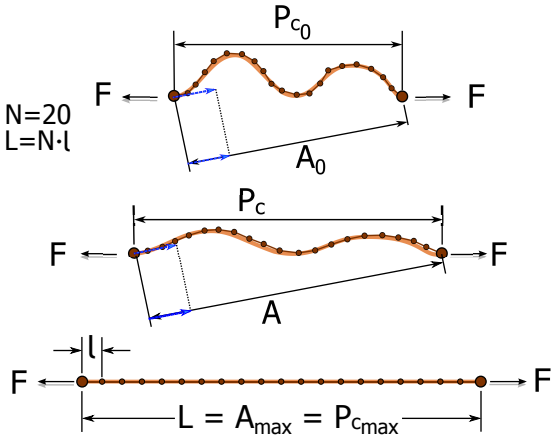

Figure 2.6: Chain representation of a 'wormlike' collagen fibre (Kuhl et al., 2005), during straightening. The collagen chain parameters is characterised by the initial distance P_{c_0} between the two ends of the chain. As the, chain is straightened by the application of a force of magnitude F, this end-to-end distances P_c changes. The chain is composed of N links of length l, thus the total chain length is $L = N \cdot l$. The persistence length A (A_0 at the reference configuration), a sum of the projected distance of each link over the vector indicating the direction of the first link, is included to take into account the pre-stresses on the collagen fibre.

Assuming that the tropocollagen molecules forming the collagen fibres —and any subsequent up-scale assemblies of these molecules —can be represented as chains of rigid links, where the distance between the chain ends is much smaller than the total chain length, the entropic elasticity is based in the probability that one of the chain ends lies within a finite volume (Holzapfel, 2004). Various entropic constitutive models have

been developed to represent the anisotropic and fibrous nature of the skin and, more particularly, that of the dermis.

Gaussian chain model

For a given single *uncorrelated* (freely jointed) polymer chain made of N rigid segments, the Gaussian chain model is used to describe the probability density of the end-to-end vector P_c distribution based on a Gaussian statistics, linking this distribution to the free energy of the chain (Holzapfel, 2004; Kuhl et al., 2005). See **Figure 2.7**a.

Wormlike chain model

Accounting for a single *correlated* wormlike chain, the helicoidal shape can be defined by a smooth curvature of the chain derived from the direction of the first rigid segment. This model incorporates the persistence length parameter A to the estimation of a probability density distribution of P_c (Kuhl et al., 2005). See **Figure 2.7**b.

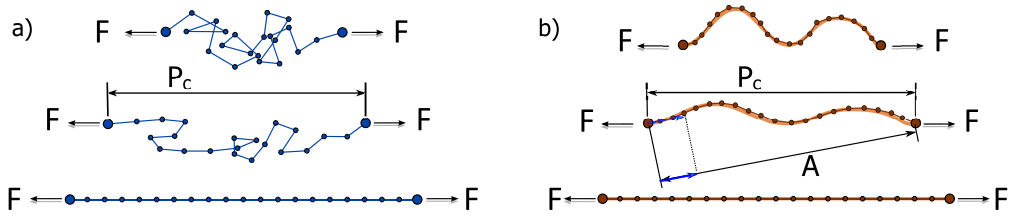

Figure 2.7: Chain configurations for *a*) the Gaussian chain model and *b*) the Wormlike chain model, under the action of a force of magnitude F. P_c indicates the end-to-end chain distance, and A the persistence length of the wormlike chain.

Isotropic eight-chain model (Arruda-Boyce)

In this model, originally proposed by Arruda and Boyce (1993) to capture the mechanics of polymers and rubber within a microscopic cubic unit cell, Bischoff et al. (2000) described the force-stretch response of collagen fibres contained within the ground substance matrix. The material arrangement is described as eight chains contained within an hexahedral bulk material volume, which coincides with the microscopic unit cell. Each fibre is attached to each vertex of the volume in one end, and to the centre of the volume in the other, as shown in **Figure 2.8**. With the use of a cubic unit cell, the fibres do not exhibit a preferred orientation.

Orthotropic eight-chain model

In their work, Bischoff et al. (2002) extended the Arruda-Boyce model to orthotropicity by relaxing the requirements of having a cubic unit cell. Each of the three cell dimensions can be distinct from each other. This simple and elegant assumption allows the modelling of anisotropic properties by controlling the relative ratios of cell dimensions (e.g. a/b, a/c).

Eight-chain transversely isotropic model

Kuhl et al. (2005) developed a eight-chain transversely isotropic model by particularising the orthotropic eight-chain model of Bischoff et al. (2002), in which case $a = b \neq c$.

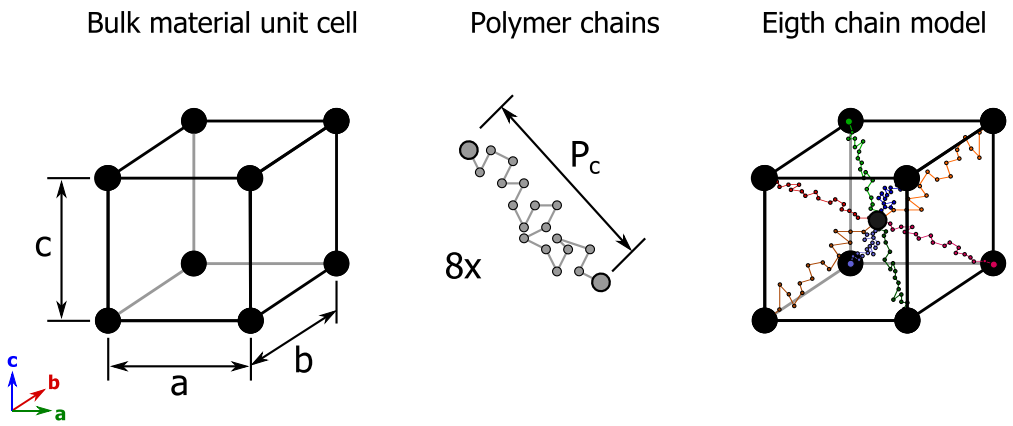

Figure 2.8: The eight-chain model is described by a unit cell of bulk material of dimensions a, b, and c, in which eight polymer chains of end-to-end vector magnitude P_c are arranged so each chain end connects at each vertex and at the centre of the unit cell. In this model, the dimensions of the hexahedral unit cell determine the fibre orientation in the tissue.

Decoupled invariant formulation

Accounting for the 'wormlike' shape of the collagen fibres and microfibrils, Limbert (2011) proposed a mesostructurally-based anisotropic model for biological soft tissues. A decoupled invariant formulation combining hyperelastic and entropic formulations was developed to represent the transversely isotropic and orthotropic behaviour of biological soft tissue. The formulation took into account separate strain energy functions for the shear interaction energy, across and along the fibres. Bischoff et al. (2002), Kuhl et al. (2005) and Limbert (2011) used the experimental results of Lanir and Fung (1974) on rabbit skin to validate their proposed formulation showing a very good fitting to Lanir's experimental results.

Six discrete fibre direction model

Flynn et al. (2011a) takes a different approach, characterising the collagen fibre bundles in sets of six discrete fibre directions, each one parallel to each of the lines drawn by opposing vertices of a regular icosahedron. The strain energy function was defined in terms of strain energy function of the collagen and elastic fibres, accounting for the probability of 'activation' of the fibres, and its contribution to the strain energy function when fully stretched.

A key aspect of the multi-physics modelling framework developed in this project is to account for deformation of the skin in multiple directions. However, data regarding on human facial skin anisotropic behaviour was not available in the literature, as highlighted by Flynn et al. (2015). In the experimental characterisation of facial skin *in vivo*, O'Callaghan and Cowley (2010) captured the tensional properties of the skin in different directions. This data was used for the development of a computational model of facial skin using the median values of the stretch-tension data, for an average skin response in all stroke directions during wet shaving.

2.4.4 Viscoelasticity

The viscoelasticity of a material refers to the combined effects of viscous and elastic behaviours captured by either the changes in the stress-strain curve at loading and unloading (i.e. hysteresis, see **Figure 2.9**a, the changes in the strain over time as a result of the application of a constant load (creep, see **Figure 2.9**b), or the changes in stress at constant strain (relaxation, see **Figure 2.9**c).

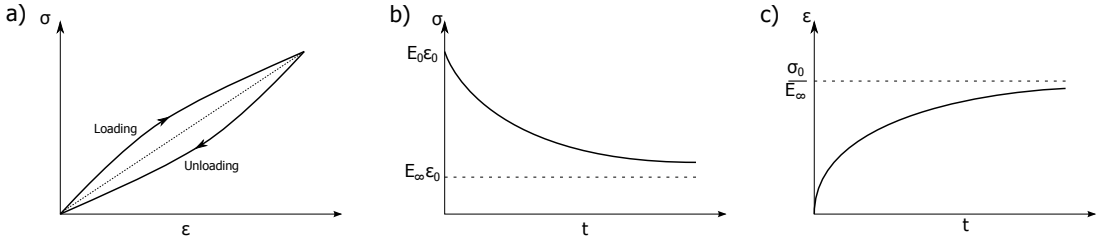

Figure 2.9: Typical viscoelastic material behaviour. It can be captured as changes in the *a*) stress-strain ($\sigma - \varepsilon$) curve at loading and unloading; *b*) changes in the stress at constant strain (i.e. changes between the initial and final Young modulus E_0 and E_∞) or *c*) changes in strain at a constant load, until E_∞ is reached.

Viscoelastic behaviour can be represented by the simultaneous action of elastic and viscous components, as it occurs in the **standard solid model**, also known as **Zener model**, where two elastic elements represent the instantaneous and the equilibrium elasticity (E and E_∞, respectively), and a dashpot represents the viscosity η of the material. The standard solid is represented by arranging these components so the instantaneous and equilibrium elasticity components are, respectively, in series with, and parallel to the dashpot element. Two representations of the standard solid are shown in **Figure 2.10**a and b. By setting $E_\infty = 0$ or $E = 0$, the Maxwell and Kelvin-Voigt viscoelastic elements can be obtained (**Figure 2.10**c and d, respectively) (Mainardi, 2010; Simo and Hughes, 1998).

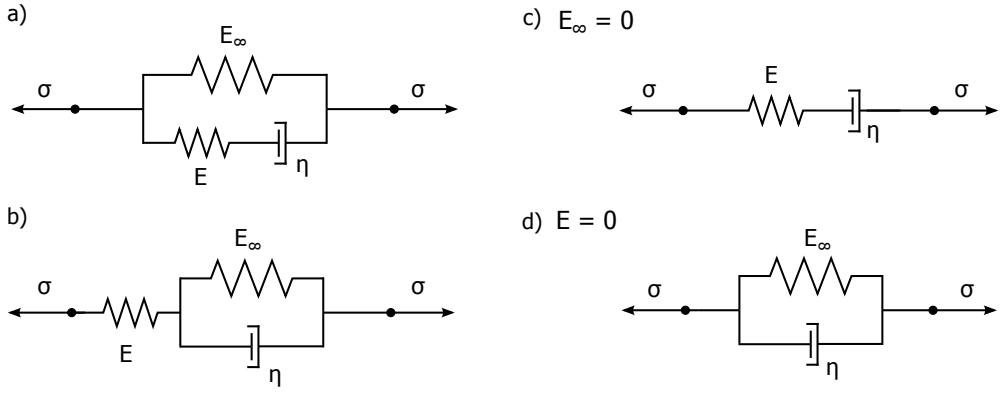

Figure 2.10: The standard solid model can be represented in the form of a) a spring representing the final elasticity E_∞ parallel to in-series spring (initial elasticity E_0) and dashpot (viscosity η), or b) an in-series initial elasticity spring with parallel arrangement of the final elasticity spring and dashpot. c) The Maxwell viscoelastic element is obtained when $E_\infty = 0$, and d) the Kelvin-Voigt one, when $E_0 = 0$.

In order to fit the short and long time effects observed in different viscoelastic materials, these elements are often combined in the form of the **generalised relaxation model** (GRM), where many parallel Kelvin-Voigt elements are added to the Standard Solid (**Figure 2.11**).

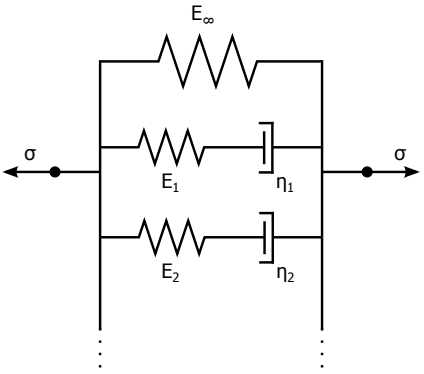

Figure 2.11: Generalised relaxation model. Taken from Simo and Hughes (1998).

Prony series describe the GMR in terms of shear (deviatoric term) and bulk (volumetric term) moduli, taking into account the material compressibility Aba (2014c). The basic hereditary integral formulation for linear isotropic viscoelasticity to describe stress is defined as:

$$\boldsymbol{\sigma}(t) = \int_0^t 2G\left(s - s'\right) \dot{\mathbf{e}}\, dt' + \mathbf{I} \int_0^t K\left(s - s'\right) \dot{\boldsymbol{\phi}}\, dt' \tag{2.21}$$

where $\dot{\mathbf{e}}$ is the deviatoric strain rate, $\dot{\boldsymbol{\phi}}$ the volumetric strain rates, $G(s - s')$ and $K(s - s')$ are the shear and bulk moduli functions of the reduced time s in the convolution integral representation, and $\mathbf{I}$ is the second order identity tensor, defined earlier in **Section 2.4.1**.

The reduced time is derived from the actual time t by:

$$s = \int_0^t \frac{dt'}{A_\theta\left(\theta_T\left(t'\right)\right)}, \qquad \frac{ds}{dt} = \frac{1}{A_\theta\left(\theta_T\left(t\right)\right)}, \tag{2.22}$$

where A_θ is the shift function accounting for the temperature θ_T effects on the viscoelastic properties of the material. As the model for this project assumes constant temperature, $A_\theta = 1$ is assumed, then $s = t$. **Equation 2.21** is then redefined for *isothermal* viscoelasticity as:

$$\boldsymbol{\sigma}(t) = \int_0^t 2G\left(t - t'\right) \dot{\mathbf{e}} dt' + \mathbf{I} \int_0^t K\left(t - t'\right) \dot{\boldsymbol{\phi}} dt' \tag{2.23}$$

The shear and bulk moduli defined by **Prony series**, respectively, as:

$$G\left(t\right) = G_{\infty} + \sum_{i=1}^{m_G} G_i \exp\left(-t/\tau_i\right); \qquad K\left(t\right) = K_{\infty} + \sum_{i=1}^{m_K} K_i \exp\left(-t/\tau_i\right) \tag{2.24}$$

where m_G and m_K are the number of terms of the Prony series, respectively, and τ_i are the characteristic relaxation times. The shear term of the integral **Equation 2.23** is then

$$\int_0^t 2\left(G_{\infty} + \sum_{i=1}^{m_G} G_i \exp\left[\frac{t'-t}{\tau_i}\right]\right)\dot{\mathbf{e}}\, dt' = 2G_0\left(\mathbf{e} - \sum_{i=1}^{m_G} G_i'\mathbf{e}_i\right)\Bigg|_0^t$$

where the instantaneous shear modulus is obtained by $G_0 = G_{\infty} + \sum_{i=1}^{m_G} G_i$ and the relative modulus of the i-th term is $G_i' = G_i/G_0$. The viscous deviatoric creep strain is defined as:

$$\mathbf{e}_i = \int_0^t \left(1 - \exp\left[\frac{t'-t}{\tau_i}\right]\right)\frac{d\mathbf{e}}{dt'}dt' \tag{2.25}$$

In an analogous form, the instantaneous bulk modulus is obtained by $K_0 = K_{\infty} + \sum_{i=1}^{m_K} K_i$ and the relative bulk modulus of the i-th term is $K' = K_i/K_0$. The volumetric creep strain is defined as:

$$\phi_i = \int_0^t \left(1 - \exp\left[\frac{t'-t}{\tau_i}\right]\right)\frac{d\phi}{dt'}dt' \tag{2.26}$$

Then, **Equation 2.23** can also be described as:

$$\boldsymbol{\sigma}\left(t\right) = 2G_0\left(\mathbf{e} - \sum_{i=1}^{m_G} G_i'\mathbf{e}_i\right)\Bigg|_0^t + \mathbf{I}\, K_0\left(\phi - \sum_{i=1}^{m_K} K_i'\phi_i\right)\Bigg|_0^t \tag{2.27}$$

Integrating **Equation 2.27** by parts and using a variable transformation, Aba (2014c) defines the stress of a linear isotropic viscoelastic material as:

$$\boldsymbol{\sigma}\left(t\right) = 2G_0\mathbf{e}\left(t\right) + \int_0^{t'} 2\dot{G}\left(t'\right)\mathbf{e}\left(t-t'\right)\, dt' + \mathbf{I}K_0\phi\left(t\right) + \mathbf{I}\int_0^{t'} \dot{K}\left(t'\right)\phi\left(t-t'\right)\, dt' \tag{2.28}$$

Within the Abaqus environment, Prony series are numerically implemented through the definition of a *Prony series expansion* of the dimensionless relaxation modulus (Aba, 2014a):

$$g_R\left(t\right) = 1 - \sum_{i=1}^{m_G} g_i^P\left(1 - \exp\left[\frac{-t}{\tau_i^G}\right]\right) \tag{2.29}$$

where g_i^P are the shear relaxation moduli of the Prony series (Aba, 2014b). The dimensionless relaxation modulus is applied directly to the hyperelastic strain energy function (**Equation 2.15**) as a factor of the material parameter C_{ij}.

Prony series representations of the viscoelastic kernel functions have been used to characterise the viscoelasticity of the *stratum corneum*, viable epidermis and dermis, under micro-indentation, with two terms by Crichton et al. (2011). Flynn and McCormack (2010) have also used a two-term Prony series to model the viscoelasticity of the hypodermis in the study of skin wrinkling response. Different studies have used other combinations of the Maxwell and Kelvin-Voigt elements to represent the viscoelastic properties of the skin (Boyer et al., 2009; Catheline et al., 2004; Clancy et al., 2010; Jachowicz et al., 2007; Khatyr et al., 2004; Zahouani et al., 2011).

2.4.5 Poroelasticity

The structure of the dermis can be described as a biphasic medium where the solid phase is constituted of the collagen and elastic fibres and the fluid phase is provided by the ground substance (Peña et al., 1998). Its characteristic viscoelasticity can be modelled from a phenomenological perspective, considering the fibres network as a porous media and the ground substance as a viscous fluid. Thus, the delayed elastic response of the human skin can be captured by incorporating the free movement of the ground substance between the collagen and elastic fibres network, with the use of the **poroelastic** constitutive model (Oomens et al., 1987).

Poroelasticity has been widely used for the characterisation of bone and cartilage materials (Cowin, 1999; Li et al., 2000). However, the required parameters for the application of poroelastic theory (e.g. porosity, permeability, compressibility of each phase, among others (Verruijt, 2015)) for the human skin have been rarely measured (Wu et al., 2003). Simple theories, not based on multiphasic (fluid/solid) formulations, are easier to implement and are sufficient to describe the multi-faceted mechanical behaviour of human skin (Oomens et al., 1987). For this reason, only few publications have used poroelasticity to represent the human skin response to deformation (Mak et al., 1994; Rim et al., 2005).

2.5 Skin contact interaction properties

During wet shaving, the skin is in contact with the cartridge components and shave prep. The skin-cartridge interaction is often oversimplified by representing the interaction phenomena in terms of a coefficient of friction; however, in the presence of a shave prep, a lubrication process takes part in the reduction of the friction forces experienced during wet shaving. In this section, the mechanisms behind the interactions occurring between the skin and the cartridge, and the skin and the shave prep fluid, are explained in more detail.

2.5.1 Frictional behaviour of the skin

For two solids in contact, the resistance to relative motion —friction —has been historically documented since the late 15$^{\text{th}}$ century by Leonardo da Vinci (Stachowiak and Batchelor, 2013). It was observed that during linear displacement (i.e. assuming 2D conditions), there was a linear relation between the magnitude of the normal and tangential forces (f_N and f_T, respectively) acting between the bodies in contact, from which the coefficient of friction was derived:

$$\mu = \frac{f_T}{f_N} \tag{2.30}$$

This relation summarises the empirical rules derived from the work of Guillaume Amontons and Charles Augustin Coulomb for dry contact, where the deformation of the bodies in contact is assumed to be (Persson, 2000; Stachowiak and Batchelor, 2013; Van der Heide et al., 2013): *a*) elastic, *b*) proportional to the normal load, and *c*) independent of the contact area and sliding velocity.

In reality, the friction response of soft materials (e.g. skin) does not follow the Amonton's laws (**Equation 2.30**) (Derler and Gerhardt, 2012; Gerhardt et al., 2009a; Sivamani et al., 2003), yet it is the result of simultaneous contribution of forces due to deformation and interfacial adhesion effects between the parts in contact (Adams et al., 2007; Derler and Gerhardt, 2012; Shpenkov, 1995; van Kuilenburg et al., 2013a; Zahouani et al., 2011).

Many factors are involved in the frictional behaviour of the skin. The compliant nature of the skin allows it to deform and take the shape of the contacting solid. This could have an effect in the distribution of pressure in the contact area, as several studies have shown lower coefficients of friction at higher contact pressures and loads (Adams et al., 2007; Derler and Gerhardt, 2012; Sivamani et al., 2003; Veijgen et al., 2013a). In high humidity environments, further increase in the contact area is induced by the plasticising effect of water as it is absorbed at the surface of the *stratum corneum* (Adams et al., 2007). The coefficients of friction of skin against various materials (stainless steel, aluminium, polyethylene, and polytetraflorethylene) have shown large variation depending on body location and level of hydration, showing values between 0.03 and 3.86 for static friction and 0.02 and 3.64 for dynamic friction (Veijgen et al., 2013a).

Such variability makes it difficult to characterise the skin frictional behaviour into a single empirical relation, so a great variety of approaches have been used to characterise it. According to Van der Heide et al. (2013), the most basic model to represent the coefficient of friction and its load-dependency is in the form of a power law (Comaish and Bottoms, 1971):

$$\mu \sim c_1 \cdot F_N^{c_2 - 1} \tag{2.31}$$

in which the constant c_1 and exponent c_2 are determined for the specific tribological scenario (e.g. adhesion and deformation, which are affected by the materials in contact, humidity levels, temperature, among others) (Van der Heide et al., 2013). To address this problem, Veijgen et al. (2013c) have proposed a multivariable model for the prediction of the human skin frictional behaviour, with a holistic consideration of the test-subject characteristics and habits, contact material properties, and contact and environmental conditions during the test. In their study, over 600 skin friction measurements were considered.

For the present PhD project, experimental data describing the skin frictional response at different wet shaving conditions has been provided by P&G. In order to estimate the coefficient of friction between the skin and the individual cartridge components, the drag (i.e. tangential) and normal forces experienced at each individual component were measured with an instrumented cartridge, known as the 'sub-cartridge force' (SCF) device, developed by P&G at their Greater London Innovation Centre in Reading (GLIC-R). In experimental work involving different lubricant fluids such as water, polyethylene glycol (PEG) solutions and corn syrup, the load-dependency of the coefficient of friction was observed. However, this load-dependency is also affected by the thickness of the lubricant film, as observed in consecutive shaving strokes.

The effects of lubrication on the skin contact interactions are reviewed in the next chapter, in the context of shave preps mechanics. With this section, the review of the physiological and mechanical aspects of the human skin in relation to wet shaving interactions is concluded.

2.6 Summary

The skin is a complex multi-layered and multi-scale tissue with mechanical characteristics optimised to provide mechanical, chemical and thermal protection to the body. As a result of this complexity, the full mechanical response of the skin tissue cannot be captured by a single experimental test. Therefore, the computational simulation of the skin mechanical response often relies on experimental data capturing only a potion of the rich set of behaviours characteristics of the skin.

A wide range of constitutive models have been applied for capturing the anisotropic, hyperelastic, and viscoelastic behaviour of the skin. Based on the experimental set up of O'Callaghan and Cowley (2010), specifically developed for the characterisation of facial skin mechanical response in wet shaving applications, the **van der Waals** hyperelastic model and quasi-linear viscoelasticity based on a **Prony series** representation have been **selected to represent the skin behaviour in the proposed multi-physics modelling framework**, which development process is presented in **Chapter 5**. This constitutive framework was shown to be appropriate to capture the stretch-stiffening

elastic response, the characteristic bulging of the skin in-between the razor blades and the delayed response to deformation observer in facial skin during wet shaving O'Callaghan and Cowley (2010).

In the development of the **anatomical skin model** (**Chapter 6**), the integration of the mechanical response of *stratum corneum* layer into the model is essential for the analysis of the skin microstructure, its influence on the distribution of strains in the subjacent skin layers (i.e. viable epidermis and dermis) during deformation, and the sensitivity of this response to environmental conditions. The mechanical properties for the *stratum corneum* captured in the literature are often expressed in terms of the Young's modulus (Delalleau, 2007; Geerligs, 2010; Pailler-Mattei et al., 2007; Wu et al., 2006b), which are easy to convert into the neo-Hookean formulation (Flynn and McCormack, 2009). Furthermore, the effects of the humidity in the *stratum corneum* have been studied, also reporting the Young's modulus of this layer (Park, 1972; Wu et al., 2006b). For this reason, **the neo-Hookean** hyperelastic constitutive model has been **selected to represent the skin layers in the anatomical model** developed in **Chapter 6**, following the approach of Flynn and McCormack (2010, 2009); Kong et al. (2011); Sopher and Gefen (2011).

Chapter 3

Shave preps mechanics, rheology and constitutive models

Shave prep plays a key role in the skin-razor interaction in wet shaving. During a shaving stroke, the lathered shave prep (foam) deforms around the cartridge, while a layer of interstitial fluid is confined beneath the blades and guards, forming a lubricating film at the skin-razor interface. In this chapter, a review of the physics underpinning the microscopic and macroscopic mechanical response of the shave prep fluid is provided, highlighting its characteristics in the form of foam, and the characteristics of its fluid-solid interactions, followed by its lubricating role in wet shaving. The bases of the rheological tests used for capturing the non-linear viscous behaviour of shave preps, applicable for both foams and interstitial fluids, are also explained, along with the different constitutive models available for the characterisation of such a viscous response. The application of the reviewed techniques is explained for the experimental characterisation of the shave prep used for the development of the shave prep model as part of the ***multi-physics modelling framework****.*

The term *shave prep* refers to any fluid used to enhance gliding of a razor cartridge over the skin surface (e.g. shaving foam, gel or cream). Its main purposes are the hydration of the skin surface and hair, and lubrication of the skin-razor interface. To achieve these functions, key physical characteristics in a shave prep include: foaming and foam stability, adhesion to the skin, and 'shear-thinning viscosity'.

In wet shaving, shave prep enhances hydration of the hair and skin. As explained in **Section 2.3**, humidity modifies the mechanical and barrier properties of the *stratum corneum*, reducing its stiffness as water is absorbed within the corneocytes and in the intercellular space (Adams et al., 2007; Masen, 2011). Likewise, constant exposure to high humidity reduces the stiffness and fracture toughness of hair (Draelos, 2012; McFeat and Ertel, 2010). As a result, maintaining high humidity conditions on the skin surface provides a more compliant contact surface, and reduces the cutting force required for the hair removal.

Shave preps typically show shear-thinning viscosity (i.e. its viscosity is reduced at high shear rates). The adhesion phenomena of shave prep to the skin and cartridge surfaces, reviewed detail in **Section 3.3.1**, contributes to shearing of this fluid during a shaving stroke, reducing its viscosity, inducing a fluid-like behaviour. This topic is covered in detail in **Section 3.2**. Furthermore, shave prep adhesion on skin allows flow of fluid under the razor cartridge. As bubbles are rather pushed away from high pressure contact areas, a film of interstitial fluid is formed between the razor and skin. This film provides hydrodynamic lubrication, thus reducing the friction between the skin and the razor cartridge (**Section 3.4**).

Shave preps used in wet shaving are typically foamed. If not delivered in this form, foam is prepared by the consumer prior shaving through a lathering process in which shear stress is applied to the fluid (e.g. rubbing between hands or using a brush), so air or other blowing agents (e.g isobutane, isopentane) are incorporated into the shave prep, forming the foam bubbles. The end product is a bi-phasic material made of a gas (i.e. bubbles) and a fluid phase (i.e. interstitial fluid). The physics behind the formation of foams are explained next.

3.1 Microsopic behaviour of foams

The microscopic behaviour of foams is conditioned by the components of the foam fluid phase. A common ingredient in many shave preps is polyethylene glycol (PEG), also known as polyethylene oxide (PEO) or its commercial name Polyox™, dissolved in an aqueous solution. When PEG is coupled to hydrophobic molecules, it produces non-ionic surfactants (Winger et al., 2009). These molecules, distinguished by a polar (hydrophilic) head and an apolar (hydrophobic) tail (**Figure 3.1**a), are responsible for the formation of bubbles in the foam.

Within an aqueous solution, surfactants arrange themselves at the interface with a non soluble gas with the polar head pointing towards the aqueous solution and the tail pointing towards the gas. At low concentrations, they are dispersed at the free surface interface (**Figure 3.1**c). As the surfactants concentration increases, the fluid free surface saturates reaching the critical micelle concentration (CMC) (**Figure 3.1**b). At concentrations above the CMC (**Figure 3.1**d), surfactants form micelles (spherical arrangements of surfactants where the polar head is facing the solution and the apolar tail faces the centre, as shown in **Figure 3.1**e). If gas is introduced to the solution (e.g. air), the surfactants arrange at the new solution-gas interface, covering the bubble (**Figure 3.1**f) and providing it with high stability (Durian, 2002; Katgert, 2008). If more gas is incorporated to the solution, more bubbles are formed, increasing the gas volume fraction (i.e. portion of volume taken by the gas contained in the bubbles) of the foam.

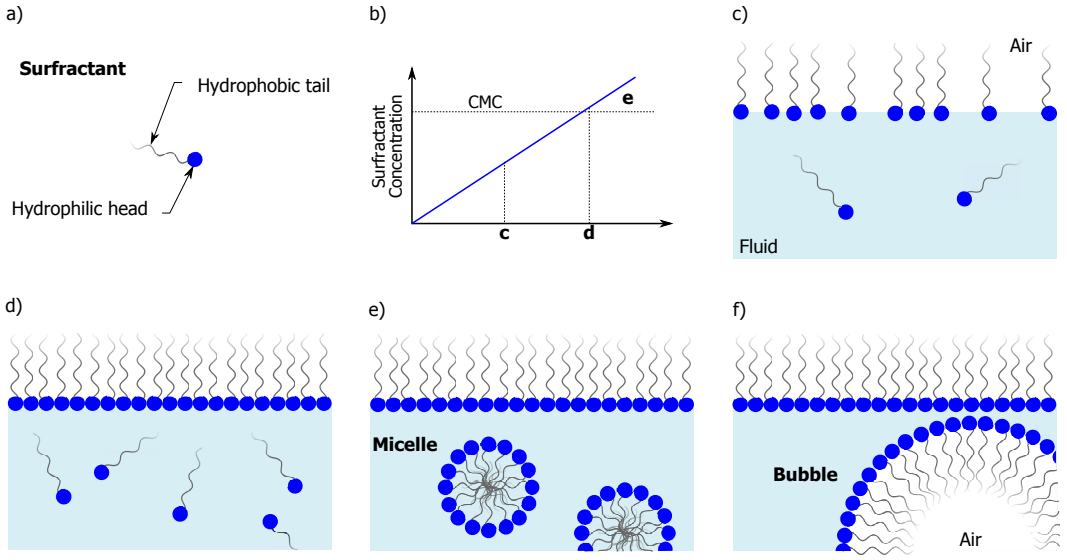

Figure 3.1: Foam formation process. The concentration of *a*) surfactants, contained in a 'soapy' solution determines the lathering process to convert the the solution into a foam. The graphic *b*) shows the position of the figures c-e regarding the surfactant concentration as follows: At *c*) low concentration, the surfactants start arranging at the air-fluid interface; *d*) as the concentration increases the fluid surface fills at the CMC (critical micelle concentration) and some surfactants are left behind; *e*) as the concentration keeps increasing the free surfactants groups in spheres, with their tails pointing to the centre of the sphere. *f)* If gas (e.g. air) is blown into the solution, the bubbles will form and the surfactants contained in the micelles will cover the bubble fluid-gas interface.

The foam structure is formed by the assembly of several bubbles. As the walls of the bubbles are made of an aqueous solution, this solution is referred as the *interstitial fluid* of the foam. When two bubbles locate next to each other, they form a thin film. In the junction with a third bubble, a Plateau border filled with interstitial fluid is formed (Katgert, 2008). According to the amount of interstitial fluid contained in the Plateau borders, the foams are classified as *wet* or *dry* (see **Figure 3.2**). More interstitial fluid is observed in the Plateau borders of wet foams, giving a rounded finish to the bubbles assembly. The interstitial fluid can be drained out from the Plateau borders and bubble walls by the action of gravity forces, increasing the gas volume fraction of the foam. In this process, foam becomes dry and the structure takes a polyhedral shape (Katgert, 2008). The changes in the Plateau borders and walls alter the equilibrium of the basic foam structure, leading to foam *ageing*.

The foam ageing process results in coarsening and coalescence of the foam bubbles as the film walls thin. **Coarsening** refers to the change of bubble size due to the diffusion of water soluble gases from one bubble to another, through the thin film. This diffusion usually occurs from smaller to larger bubbles in order to balance concentration gases. If the insoluble gas concentration in the smaller bubbles increases, the gas concentration equilibrium is obtained by diffusion of soluble gases back to smaller bubbles (Cohen-Addad and Höhler, 2001; Katgert, 2008). **Coalescence** occurs when the thin film breaks, fusing two bubbles together (Durian, 2002; Katgert, 2008). See **Figure 3.3**. As a result, irregular bubble shapes are observed in aged foams. More details

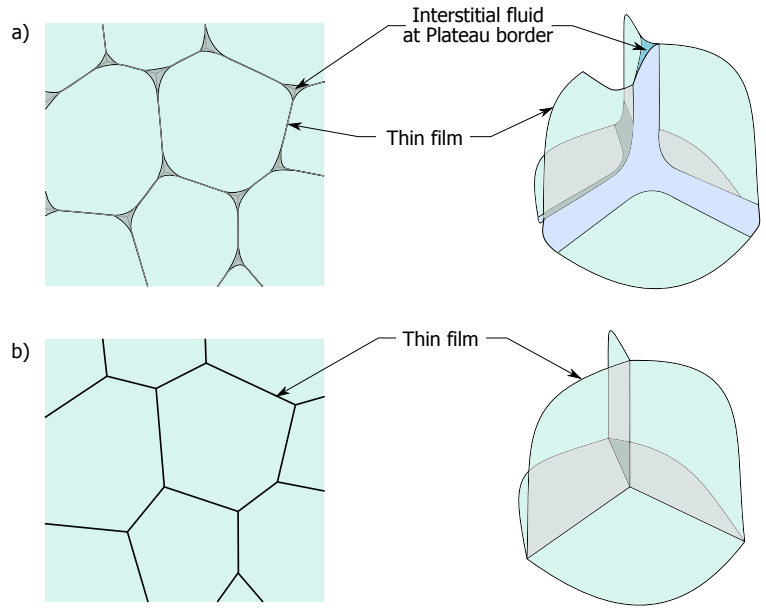

Figure 3.2: Wet and dry foams. *a*) Wet foams are characterised by a more spherical bubbles, forming Plateau borders between bubbles which are filled with interstitial fluid. *b*) Dry foams are characterised by polyhedral shaped bubbles joined with other bubbles by thin films. 2D foam views shown on the left, 3D bubbles junctions on the right.

about the physics laws characterising the balance of forces in the foams can be found in the work of Katgert (2008). The coarsening effects on Gillette® shave prep foams take about 20 minutes to occur (Park and Durian, 1994), thus this effect is not relevant for this PhD research as it goes beyond time-scales relevant for wet shaving.

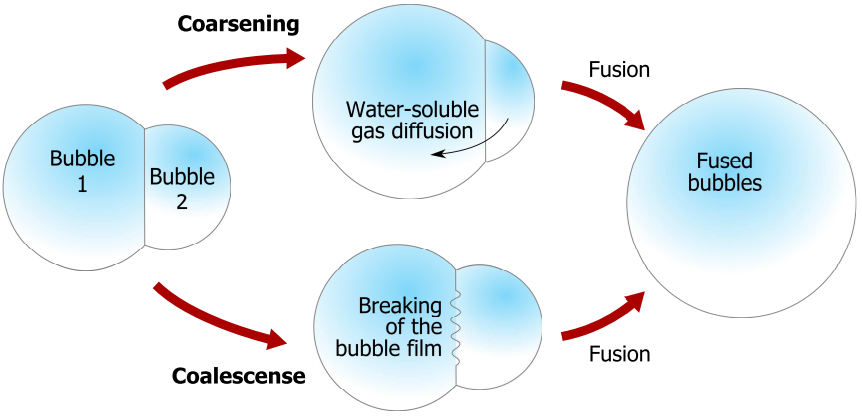

Figure 3.3: Foam ageing processes. **Coarsening** accounts for the fusion of bubbles due to diffusion of water-soluble gases from a bubble to another (generally from a small - bubble 2, to a larger one - bubble 1). **Coalescense** occurs due to breaking of the film between the two bubbles.

The macroscopic mechanical behaviour of wet foams differ substantially from that of interstitial fluid. In the next section, the link between the foam microstructure and its macroscopic viscous behaviour is explained.

3.2 Macroscopic behaviour of foams

The macroscopic mechanical response of foams is dependent upon the interstitial fluid viscous behaviour, the foam structure, and the shear rate applied. The viscous behaviour of the interstitial fluid defines the drag forces experienced by bubbles. Along with it, the bubbles size and thickness of the Plateau borders define the flow conditions of the interstitial fluid, having a direct effect on the viscous drag and elastic response of the foam.

The thickness of the Plateau borders creates a channel that provides higher mobility to bubbles in the foam. This is observable as wet foams have lower shear modulus than dry ones, where there is not enough fluid for the bubbles to flow without breaking their thin film (Cantat et al., 2013). The bubbles size and homogeneity are also related with shear modulus observed in foams. In a monodisperse foam where the bubbles sizes are homogeneous, bubbles arrange in a face centred cubic (FCC) arrangement, where shear modulus is inversely proportional to the bubbles radius (Cantat et al., 2013). However, in polydisperse foams where bubbles differ in size up to 10% (Katgert, 2008), the grid becomes disordered and the larger bubbles deform the most. The effect that this phenomenom has on the shear modulus of the foam remains unclear (Cantat et al., 2013).

The applied shear strain rate defines the level of deformation, according to its intensity. At low shear rates, high viscous drag forces are experienced in the interstitial fluid making the foam show a solid-like behaviour (Gopal and Durian, 1999; Katgert, 2008; Park and Durian, 1994). In such conditions, deformed bubbles are able to recover their original shape. Conversely, for higher shear rates, viscous drag forces of the interstitial fluid are overcame by shear forces, allowing bubbles to flow on top of each other, in a laminar flow (Gopal and Durian, 1999; Katgert, 2008; Park and Durian, 1994). This is illustrated for a 2D foam in **Figure 3.4**.

In the shaving process, both solid and fluid-like behaviour of foam are observed. In resting conditions, after application of shave prep, it is due to adhesive forces that shave prep adheres to the skin surface. As no shear forces are applied, high viscous drag forces allow the foam to maintain its shape, showing solid-like behaviour. During a shaving stroke, the forces applied by the cartridge shear the foam in multiple directions, causing bubbles to flow around its geometry. At the contact areas between the skin and cartridge (i.e. the blades and guards), the applied forces displace bubbles out of the areas of high pressure (Moir and Craig, 2010). However, adhesive forces between the skin and shave prep create a non-slip condition at the skin-fluid interface, allowing formation of a thin film of interstitial fluid (i.e. aqueous solution) at the skin-razor interface to provide lubrication.

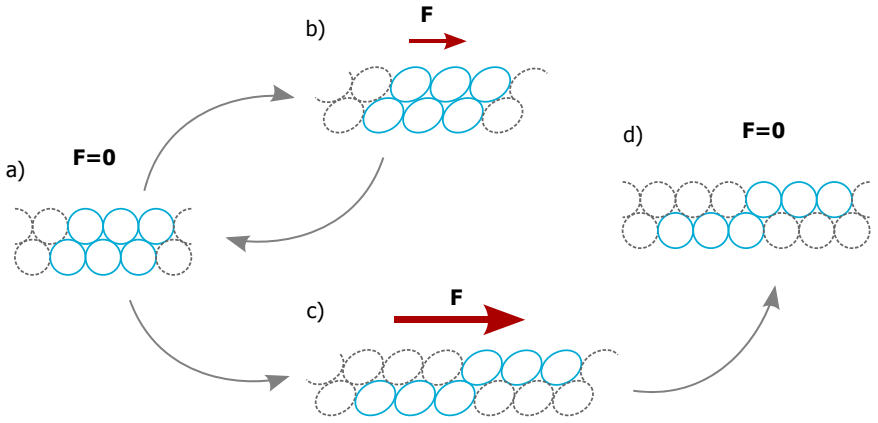

Figure 3.4: Macroscopic behaviour of foam under loading. *a*) The foam in its original state keeps its form and shape (ignoring the ageing of foam). *b*) If a small force is applied, the bubbles deform elastically but the viscous drag forces at the bubbles interface do not allow the flow of foam. If the shearing force is released, the foam will recover its original shape. *c*) If a larger shearing force is applied, the foam will flow. *d*) If the large force is withdrawn, the displacement of the bubbles is irreversible.

Due to the crucial role of solid-fluid contact interaction for the formation of lubrication layers, this phenomena is explained below.

3.3 Fluid-structure interactions

Mechanical problems involving interaction of fluids and solids where their deformation co-depends on the other are known as *fluid-structure interaction* (FSI) problems (Bazilevs et al., 2013). Wet shaving can be considered as a solid mechanics problem if the shave prep hydrodynamic lubricating effects are simply defined as a coefficient of friction for the skin-razor system. However, the shave prep fluid not only provides lubrication, but also contributes to the skin deformation. At the initial stage of the shaving stroke, the first contact interaction is between the razor cartridge and shave prep. While resting on the skin, the shear strain rate applied to the shave prep is at is minimum (caused by the action of gravity forces only), so the shave prep viscosity is high enough to transmit the cartridge forces to the skin as it resists to flow. This means that the skin is deformed even before the blades get in contact with the skin surface. As the shave prep is sheared, its viscosity reduces and it flows around the cartridge parts. Then, the formation of a protection layer of shave prep (to prevent skin cuts) is simultaneously dependent of:

a) the velocity and indenting force of the shaving stroke;

b) the adhesion of shave prep to the skin and cartridge surfaces; and

c) the deformation of skin caused by both contact with the razor components and pressure within the shave prep.

Understanding the complexity of the skin-shave prep-razor interaction is crucial for the design of improved wet shaving systems. Wet shaving *is* and should be treated like an FSI problem. With the advantages of current computational tools, an FSI modelling approach can be used for the analysis of the multi-physics interaction of skin and wet shaving products.

An important challenge in this analysis is the characterisation of the contact interactions at the fluid-solid interface. These interactions are dependent on a vast number of parameters that involve the mechanical properties of the solid and fluid (viscous and elastic forces), their intermolecular forces (electrostatic, magnetic, van der Waals), and forces derived from the conditions on which the interaction takes place (velocity, inertia, gravity, pressure) (Barnes, 1995; Sochi, 2011). In rheology and fluid mechanics, the interaction at the fluid-solid interface is related to the relative velocity between the fluid and the solid surface. This is known as *wall slip*. A common assumption in fluid mechanics involves that the fluid 'sticks' to the solid surface so their relative velocity is zero: a 'no-slip' condition. However, such assumption is often invalid (Granick et al., 2003; Hatzikiriakos, 2015). Wall slip is often detected indirectly by sudden drops in viscosity observed in rheological tests, or by direct measurement of fluid velocities higher than the wall velocity at the fluid-solid interface (Schmatko et al., 2005; Sochi, 2011).

In an in-depth review of slip at fluid-solid interfaces, Sochi (2011) summarised the complexity of the fluid-solid interactions. In their work, it is explained how wall slip can be either true or apparent. The concept of *true slip* is self explanatory: it occurs when the relative velocity of the fluid with respect to the wall is larger than zero at the interface. However, this does not often apply. In the case of multi-phasic materials, a *slip layer* of a gas or an additive substance can formed at the fluid-solid interface, acting as a lubricant for the bulk fluid material (Granick et al., 2003). In other cases, physical changes in the fluid (e.g. lower viscosity due to viscous heating) at the solid interface would generate such a slip layer, so the fluid technically lubricates itself. In these situations, although a 'no-slip' conditions is met at the slip layer, the velocity profile shows otherwise *apparent slip*, which is a common mechanism for wall slip (Sánchez et al., 2001; Sochi, 2011), mostly for polymer solutions (Hatzikiriakos, 2015) such as shave preps.

Wall slip is a complex phenomenon. As mentione above, it involves a vast number of variables, so the characterisation of wall slip in analytical or even empirical models is "virtually impossible" (Sochi, 2011). However, experimental evidence indicates that interfacial forces between a fluid and a solid surface strongly influence the wall slip, as indicated by Sochi (2011) and references there in. A general parameter that can be used to approximate the strength between the fluid and solid surface is the advancing contact angle and liquid surface tension (Schmatko et al., 2005). The contact angle is

directly proportional to the **fluid-solid adhesion** forces (Israelachvili, 1991), indicating whether the fluid has a tendency to stick or separate from the solid surface. These forces, along with the cohesion of the fluid material and its viscous behaviour, allow the estimation of the parameters describing the **fluid-solid contact interactions**. That is, the fluid-solid boundary conditions that determine the relative motion to the solid surface interface in the FSI problem (Bazilevs et al., 2013). Determining the most appropriate boundary conditions is of "extreme importance" in a number of situations involving micro-flow (Henry et al., 2004). The dimensions expected in the formation of a lubrication film layer in-between the cartridge and skin is in the microns range (Lawler, 2001; Moir and Craig, 2010). Therefore, a thorough analysis was taken to capture the shave prep adhesion and how the wall slip can be approximated in the FSI model. The theory used for this analysis is provided below.

3.3.1 Fluid-solid adhesion

In solid-fluid interactions, adhesion of two different materials is driven by intermolecular forces acting between them. This involves cohesion forces keeping the material molecules together, adhesion forces occurring at a two-materials interface (where a positive value means attraction, and a negative one, repulsion), and the surface energy of both materials (Israelachvili, 1991).

In the case of solid-fluid interactions, the energy required to separate the two materials can be obtained by the measurement of the contact angle, formed at the vertex between the planar and curved area of a droplet of fluid resting on the solid surface. The free energy change per unit area W (also known as reversible work) required to separate two planar surfaces is determined by the surface energy γ of the materials (or surface tension in fluids). For a material 1, the relation between its surface energy and *cohesion work* (i.e. energy required to separate two planar plates of the same material) is given by:

$$\gamma_1 = \frac{1}{2} W_{11} \tag{3.1}$$

The interfacial energy between material 1 and material 2 (with γ_2, W_{22}) in a vacuum medium is given by:

$$\gamma_{12} = \frac{1}{2} W_{11} + \frac{1}{2} W_{22} - W_{12} = \gamma_1 + \gamma_2 - W_{12} \tag{3.2}$$

so the *adhesion work* (i.e. energy required to separate two planar plates of different materials) is:

$$W_{12} = \gamma_1 + \gamma_2 - \gamma_{12} \tag{3.3}$$

The work of adhesion in a third medium (material 3) is:

$$W_{132} = \gamma_{13} + \gamma_{23} - \gamma_{12} \tag{3.4}$$

Setting a system where material 1 is a solid base, material 2 a droplet fluid, and material 3 an immiscible medium containing the others materials, the total surface energy is defined as (Israelachvili, 1991):

$$W_{\text{tot}} = \gamma_{23} \left(A_f + A_c \right) - W_{132} A_f \tag{3.5}$$

where A_f and A_c the curved and flat areas of the droplet surface. Accounting for equilibrium conditions where $W_{\text{tot}} = 0$, **Equation 3.5** can by divided by A_f, so:

$$W_{132} = \gamma_{23} \left(1 + \frac{A_c}{A_f} \right) \tag{3.6}$$

The contact angle θ, formed at the vertex between A_c and A_f, can be determined by:

$$\frac{A_c}{A_f} = \cos \theta \tag{3.7}$$

So, with the use of **Equations 3.7** and **3.6**,

$$W_{132} = \gamma_{23} \left(1 + \cos \theta \right) \tag{3.8}$$

Therefore, the contact angle can be used as an indication of the adhesion energy between the fluid and solid (Israelachvili, 1991). For values of θ close to 180°, the adhesion energy is at its minimum, allowing the fluid to easily separate from the surface. In contrast, values of θ close to zero indicate that the adhesion energy is at its maximum, pulling the fluid towards the surface so a wetting condition is met as 'no-separation' of the fluid is allowed. See **Figure 3.5**.

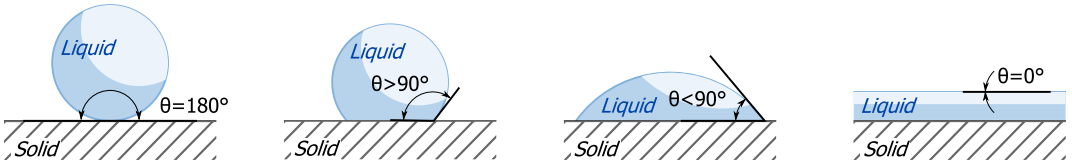

Figure 3.5: The contact angle θ formed by flat and curved surfaces of a droplet resting on a solid, is linked to the adhesion energy per unit area between the fluid and the liquid. If $\theta = 180$, the energy is minimum, so the fluid does not stick to the surface, as it occurs when the contact angle is reduced. For $\theta = 0$, the adhesion energy is at its maximum, so the fluid spread on the fully wettable surface.

In order to measure the surface energy of a fluid, Macdougall and Ockrent (1942) proposed a technique in which the solid surface was tilted at an angle θ_s, so the fluid was displaced by gravity forces (i.e. weight). In these conditions, the advancing angle θ_A (at the lowest point) was larger or equal to the receding angle θ_R (at the highest point), as shown in **Figure 3.6**. Setting the transversal area of the droplet A_d, perpendicular to the solid surface and the rotation axis, the surface energy of the fluid can be

obtained by (Macdougall and Ockrent, 1942):

$$\gamma = A_d g \rho \left(\frac{\sin \theta_s}{\cos \theta_R - \cos \theta_A} \right) \tag{3.9}$$

where ρ is the density of the fluid and g the gravity acceleration. Similarly, the study

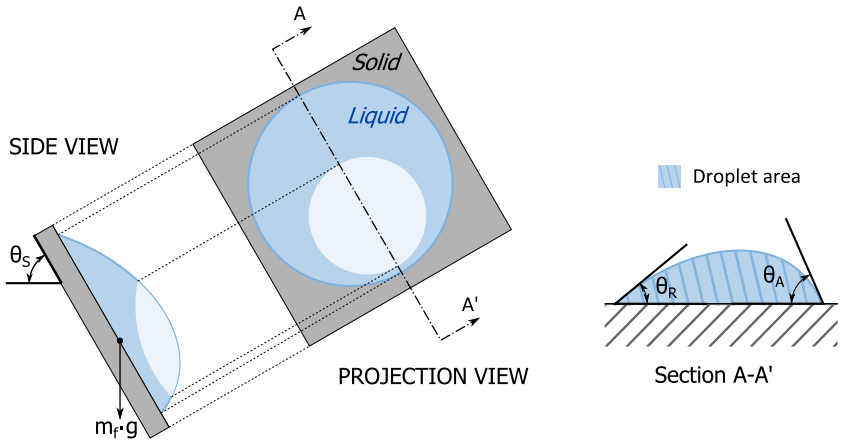

Figure 3.6: Droplet in mechanical equilibrium on a tilted surface. For a droplet of fluid, with weight $m_f \cdot g$, resting in equilibrium on a solid surface tilted at an angle θ_s, the component of the weight tangential to the surface acts on the droplet generating and advancing contact angle (θ_A) and a receding one (θ_R).

of droplets of non-Newtonian power-law fluids on a tilted surface has been applied for the analysis of the fluids' spreading behaviour, (Ahmed et al., 2013).

On the skin surface, the contact angle depends on the hydrophilic/hydrophobic properties of the skin. Such properties are partly conditioned by the content of sebum on the skin, which varies with body region and personal grooming habits (as it can be easily washed out of the skin). Although the sebum can act as a lubricant film (Gerhardt et al., 2009b), its role in the frictional response of skin is unclear (Derler and Gerhardt, 2012).

3.3.2 Fluid-solid contact interactions

Fluid-solid contact interactions are defined in FSI problems by two *traction boundary conditions*. Normal to the surface of contact, a 'no penetration' condition between material phases is established. Tangential to the solid surface, a wall condition defines the fluid behaviour at the boundary layer at the fluid-solid interface (Bazilevs et al., 2013). While the 'no penetration' condition is applied to ensure that the solid and fluid do not coexist within the same space, the wall condition should be representative of the complex wall slip behaviour. The most common way to represent the wall slip conditions is by specifying either 'slip' or 'no-slip' at the fluid-solid interface (i.e. frictionless or tied contact). In rough surfaces, it is widely accepted to assume 'no-slip' because it is thought that the fluid "interlocks" with the surface, so the relative velocity between the

fluid and solid is zero at the interface. For example, in rheological experiments, slip is prevented by roughening the surfaces (Barnes and Nguyen, 2001; Meeten, 2008). In the macroscale fluid-structure interactions, the assumption of 'no-slip' at the wall interface usually provides good results Schmatko et al. (2005). Under the thought that surface roughness dominates the 'no-slip' condition (which is not always the case (Sochi, 2011)), 'slip' is usually implemented in FSI studies involving smooth surfaces such as wind-turbine blades (Bazilevs et al., 2014; Takizawa et al., 2015), or the surfaces of a razor cartridge, as reviewed in **Chapter 4** for the models of Lawler (2001) and Moir and Craig (2010).

Experimental test such as direct observation (Hale et al., 1955), laser Doppler velocimetry (Tomonaga et al., 1981) and duplex ultrasonography (Kamenskiy et al., 2011) (among many others) can be used to detect wall slip in a given set of conditions. It is on these experiments that 'partial slip' has been frequently detected, challenging common assumptions such as those mentioned above (Sochi, 2011). Although 'partial slip' can be modelled as a ratio of the velocity at the wall, a realistic implementation of slip in FSI problems is far more complex —if not yet impossible. As earlier reviewed, wall slip depends on so many chemical, mechanical and physical factors (Sochi, 2011) that changing the conditions of the fluid-structure interaction (e.g. flow rate, velocity, geometry) could modify the wall slip conditions. If a fixed wall slip parameter is selected, it could lead to unrealistic results in the simulations.

Measuring wall slip in wet shaving conditions would require an exhaustive analysis, not feasible within the context of this PhD project. However, given the significance of the implications of selecting either 'slip', 'no-slip' or 'partial slip', especially on the shear stress/viscosity observed in the shave prep, the selection of a wall conditions should be appropriately justified. In the finite element environment used for this project, fluid-solid contact interactions were defined as a coefficient of friction affecting the tangential fluid behaviour at the solid surface, where a 'slip' condition can be set as frictionless, a 'no-slip' condition with infinite coefficient of friction, and partial slip can be determined by a given coefficient of friction between zero and infinity (non inclusive). By applying the tilted surface technique (Macdougall and Ockrent, 1942), the angle of the surface at which the droplet starts to slide (sliding angle) could be used to estimate the coefficient of friction between the fluid and surface, decomposing the normal and tangential forces caused by the weight of the droplet, treating the problem as simply solid friction, and using **Equation 2.30**. Although this approach would not provide a realistic value to define the wall slip condition, it allows an estimation of the boundary conditions at the fluid-solid interfaces, identifying some differences between one contact material or another (e.g. blades, elastomer guard).

3.4 Lubricating role of the shave prep

The lubricating properties of shave preps are provided by the long chain polymers of PEG. When dissolved in water, these polymer chains form an aqueous polyelectrolyte lubricant capable to reduce the friction between the skin and razor cartridge (Stachowiak and Batchelor, 2013). Contained within the interstitial fluid of the shave prep foam, this lubricant creates a thin film that stays on the skin surface even after the foam is removed. This film is crucial to ensure hydrodynamic lubrication, and also provide a skin-blade clearance that enhances protection against nicks and cuts during wet shaving.

Lubrication can take place in three different regimes, depending on the dynamic viscosity of the lubricant fluid η, the magnitude of the contact normal load F_N and relative velocity V_R between the contacting parts. These parameters are related in the so called Stribeck parameter, defined as:

$$S_N = \eta \cdot V_R / F_N \tag{3.10}$$

which is used for the identification of the lubrication regimes. With low S_N, the two surfaces are in direct contact, showing high coefficients of friction as geometrical interlocking between surface asperities produce resistance to relative motion. This is known as the *boundary lubrication* regime. As S_N increases (higher velocity, higher viscosity or lower load), the interaction conditions encourage formation of a hydrodynamic film that provides support in-between contacting parts, thus reducing interlocking contact. This is observed by a sudden reduction in coefficient of friction in the transition regime or *mixed lubrication*. At higher S_N, a linear relation between the Stribeck parameter and the coefficient of friction describes the *hydrodynamic lubrication* regime (Stachowiak and Batchelor, 2013). See **Figure 3.7**.

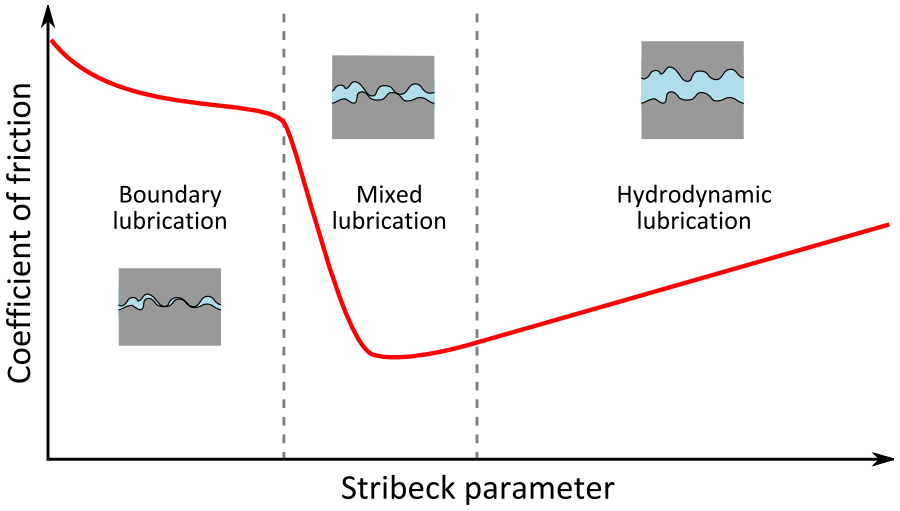

Figure 3.7: Stribeck curve representing changes in friction coefficient at the different lubrication regimes.

Derler and Gerhardt (2012) reviewed the effects of water absorption rate in the *stratum corneum*, showing that fully hydrodynamic lubrication changes into a mixed or boundary lubrication as water gets absorbed or evaporates. In wet shaving, the lubricant film is maintained 'fresh' as evaporation of interstitial fluid at the skin interface is prevented by application of a thick layer of shave prep.

For the analysis of lubrication in wet shaving conditions, it is important to note that the Stribeck curve is influenced by the shear-thinning behaviour of shave prep viscosity. Such behaviour is observed at different scales in the interstitial fluid and foams. It is therefore important to have access or develop robust techniques for experimental characterisation of changes in viscosity due to varying shear rate. Such rheological testing methods are described in the next section, and subsequently applied to characterise the rheology of various shave prep formulations.

3.5 Rheological testing of shave preps

Rheology refers to "the study of flow and deformation of materials" (Barnes, 2000). For characterising rheological properties of non-Newtonian fluids (such as shear-thinning shave preps), several measurement devices have been used, among which rheometers are the most often preferred.

Rheometers are used for calculation of viscosity as a function of shear stress τ and shear strain rate $\dot{\gamma}$:

$$\eta = \frac{\tau}{\dot{\gamma}}, \tag{3.11}$$

By trapping a fluid into two axy-symmetric geometries (e.g. cone and plate, cone-cylinder, concentric cylinders, among others), a 'no-slip' condition between the fluid and solid geometry must be ensured for application of shear stress (through a torque) and measurement of shear strain rate (deformation) or *vice versa* (Barnes, 2000; Cantat et al., 2013). These parameters can be measured using the fluid thickness h, magnitude of the velocity and force tangential to the shearing motion (referred as tangential velocity or tangential force, respectively) V_T and F_T and fluid contact area A, as follows:

$$\dot{\gamma} = \frac{V_T}{h}; \qquad \tau = \frac{F_T}{A} \tag{3.12}$$

In this radial arrangement, torque T is defined as $T = F_T \cdot r$, where r is the radial distance from the rotation axis, and $V_T = \omega \cdot r$, where ω is the angular velocity (units rad/s). **Figure 3.8** shows different forms of **Equation 3.12** for some of the most common rheometrical geometries.

Testing PEG solutions does not require special procedures except of the use of appropriate geometry that can contain the tested fluid (e.g. for a low viscosity fluid, concentric cylinders geometry would be required). In the case of shave prep foams, lathering

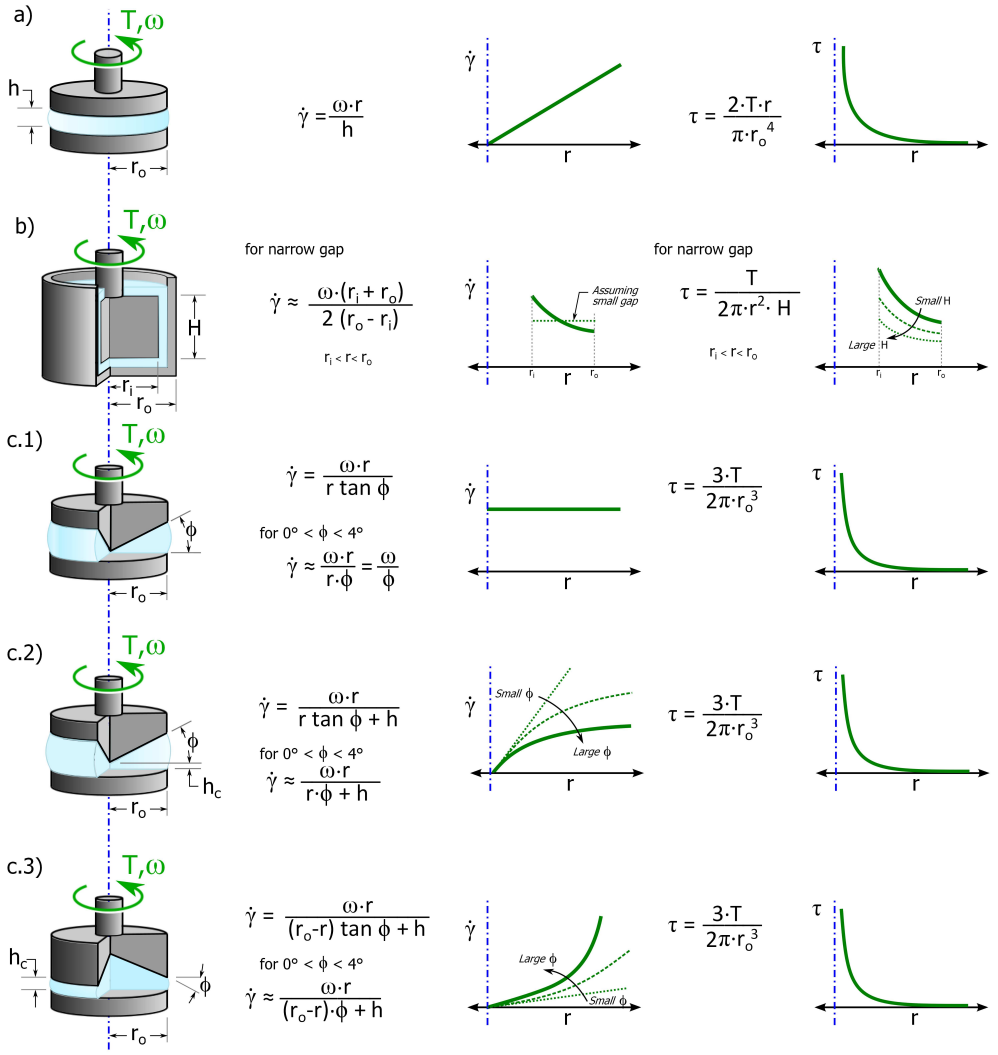

Figure 3.8: Rheometer's formulas to obtain strain rate and shear stresses for different rheometer geometries: *a)* parallel plates, *b)* concentric cylinders, *c.1)* cone and plate, *c.2)* separated cone and plate, and *c.3)* re-entrant cone and plate, are described by the separation between the components of h, a fluid outer radius r_o, fluid inner radius r_i, the inner cylinder height H, and a cone angle Φ. By the application of a torque T and the measurement of the angular velocity ω or *vice versa*, the shear stress τ and shear strain rate $\dot{\gamma}$ are given by the corresponding formulas, and their variation as a function of the distance from the rotational axis is shown in the graphs at the right of the formula. Compilation from Barnes (2000); Cantat et al. (2013); Rheosys LLC. (2011). Graphs are purely qualitative.

can affect the sample rheological properties, and development of a specific test protocol was required, as described in **Section 3.7**.

Rheological techniques have been applied by P&G for analysis of viscous-shear strain rate response of shave preps in the form of interstitial fluid (PEG solutions). A set of viscosity-shear strain rate curves for two PEG water-soluble resins with different molecular weight, both at 1% and 0.2% w/w (weight/weight concentrations) in water is shown in **Figure 3.9**. It was observed that even at low concentrations such as 0.2% w/w PEG in water, the viscous behaviour observed in water was altered, causing an

increase in viscosity and a more pronounced shear-thinning behaviour at larger PEG concentrations.

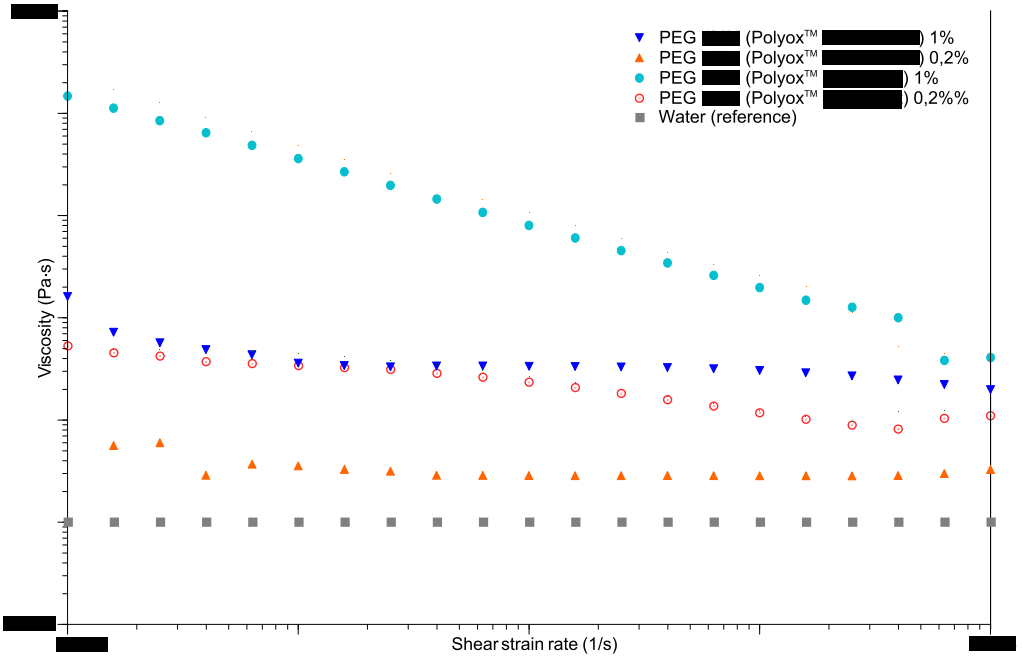

Figure 3.9: PEG (Polyox™) solutions viscosity curves. The viscosity-shear strain rate response of PEG 1MM (Polyox™ N-12K, molecular weight 10^6) and 5MM (Polyox™ coagulant, molecular weight $5 \cdot 10^6$) was tested at 1% and 0.2% concentrations in water. Such a small concentrations significantly alter the viscous behaviour of water (shown for reference). **Proprietary data (P&G). Do not disclose**.

The viscosity curve of shear-thinning fluids is usually characterised by an "S" shape where the viscosity behaviour can be separated in three stages: (I) the transition from a constant viscosity at very low shear strain rates to a constant drop in viscosity (II), and (III) a final transition to a constant high shear strain rate viscosity. This behaviour can be captured by constitutive models such as the Power Law, Hershel-Bulkley, Sisko, Cross and Carreau models (Barnes, 2000), which apply at different stages, as shown in **Figure 3.10**. These models are explained next.

3.6 Constitutive models of shear-thinning fluids

Newtonian fluids show a linear relation between shear stress and shear strain rate, showing a constant viscosity at any shear strain rate (Stachowiak and Batchelor, 2013). In non-linear materials, as shown in the previous section, the fluid viscosity changes at different shear strain rates, so the dynamic viscosity can be expressed as $\eta(\dot{\gamma})$.

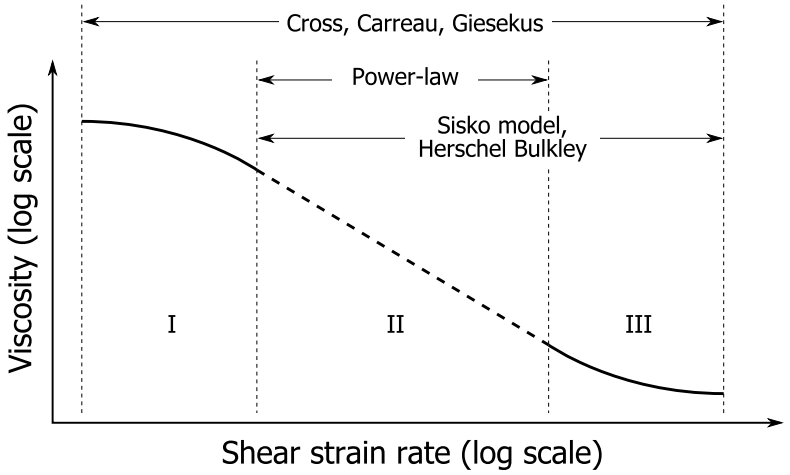

Figure 3.10: Applicability of shear-thinning constitutive models. The shear-thinning behaviour of shave preps is represented in three stages: (I) high viscosity at very low shear strain rate; (II) logarithmic drop in viscosity with increasing shear strain rate; and (III) constant high shear strain rate viscosity. While constitutive models such as Power-law can capture only stage II, Sisko and Herschel-Bulkley models capture stages II and III, and Cross, Carreau and Giesekus models are capable to capture the three stages of the shear-thinning behaviour. Adapted from TA2 (2004); Barnes (2000).

Power Law based-models are widely used to describe non-linear viscosity. Using a power factor n as an index of the shear strain rate, the model is capable of capturing Newtonian viscosity, ($n = 1$), shear-thickening viscosity ($n > 1$), and shear-thinning behaviour observed in shave preps ($n < 1$). Power Law-based models are expressed in terms of either shear stress or viscosity (using **Equation 3.11**), as follows.

The **Power Law model** is based on a logarithmic change in viscosity given by:

$$\tau = K\dot{\gamma}^n; \quad \eta = K\dot{\gamma}^{n-1} \tag{3.13}$$

where K (also known as the viscosity factor) and n a power factor. This model only focuses on the main shear-thinning slope, ignoring any stabilisation of the fluid (bringing the fluid into a Newtonian state) at higher shear strain rates (i.e. stages I and III, **Figure 3.10**).

The **Herschel-Bulkley model** is defined as (Katgert, 2008):

$$\tau = \tau_0 + K\dot{\gamma}^n; \qquad \eta = \eta_0 + K\dot{\gamma}^{n-1} \tag{3.14}$$

accounts for the viscous behaviour at stage III, so at high shear strain rates where $\eta \to 0$, η_0 overcomes a high shear strain rate Newtonian (constant) viscosity.

Likewise, the **Sisko model**, defined as (Barnes et al., 1989; Servais et al., 2002):

$$\tau = \eta_\infty\dot{\gamma} + \frac{\eta_0}{K\dot{\gamma}^{(n-1)}}; \qquad \eta = \eta_\infty + \frac{\eta_0}{(K\dot{\gamma})^n} \tag{3.15}$$

is able to capture transition into a Newtonian fluid at high shear strain rates, by accounting for the limiting viscosity η_∞ at infinite shear strain rate and limiting viscosity η_0 at zero shear strain rate, under the assumption that $\eta_0 \gg \eta_\infty$ and $K\dot{\gamma} \gg 1$. This model is derived from the **Cross model**, defined by Barnes (2000) as:

$$\eta = \eta_\infty + \frac{\eta_0 - \eta_\infty}{1 + (K\dot{\gamma})^n} \tag{3.16}$$

which accounts also for solid-like behaviour, characteristic of shaving foams at low shear strain rates (Gopal and Durian, 1999; Katgert, 2008; Park and Durian, 1994).

This wide shear strain rate range can be also covered by Geisekus and Carreau models (Lawler, 2001).

The **Giesekus model**, designed for characterisation of non-linear elastic fluids (Giesekus, 1982), accounts for normal stresses in shear flow, large stresses when elongational rates are high, as well as time-dependent stresses in transient flows (Lawler, 2001). Developed for a superposition of a solvent and a polymer (Bird et al., 1987), it is defined by the following equations:

$$\boldsymbol{\tau}_f = \boldsymbol{\tau}_p + \boldsymbol{\tau}_s \tag{3.17}$$

$$\boldsymbol{\tau}_p + \lambda_1^t \dot{\boldsymbol{\tau}}_p - a_g \frac{\lambda_1^t}{\eta_p} (\boldsymbol{\tau}_p \cdot \boldsymbol{\tau}_p) = -\eta_p \dot{\boldsymbol{\gamma}} \tag{3.18}$$

$$\boldsymbol{\tau}_s = -\eta_s \dot{\boldsymbol{\gamma}} \tag{3.19}$$

$$\eta_s = \frac{\lambda_2^t}{\lambda_1^t - \lambda_2^t} \eta_p \tag{3.20}$$

where $\boldsymbol{\tau}_f$ is the fluid shear stress tensor, and the viscosities and shear stresses subscripts s and p stand for solvent and polymer components; a_g represents the mobility parameter, and λ_1^t and λ_2^t are relaxation and retardation times of the Giesekus model. In this case, the shear strain rate is included as the tensor $\dot{\boldsymbol{\gamma}}$.

The **Carreau model** is defined as (Carreau et al., 1997):

$$\eta = \eta_\infty + (\eta_0 - \eta_\infty) \left[1 + \left(\lambda^t \dot{\gamma}\right)^2\right]^{\frac{n-1}{2}} \tag{3.21}$$

Lawler (2001) characterised the shaving preparation, combining the **Carreau** and the **Giesekus** models, for the simulation of shave prep flow under a razor blade. In order to adapt these models for shaving preparation, Lawler (2001) substituted the solvent viscosity component defined in **Equation 3.20** with **Equation 3.21**, so the solvent viscosity becomes a function of the shear strain rate.

The **Carreau-Yasuda model**, which can be viewed as a generalisation of the Carreau model described above for $a_y = 2$, is defined as (Aba, 2014c):

$$\eta = \eta_\infty + (\eta_0 - \eta_\infty)\left[1 + \left(\lambda^t \dot{\gamma}\right)^{a_y}\right]^{\frac{n-1}{a_y}} \tag{3.22}$$

where λ^t is the Carreau-Yasuda time constant and a_y the Yasuda material parameter.

3.6.1 Fluid compressibility

Another important physical characteristic of fluids is their degree of compressibility. In isotropic *solid* materials, in the low strain regime, this property is captured by bulk modulus κ_0, described in terms of the Young's modulus and Poisson's ratio (**Equation 2.17**). It can be also related to density ρ and longitudinal wave propagation velocity (also referred as *sound speed*) c_0 as:

$$\kappa_0 = c_0^2 \rho \tag{3.23}$$

In *fluid* materials, their volumetric strength can be captured with the use of an *equation of state*. The equation of state provides a hydrodynamic model for the material, where its hydrostatic pressure is represented as a function of its density and internal energy. In order to capture the fluid compressibility, pressure in a shock-compressed material can be considered as a function of its internal energy (Heuzé, 2012). When a material is subject to sudden acceleration (e.g. impact), the velocity of a shock wave U_s and that of particles U_p can be related to the longitudinal wave propagation velocity (sound speed) assuming a linear relation between the shockwave and particle velocities:

$$U_s = c_0 + S U_p \tag{3.24}$$

where $S = \partial U_s / \partial U_p$ is the linear Hugoniot slope factor. The **Mie-Grüneisen** equation of state, available in Abaqus to represent the fluid compressibility, provides the material pressure p in isothermal conditions, as a function of volume and mass (i.e. density) (Aba, 2014a; Heuzé, 2012) as:

$$p - p_H = \Gamma \rho \left(E_m - E_H\right) \tag{3.25}$$

where p_H is the Hugoniot pressure, Γ is the Grüneisen parameter, and E_m and E_H are internal energy per unit mass and Hugoniot energy, respectively. The **Hugoniot** pressure is given by (Aba, 2014a; Ahrens, 1993):

$$p_H = \frac{\rho_0 c_0^2 \eta_v}{\left(1 - S\eta_v\right)^2} \tag{3.26}$$

The Grüneisen parameter is obtained in the reference configuration (Γ_0) relating the volume of the material with changes of pressure with respect to changes in energy, so in the current configuration the Grüneisen parameter is given by:

$$\Gamma = \Gamma_0 \frac{\rho_0}{\rho} \tag{3.27}$$

The Hugoniot energy is defined as:

$$E_H = \frac{p_H \eta_v}{2\rho_0} \tag{3.28}$$

where $\eta_v = 1 - \frac{\rho_0}{\rho}$ is the nominal volumetric compressive strain defined by changes of density in both the reference and current configuration (ρ_0 and ρ, respectively).

Then, using **Equations 3.27**, **3.28** and **3.25**, the fluid pressure can be defined as:

$$p = \Gamma_0 \rho E_m + p_H \left(1 - \frac{\Gamma_0 \eta_v}{2}\right) \tag{3.29}$$

3.7 Experimental characterisation of shave preps foams

Building a computational model requires information about how the materials behave in real loading conditions, so that appropriate constitutive models and associated parameters can be selected. For the **computational modelling framework** developed in this PhD project, experimental data of the viscoelastic behaviour of skin and mechanical properties of cartridge parts materials were readily available. Rheological viscous data of shave preps in the form of interstitial fluid was also available, and that in the form of foam was generated in this project through rheological measurements.

The key characteristics to be captured in the shave prep model are its compressibility, viscous behaviour, and contact interaction properties. These characteristics were defined in the Abaqus (Simulia, Dassault Systèmes, Providence, RI, USA) finite element environment in terms of viscosity, density, longitudinal wave propagation velocity, coefficient of friction and important assumptions concerning if separation between the fluid and solid parts was or not allowed. Testing the longitudinal wave propagation velocity in non-linear fluids is not a trivial task, and many considerations must be taken into account in order to obtain meaningful results (Leighton et al., 2004). In bubbly fluids and foams, longitudinal wave propagation measurements are affected by gas volume fraction, bubble size, and frequency of sound as it has been documented in internal P&G research (Holt). Developing a dedicated experimental set up for the measurement of the wave propagation velocity in shave preps was deemed too time-consuming and beyond the scope of this PhD project. For this reason, these properties were gathered from the literature and combined with reasonable assumptions, as discussed in **Appendix B**.

3.7.1 Experimental characterisation of the shave prep viscous behaviour

Rheological testing of shave preps in their aqueous solution form follows the requirements of any regular fluid. However, in foam, the lathering process to prepare the foam plays an important role as homogeneity of the sample is crucial. In preliminary tests of Gillette® Series Sensitive Gel, high sensitivity of the rheological behaviour to the sample preparation (user) was observed. For this reason, different lathering processes were tested in order to set the recipe for ensuring sample homogeneity. The approach taken for sample preparation, measurement of density, rheological testing parameters, and the documentation of structural changes in the foam before and after the test are described as follows.

Lathering process

This process accounts for the consumer action of shearing the product from the can (e.g. gel) in-between the hands to form the foam prior to application on the shaving area (e.g. face). In order to ensure sample homogeneity, the gel was stirred (in a medium size beaker) during 30-50 seconds, followed by a visual inspection at a final stir. Another two different lathering methods were proposed in the protocol (see **Appendix A**), with no significant differences in the results, as indicated in **Section 3.7.1.1**. After the lathering process, the sample was evaluated in terms of density and gas volume fraction as explained next.

Measurement of density and gas volume fraction

The density of the shave prep samples (gel and foam) was obtained through the shave prep specific gravity. A beaker was topped with water and weighted to obtain the water mass, and the procedure was repeated with the shave prep gel and foam samples to obtain the sample mass. The same beaker was used in all measurements to maintain a constant volume measurement (estimated by the measured weight of water), and a constant beaker mass that could be extracted from the measurements. With a constant volume, the specific gravity of the gel and foam samples was obtained as the ratio of mass of the sample with respect to the water mass, and its density by multiplying the sample specific gravity by the known density of water.

Assuming the foam gas does not contribute to the weight of the foam sample, the mass measured in the foam sample was taken as the content of ‘fluid’ in the foam. As the density of the gel sample is constant, the ratio between the mass of the foam with respect to the mass of the fluid is equivalent to the foam’s fluid volume fraction. This, subtracted form the unity results on the gas volume fraction. After these values were recorded, the sample was ready for testing.

Rheometric testing parameters

For the rheometric test, an ARG2 rheometer (TA Instruments Ldt., New Castle, Delaware, U.S.) was used. Two different geometries, concentric cylinders and cone-and-plate (see **Figure 3.8**), were employed with no significant differences in the results. The main concern with the use of concentric cylinder geometry was the air encapsulation between the sample and inner cylinder, forming a considerably large bubble that reduced contact between the sample and outer cylinder. Thus, the use of cone and plate was preferred.

Test parameters were set for a constant temperature of 25°C (Lipic and Smith, 2012) in order to avoid a phase transition in the sample, within a 0.001-1000 /s shear strain rate range. The test was performed within 20 minutes to prevent foam ageing. Because of this time limit, the procedure was set to take no extra equilibration time after the test started and data points were recorded when either 3 consecutive measurements were taken within a 3% tolerance or a 5 minutes limit was reached. The detailed protocol can be found in **Appendix A**, where the recording of foam structural changes was also indicated by taking micrographs, with an optical microscope, of foam on smooth glass prior and after the tests, and comparing them to the structure of the aged foam. This procedure was repeated for each sample, as shown in **Figure 3.11** for a shave prep sample with 20% (mass) water.

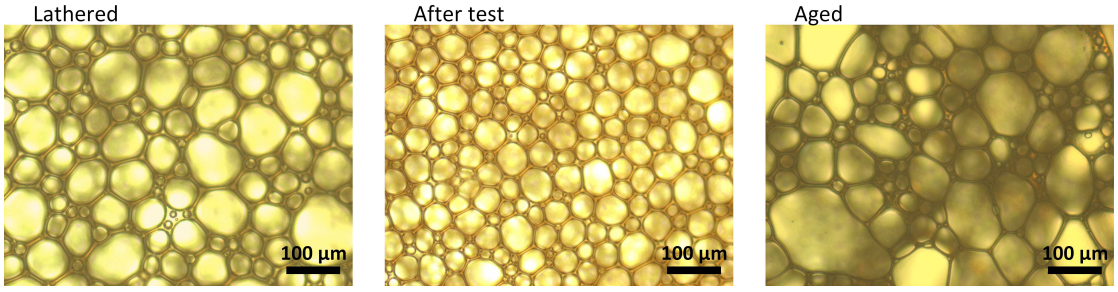

Figure 3.11: Structural changes in shaving foam during testing. The 10x magnification images of Gillette® Series Sensitive gel foam diluted with 10% mass water, show the characteristic foam structure observed in most of the samples right after preparation (lathered) and after rheological test. The effects of ageing (coarsening, coalescense, and thinning of the changes in the structure of Plateau borders are observed the aged foam (18 minutes).

3.7.1.1 Results: Shave prep viscous behaviour

A preliminary test at 30°C showed that samples prepared under the protocol specification (lathering process “a”, see **Appendix A**) were consistent with each other, compared with a non-lathered sample (see **Figure 3.12**).

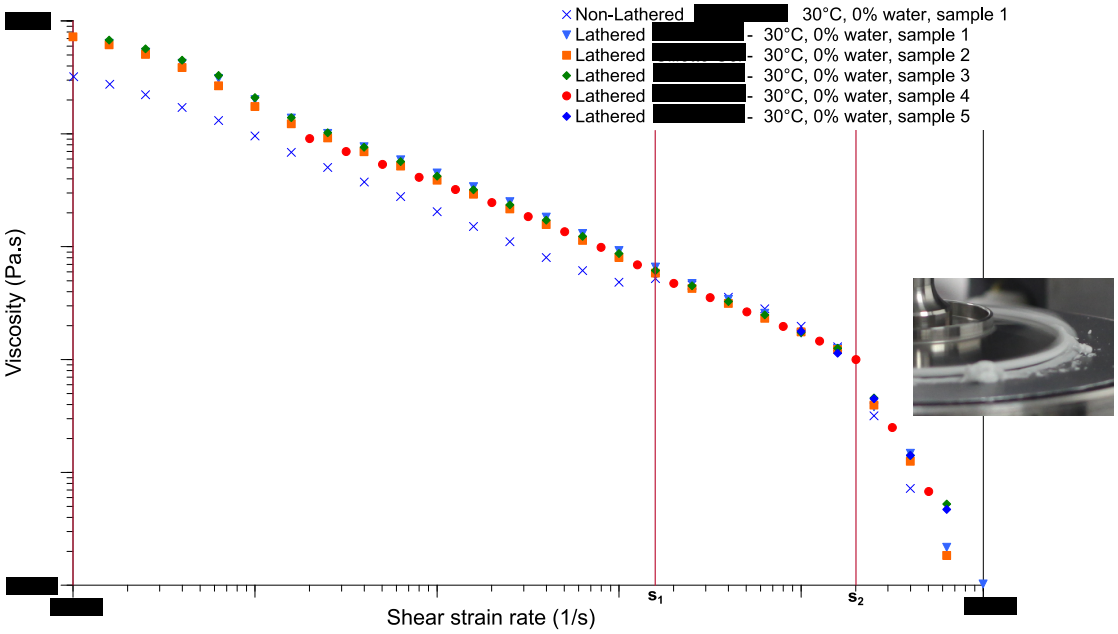

Figure 3.12: Consistency evaluation of protocol for foam sample preparation. Five Gillette® Series Sensitive gel samples (0% water dilution) were compared with the non-lathered shave prep (gel) for reference. At shear strain rate s_1, the applied shear has lathered the gel sample shifting the viscosity curve to the same trend observed for pre-lathered samples. After shear strain rate s_2 is reached the viscosity results are discontinuous due to separation of the foam between the geometry walls. **Proprietary data (P&G). Do not disclose**.

The lathered samples showed a shift in viscosity compared with the non-lathered prep sample up to s_1 shear strain rate, after which the non lathered sample showed a transition joining the lathered ones (i.e. it lathered due to the applied shear). For the lathered samples, a consistent behaviour was observed. While samples 1-3 were tested in the same range, testing of sample 4 was initiated at a higher shear strain rate, following the same path as the previous samples. In order to evaluate the effects of ageing, sample 5 was tested from at much higher shear strain rate, for which it also joined the path of the previous samples. The congruency of the viscosity curves to the samples a different shear strain rate ranges reflected the stability of the foam samples along the test.

Testing the samples at 25°C showed more stable results, and the lathering processes "a" and "b" (pure gel lathered by stirring or lathering by rubbing it on hands, see **Appendix A**) showed consistent results. The parameters of Gillette® Series Sensitive gel samples, tested with cone and plate geometry, are described in **Table 3.1**, grouping the samples in sets A to E according to the applied conditions of the test.

Rheological test results, showed that the non-lathered sample (test set A) had lower initial viscosity than the lathered one (test set B), at 30°C. Set C showed less dispersion than set B by lowering the temperature to 25°C as advised by Lipic and Smith (2012). As the dispersion of values was resolved, an inclusion of 10% mass (weight) of water

Table 3.1: Description of the rheological tests on Gillette® Gel shave prep. **Proprietary data (P&G). Do not disclose**.

Set	Temp [°C]	Shear strain rate [1/s]	Water dilution [% mass]	Samples	Gas Volume fraction [%]	Density [kg/m^3]
A†	30	0.01-1000	0	1	0	786.84
B	30	0.005 - 1000	0	6	89.73	89.67
C	25	0.005 - 1000	0	6	88.99	86.65
D	25	0.01 - 1100	10	5	88.51	90.38
E	25	0.05 - 1100	20	1	85.5	114.06

†Non-lathered samples set.

was included in the samples (set D), showing a slight shift of properties, lowering the initial viscosities. The same behaviour was observed in the 20% mass water sample (set E). All samples showed the same discontinuity in the viscosity curve at shear strain rate s_2, although preliminary tests showed viscosity at shear strain rate greater than s_2 could be captured with higher water concentrations. See **Figure 3.13**.

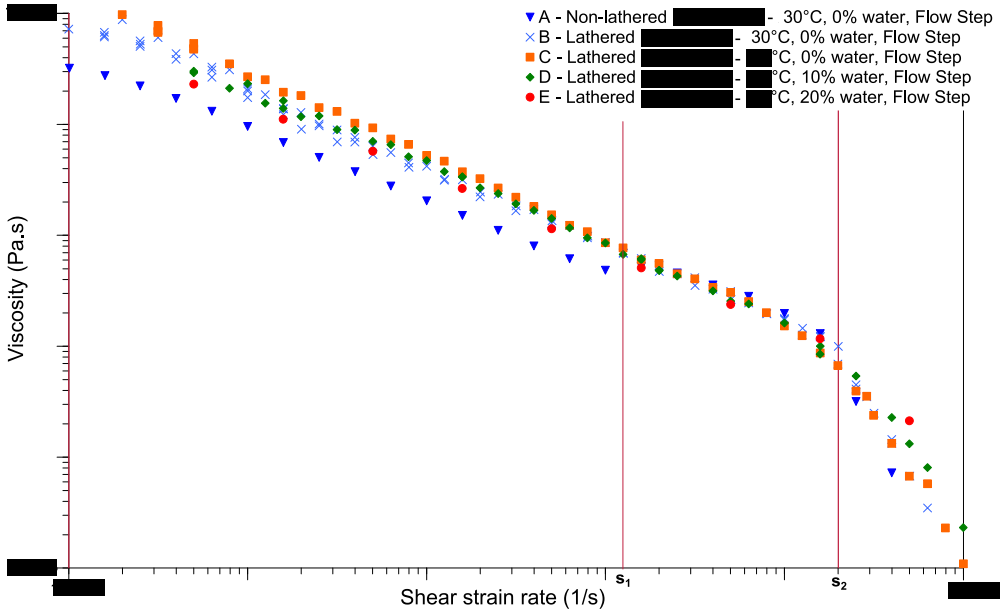

Figure 3.13: Shave prep rheological results. Less scatter is shown in the samples at 25°C (set C) than in the ones at 30 °C (set B, blue X). The decrease of temperature shifts up the sample viscosity with 0% water inclusion (orange squares). A shift down is in the viscosity curve is observed while the water inclusion increases from 10% (set D, green diamonds) and 20% (set E, red circles) in mass. The non-lathered shave prep (set A, blue triangles) is shown for reference. **Proprietary data (P&G). Do not disclose**.

Although these results proved reliability of the foam preparation procedure, viscous behaviour of shave prep foams at high shear strain rates (such as the applied ones during shaving) was not evaluated in the current rheology test, due to the discontinuity

observed in the viscous curve at shear strain rate greater than s_2 (**Figures 3.12** and **3.13**).

The viscosity curves obtained were fitted to the constitutive models reviewed in **Section 3.6**, giving in all cases a close fit to experimental data, as shown for set C in **Figure 3.14**. For this reason, the constitutive model selected to characterise the shave prep in the **computational modelling framework** was determined according to the runtime performance (i.e. the constitutive model providing the faster runtime in the simulations).

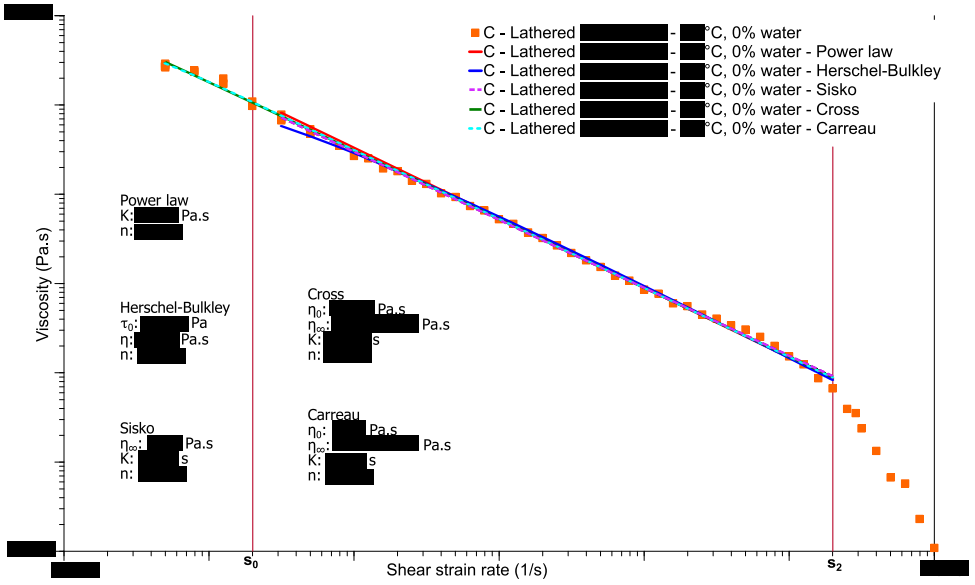

Figure 3.14: Model fitting of the experimental data (set C) to the Power law (red), Herschel-Bulkley (blue), Sisko (purple), Cross (green) and Carreau (pale blue) models. It is observable that the fluid yields into the power law behaviour at shear strain rate $> s_0$. **Proprietary data (P&G). Do not disclose**.

3.7.2 Experimental characterisation of shave prep contact interaction properties

As mentioned in **Section 3.3**, using an appropriate boundary conditions a the fluid-solid interface (wall slip) can be essential to capture the shave prep behaviour. In the **multi-physics modelling framework**, the shave prep interacts with the skin and with each of the materials of the razor cartridge. Within the finite element analysis environment, the fluid-solid interactions were defined in terms of adhesion, stating if separation of the fluid from the solid surface was allowed or not, and coefficient of friction, defining the level of slip between the two materials.

For the contact interaction between shave prep and cartridge parts, the polymeric materials and blade coating were initially assumed to be hydrophobic, where no adhesion

took place, providing a 'slip' interaction where no adhesion was occurring between the fluid and solids (i.e. separation was allowed). However, such assumption was dismissed as it was observed by setting droplets of water or shave prep aqueous solution on the blade or elastomer guard surfaces, the droplets did not slip from the surface, but attached to it due to adhesion forces. Therefore, it was concluded that the intermolecular forces acting in the fluid-solid contact interface are required to be measured, for the appropriate characterisation of fluid-solid interaction in the shaving stroke simulations.

In order to capture these two parameters, the following experiments where used:

- **Adhesion:** Measurement of contact angle between a droplet of fluid and a flat surface.
- **Friction:** Measurement of sliding velocity of a droplet of fluid on a tilted surface.

These experiments were only performed in the cartridge materials (i.e. blade and elastomer guard). On the skin surface, the wall slip conditions was determined with the following analysis. The skin surface energy is dependent on the lipid content (Mavon et al., 1997), so assuming pre-shaving cleansing (i.e. sebum removal), the skin can be considered to be hydrophilic so adhesion was accounted for in the skin-shave prep interaction. In addition, the skin surface roughness provides asperities for interlocking of the foam bubbles. Also considering that with the application of shave prep it sticks on the skin surface as it is applied, a 'no-slip' condition was assumed at the skin interface. The procedure followed for the characterisation of adhesive behaviour of shave preps on the cartridge materials is described next.

The fluid-solid contact pairs analysed consisted of the following materials/structures:

- **Fluids samples:**
  - Lathered Gillette® Series Sensitive Gel (foam)
  - Deionised water (reference)
  - PEG 1MM (Polyox™ N-12K) 1% w/w solution in water
  - PEG 5MM (Polyox™ Coagulant) 1% w/w solution in water
- **Solid surfaces:**
  - Glass (reference)
  - Razor blade
  - Razor guard elastomer

With the use of a Drop Shape Analyzer DSA100 (KRÜSS GmbH, Hamburg, Germany), the contact angle of a 1 μl droplet was analysed in two conditions:

- Contact angle on a flat surface for the evaluation of adhesive behaviour.
- Tilted plate for the detection of the sliding angle; this angle is required for the estimation of the fluid-solid coefficient of friction to be implemented in the simulations.

The procedure consisted of placing a droplet on the surface of contact, and capturing the image of the droplet for the measurement of the contact angle using the Drop Shape Analysis software (version 1.90.0.11), at both flat and tilted conditions. At least five measurements were taken for each contact pair, at each surface position. The shave prep foam was excluded from the contact angle analysis because of its high viscosity behaviour at low shear strain rate: in these conditions, no shearing load is affecting the fluid so solid-like behaviour was expected. However, its adhesive behaviour was captured in terms of deformation at the application process as explained below.

3.7.2.1 Results: Shave prep contact interactions

The shave prep foam sample was carefully prepared, ensuring homogeneity of the foam. It was then applied to each surface with the aid of a spatula. In the three surfaces, it was observed that due to adhesion forces acting simultaneously on the tested surface and the spatula, the foam sample behaved as a solid material under uniaxial tension. This caused the foam sample to reproduce a ductile fracture, as observed in **Figure 3.15** by the formation of a pointy tip (also observed in the foam left on the spatula). As a result of low density (i.e. low weight) and high viscosity, no changes in the foam sample shape nor sliding was observed when the surfaces were tilted by 60°. The adhesive behaviour of the aqueous solutions to each surface was captured by the analysis of droplet shape (i.e. contact angle) on each of the tested surfaces. Higher work of adhesion was observed on the glass surface with the PEG solutions, and lower work of adhesion on the elastomer surfaces (see **Figure 3.16**). The average contact angles of the contact pairs are summarised in **Table 3.2**.

Table 3.2: Mean contact angles and standard deviation (S.D.) measured at a $\theta_s = 0°$ for the contact pairs of deionised water, PEG 1MM solution 1% w/w in water, PEG 5MM solution 1% w/w in water (fluids) with glass, razor blades and guard elastomer (solid surfaces). **Proprietary data (P&G). Do not disclose**.

Fluid	**Glass** [°]		**Blade** [°]		**Elastomer** [°]	
	Mean	S.D.	Mean	S.D.	Mean	S.D.
Deionised water	62.8	3.8	98.5	5	105.1	2.7
PEG 1MM 1%	20.0	1.4	83.8	1.3	102.4	1.7
PEG 5MM 1%	30.2	3.3	84.0	1.2	103.0	7.8

For the evaluation of the sliding angle, adhesion forces showed larger than droplets weight, preventing any sliding of the fluids. Although sliding could be induced with

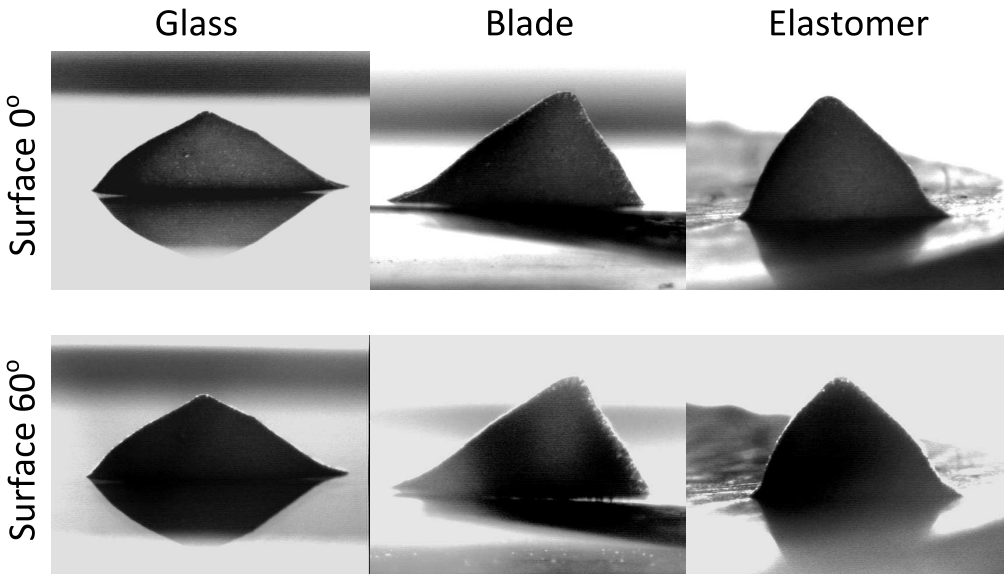

Figure 3.15: The adhesive behaviour of shave prep foam cannot be captured with measurements of contact angle due to its high viscosity at low shear strain rate: it behaves as a soft solid rather than a fluid droplet. After tilting the surface to 60°, no changes in the sample shape nor sliding was observed. **Proprietary data (P&G). Do not disclose**.

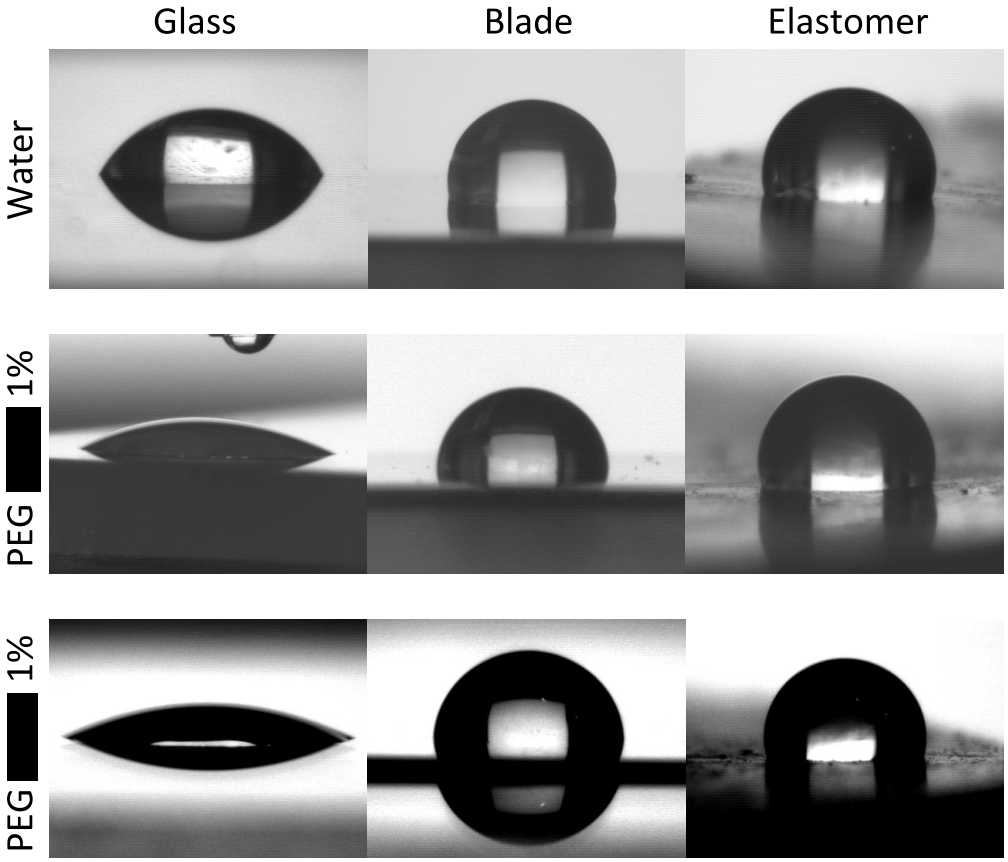

Figure 3.16: Deformation of the fluid droplet for the contact pairs of deionised water, PEG 1MM solution 1% w/w in water, PEG 5MM solution 1% w/w in water (fluids) with glass, razor blades and guard elastomer (solid surfaces), showing different adhesive behaviour. **Proprietary data (P&G). Do not disclose**.

the use of larger droplets, the size of the droplets was limited by the area of the blade and elastomer samples. By tilting the surface up to $\theta_s = 90°$, no sliding was observed, concluding that the area of blade and elastomer surfaces was not appropriate (i.e. too small) for the test.

In order to relate the intermolecular adhesion forces, as reviewed in **Section 3.3.1**, to the coefficient of friction between the fluid and contact surface, the following procedure was proposed:

- Expand the contact-interaction experiments to obtain the work of adhesion between the fluid droplets and the surface.
- With the use of larger droplets (and larger test surfaces), investigate the sliding angle and record the sliding velocity of the droplet.
- Implement a simulation process to represent the conditions of the droplet sliding experiment, iteratively tune the coefficient of friction, aiming for a match between the sliding velocity observed in the simulations and the experiments.

Implementation of the latter step was attempted, but aiming a zero sliding velocity proved to be computationally expensive, as explained in **Section 5.3.2.1**.

If the sliding velocity is captured, the optimal tuned coefficient of friction would be the one to be implemented in the subsequent simulations. Similar procedure has been used for the estimation of coefficient of friction of stent-grafts and inner wall of abdominal aortas was developed by Vad et al. (2010). If a relation between the coefficient of friction and the work of adhesion is found, it would be easier to estimate the appropriate coefficient of friction required for future simulations in the Abaqus finite element analysis environment.

With these experimental tests, the review of the physical and mechanical characteristics of shave preps is completed, setting the required background for its implementation in the **multi-physics modelling framework**.

3.8 Summary

Shave preps are non-Newtonian fluids that provide lubrication to wet shaving interaction (i.e. between the various components of a razor and the skin surface). Their shear-thinning behaviour, captured through rheological tests, is directly affected by the chemical composition and the geometrical structure of the foam (i.e. bubble size, homogeneity of bubble sizes, thickness of the Plateau borders). Two experimental procedures were developed in this PhD project and presented in this chapter for evaluation of the shave prep behaviour. Non-linear viscous shear response was captured through rheological testing, and adhesive behaviour through analysis of shave prep fluid droplets, applied to different contact surfaces. Such experiments provided essential data to feed constitutive models characterising the fluid behaviour in the **computational modelling framework** developed in this PhD project.

Rheological tests provided viscosity of the fluids at different shear strain rates. This data was used to fit the different constitutive models reviewed in **Section 3.6**. A very good agreement was obtained between experimental data and predicted theoretical values. For this reason, selection of an appropriate constitutive model to represent the shave prep viscous behaviour in the finite element environment was made in terms of performance and wall clock time required to complete the simulations (explained later in **Section 5.2.3.1**).

In the finite element environment used for this project, contact interactions are defined in terms of coefficient of friction for traction behaviour, and allowing or not separation to account for adhesive interaction ('no separation' was set for fluids where adhesion was observed). The contact angle measurements revealed an adhesive behaviour between the shave prep and the cartridge parts. With a contact angle lower than 90°, the 'no-separation' condition is present in the shave prep-blade interaction. With a contact angle larger than 90°, the interaction between the elastomer guard and shave prep can be set as 'allow separation'. For skin-shave prep interactions, skin was expected to have low sebum content due to skin anticipated cleansing prior to a shave. This increases hydrophilic behaviour in skin, thus high adhesion is expected at the skin-shave prep interface. Therefore, a 'no-separation' condition was defined for the contact interaction. A high coefficient of friction was selected to fit the 'no-slip' condition expected on the skin surface. However, the selection of such coefficient of friction was limited in the simulation by the reaction forces in the skin substrate, as reviewed in **Section 5.3.2**. For this reason, the effects of the this parameter was explored in the multi-physics simulations, in **Chapter 5**.

Chapter 4

Shaving mechanics: tribological aspects and state-of-the-art multi-physics computational models of wet shaving

Wet shaving features a complex interplay between the skin, shave prep and razor cartridge. This multi-physics phenomenon has been previously investigated by the development of micro-scale models to characterise the shave prep flow underneath the razor cartridge. This chapter includes a review of two models, which served as a basis for the ***multi-physics modelling framework*** *developed in this project. The first model corresponds to the use of computational fluid dynamics (CFD) techniques for the investigation of shave prep flow around a single blade. The second one, investigates the formation of a 'protection layer' beneath the blades, through a mathematical model characterising the shave prep ploughing and flow around the elastomer guard and blades. At the end of this chapter, the advantages and limitations of the models are highlighted, providing justification for the objectives and original contributions achieved in this PhD project with the development of the* ***multi-physics modelling framework****: implementation of the shave prep in its free surface form in a multi-physics 3D finite element environment, for the analysis of its deformation and lubrication effects.*

Wet shaving involves complex physical interactions between the skin, razor cartridge and shave prep. In a shaving stroke, the consumer applies both a force normal to the skin surface and a displacement at a given tangential velocity, as shown in **Figure 4.1**a. This induces deformation of the skin and shave prep, causing the latter to displace around and flow underneath the cartridge parts.

The skin deformation depends on its mechanical properties, loading conditions and soft and hard tissue beneath the cartridge. At the upper cheek and chin the layer of fat and muscular tissue is thin, so skin deformation is restrained by the zygomatic bone and mandible; at the cheeks, the fat layer is thicker so larger deformations are observed before the maxillary bone or teeth provide any resistance (see **Figure 4.1**b). It is in this facial area that the higher viscoelastic effects are observed (Kumagai et al., 2011).

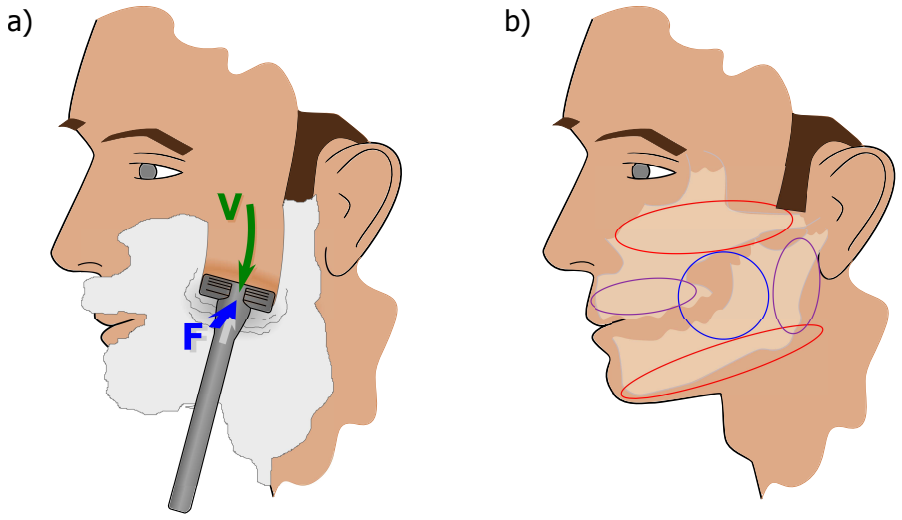

Figure 4.1: The shaving stroke loading conditions are defined by a) force of magnitude F normal to the skin surface and a velocity of magnitude V in a direction parallel to it. b) During a stroke, skin deformations are highly dependent on the mechanical characteristics of the tissue underneath the skin: the bone protuberances (red ellipses) restrain the deformation, while in areas where thicker muscles lies between the skin and bone (purple ellipses), higher deformations are allowed. However, at the centre of the cheek the highest deformations are observed (blue circle) as thicker fat tissue is found at this location and no constraint is encountered until the cheek tissue makes contact with the molars.

As mentioned in **Section 2.2**, the skin mechanical response is influenced by its current state of deformation, due to its stretch-stiffening and viscoelastic characteristics, and environmental conditions affecting the outermost layer of the skin. In wet shaving, these conditions affecting the mechanical response of skin layers are dependent by the consumer's personal habits: pre-loading of the skin, and facial cleansing.

A common shaving habit consists in pre-stretching the skin. Some techniques involve pulling the skin taut at the cheeks, folding the lips or turning the head for stretching the skin at the neck. This physically intuitive action stiffens the dermal layer providing a stiffer and more stable surface for the shaving stroke. Furthermore, it reduces the depth of the skin furrows thus providing a flatter surface for better compliance with the razor blades.

Facial cleansing provides many benefits in wet shaving. On the face, the skin contains larger amounts of sebaceous glands compared to other parts of the body (Kumagai et al., 2011), producing a sebum layer that traps dirt particles that get in contact with

skin. Although the sebum and *stratum corneum* provide a strong chemical and mechanical barrier against pathogens (see **Chapter 2**), cleansing is recommended by shaving products companies for the removal of sebum and dirt to prevent infections in case of cuts. Furthermore, cleansing hydrates skin and hair leading to a softer *stratum corneum* and hair. Hair softening also reduces the hair cutting force, which is more significant after two minutes exposure to water (Draelos, 2012; McFeat and Ertel, 2010). However, the cutting force is further reduced as exposure time to hydrating conditions is increased. This is directly related to consumer cleansing habits: a face wash can take only a few seconds, while a shower takes at least a couple of minutes. The use of a shave prep not only maintains hair constantly hydrated, softening it until it is shaved, but also acts as a lubricant for a smoother shave, therefore providing a more comfortable shaving experience for the consumer.

As explained in **Section 3.4**, shave prep reduces skin-cartridge friction forces and creates a protective layer between the skin and blades (McFeat and Ertel, 2010). Based on this principle, two computational models have been previously developed for the analysis of how mechanical properties of the shave prep fluid influence thickness and formation of such protective layer: the "Skin-blade-fluid model" by Lawler (2001) and the "Protection model" by Moir and Craig (2010). In the following sections, these models are described in detail, and their contribution of the study of shaving mechanics is analysed. In a later **Section 4.2**, a critical review expands on the advantages and limitations of these models and how these limitations are addressed by the development of the **multi-physics modelling framework** proposed in this PhD project.

These models are P&G proprietary data. Do not disclose.

4.1 Review of existing computational wet-shaving models

4.1.1 Blade-Skin-Fluid model (Lawler, 2001)

The **blade-skin-fluid model** was focused on shave prep flow ahead and underneath the blades at a micro-scale, considering a region of approximately $5 - 30$ μm around the tip of the blade. This 2D model was developed by Lawler (2001) to investigate the role of shave prep viscoelastic properties on skin deformation. The skin was represented as a bilayer linear elastic material, and the blade as a rigid body. The shave prep domain considered two regions: the inlet, ahead of the blade, and a much thinner outlet meniscus, after the blade tip, as shown in **Figure 4.2**. With the use of CFD techniques, the flow of shave prep against the blade was simulated, subject to the following boundary conditions:

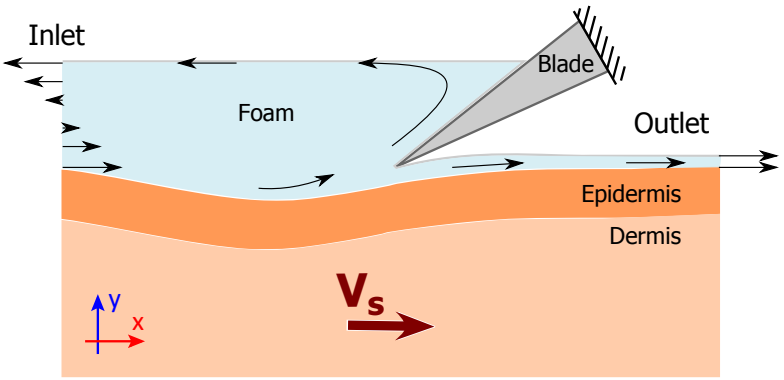

Figure 4.2: Blade-Skin-Fluid model. Flow of shave prep (foam) is driven by motion of the skin with respect to the blade at a velocity V_s. A 'no-slip' condition drags shave prep at the skin interface at a velocity equal to V_s. As foam flow gets closer to the blade, the foam velocity profile is deflected by the rigid blade, fixed in a static position (i.e. its velocity is zero), so the fluid is allow to exit the inflow surface. At the outlet, a meniscus of fluid is formed, allowing fluid to escape the outflow surface at the same velocity than the skin. The skin, composed by two layer representing the dermis and epidermis, deforms elastically under the blade, by the action of the shave prep pressure distribution. The size of the structures represented are not scaled up. Image adapted from Lawler (2001).

- **Inflow surface:** The fluid velocity profile was specified, restricted to be in the direction parallel to the skin surface.
- **Outflow surface:** The fluid velocity was restricted to be in the direction parallel to the skin, allowing the fluid to exit only through this boundary.
- **Fluid bottom surface:** 'No-slip' condition at the shave prep-skin interface was enforced by matching the fluid velocity to the velocity of the skin relative to the blade.
- **Fluid top surface, inlet region:** The fluid velocity was restricted to be in the direction parallel to the skin surface, simulating 'free surface' conditions by allowing fluid flow back to the inflow surface.
- **Fluid top surface, outlet region:** The fluid velocity was equal to that of the skin, restricted to be in the direction parallel to the skin surface.
- **Blade surface:** Although the results suggest 'no-penetration' and 'slip' contact conditions for the fluid-blade interaction, these are not explicitly indicated by Lawler (2001).

  As **initial conditions**, the blade-skin clearance distance and skin velocity were specified in the model.

In the study, Lawler (2001) compared the effects on skin deformation by implementing in the simulations three different fluids. The first one was a Newtonian fluid, setting a comparison point for the subsequent analyses. The other two fluids account for the shear-thinning viscous response of an aqueous polymer-xanthan gum solution, characterised through rheological experiments, for which viscoelastic effects were expected.

Of these shear-thinning fluids, one was represented as inelastic (purely viscous) with the **Carreau** constitutive model; the other one, accounted for the fluid visco-elastic response by combination of the **Giesekus** constitutive model of viscoelasticity with the shear-dependent response of the **Carreau** model. The model parameters were set to fit the shear-thinning response observed in the experimental rheological data.

Lawler (2001) built the blade-skin-fluid model by stage, going from simple to more complex. In this process, the model went through mesh optimisation and calculation of the parameters required to set the initial conditions of the computational model. These stages are described below.

The first stage consisted in the calculation of the velocity field (to be applied as boundary condition), assuming the skin and blade as rigid bodies. This calculation was obtained considering the viscosity of a Newtonian fluid and the skin velocity. Showing difficulties to achieve converged solutions at varied viscosities, Lawler (2001) applied a continuation process where the viscosity parameter was modified step by step, ensuring convergence from one solution to another, until the desired value was achieved. This numerical technique is applicable to any parameter required in the simulations.

In the second stage, the inelastic **Carreau** fluid was implemented, using the acquired velocity profile. The elastic response of the skin, previously model as a rigid body, was re-incorporated, and the resolution of the results was improved through optimisation of the fluid and skin meshes. In these simulations, an analysis of the effects of specified initial blade-skin clearance on the skin deformation were explored. A range of $0.5 - 5.0$ μm initial clearance values estimated by the use *residual film thickness* studies, was evaluated. The skin deformation results were linked to the changes in pressure distribution on the skin surface, as a consequence of the alteration of the initial blade-skin clearance.

Prior to implementation of the viscoelastic fluid in the blade-skin-fluid model, validation and verification of the viscoelastic fluid were performed with **capillary flow** simulation. The geometry of this model consisted of a pipe with a sudden diameter reduction, as shown in **Figure 4.3**a. For a fluid flowing at a given velocity profile, this diameter contraption causes a drop of fluid pressure along the axial position. Lawler (2001) indicated that this response can reveal the elastic characteristics of the fluid. Under such conditions, the simulations were in agreement with experimental results in the literature and the analytical calculations.

For the viscoelastic fluid, an attempt to impose the fluid stress field in the simulation was performed through the **box** model. In the box geometry, the inlet region conditions of the blade-skin-fluid model were replicated (imposed velocity profile at the inlet surface, free horizontal motion in the top surface, fluid velocity equal to that of the skin at the bottom surface). For this specific fluid, the fluid stresses were achieved in the simulation of the blade-skin-fluid model, so this step could be omitted.

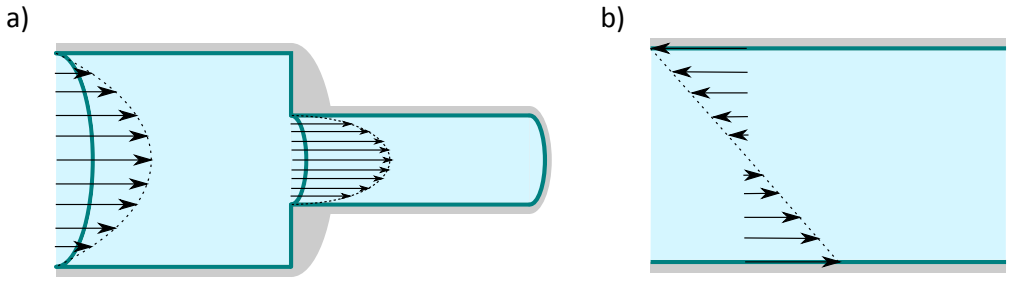

Figure 4.3: The viscoelastic flow models. a) Capillary flow geometry, build for the validation and verification of viscoelastic model. b) Box model, built for the estimation of stress distribution in the inlet region of the blade-skin-fluid model.

At the last stage, viscoelastic fluid properties were incorporated into the model. First attempts involved the simplification of the model by removing the blade and skin nodes from the calculation domain, and reducing the geometric order of the elements. The continuation process was applied for the achievement of converged solutions. However, it was noted that modification of the parameters of the elastic fluid can affect its viscous behaviour. Therefore, special attention was taken to ensure that the parameters defining the fluid elasticity would maintain the same shear-thinning response. The final analysis compared the effect of using different elastic parameters with equivalent shear-thinning behaviour in the deformation of the skin against the results of the inelastic fluid, showing high sensitivity of the skin deformation to these changes.

In this study, Lawler (2001) highlighted the sensitivity of the skin deformation to the initial conditions of the simulation, and the parameters defining the fluid behaviour. During a shaving stroke, the pressure distribution on the skin surface, caused by the shave prep flow around the blade, contributed to the skin deformation in this area. As the blade interfered with the shave prep flow, it created a pressure drop after the blade tip that pulled the skin towards the blade. Therefore, the initial blade-skin clearance had an important role on the skin deformation, as this parameter can be a determining factor for a safe close shave or a cut. Shear-thinning fluids showed a viscosity reduction due to high shear rate under the blade, so less pronounced pressure drops were observed. However, with identical shear rate-viscosity behaviour, the elastic properties of the fluid modified the pressure profile on the skin, either increasing or reducingd skin protection. With these results, Lawler (2001) provided the tools to investigate specific fluid characteristic for their implementation into shave preps.

4.1.2 Protection model (Moir and Craig, 2010)

The **Protection model** of (Moir and Craig, 2010) analysed the sensitivity of the shave prep characteristics on the formation of a protective layer preventing direct contact between the blades and the skin (i.e. nicks and cuts) whilst allowing a close shave. This model was adapted for its application in two areas of interest: the blade tips and the

elastomer on the front guard (with respect of the stroke motion). For these areas, the **blade tip** and **glide height** protection models were specified, respectively, as shown in **Figure 4.4**.

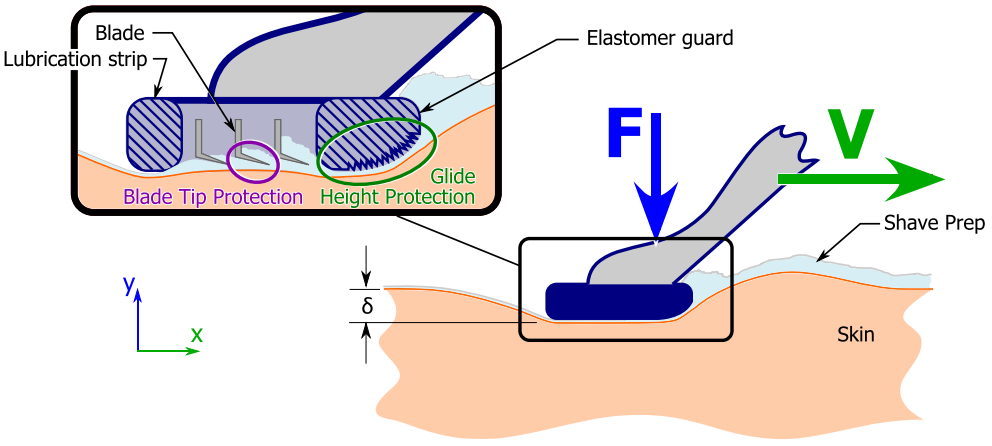

Figure 4.4: The protection model characterises the formation of a protective layer of shave prep underneath the blades, in the **blade tip protection model**, and beneath the elastomer guard in the **Glide height protection model**. The model accounts for shave prep displacement and its flow beneath the cartridge, the spring-like motion of the blades, and the skin elastic deformation (deflection δ) caused by an indenter force of magnitude F and a sliding velocity of magnitude V applied during a shaving stroke.

In both models, Moir and Craig (2010) represented skin as a linear elastic half space and shave prep as a shear thinning fluid, with the Herschel-Bulkley constitutive model. The blades were characterised as not deformable, but their motion was considered with a linear spring reaction. The skin elastic response, calculated base on an analytical model for line contact (Johnson, 1985), was determined by the reaction forces at the front and rear guards. This allowed the estimation of the clearance between the blades and skin, which tended to zero.

Two approaches were used for the investigation of the protection layer formation: *wedge flow*, where fluid was pushed and deflected by a 'wedge' geometry, and *lubrication theory*, where formation of a film of fluid allowing hydrodynamic lubrication was considered. Wedge flow, implemented for fluid interaction with the front faces of the blade tip and elastomer guard, reduced the pressure taken by the fluid trapped beneath the guard, where flow was calculated through lubrication theory. See **Figure 4.5**. The individual models are described below.

In the **blade tip protection** model, the tip of the blade was represented as a wedge whose front face was located at an angle α with respect to the skin surface (**Figure 4.5**a). The shave prep boundary conditions were defined as 'partial no-slip' at the skin surface (introduced as a factor of the blade velocity), and 'slip' at the blade surface, so as the blade moved at a given velocity, the shave prep on the skin was displaced by the blade. A flow of fluid underneath the blade was essential to enable protection. So, even though no fluid was allowed to flow underneath the blade on this simulation, the

effect of the blade-skin clearance (calculated by the elastic response of the skin) was accounted for by the application of clearance-dependent pressure saturation at the corner formed by the blade and skin surfaces.

In the **glide height protection** model, the elastomer guard was represented as a wedge whose front face was located at an angle $\alpha = 90°$ with respect to the skin surface (see **Figure 4.5**b). Similar to the blade tip model, the shave prep in front of the guard was pushed by its front face, forming a plough. Underneath the elastomer guard, an inclined wedge was assumed to form a lubrication channel capable of supporting the load applied by the consumer. The channel inlet height was considered to be of the same order of the skin surface roughness, if foam was not considered; otherwise, it was assumed that the bubbles resistance to enter the channel (experimental observations indicate that no bubbles enter the channel) influenced the channel inlet height, which was set equal to the mean bubble diameter. The outlet height was defined in terms of the pressure and channel length. The inlet pressure in the channel was defined by the pressure at the shave prep plough, calculated through the wedge flow approach, and set to zero at the channel outlet. In the wedge flow approach, the fluid flow was represented by Navier Stokes equations, simplified for creeping steady flows; in the lubrication channel, the Dien-Elrod approximation to the non-Newtonian Reynolds equation was used (Khan, 1988).

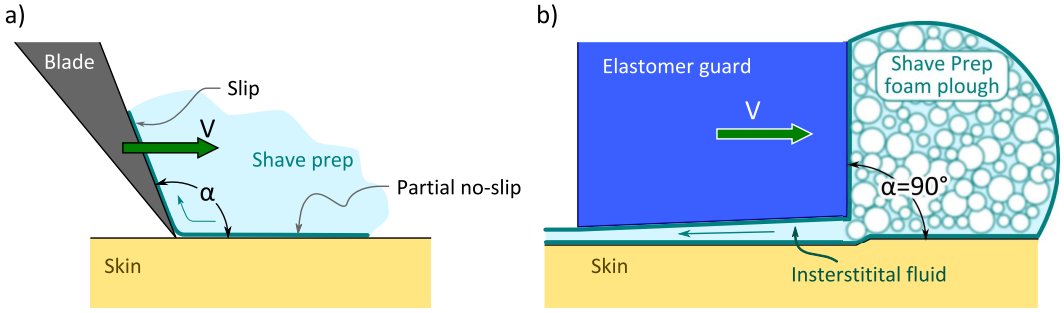

Figure 4.5: Geometrical simplification of protection models. *a*) **Blade tip** protection model: The blade tip is simplified as a wedge with the fluid-contact surface at an angle α. *b*) **Glide height** protection model: The elastomer guard is simplified as a inclined wedge where $\alpha = 90°$ for the interaction with the shave prep foam. With a razor cartridge moving at a velocity V with respect to the skin, the shave prep is pushed by the wedge geometries (blade and guard). Beneath the elastomer guard a channel of interstitial fluid is formed.

In their report, Moir and Craig (2010) analysed the effects of the shaving stroke force and velocity, and the sensitivity of the model to shave prep characteristics, foam bubble radius, Herschel-Bulkley parameters, cartridge dimensions and skin elasticity. The model showed that glide and blades protection increased with an increasing velocity. By increasing the normal force, the glide protection was reduced while protection at the blades remained constant.

As part of the protection analysis, the effects of a 'protuberance' (e.g. scar tissue or acne spot) in skin were included. The presence of a protuberance changes the angle

of the blade with respect to the skin surface, so cleavage is likely to occur. In this case, the protection relied on displacement of the skin protuberance being higher than the clearance between the skin and blades.

Furthermore, Moir and Craig (2010) also considered the case of a second stroke, where no shave prep plough was formed. This analysis showed the relevance of the shave prep plough in the distribution of pressure in the elastomer guard channel. As higher pressures were taken under the guard, the channel height was reduced and so was the skin protection.

With these results, Moir and Craig (2010) proposed a number of experiments for verification of the results and a series of recommendations for improved skin protection, involving physical characteristics of the shave prep and cartridge design.

4.2 Analysis of existing computational wet-shaving models: advantages and limitations

The reviewed **skin-blade-fluid** and **protection** models provided essential information about the FSI phenomena from a microscopic perspective (at a tip-of-the-blade scale). The natural complexity of the interaction led to simplification the problem with assumptions of linear elasticity of the skin and flat geometries of the blade and elastomer guard as wedges. However, the studies presented by Lawler (2001) and Moir and Craig (2010) explored different scenarios by assessing the sensitivity of the parameters describing the mechanical behaviour of shave prep and consumer shaving style to skin deformation and formation of a protection layer on the skin surface.

The two models incorporate the skin deformation with the pressure effects of the fluid underneath the cartridge parts but with two different approaches. On the one hand, Lawler (2001) estimates the magnitude of the blade-skin clearance based on *residual film thickness* theories, and given this value, the skin deformation was linked to the pressure build-up in the shave prep fluid. On the other hand, Moir and Craig (2010) estimated the skin-blade clearance from the skin elastic response, and the formation of an interstitial fluid channel beneath the ruffle strip in terms of the skin surface roughness or the bubble radius (if present). This provided an estimate of the protection layer thickness underneath the blade, which was used to estimate the changes in pressure incorporated to the shave prep flow ahead of the blade.

The main drawback of these models lies in the de-coupled approach to incorporate multi-physics interactions in the shaving stroke simulation. Modelling assumptions were made to estimate formation of fluid film beneath the cartridge. Furthermore, the analyses were performed in a plane strain 2D scenario, failing to capture the real 3D

interactions between shave prep, cartridge and skin, and the distribution of shave prep around the cartridge structure. The limitations of these models are listed as follows:

- Both models (Lawler, 2001; Moir and Craig, 2010) were developed in 2D, thus no shave prep distribution around the different geometrical features of the cartridge could be captured.
- Although the models consider the formation of a shave prep film at a microscopic scale, at which it is thought that skin microrelief (i.e. topographic features) might have a large effects on the film formation, the skin was assumed to be a flat linear elastic substrate.
- The fluid-solid contact interactions were modelled in terms of no-slip condition (Moir and Craig, 2010) or equal velocity at the fluid and skin (Lawler, 2001), and as a contact slip condition at the cartridge parts, without considering any different adhesive forces at each of the cartridge parts.
- In both reviewed models, no validation for the formation of the protection film against experimental data was provided. While Lawler (2001) only validated the fluid elastic behaviour in terms of pressure drop (capillary flow model), Moir and Craig (2010) did not validated any aspect of their model. They clearly stated that their results were for understanding the effects of shave prep properties in the formation of a protection layer.

Another area of discussion is the effect of hair during the shaving interaction. Moir and Craig (2010) considered either the bubble radius or the skin surface roughness to estimate the dimensions in the channel formed between the skin and the elastomer guard. However, being the guard the first area of contact in the stroke direction (i.e. no hair is cut at this stage), the hair diameter is more likely to define the thickness of the 'glide' layer under the guard. Then, hair provides an obstacle in front of the blade, so it is caught by the blade tip and it gets pulled out of the hair root sheath as the razor moves. Being partially cut, hair under the blade pushes the skin down creating a gap under the blade, potentially larger than that calculated with lubrication analytical models. Once the hair is cut by the first blade, the skin gets back in contact with the blade, being at this point that the protection layer is more relevant —before the next hair comes to play. Because of the viscoleastic nature of the skin, hair pulled out by the first blade is caught by the next blade before it retracts to its original position, repeating the process mentioned above at each blade, providing a closer shave. It is easy to deduce that, in this process, the direction of hair with respect to the shaving stroke (i.e. either against or with the grain) would have an effect on the gap formed

between the blade tip and the skin surface. Likewise, differences in the blade gap dimension can be expected with the changes in the hair geometry after consecutive shaving strokes. Despite its importance in the skin and blade deformation (which can potentially modify the whole lubrication process), none of the shaving models reviewed above considered the effect of hair during a shaving stroke.

4.3 Contribution of the multi-physics modelling framework to the study of wet-shaving tribological interactions

The **multi-physics modelling framework** developed in this project, is a logical extension of the two reviewed models. A more realistic 3D and fully coupled multi-physics finite element approach was taken, evaluating the effects and mechanical behaviour of shave prep at a macroscopic scale. The main contributions of this modelling framework to existing models involve the skin and shave prep models, and the integration of the fluid-structure contact interactions in a flexible multi-physics finite element environment, as explained below.

Skin model

The implemented skin model was developed by O'Callaghan and Cowley (2010) through experimental characterisation of facial skin, capturing the skin elastic and viscoelastic characteristics, including the bulging response observed in-between blades. This model consisted of three layers (epidermis, dermis and hypodermis), idealised as flat layers for the analysis of shaving mechanics in a macroscopic scale.

From a microscopic scale perspective, an **anatomical skin model** was developed, based on images of histological sections of human skin. This model captured in 2D the intricate anatomical geometry of the skin microrelief and that of the interfaces between skin layers, considering the *stratum corneum*, viable epidermis and dermis. The skin layers were represented as hyperelastic neo-Hookean materials. Extension of this model into a one-element thick 3D model can be applied for the analysis of shaving mechanics in the microscopic scale.

Razor cartridge

The implemented razor cartridge model reassembled the detailed geometries of a Gillette® *Fusion* cartridge parts, with their corresponding materials and mechanical properties, provided by the sponsor. In order to reduce computational cost, optional modelling of the parts as rigid bodies was available. The model accounted for the pivoting and retraction mechanisms that allowed the cartridge to tilt freely along the face contours. Each cartridge part was easily replaceable for the assessment of different cartridge designs.

Implementation of the shave prep model

Shave preps were **experimentally characterised** in order to capture their shear thinning viscous behaviour, and their adhesive properties to materials found in the razor cartridge. A protocol for rheological testing of shave prep foams was designed to ensure consistent results of shear strain rate effects on the foam viscosity, considering the methodology for sample preparation, measurement of the fluid density, and qualitative assessment of the foam structure (bubble ratio). The adhesive behaviour of shave preps was evaluated through measurements of contact angle of PEG solutions droplets deposited on test surfaces corresponding to cartridge parts (blade and elastomer guard). By rotation of the surface, the experimental analysis included the assessment of the gravity effects pulling the droplet along the surface, documenting the changes in the advancing and receding contact angles. The experimental conditions were not suitable to induce sliding of the droplet for the estimation of a coefficient of friction for the fluid-solid contact pair. However, a series of improvements and an iterative simulation process was proposed for characterisation of shave preps adhesive behaviour in terms of coefficient of friction and adhesion (allowing no separation between the materials).

The **shave prep model**, developed from the experimental characterisation of shave preps, was implemented in the modelling framework as a free surface non-Newtonian fluid. Under the action of the razor cartridge, the fluid freely deformed, capturing the flow around the cartridge structure under indentation, and channelling of shave prep underneath the cartridge as it moved. Such channelling was captured through definition of **fluid-structure contact interactions** between shave prep and cartridge parts in terms of adhesion and coefficient of friction, providing higher fidelity to the simulation than that under common 'slip'/'no-slip' boundary conditions.

Modular modelling environment

The computational modelling framework was built in **modular modelling environment** in which the razor cartridge and skin model were interchangeable. Likewise, the mechanical properties and constitutive model representing the shave prep material and its specific interaction properties could be tailored to represent different shave prep formulations.

The **multi-physics modelling framework** developed in this PhD project incorporated most of the elements present in wet shaving: the whole cartridge structure, applied loading, a skin material model, and a free surface shear thinning shave prep constitutive model. This modelling framework was developed in a robust industry-grade coupled Eulerian-Lagrangian finite element environment that coupled fluid effects with the deformation of skin under the action of applied force in a 3D space. Furthermore, it incorporated the adhesive behaviour of shave prep to skin and cartridge surfaces,

established through dedicated experimental tests. The fidelity of the multi-physics model can be augmented by incorporating experimentally-based fluid-structure contact properties for each solid material, following the recommendations for a coupled experimental-computational analysis of sliding fluid droplets (**Section 3.7.2.1**). This modular framework allowed for interchangeability of model parts for the analysis of different guard forms and skin conditions. For example, the framework can accommodate anatomically-realistic skin microrelief to study micromechanics shaving interactions, and the effect of hair. With these characteristics, the **multi-physics modelling framework** provided a comprehensive toolbox for the analysis of skin deformation and lubrication effect for cartridge designs, shave preps and skin conditions.

The research methodology followed for the development of the **multi-physics modelling framework** is explained in the following chapter.

Chapter 5

Shaving mechanics: coupled Eulerian-Lagrangian multi-physics models of shaving tribophysics

Solid and fluid materials show notable differences in deformation response for given loading conditions and time scales, so their analysis in finite element (FE) methods require different approaches. Fluid-structure interactions (e.g. wet shaving) involve the combination of Lagrangian and Eulerian methods applicable for solid and fluid analyses respectively, in a coupled Eulerian-Lagrangian (CEL) approach. In this chapter, the theory behind the finite element methods and its application to characterise the interactions between the skin, razor cartridge and shave prep are described. The modelling process must capture the physics (i.e. mechanics) of the individual components of the systems (skin, razor, shave prep) as well as the physics of their interactions (coupled physics). Along this process, a model optimisation process is described, evaluating the sensitivity of the model runtimes to the parameters describing the fluid material, the fluid mesh characteristics and the computational resources used for the analysis (parallelisation). The knowledge gathered from these models and analyses set the basis of the computational modelling framework for the characterisation of the skin interactions with wet shaving products. Some applications of this modelling framework are described at the end of this chapter.

In a shaving stroke, three individual components, the *skin*, *razor cartridge* and *shave prep*, interact together via multi-physics phenomena (i.e. fluid-structure coupling). The process of developing the **multi-physics modelling framework** for this PhD project consisted of three stages: *I*) development/implementation of individual shaving stroke components; *II*) implementation of two-components interactions accounting for friction, shearing and adhesion effects (solid-solid and fluid-solid interactions); and *III*) implementation of the three-component interactions models, describing the full fluid-structure interactions (FSI) of the shaving stroke problem, as illustrated in **Figure 5.1**.

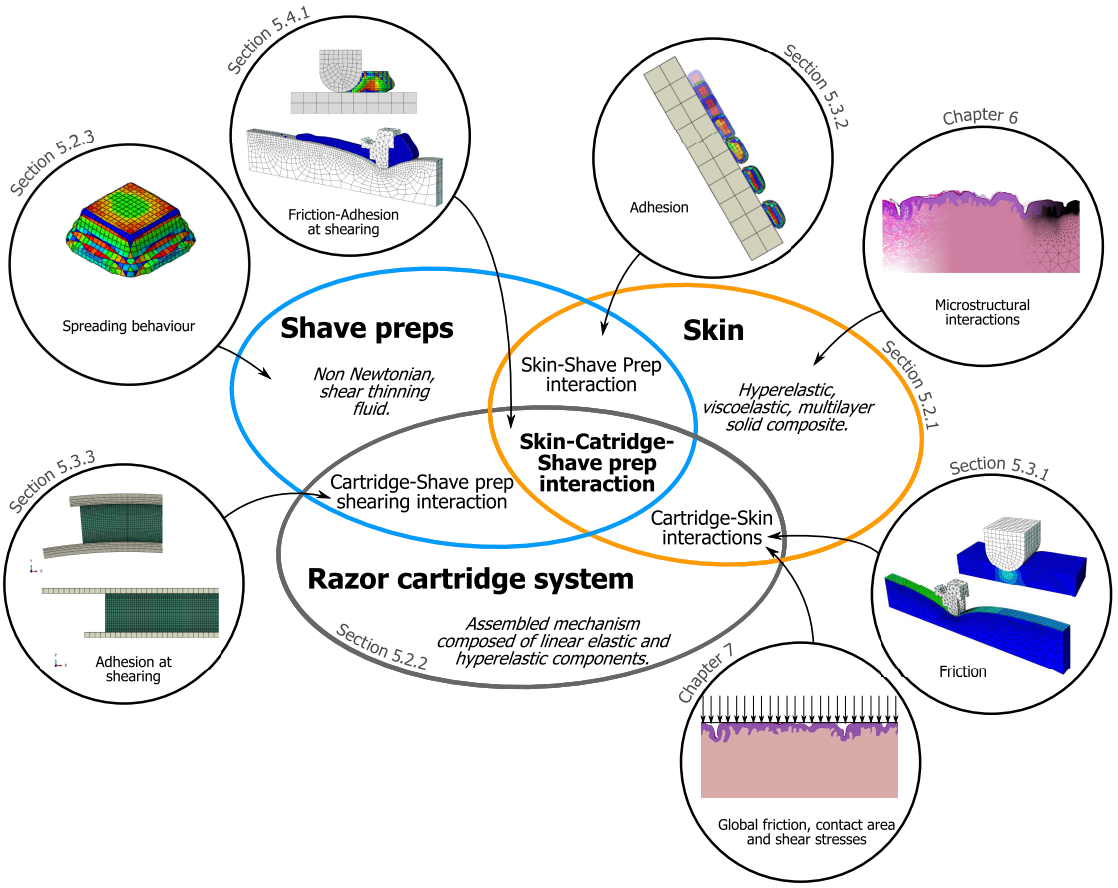

Figure 5.1: Computational characterisation of shaving stroke interactions. The multi-physics modelling framework accounts for the individual shaving stroke components (skin, razor cartridge and shave prep), and the interaction between each of the components (cartridge-skin, cartridge-shave prep and skin-shave prep). An anatomical skin model (described in **Chapter 6**) is proposed for the more fundamental analysis of the effects of the skin microstructure on its macroscopic deformation (**Chapter 6**) and tribological response such as shaving interactions (**Chapter 7**). Snap-shots of the developed models at different stages of the modelling process are included in the diagram.

The **first stage** of development consisted in the characterisation of the individual shaving stroke components in the finite element environment. In **Section 5.2**, the geometrical characteristics and parameters required for the constitutive models are described. In the case of the shave prep model, which was fully developed as part of this PhD project, additional information about the verification process and sensitivity analysis of the model performance to viscous properties, mesh characteristics, and parallelisation level is provided. The **second stage** of development involved the implementation of the shaving stroke components into two-component interaction models in the finite element environment, for the analysis of the different interaction conditions observed during a shaving stroke. These models included the **skin-cartridge** 'dry' interactions for the analysis of frictional effects, the **shave prep-skin** interaction accounting for the shave prep adhesive behaviour, and the **shave prep-cartridge** interaction for the analysis of viscous effects in the shave prep due to shearing conditions applied by the solid parts. The description of the boundary and loading conditions of the two-components models and the implications observed at each interaction pair are given in **Section 5.3**.

The **third stage** of development integrated the individual components and interaction models in a unified environment that served as a test platform for the fully-coupled modelling framework towards the multi-physics simulation of a shaving stroke, as described in **Section 5.4**.

As reviewed in **Chapters 2** and **3**, the mechanical response of each material in the shaving stroke components can be represented through different constitutive models. Within finite element methods, constitutive equations are augmented by a series of equations in order to enforce material continuity during the analysis. Such equations can be solved with either a Lagrangian or an Eulerian description, depending on the level of deformation expected: Lagrangian methods are typically used for low deformation problems where the material can be easily tracked (e.g. skin, cartridge parts), and Eulerian methods for problems where the deformation rate is so large that the material points are difficult to track (e.g. shave prep). In the following sections, the theory behind these descriptions and how they are coupled in the finite element method for solving FSI problems is described (**Section 5.1**), followed by the description of the three developing stages of the **multi-physics modelling framework** adopted in this PhD project in **Section 5.2-5.4**.

5.1 Computational modelling of fluid-structure interactions: Coupled Eulerian-Lagrangian formulation

The deformation and response of continuum media can be described by either a Lagrangian (material) or an Eulerian (spatial) approach. In both cases, the quality of the mesh is crucial to obtain accurate solutions. The Lagrangian description is often used in solid mechanics problems involving relatively low deformations, because at large deformations, the quality of the mesh deteriorates leading to higher computational cost and inaccurate solutions if any. The Eulerian description captures flow of material as it moves through a fixed mesh. This description is appropriate for the analysis of fluid materials and simulation of material fragmentation and projectile splattering. As the material flows through the mesh, the elements can be either full of material, void (i.e. be empty) or be partially filled. The main drawback of the Eulerian description remains on the definition of moving boundaries, surfaces and interfaces, as the material surfaces are not physically described (Belytschko et al., 2000).

For complex multi-physics problems such as wet shaving, mud-tyre contact, paste extrusion, among others, where fluids and solids interact and deform simultaneously, it is possible to combine both Lagrangian and Eulerian descriptions to capture fluid-structure interactions. In the next section, these two approaches are first described separately, and then the coupling of these descriptions is explained.

5.1.1 Mesh definitions: Lagrangian and Eulerian descriptions

The **Lagrangian description** is also referred to as *material description* because it tracks the location of the material points as deformation occurs. Each element node corresponding to a specific material point form the mesh within the body itself, so the analysis is made from the material perspective. The **Eulerian description**, also known as *spatial description* because material flow is tracked from a fixed position in space, is capable of tracking the motion of the material points through the spatial coordinates, so the element nodes are preserved in their position, independently from the material points (Belytschko et al., 2000). For this description, the space where material can exist is delimited by the *Eulerian domain* (also known as Eulerian space) in which the Eulerian mesh is built. The analysis results combine the output parameters at the nodes with a convective term that describes the material flow. The amount of fluid contained within an Eulerian element is described by the ratio of volume the material occupy, with respect to the element volume, known as *volume fraction* (i.e. volume fraction of 1 represents a full element, and 0 an empty one) (Aba, 2014b). The inverse approach is referred as *void ratio*. See **Figure 5.2**.

In the finite element method, the initial conditions of the problem are defined in the *initial configuration* domain Ω_0, and the problem response can be described in either material or spatial terms in the *current configuration* domain Ω. The material points in the Lagrangian description are defined by their material coordinates $\mathbf{X}$ and time t. Likewise, in the Eulerian description, the material points are defined by their spatial coordinates $\mathbf{x}$ and t. The *motion* of a body in the current configuration is described by the mapping function $\boldsymbol{\phi}(\mathbf{X}, t)$ that relates the initial configuration with the current one, providing the *spatial position* of the material points at a given time, as:

$$\mathbf{x} = \boldsymbol{\phi}\left(\mathbf{X}, t\right) \tag{5.1}$$

In the initial configuration, the material and spatial coordinates are coincident so the position at $t = 0$ is the identity mapping is given by:

$$\boldsymbol{\phi}\left(\mathbf{X}, 0\right) = \mathbf{x} = \mathbf{X} \tag{5.2}$$

The *displacement* of a material point is described by the difference between the position in the current and original configurations:

$$\mathbf{u}\left(\mathbf{X}, t\right) = \boldsymbol{\phi}\left(\mathbf{X}, t\right) - \boldsymbol{\phi}\left(\mathbf{X}, 0\right) = \mathbf{x} - \mathbf{X} \tag{5.3}$$

In the Lagrangian description, the *velocity* of a material point is written as a derivative of displacement with respect to time:

$$\mathbf{v}\left(\mathbf{X}, t\right) = \frac{\partial \mathbf{u}\left(\mathbf{X}, t\right)}{\partial t} \tag{5.4}$$

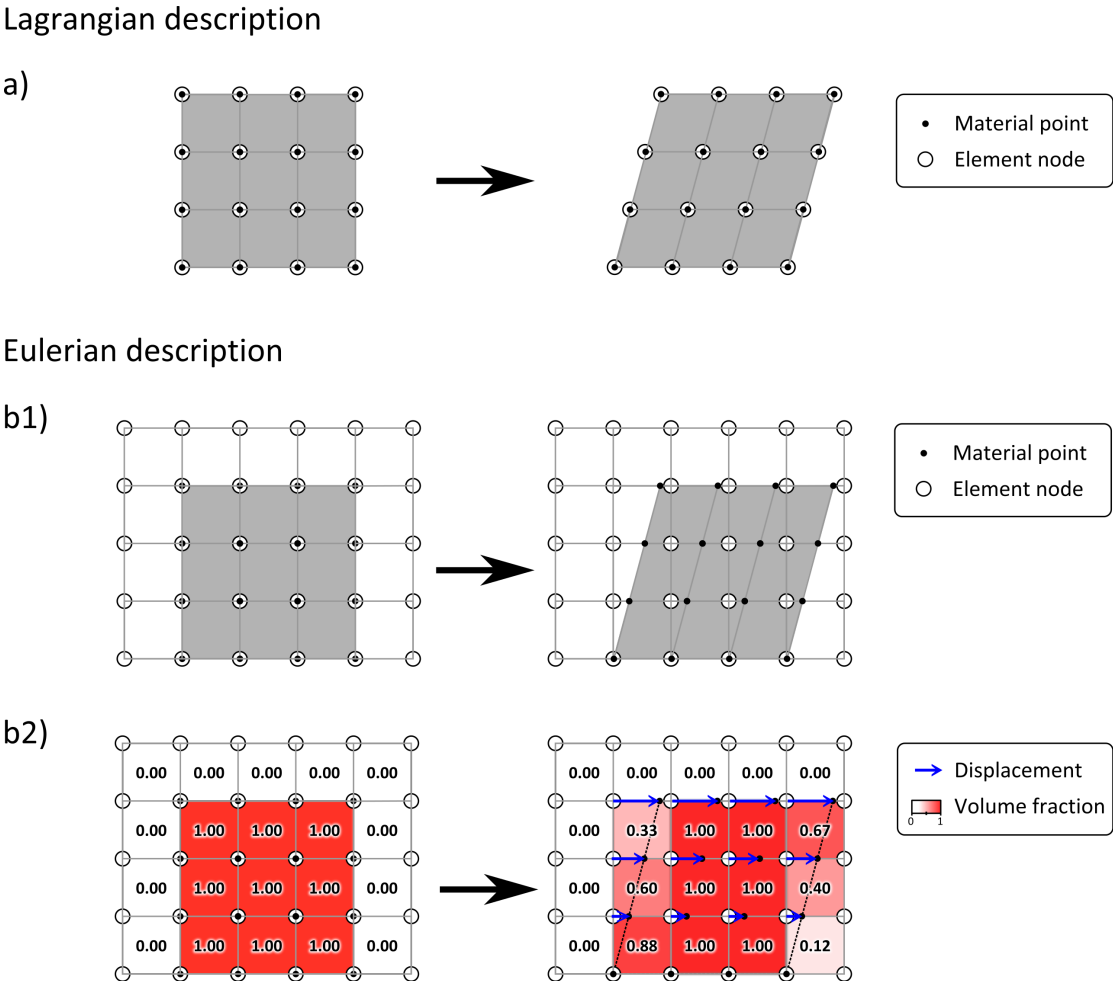

Figure 5.2: Lagrangian and Eulerian mesh definitions. In the finite element method, the mesh corresponds to the discretisation of the body in a finite number of elements. *a*) In the Lagrangian description, as the material deforms, so do the elements, maintaining a coincident location between the material points and element nodes. *b*) In the Eulerian (spatial) description, the elements define an Eulerian domain where the body material can exist - but they do not define the body itself. The material points move with the deformation while the element nodes remain immobile (b1). The analysis shows the results at the fixed node locations and the amount of fluid present in the elements is indicated by the volume fraction, where 0 is shown for empty elements, and 1 for full ones (b2).

Likewise, the material point *acceleration* is given by:

$$\mathbf{a}\left(\mathbf{X},t\right)=\frac{\partial\mathbf{v}\left(\mathbf{X},t\right)}{\partial t}=\frac{\partial^{2}\mathbf{u}\left(\mathbf{X},t\right)}{\partial t^{2}} \tag{5.5}$$

In order to express any vector function $\mathbf{M}$ of the material points in the Eulerian description, it is first expressed in terms of the spatial coordinates and time. That is, $\mathbf{M}\left(\mathbf{x},t\right)=\mathbf{M}\left(\boldsymbol{\phi}\left(\mathbf{X},t\right),t\right)$. The material time derivative of this function provides two terms:

$$\frac{D\mathbf{M}\left(\mathbf{x},t\right)}{Dt}=\frac{\partial\mathbf{M}\left(\mathbf{x},t\right)}{\partial t}+\frac{\partial\mathbf{M}\left(\mathbf{x},t\right)}{\partial\mathbf{x}}\cdot\frac{\partial\mathbf{x}}{\partial t} \tag{5.6}$$

where the spatial time derivative is given in the first term on the right hand side of **Equation 5.6**, and the convective term that captures the transport in the Eulerian mesh,

in the second term.

Due to the vectorial nature of $\mathbf{x}$ and $\mathbf{M}$,

$$\frac{\partial \mathbf{M}(\mathbf{x},t)}{\partial \mathbf{x}} = \frac{\partial M_i}{\partial x_j} = \nabla M \tag{5.7}$$

Taking **Equation 5.1**, then:

$$\frac{\partial \mathbf{x}}{\partial t} = \frac{\partial \boldsymbol{\phi}(\mathbf{X},t)}{\partial t} = \mathbf{v}(\mathbf{X},t) \tag{5.8}$$

which is described in **Equation 5.4**. With the commutative properties of dot product, **Equation 5.6** can be re-written as

$$\frac{D\mathbf{M}(\mathbf{x},t)}{Dt} = \frac{\partial \mathbf{M}(\mathbf{x},t)}{\partial t} + \mathbf{v}(\mathbf{X},t) \cdot \nabla \mathbf{M} \tag{5.9}$$

or in a generic way,

$$\frac{D(M)}{Dt} = \frac{\partial (M)}{\partial t} + \mathbf{v} \cdot \nabla (M) \tag{5.10}$$

which is applicable to any other scalar or tensor function such as the velocity $\mathbf{v}$, acceleration $\mathbf{a}$, or stress $\boldsymbol{\sigma}$, to express them from the Lagrangian to Eulerian description.

5.1.2 Coupled Eulerian-Lagrangian formulation

The multi-physics modelling framework was developed within the finite element platform provided by Abaqus 6.13/6.14 (Simulia, Dassault Systèmes, Providence, RI, USA). Within this platform, a "Lagrangian-plus-map" procedure is applied to evaluate Eulerian bodies in two phases: Lagrangian deformation and Eulerian convection (re-map) (Aba, 2014a). The first phase allows the deformation of the finite elements in a material description, maintaining the material points and nodes coincident; in the second phase, the elements deformation is analysed into the spatial description (as in **Equation 5.10**) and the mesh is re-mapped into its original location so the deformation is interpreted as material flow (see **Figure 5.3**a). The results are then computed at the element nodes, as shown in **Figure 5.2**b2.

The same procedure is used for analysing contact interactions in the CEL approach. Lagrangian bodies can co-exist within the Eulerian domain as long as the space occupied by the Lagrangian body is void-filled (i.e. no Eulerian material is contained in the occupied space). When the Lagrangian body reaches a filled element, the Eulerian body deforms to a target Eulerian-Lagrangian contact surface defined by the Lagrangian body. As this surface moves during the contact interaction, the Eulerian material is displaced so that penetration of the Eulerian material into the Lagrangian body is prevented (Aba, 2014a). See **Figure 5.3**b. Under these conditions, the contact interaction

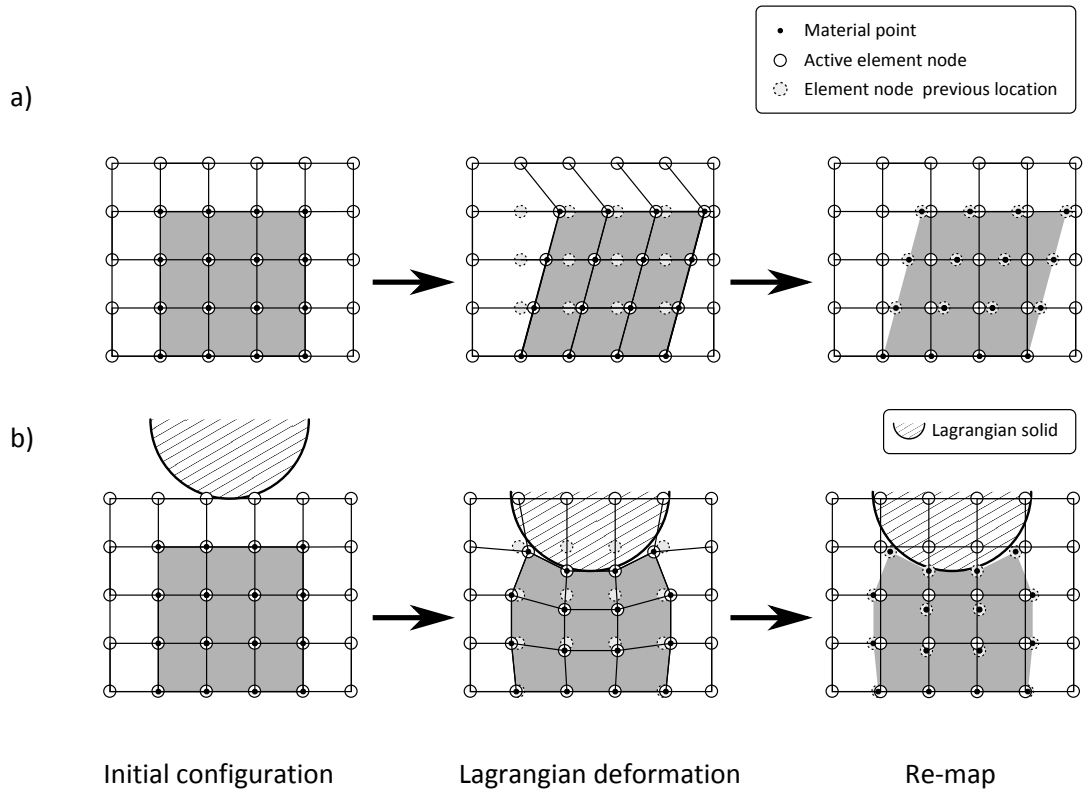

Figure 5.3: Eulerian analysis procedure. *a*) The "Lagrangian-plus-map" procedure used for analysis of Eulerian bodies consists in two steps: Lagrangian deformation (centre), and re-maping (right) of the mesh into the shape of the original configuration (left). *b*) Lagrangian bodies can exist in an Eulerian domain (or space), so when in contact with Eulerian bodies, an Eulerian-Lagrangian contact surface is formed, replacing the overlapping area of the elements filled with void.

between the Eulerian and Lagrangian bodies can be then specified in similar conditions as expected for Lagrangian-Lagrangian contact.

Other approaches have been developed for the analysis of fluid-structure interactions. One example of this is the smoothed particle hydrodynamics (SPH) technique, a mesh-less method, also available in Abaqus, where the material nodes are represented as particles with a given volume and zone of influence. This method is often used for free surface fluids modelling. However, this approach is less accurate than CEL (Aba, 2014a), with a current technological limitation of not being able to support parallel computations (Aba, 2014a). Due to the complexity of the problem presented in this project, for the analysis of shaving interactions a fine mesh is required so it could capture the detailed geometry of the razor cartridge. Furthermore, analyses including contact interactions significantly increase the computational cost. Therefore, given the high computational cost expected for the FSI analyses of shaving strokes, it is imperative to have access to efficient solvers capable of running on multiple processors. This requirement made CEL the most appropriate framework in the Abaqus environment for the development of this project.

5.1.3 Parallel computing

All the characteristics of a problem (e.g. geometry, mesh, loading and boundary conditions, material properties) are described in a *job*. When this job is submitted for analysis, the calculations of the analysis are performed in processing units (processors). It is important to distinguish that while the *simulation time* refers to the time frame of the problem described in the job physical time, the wall clock time (WCT) taken to solve the problem is referred as *runtime*. While a single processor is capable to run a simple task on its own, large problems requiring significantly more computations (as it is the case for the FSI simulations of shaving mechanics) can make use of multiple processors working in parallel and communicating to each other to provide faster solutions. This is known as *parallel computing* (Almasi and Gottlieb, 1994), for which the *computational cost* is described in terms of runtimes and processing resources used (parallelisation level).

For parallel computing, the runtime involves the sum of processing and communication times. It is expected that larger number of processors working in parallel require larger communication times, reaching a limit of efficiency in which the use of more processors would result in larger runtimes. Both processing and communication times are dependent on the software and the communication system (e.g. types of processors, connection architecture). Therefore, the analysis of optimum number of parallel processors for a given problem size is advised for different computing facilities, as the performance can vary from one computer to another. In the simulations discussed in this chapter, the optimum number of parallel processors used was selected with the following approach: The job indicating the simulation instructions was submitted for its analysis with different numbers of parallel processors for a short time; then, the results were linearly interpolated to estimate an approximated completion time, being the shorter estimated completion time the parameter used to select the parallel processors required for the simulations. The simulations described in this chapter were performed in the high-performance computing facilities provided by P&G.

In the multi-physics modelling framework, the skin and cartridge parts were modelled as Lagrangian bodies, and shave prep as an Eulerian one. The skin and cartridge models have been previously developed by P&G for the assessment of the skin response during wet shaving, where the lubricating effects of shave prep were accounted for in terms of a low coefficient of friction. In this PhD project, the shave prep model was developed based on the experimental characterisation of shave prep fluids (**Chapter 3**), and implemented in the shaving stroke simulations, incorporating the lubrication phenomena in the analysis of wet shaving mechanics. In the next section, the skin and cartridge models are described, followed by the implementation of the shave prep model, for the individual characterisation of each shaving stroke component.

5.2 Modelling framework development, stage I: models of the individual shaving stroke components

The development of the **multi-physics modelling framework** required the characterisation of the individual shaving stroke components into finite element models as a first step. The skin was represented according to the work of O'Callaghan and Cowley (2010), and the cartridge model corresponds to the geometrical and material characteristics provided by P&G design team. A key task for the development of this project was the experimental characterisation of the constitutive behaviour of shave prep for its implementation into the finite element modelling framework. The finite element models of each individual shaving stroke component are described next. As part of the shave prep model description, the analysis for mechanical behaviour verification, and sensitivity of the computation times to the different mechanical properties and Eulerian mesh characteristics, are also included.

5.2.1 Skin model

The model of the skin tissue was implemented according to experimental measurements conducted by O'Callaghan and Cowley (2010), resembling the layered composite structure of the skin, accounting for the epidermis, dermis and hypodermis layers, whose thickness corresponded to measurements obtained with ultrasound and optical coherence tomography on facial skin. In their work, the most accurate mechanical response in finite element simulations was obtained by fitting to the van der Waals hyperelasticity (**Equation 2.29**) and Prony series viscoelasticity (**Equation 2.18**) constitutive models the experimental data obtained through indentation, extensometry and skin bulge tests. For this reason, these constitutive models were selected to represent the skin mechanical behaviour. The skin layers were described as isotropic, assuming that during the shaving stroke the skin will not be stretched to the point of 'activation' of the collagen fibres, leaving the resistance to the elastin fibres and viscoelasticity to the ground substance. The parameters describing the skin model are subject to confidentiality, and not shown. The testing and modelling methods, as well as the range of forces and deformation in which the model is applicable is described in detail, and **protected by patent WO 2010/114947 A1** (O'Callaghan and Cowley, 2010).

5.2.2 Cartridge model

The cartridge model was provided by P&G, and corresponded to the design of the Gillette Fusion® cartridge. The model was built as an assembly of blades, guard, clips, lub-strip and ruffle-strip elastomer guard. The hinge mechanism at the handle-cartridge interface was included for appropriate simulation of the adaptive motion of the cartridge

to the skin surface. Each part was represented with the corresponding constitutive model and mechanical properties of each material, describing the elastic behaviour of the metallic parts (e.g. clips, blades and blade supports) as linear elastic, and the one of the elastomeric parts (guards) as hyperelastic. Although specifying the full elastic behaviour of the parts would provide more accurate results, solid parts where no deformation was expected were simplified by applying rigid body constraints for faster simulation times.

5.2.3 Shave prep model

The skin and razor cartridge models, developed and validated by P&G and O'Callaghan and Cowley (2010), have been previously applied in the company for 'dry' simulations where no shave prep was considered. In this PhD project, the shave prep finite element model has been developed, based on the experimental characterisation of the mechanical behaviour of various shave prep fluids and foams (viscosity and adhesion, see **Chapter 3**), for its implementation in multi-physics simulations of wet shaving. The development process consisted in the **selection of the constitutive model** to represent the shave prep behaviour, **verification** of the fluid viscous behaviour, and analysis of the **runtime sensitivity** of the fluid model to the different parameters describing the shave prep in the finite element environment (mechanical properties and mesh characteristics). Such process was achieved with the use of three test models built for the representation of specific conditions observed in shave preps during a shaving stroke. The **droplet model**, accounting for the free-surface conditions of the shave prep observed in wet shaving, provided a platform to analyse the solely contribution of the fluid material to the simulation runtimes; and two **shear models**, simulating the shearing conditions observed in the rheological tests (radial arrangement) and under the cartridge (planar arrangement), provided the conditions to verify the fluid viscous behaviour was appropriately captured in the simulations. These models, which accounted only for the fluid behaviour (i.e. no contact interactions nor solid deformation was involved), and their application in the computational characterisation of the shave prep model, are described below.

5.2.3.1 Shave prep test models

Droplet model

The droplet model comprised a droplet of fluid contained within an Eulerian domain, located near the top surface. The droplet, pulled down by the action of gravity, was restrained to leave the Eulerian domain by specifying the velocity normal to each surface as zero. Although such boundary condition emulated a frictionless wall, its contribution to the simulation runtimes was limited to fluid

velocity condition, so no fluid-solid contact interaction was accounted for in the simulations (see **Figure 5.4**). As the droplet hit the lower boundary, the fluid spreading behaviour was visually assessed, as faster spreading at the base of the Eulerian domain was expected for fluids with lower viscosity.

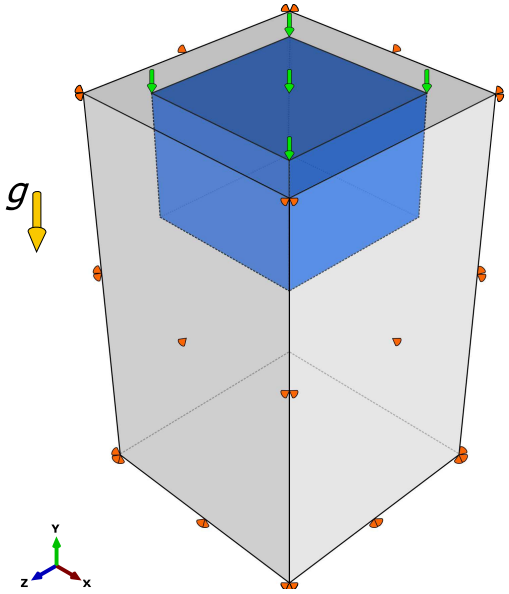

Figure 5.4: Droplet model. The droplet model comprises a fluid droplet (blue) falling freely (by setting the Eulerian boundary void-inflow at the top surface -green arrows- the droplets falls as a single entity) under gravity forces ***g*** in contained the Eulerian domain volume (grey) by setting the velocities normal to each surface to zero (orange).

The Eulerian domain was defined by a $0.3 \times 0.3 \times 0.5$ mm^3 volume, containing a $0.2 \times 0.15 \times 0.2$ mm^3 fluid droplet at the centre of the top boundary. The parts were meshed with a 0.015 mm global seed, generating 11,913 linear hexahedral Eulerian elements (EC3D8R). The simulation step (i.e. physical time described in the job) was set to 0.05 s accounting for the time requiring for the droplet to hit the lower surface at the scale of this model.

Radial shear model

This model comprised the application of shear to a thin section of fluid (one element thick) contained within two concentric cylinders, as observed in rheological test (**Section 3.5**, **Figure 3.8**b). The Eulerian domain was defined by a ring with 7 mm inner radius and 7.375 mm outer one, providing a gap of $d = 0.375$ mm. 'No-slip' conditions at the cylinder walls were imposed by setting the angular velocities at the radial surfaces, one at zero and the other one at an angular velocity ω. In order to contain the fluid within the Eulerian domain, the velocity in the axial direction was set to zero on the lateral surfaces. The ring was meshed with a 0.075 mm global seed, generating 3,000 linear hexahedral Eulerian elements (EC3D8R). The simulation step was set to 0.5 s. See **Figure 5.5**a.

Planar shear model

This model comprised the application of shear to a fluid, in planar conditions alike the ones observed underneath the razor cartridge, considering a one element thick section of an infinitely wide channel. The Eulerian domain was defined by a box of 4 mm length and thickness of 0.375 mm (representing the gap d between two surfaces). The shearing conditions were imposed by setting zero velocity on the bottom boundary, and a V_T velocity on the top one. Like the radial shear model, zero velocity in the width direction was set on the lateral surfaces. In the intake boundary, the displaced fluid was replaced by new fluid (free-inflow Eulerian boundary), and in the outflow boundary a zero pressure free flow was enforced. The box was meshed with a 0.075 mm global seed, generating 265 linear hexahedral Eulerian elements (EC3D8R). The simulation step was also set to 0.5 s. See **Figure 5.5**b.

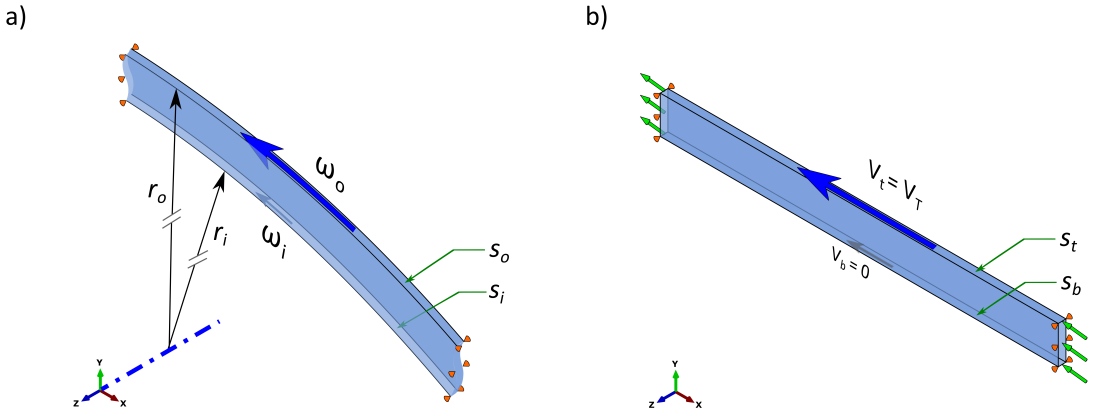

Figure 5.5: The shear models comprise a thin section of fluid subject to shear in radial and planar conditions. a) In the radial shear model, where the fluid is contained in between the inner and outer surfaces (s_i and s_o) of radii r_i and r_o, respectively, shear is imposed by setting the angular velocity ω at either s_i or s_o to zero and the other one to a $\omega \neq 0$. b) In the planar shear model, the shear is imposed by setting the velocity in the bottom surface s_b to $V_b = 0$, and the velocity in the top surface s_t to $V_t = V_T$, where the tangential velocity $V_T \neq 0$. The fluid is contained within the Eulerian domain (light blue) by restricting the velocity normal to the later boundaries to zero (orange).

5.2.3.2 Selection of the shave prep constitutive model

In terms of compressibility, the longitudinal wave propagation velocity (sound speed) and density of the fluid provide enough information for its representation with the use of the Mie-Grüneisen equation of state in the Hugoniot form (**Section 3.6**). The viscous behaviour of the shave prep, however, could be represented by a wide range of Power Law-based constitutive models, given the results of the rheological test (**Section 3.7**), as shown in **Figure 3.14** (page 64). Therefore, the first step in the computational characterisation of the shave prep model consisted in the identification of the appropriate Power Law-based model to represent its shear-thinning behaviour.

Considering the free-surface conditions of shave prep in the wet shaving process, the droplet model was applied for the selection of the viscosity constitutive model according to the simulation performance (runtime and simulation accuracy). The droplet model simulation provides two stages for this analysis: *I*) free falling, in which the fluid is fully unconstrained and viscosity effects are negligible —there are no contact boundaries that affect the fluid flow (Graebel, 2007); and *II*) spreading of the fluid, in which the fluid reaches the bottom boundary, and the viscous forces determine how the droplet spreads. In the first stage, the changes in the simulation runtime should be affected only by the number of calculations, so the simulation performance can be assessed and compared to that of a reference inviscid fluid (i.e. Newtonian fluid with viscosity zero). Using mechanical properties gathered from the literature, experimental data and preliminary results of the rheological test on shave prep foams, seven different fluids, were tested in the droplet model, in the free falling stage. These fluids were represented with equal density and longitudinal wave propagation velocity (sound speed) within the same order of magnitude. Their viscosity was represented with the Newtonian, Herschel-Bulkley (Moir and Craig, 2010), Carreau-Yasuda (Aba, 2014c; Lawler, 2001), and Power Law constitutive models (see **Section 3.6**). } For a description of the mechanical properties representing each fluid model, as listed in **Table 5.1**, and how these properties were obtained, the reader is referred to **Appendix B**, **Table B.1**.

The performance of each fluid was measured as a ratio of runtime with respect to the reference fluid. The non-Newtonian fluid simulations showed a considerable increase in runtime, showing performance three orders of magnitude slower for the Herschel-Bulkley model, two orders of magnitude for the Carreau-Yasuda model. In contrast, performance of only one order of magnitude slower was observed for the Power Law model (see **Table 5.1**). As a result, the Power Law constitutive model (**Equation 3.13**) was selected to represent the viscous behaviour of the shave prep fluids in the subsequent simulations.

Table 5.1: Performance of the different constitutive models for shave prep fluids, compared to an inviscid fluid for reference. The performance value is calculated by dividing the estimated completion time of the inviscid fluid over the estimated completion time of the analysed fluid.

Formulation	Fluid	Performance
Inviscid	SP00	1.000
Herschel-Bulkley	SP01	0.001
Carreau-Yasuda	SP02	0.016
Power-Law	SP03	0.505
	SP04	0.512
	SP05	0.505
	SP06	0.439

5.2.3.3 Verification of the shave prep model

An important step in the development of the shave prep model involved a 'sanity-check' in which it was verified that the viscous behaviour of the fluids was consistent with the specified viscous properties. The verification of the shave prep behaviour was performed in two steps:

1. Visual inspection of the fluid spreading behaviour: using the droplet model, the shave prep spreading behaviour was compared against a variety of well-known fluid properties.
2. Analytical analysis of the viscous response: using the shear models, the specified viscosity of these fluids was verified against the analytical value obtained from the shear stress and shear strain rate.

For the **spreading behaviour verification**, water and corn syrup (Newtonian fluids) were compared to the non-Newtonian shave prep fluids in the form of interstitial fluid (PEG 4MM 1% solution in water) and shaving foam A (see **Appendix B**, **Table B.2** for description and values of mechanical properties of the fluids). By running the analysis jobs with 32 parallel processors, the runtimes obtained varied between 24 and 25 hours. In the simulations, it was observed that the original shape of the fluid droplet was maintained during the free-fall stage. However, once the bottom boundary was reached, the fluid was allowed to flow and fill the base of the Eulerian domain, restrained only by the viscous forces within the fluid driving changes in droplet shape. The water droplet showed the least resistance to flow while the corn syrup, PEG 4MM 1% solution and shave prep showed higher resistance to flow. Of these viscous fluids, the PEG solution droplet showed larger differences in the shape, which can be observed by changes in void ratio at the droplets free surface (**Figure 5.6**).

The **verification of the viscous response** was performed with the shear models, ensuring a constant shear strain rate was maintained throughout the simulations. The tangential and radial velocities imposed were consistent with a laminar regime (where the fluid flows parallel to the imposed velocity and no vorticity is observed). This was enforced by ensuring that the Reynolds number Re did not exceed a critical value, according to the geometry of the model. Re is defined as:

$$Re = \frac{V_T \cdot D_H \cdot \rho}{\eta} \tag{5.11}$$

where η and ρ are the fluid dynamic viscosity and density, D_H is the hydraulic diameter. The latter, used for flows in non circular channels or ducts, is equivalent to four times the transversal area over the wetted perimeter (Rennels and Hudson, 2012). Being d the gap distance between the shearing parts, it is noted that for concentric cylinders $D_H = d$ (Marrington et al., 2005), while for planar shearing in infinitely wide

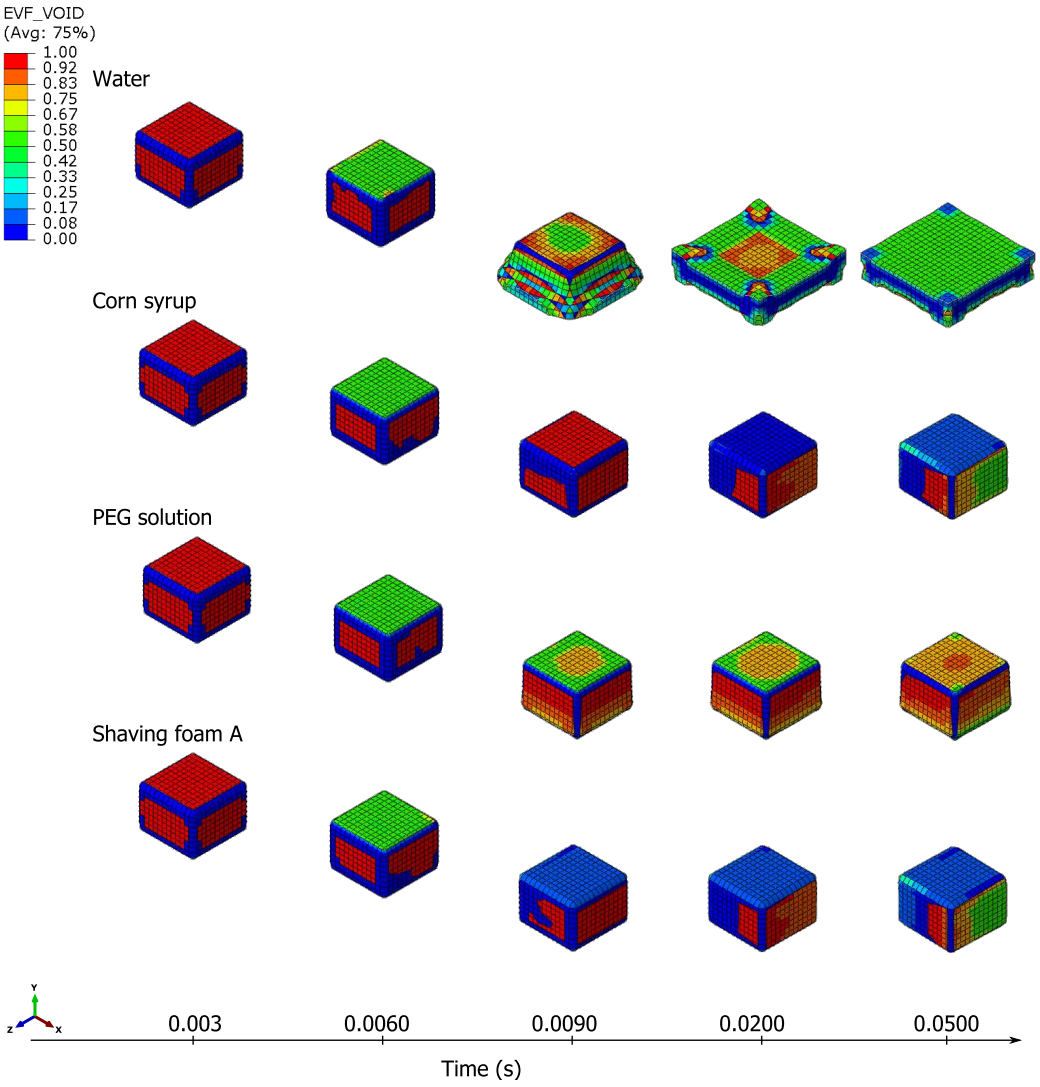

Figure 5.6: Droplet model spreading behaviour. Water (top), corn syrup, PEG solution and shaving foam (bottom) droplets were compared, showing the effects of the viscosity in their spreading behaviour. At 0.02 s, water was fully spread at the base, while the viscous forces in the other fluids prevented them to flow at this short simulation time, showing the PEG solution a higher tendency to flow. The EVF VOID legend indicates the void ratio in the Eulerian elements (i.e. full materials show a void ratio of zero).

channels $D_H = 2d$. According to Andereck et al. (1986), the laminar flow is maintained in the concentric cylinders geometry when the difference in Reynolds number at each surface is lower than 107. In most cases of hydrodynamic lubrication, $Re < 1,000$ (Persson, 2000). With no changes in the pressure within the flow, the fluid is subject to pure shear flow (also known as Couette flow), so the velocity profile in the shear models is given by a linear function of d, where the velocity is zero at the static surface interface, and maximum velocity is observed at the moving surface interface (equal to that of the moving surface, as 'no-slip' is assumed) (Panton, 2013).

Under these conditions, it was analytically known that the simulation output would consist in a laminar Couette flow with a linear variation of fluid velocity through the

fluid thickness. By knowing the shear conditions and measuring the output shear stress within fluid, the 'output' viscosity can be calculated and compared to the input one. Then, these two parameters (velocity profile and viscosity) can be used to verify that the simulation accurately captures the fluid viscous behaviour. The relative error between the analytical/input values to the ones captured in the simulation were used as a metric to assess the accuracy of the results.

Like for the spreading verification test, the simulations were performed for water, corn syrup, PEG 4MM 1% solution and shaving foam A to verify accurate viscous response for various fluids. The simulations were able to capture the laminar flow and the linear velocity profile, as show in **Figure 5.7** for an applied tangential velocity of $V_T = 2.67$ mm/s. The shear strain rate was calculated for various velocities according to the formula provided for concentric cylinders (see **Figure 3.8**b), and with **Equation 3.12** for the planar shear. The analytical value of viscosity was calculated from the obtained shear stresses (simulation output), obtaining relative errors lower than 2% with respect to the viscosity of the fluids at the given shear rate (**Table 5.2**). These results demonstrated the excellent accuracy of the model and therefore the verfication process was succesfully completed.

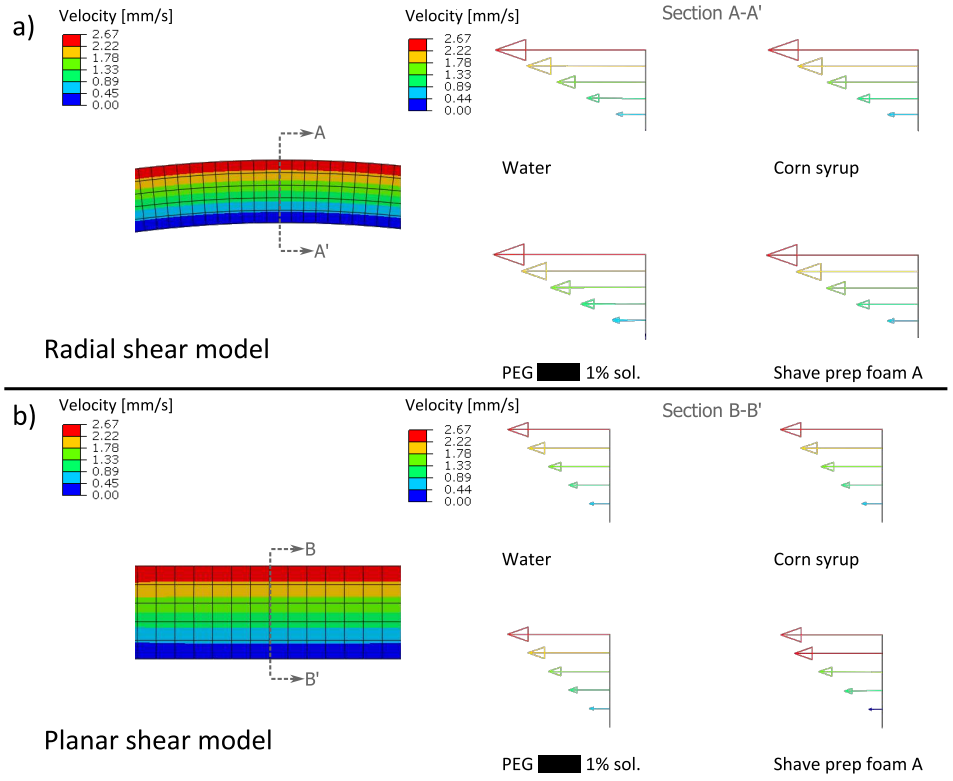

Figure 5.7: Shear models velocity profiles (in mm/s). In all the studied fluids, the laminar Couette flow was captured.

Table 5.2: Verification of the fluids viscous behaviour. The Reynolds number (Re) of each fluid is within the laminar regime for the given models, and the error between the input viscosity and analytical one is lower than 2%.

	Fluid	Re	$\dot{\gamma}$ **[s^{-1}]**	τ **[MPa]**	**Viscosity relative error [%]**
Radial	Water	0.9747	6.931	6.88×10^{-9}	0.724
	Corn syrup	0.0002	6.931	4.74×10^{-5}	0.13
	PEG 4MM	0.0012	6.931	5.74×10^{-6}	0.171
	Shave prep A	2.5×10^{-5}	6.931	2.37×10^{-5}	0.151
	Corn syrup	0.0029	102.679	7.02×10^{-4}	0.12
	PEG 4MM	0.0902	102.679	1.64×10^{-5}	0.168
	Shave prep A	0.0009	102.679	1.49×10^{-4}	0.258
	Corn syrup	0.0556	1949.153	1.32×10^{-2}	1.047
Linear	Water	2.0003	7.112	7.1×10^{-9}	0.127
	Corn syrup	0.0004	7.112	4.87×10^{-5}	0
	PEG 4MM	0.0025	7.112	5.8×10^{-6}	0.003
	Shave prep A	0.0001	7.112	2.43×10^{-5}	0.017
	Water	562.5	2000	1.86×10^{-6}	0.65
	Corn syrup	0.1141	2000	1.37×10^{-2}	0.015
	PEG 4MM	21.4975	2000	5.31×10^{-5}	1.392
	Shave prep A	0.3439	2000	2.85×10^{-4}	0.042

5.2.4 Sensitivity analysis of the shave prep model

As part of the runtime optimisation process for the **multi-physics modelling framework**, the droplet model was used for the analysis and identification of the parameters characterising the fluid model that have the largest effects on the simulation runtimes. The fluid model performance sensitivity was evaluated against *a*) the constitutive parameters describing the fluid behaviour, and *b*) the mesh size and parallelisation level, as explained next.

5.2.4.1 Performance sensitivity to the mechanical properties describing the fluid behaviour

The mechanical properties representing the fluid behaviour in the finite element environment are density, longitudinal wave propagation velocity (sound speed) and viscosity. In order to understand the effect of each parameter in the simulation runtimes, uniformly distributed variation of these parameters was considered in order to build 25 models with sets of properties within the ranges of the material properties of the test fluids (i.e. water, corn syrup, PEG 4MM 1% solution and shaving foam A). A pseudo random space filling sampling plan was built with values between 0 and 1, using the Sobol sequence from the Intel® Math Kernel Library (MKL) generator through Mathematica (Wolfram Research, Inc., Champaign, IL 61820-7237, USA). The Sobol sequence is a low-discrepancy sequence that provides a uniform distribution of values for

random sampling generation (Sobol', 1967). A 'seed' value of 1 was specified in order to maintain the same sequence of pseudo-random values in consequent analyses. A 3D map of the space filling sampling plan, shown in **Figure 5.8**, represents the design of experiment (DoE) of the non-dimensional mechanical properties. The values of 0 and

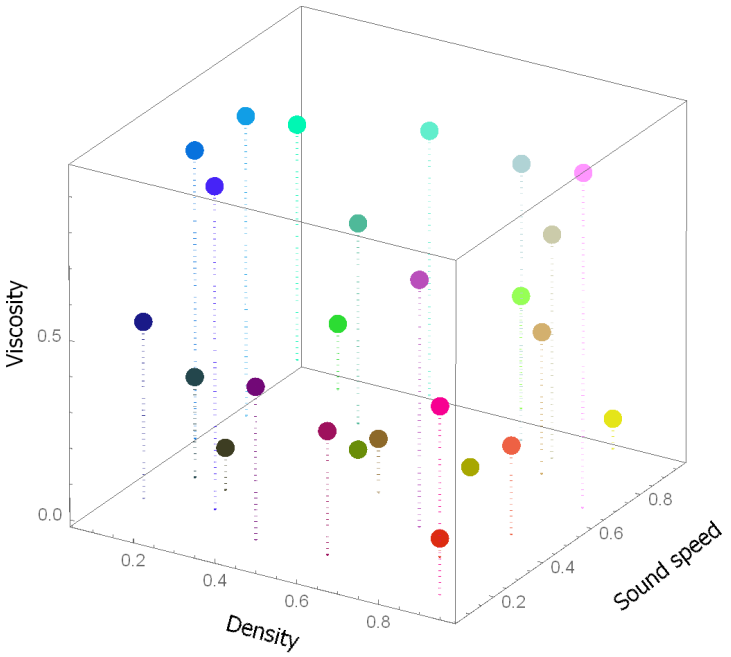

Figure 5.8: Non-dimensional design of experiment for the sensitivity analysis. The 3D map of the space filling sampling plan shows 25 sets of simulations (dots) located at the coordinates corresponding to the non-dimensional values for density, sound speed and viscosity. The sampling plan was generated as a pseudo-random Sobol sequence, using the Intel® MKL (Math Kernel Library) generator within the Mathematica (Wolfram Research, Inc., Champaign, IL 61820-7237, USA) environment, setting the random 'seed' as 1.

1 are representative of the lower and upper limits, P_{min} and P_{max} respectively, of the range considered for each of the mechanical properties. The non-dimensional values $0 \leq P_{sf} \leq 1$ where converted to their corresponding dimensional value P_v by:

$$P_v = (P_{max} - P_{min})\, P_{sf} + P_{min} \tag{5.12}$$

The ranges of parameters considered in the sensitivity analysis (SA) are shown in **Table 5.3**.

Table 5.3: Parameters range for the parameters-runtimes sensitivity analysis (SA) and the extended sensitivity analysis (xSA).

Analysis	Limits	Density [Ton/mm^3]	Sound speed [mm/s]	Viscosity [MPa·s]
SA	min	$8.665{\cdot}10^{-11}$	$4.5{\cdot}10^{4}$	$8.615{\cdot}10^{-10}$
	max	$1.389{\cdot}10^{-9}$	$1.905{\cdot}10^{6}$	$6.849{\cdot}10^{-6}$
xSA	min	$8.665{\cdot}10^{-13}$	$4.5{\cdot}10^{2}$	$8.615{\cdot}10^{-12}$
	max	$1.389{\cdot}10^{-7}$	$1.905{\cdot}10^{8}$	$6.849{\cdot}10^{-4}$

All models were run at equal parallelisation levels. By tracking the simulation progress with respect to the runtimes, a linear relation was found between these two parameters. This finding allowed to run each model for only one hour, using the linear relation to calculate the estimated completion time. In Abaqus, the stable increment is directly proportional to the element size, and indirectly proportional to the longitudinal wave propagation velocity (sound speed) (Aba, 2014c). However, with the sensitivity analysis SA, no correlation was found between the simulation completion times and any of the parameters within these ranges. As a result, the parametric domain of sensitivity analysis was extended by two orders of magnitude at each limit (xSA in **Table 5.3**).

In the extended sensitivity analysis (xSA), the results showed high correlation between the longitudinal wave propagation velocity (sound speed) and the required completion times ($R^2 = 0.9982$), showing , as expected, that a lower sound speed value accelerates the simulation, increasing the simulation performance (see **Figure 5.9**). However, this correlation was found outside the range of parameters required for the shave prep model. Therefore, further analysis for the optimisation of the runtimes was performed by the assessment of the sensitivity of the model performance to the mesh characteristics (size and density of elements) and the parallelisation of the jobs, as shown next.

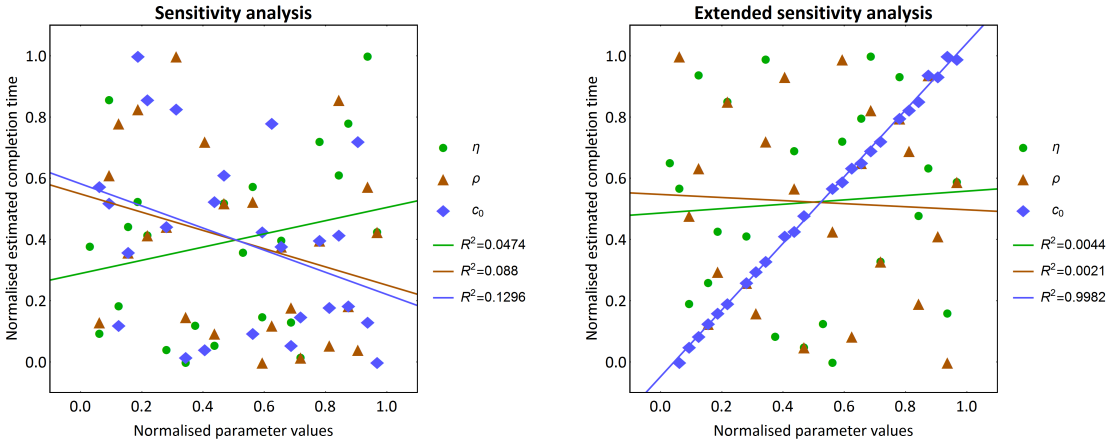

Figure 5.9: Fluid parameters-runtimes sensitivity analysis. In the sensitivity analysis (left) performed within the range of viscosity η, density ρ and longitudinal wave propagation velocity (sound speed) c_0 of water, corn syrup, interstitial fluid and shaving foam, no correlation with the simulation completion times was found. The parameter ranges were extended by two orders of magnitude at both limits in the extended sensitivity analysis (right), showing a clear correlation between the longitudinal wave propagation velocity and the estimated completion times.

5.2.4.2 Performance sensitivity to the mesh characteristics and parallelisation level

The size of the elements in the Eulerian mesh proved to have as great influence in both, capturing the appropriate fluid behaviour in the simulations, and the runtime

performance. Although smaller elements are recommended to capture the fluid behaviour in detail (Aba, 2014c), reducing the element size results in larger runtimes required for the computations: the time increment in the analysis also depends directly on the element size, and the number of elements (and so the equations to solve) increases exponentially (Aba, 2014a). In preliminary results, it was shown that the water droplet simulation with 216 elements (low resolution) run with a single processor took 1.2 hours, compared to 24.8 hours for a 11,913 elements (high resolution) job run in parallel with 32 processors. For this reason, a mesh-parallelisation sensitivity analysis was performed, considering for 1 mm^3 of shave prep fluid (shaving foam B, **Table B.2**): *a*) variation in volume of the Eulerian domain, *b*) variation in element size for the Eulerian mesh, and *c*) simulations run with 20, 40, 60 and 80 parallel processor (in 20-processor nodes).

Using the same pseudo-random Sobol sequence as in the previous analysis, 25 sample jobs were generated in a 2D space, setting the ranges of Eulerian domain volume to 100-500 mm^3 and element size to 0.1-1.0 mm. Each job was run at the four different parallelisation levels for a total of 100 analyses. Each model was run for five hours, and the estimated completion time was calculated as a linear extrapolation of the total progress observed at the end of the simulation, like in the previous analyses. Analysing the effects of this assumption throughout completed simulations, the relative error varied between 6% and 14% up to a simulation progress of 30%, and lower than 6% afterwards. Nevertheless, considering that the estimated completion time of some simulations was larger than 600 hours, a linear relation between runtime and simulation progress was considered to be reasonable assumption. The estimated completion time was used as the parameter to determine the performance of the simulations. The analysis showed that the neither the total volume of the Eulerian domain nor the ratio of fluid contained within have any correlation with the runtimes. Although faster runtimes where observed for larger element sizes, direct correlation between these two parameters was not found in this study. This implied that other factors, such as the number of elements in the mesh or the level of parallelisation, have a stronger influence in the simulation performance (i.e. processor communication time). See **Figure 5.10**.

A parameter of interest for this study was the number of Eulerian elements per processor used in the simulations, for which a non-linear correlation was found with the simulation performance. The effects of communication time between processors were observed in the results, being the analyses run with 80 processors the ones with longer runtimes at a given elements per processor value, as shown in **Figure 5.11**. Fitting the data of each parallelisation level to a quadratic function, the number of elements per processor at which performance start to decrease with more elements per processor can be estimated, as shown also in **Figure 5.11**; however, the low performance at lower elements per processor was not captured. In order to capture the optimal value

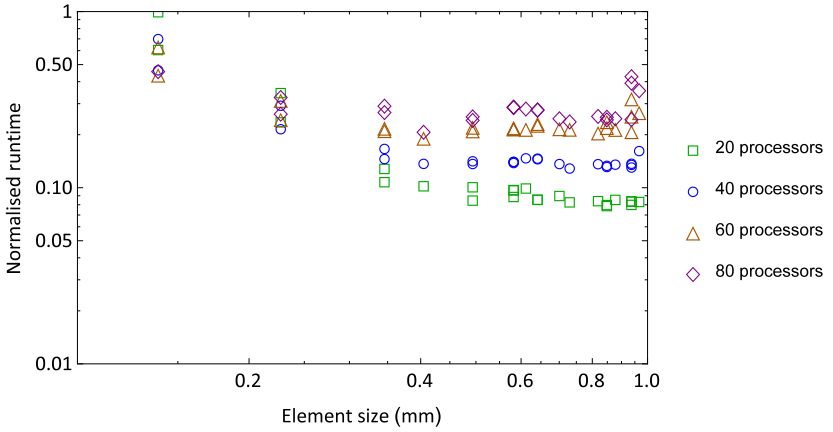

Figure 5.10: Mesh-parallelisation sensitivity analysis to mesh size. Although no specific trend is found in the data, the parallelisation indicates an influence in the simulation performance.

of elements per processor, a non-linear function, applicable for the range of elements per processor used in this study, was proposed to estimate the number of elements per processor that would provide maximum performance (i.e. lower runtimes), as show in **Figure 5.12**. Such function provides a correlation of R^2=0.75.

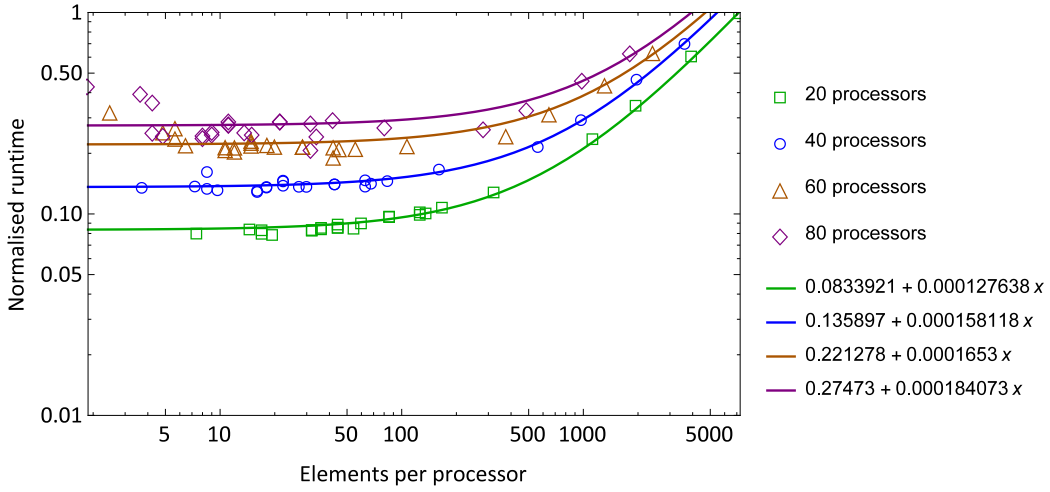

Figure 5.11: Mesh-parallelisation sensitivity analysis to elements per processor used. A quadratic fitting of the data is provided at the for parallelisation levels studied, showing the limit of Eulerian elements present in the mesh per processor used at which the performance of the simulations is reduced.

These results show only the effects in runtime accounting only for the fluid deformation. However, it was observed that specific boundary and interaction conditions in a FSI analysis could modify the expected results, for which a specific mesh-parallelisation sensitivity analysis is recommended at different applications. As for appropriate contact interaction the resolution of the fluid mesh is of high relevance (as explained later in **Section 5.3.3**), a short parallelisation analysis was run at each model stage to investigate the number of processors that would provide the best performance. In such short parallelisation analysis, this study provided a guideline for an approximation of

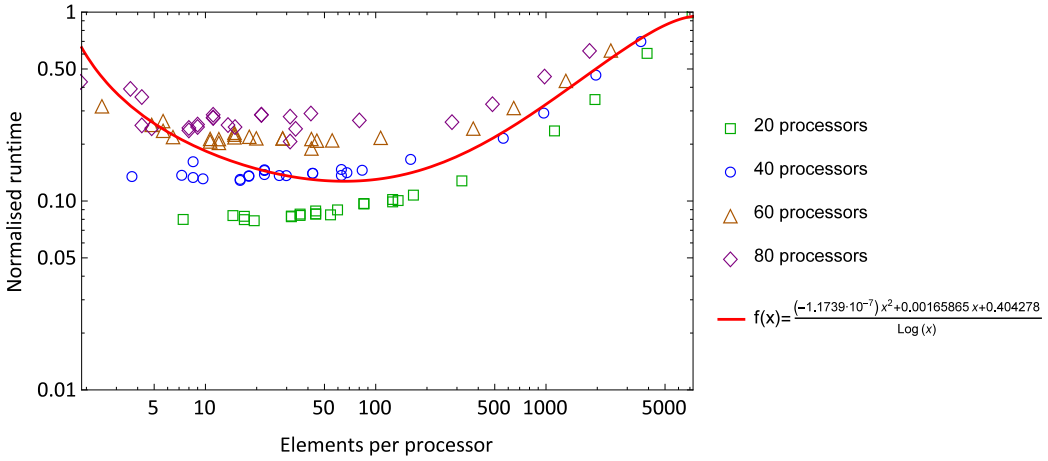

Figure 5.12: Fitting of the mesh-parallelisation sensitivity analysis data to a non-linear function to estimate the limit of Eulerian elements present in the mesh per processor at which maximum performance (lower runtimes). Fitting correlation R^2=0.75, mean square error of 0.6%.

the optimal parallelisation level. The results shown in this analysis are applicable for the characteristics of the high performance computing facilities provided by P&G.

5.3 Modelling framework development, stage II: Two-component interactions

The interactions between the skin, razor and shave prep can be separated into two-component interactions for an isolated study of the concurrent phenomena observed during a shaving stroke. The two-component interactions models include two of the individual component models described in **Section 5.2**, assessing the role of the contact interaction parameters in the mechanical response of each component:

Cartridge-Skin

At the cartridge-skin interface, the coefficient of friction between the contact surfaces interplays with skin deformation. This interaction was studied in the **dermis-rigid solid (DRS)** and **skin-guard (SG)** models, simulating the shaving stroke motion of a solid indenter on the skin surface.

Skin-Shave prep

The interaction between the skin and the shave prep is dominated by the adhesive forces at the fluid-solid interface. The evaluation of the coefficient of friction required to account for these forces was performed with the use of the **droplet sliding (DS)** model, simulating the experimental conditions of a droplet on a tilted surface (see **Figure 3.6**, **Section 3.3.1**).

Cartridge-Shave prep

The forces applied through the cartridge cause the shave prep to shear and flow. The flow is enhanced by a dynamically reduced viscosity of the prep due to its shear-thinning properties. These shearing conditions were studied at low shear rates within the laminar regime with **Taylor-Couette flow (TCF)** and **laminar flow (LF)** models, simulating fluid trapped between two surfaces in radial and planar configurations. These models aim to replicate the rheological test (**Section 3.5**) and the conditions underneath the cartridge guards (**Section 4.1.2**).

In the following sections, these models and their application in the analysis of these two-component interactions are explained.

5.3.1 Cartridge-Skin interaction models

The cartridge-skin interaction models simulate the contact between a soft substrate (skin) and a much stiffer body (cartridge) which dynamically indents and slides over the substrate (i.e. normal force and tangential velocity). While the skin was modelled as described in **Section 5.2.1**, the cartridge parts were modelled as rigid bodies, focusing the simulation on skin deformation. In earlier developments, a simple model was built accounting for a single layer of skin and a simplistic indenter representing the cartridge. This model worked as a basis for a more complex model considering a multi-layer skin tissue in contact with a geometry taken from the cartridge design. These two models are described next.

5.3.1.1 Dermis-rigid solid model (DRS)

The DRS model provides a simplified representation of a shaving stroke, in 'dry' conditions (i.e. no shave prep involved). The skin was represented as a deformable body with a $30 \times 5 \times 10$ mm^3 cuboid geometry, and the material properties of the **dermis**.The indenter was defined by a shell rigid body with a semi-cylindrical contact surface of 10 mm diameter, fitted in a $10 \times 10 \times 10$ mm^3 volume. The skin and solid were meshed with a 0.5 mm and 1 mm global seed size, respectively, generating 12,000 linear hexahedral elements (C3D8R) for the skin, and 585 mixed quadrilateral and triangular linear elements (R3D4 and R3D3) for the solid indenter.

The shaving stroke conditions were simulated as a 5 Pa pressure gradually applied to the indenter, and a gradual velocity of 100 mm/s restricted to the stroke direction, both reaching their maximum amplitude value at 0.2 s (for a total step time of 0.3 s). The interaction was defined as a frictionless contact. The skin was pinned at the base and symmetrical boundaries were set at the sides. The shaving stroke simulation with the solid indenter is shown in **Figure 5.13**.

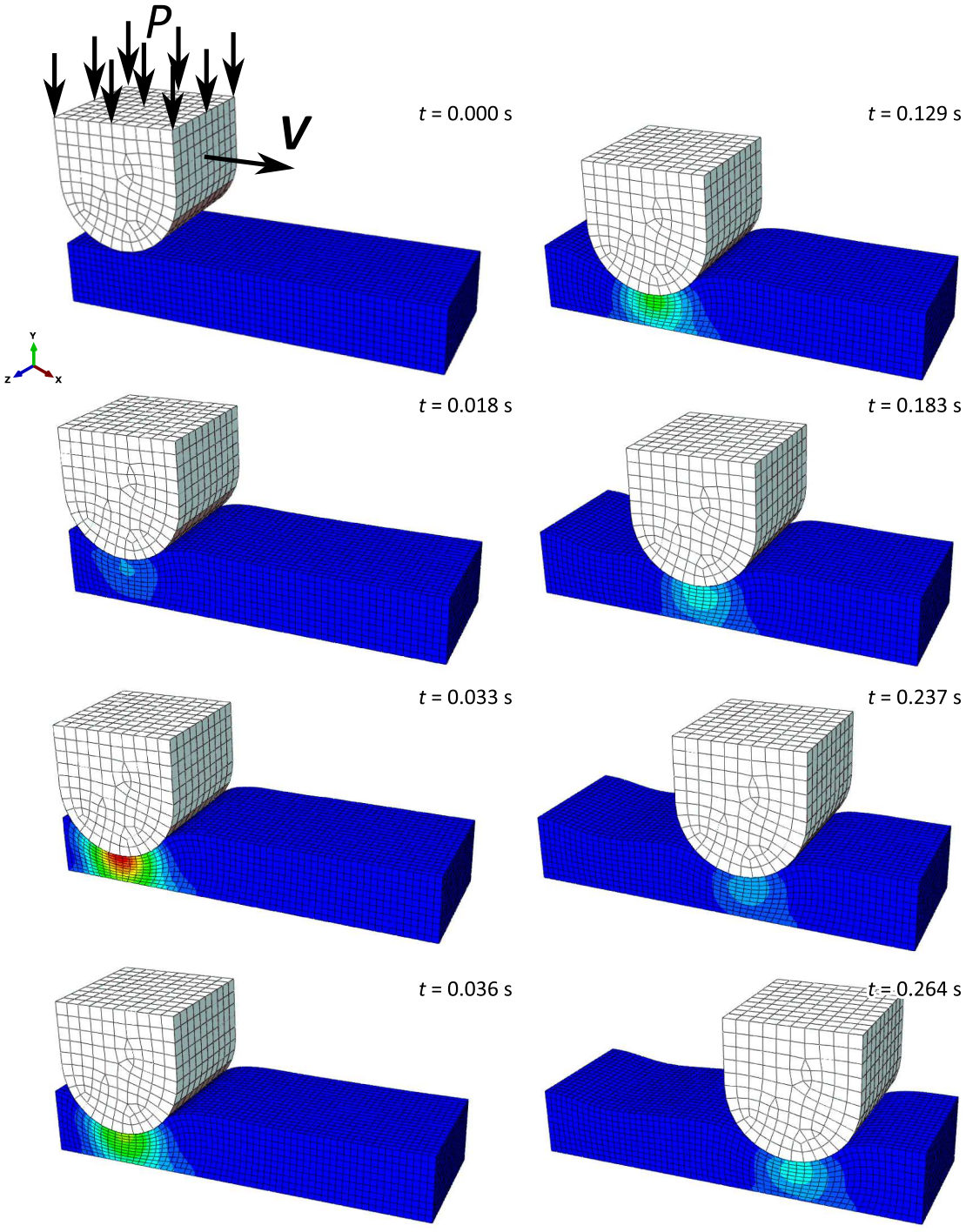

Figure 5.13: The dermis-rigid solid model comprises the simulation of the shaving stroke motion, defined by a pressure P and a velocity of of magnitude V, applied by a rigid solid indenter to a soft, hyperelastic, viscoelastic skin.

5.3.1.2 Skin-Guard model (SG)

In the SG model, the simple indenter was replaced by a section of the comb guard (part of the razor representing the whole cartridge), and the skin by a bi-layer tissue comprising the dermis and epidermis, for a more realistic simulation of skin deformation. The skin was defined by a $10\times2\times0.5$ mm^3 cuboid body, where the epidermis was 50 μm thick. This tissue was constrained by symmetric boundaries in all of its faces with the exception of the epidermal contact area. The comb guard geometry design (provided by P&G) provides a teeth-like structure that allows the skin to bulge in between its teeth when a normal force is applied. For the skin, the mesh seed size was set to vary from 0.5 to 0.1 mm, specifying a minimum of two elements thickness in the epidermal layer, providing 4,795 linear hexahedral elements (C3D8R). The guard's global seed size was 0.2 mm, refining the elements to 0.05 mm at the contact surface, for 978 quadratic tetrahedral rigid elements (C3D10M). To simulate the shaving stroke, a 30 mN load was gradually applied at the indenter, and a gradual velocity of 20 mm/s, both reaching their maximum value at 0.2 s, for a simulation step time of 0.5 s. The interaction was enforced using an augmented Lagrangian method, and defined with a coefficient of friction. By running the simulation job with 48 parallel processors, the simulation took 2.5 hours runtime. The shaving stroke simulation with the comb guard is shown in **Figure 5.14**.

This model was used to study the effects of the contact friction between the skin and the cartridge on skin deformation. It was observed that higher coefficient of friction increases the height of the skin bulge in front of the guard, affecting as well the distribution of strains in the dermis, as shown in **Figure 5.15**. These effects are relevant to capture the correct skin deformation during a shaving stroke, demonstrating the importance of setting the correct coefficient of friction between the skin and the contact elements at the cartridge.

In the simulations, the coefficient of friction specified in the contact interaction definition refers to the local coefficient of friction at the skin-cartridge interface. In experimental tests, a global coefficient of friction is measured as a result of the reaction forces derived from the small-scale contact interaction. The human skin shows a load-dependent coefficient of friction, which can be related to the deformation of the skin (Derler and Gerhardt, 2012; Koudine et al., 2000; Pailler-Mattei et al., 2007, 2011; Veijgen, 2013). Such effects and the influence of the skin topography and microstructure are studied in more detail in **Chapter 7**.

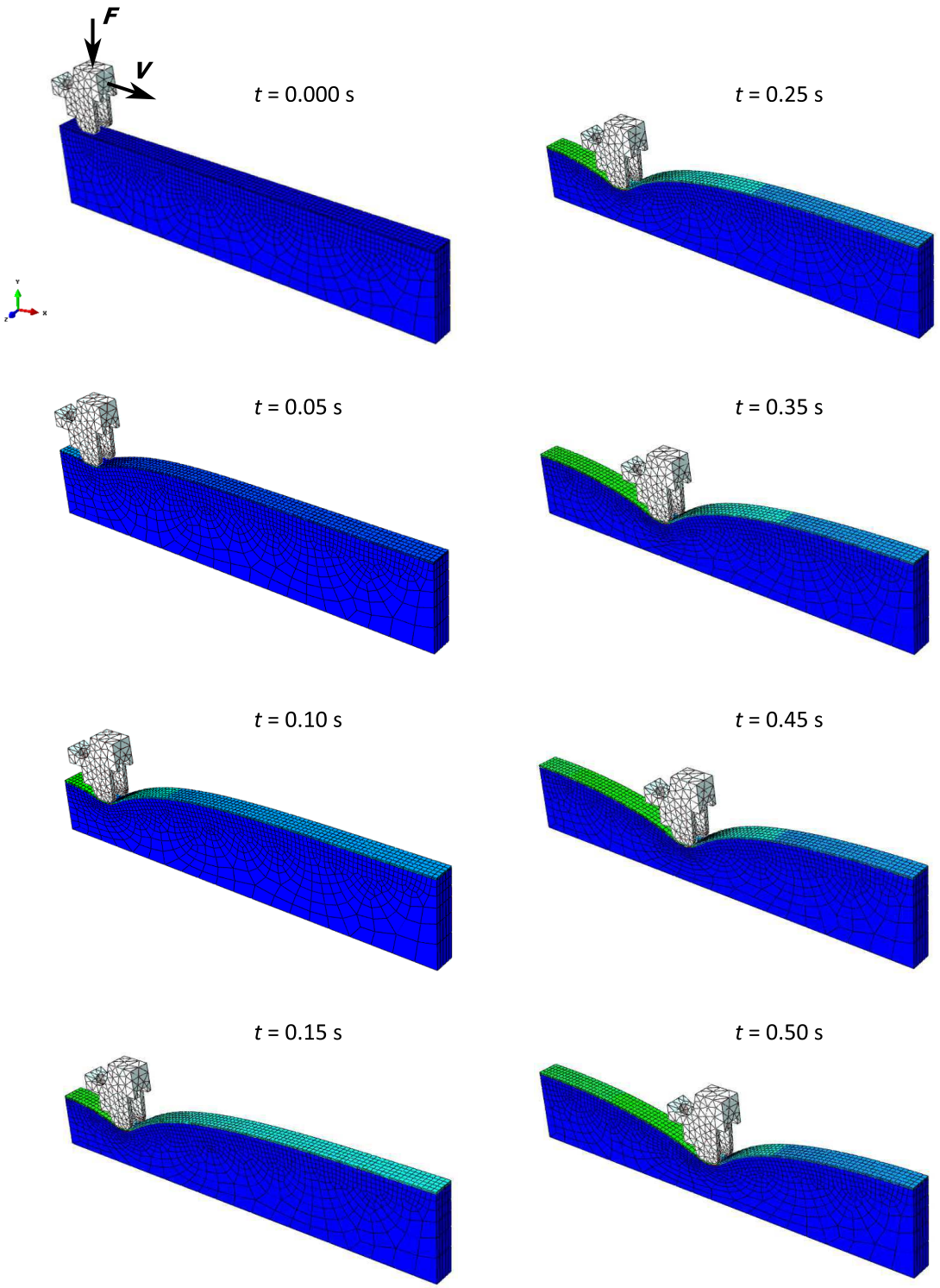

Figure 5.14: The skin-guard model comprises the simulation of the shaving stroke motion, defined by a normal force of magnitude F and a velocity of magnitude V, applied by a rigid solid indenter (the cartridge's comb guard), to a soft, hyperviscoelastic, bi-layer skin.

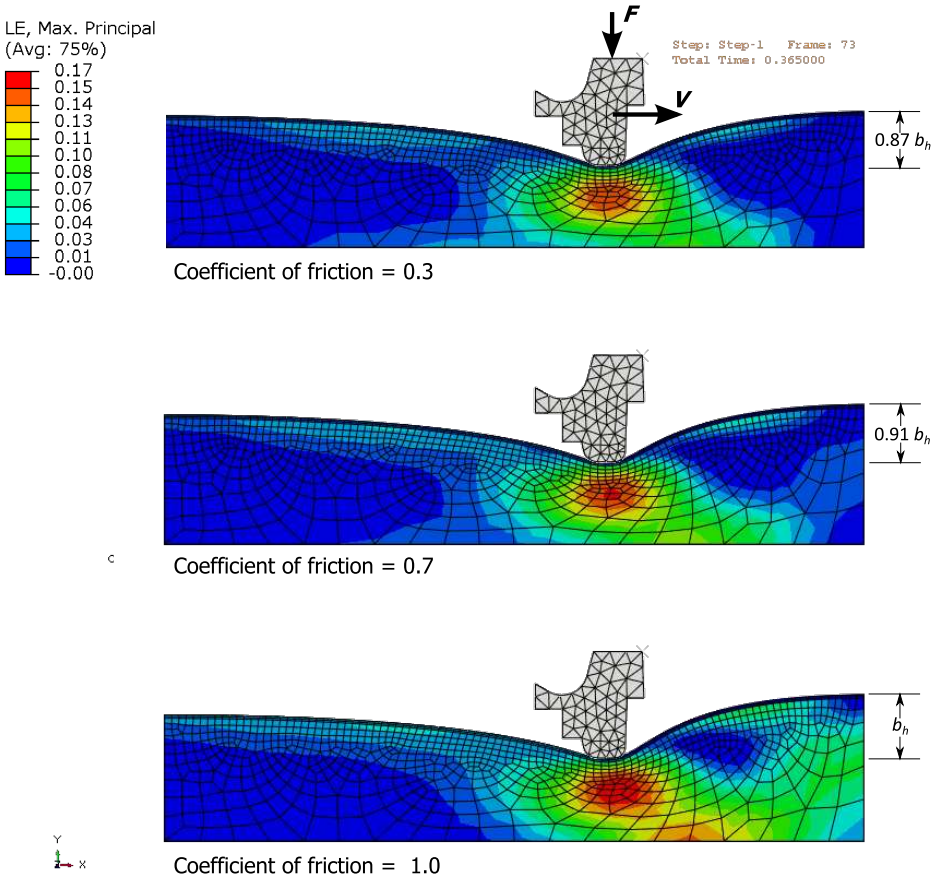

Figure 5.15: Effects of the coefficient of friction on skin-solid interactions. By setting equal parameters to simulate a shaving stroke motion (indenting force of magnitude F and velocity of magnitude V), different friction coefficients define the interactions between an indenter and the skin. At 0.3 coefficient of friction (top), the maximum principal logarithmic strains (LE) are concentrated under the indenter, but as the coefficient of friction increases to 0.7 (middle) and 1.0 (bottom), the strains are distributed ahead the indenter, promoting higher bulging of the skin, as compared with the bulging height b_h for the coefficient of friction of 1.0.

5.3.2 Skin-Shave prep interaction models

The skin-shave prep interaction accounts for the pre/post shearing conditions (i.e. when the fluid is at rest prior to and after the shaving stroke). It is easy to observe that when the shave prep is applied on the skin, it stays on the surface as the combination of adhesion forces at the skin surface and cohesive forces within the shave prep are stronger than gravity forces. A common approach for FSI is to assume 'no-slip' conditions, that would be represented in Abaqus/CEL environment as an infinite coefficient of friction between the shave prep and skin. However, this condition caused unexpected deformation of the skin surface. For this reason, the fluid-solid interaction required the specification of a coefficient of friction. To account for the surface adhesion, it was considered that for an experimental measurement of contact angle lower than 90°, the 'no-separation' condition was specified; otherwise, 'allow separation' was specified. By implementation of the shave prep droplet model (**Section 5.2.3.1**) in contact with a solid tilted surface, the parameters for the characterisation of fluid adhesion

were analysed in the droplet sliding model. This model was also applied to explore other interactions where rather than full adhesion, slipping of the fluid is observed (as observed in some of the cartridge parts), as explained next.

5.3.2.1 Droplet sliding model (DS)

The DS model comprises the simulation of a fluid droplet resting on a tilted surface as described in **Section 3.7.2**, exploring the interaction parameters that could capture droplet adhesion as it is counterbalanced by gravity forces. A $4 \times 2 \times 4$ mm^3 cuboidal fluid droplet was defined within a $30 \times 5 \times 10$ mm^3 Eulerian domain resting on the 30×10 mm^2 surface of the 5 mm thick skin, defined as a semi-rigid body with iron like properties (so the analysis was focused in the droplet deformation only). The skin was tilted by $60°$, allowing gravity forces to 'pull' the droplet down through the Eulerian domain. See **Figure 5.16**. These tilting conditions have been used by Rouyer et al. (2005) to test the yield stress in Gillette® shaving foam. In this simulation, the adhesion forces between the fluid and surface were captured by the deactivation of the 'allow separation' settings (referred as 'no-separation' conditions) and the specification of contact by a penalty friction coefficient.

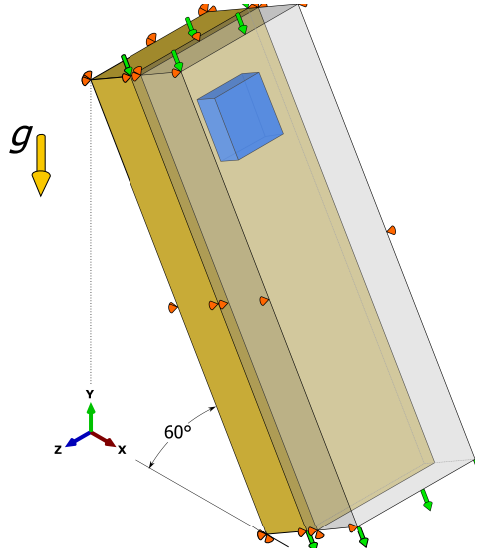

Figure 5.16: Droplet sliding model. The **droplet sliding model** comprises a fluid droplet (blue), contained withinthe Eulerian domain volume (grey), sliding over a 60° tilted surface (beige) by the action of gravity forces ***g***. Despite of the contact surface, the skin surfaces are fixed by a symmetric boundary condition (orange) a long with the lateral surfaces of the Eulerian domain. The fluid is allowed to flow freely through the top and bottom surfaces (green arrows).

The skin mesh was relatively coarse (global seed size 2.5 mm, resulting in 60 linear hexahedral C3D8R elements). The fluid was meshed with a global seed size of 0.5 mm, generating 12,000 linear hexahedral Eulerian elements (EC3D8R). The fluid was restrained from leaving the Eulerian domain by setting symmetry boundaries at the lateral surfaces of the Eulerian domain, parallel to the fluid flow, but was allowed to

freely leave the Eulerian domain at the outflow surface. The physical simulation step was 1.0 s.

Water, corn syrup, PEG 4MM 1% solution and shaving foam A (see **Table B.2**, **Appendix B**) were tested with coefficients of friction of 0.0, 0.25, 0.50, 0.75 and 1.0. By running the simulation jobs with 16 parallel processors, the simulations took 1-9 h runtime. With these four fluid samples, it was found that both, the longitudinal wave propagation velocity (sound speed) and density, had direct correlation with the runtimes, with $R^2 \sim 0.94$, while the specified coefficient of friction did not show correlation, resulting in a $R^2 = 2.3 \times 10^{-8}$, as shown in **Figure 5.17**. Although the correlation found for the density and wave propagation velocity does not reflect the sensitivity of the parameters in a wider parametric space (see **Figure 5.9**), this analysis served to evaluate only the effects of the coefficient of friction on the simulation performance.

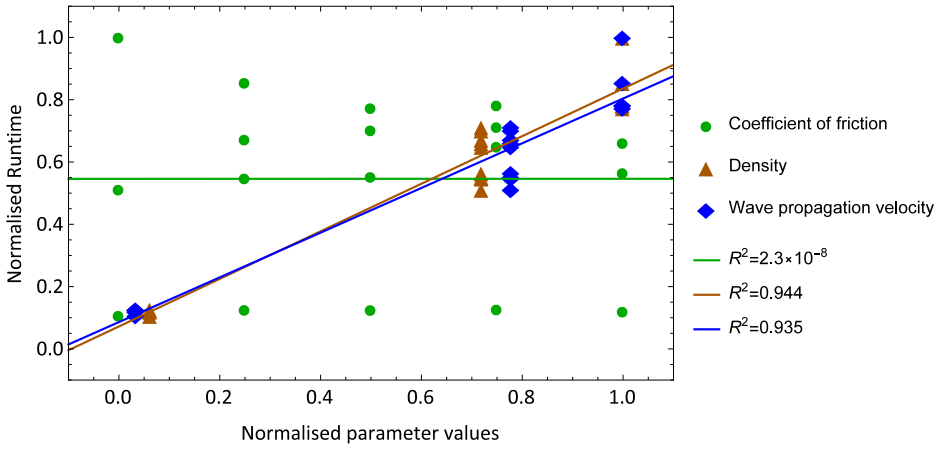

Figure 5.17: DS model parameters correlation to runtimes. For the droplet sliding simulation analysis, both density and wave propagation velocity showed direct correlation with the simulation runtimes. In contrast, no correlation was observed in terms of variation of coefficient of friction.

With the application of 'no-separation' conditions in the simulation, the fluid droplet attaches to the surface, allowing the interaction behaviour to be driven by the combination of the viscous and frictional forces. The droplet sliding velocity was highly sensitive to the coefficient of friction, which can be related to the work of adhesion between the fluid and the solid part. In a lower scale, the viscosity of the fluid also affects sliding velocity as the flow within the fluid droplet (spreading behaviour) sums up to the sliding velocity of the whole droplet with respect to the plate. This can be observed in **Figure 5.18** for corn syrup and shaving foam A.

As discussed in **Section 3.7.2.1**, describing the experimental characterisation of the shave prep contact interactions, no sliding of the shave prep fluids was observed for the surface samples available. Therefore, a trial iterative process was implemented aiming at a sliding velocity of zero. In order to ensure that full adhesion was captured, no sliding should be captured after a reasonable time in the simulation: small sliding distances could be mistaken as 'no-sliding' in short simulations, but it would be easier

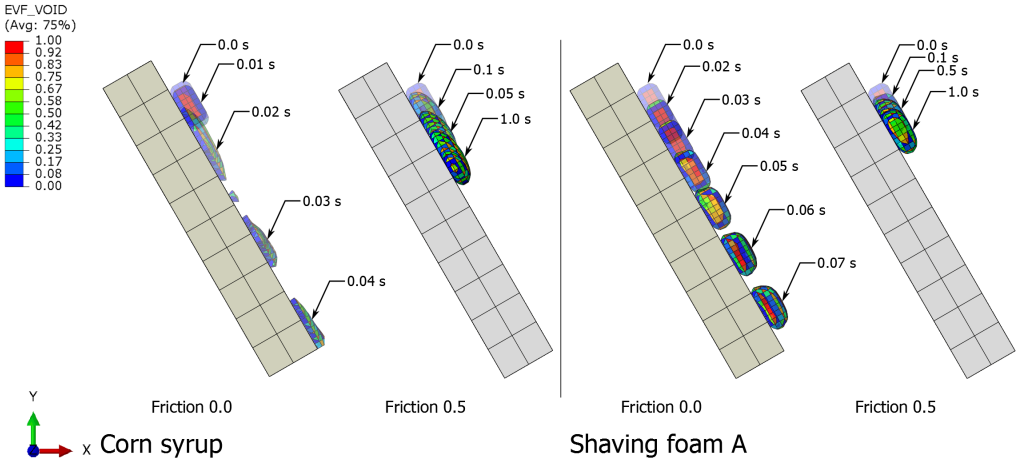

Figure 5.18: Droplet sliding model: test models simulations. The simulation of corn syrup (left) and shaving foam (right) fluid on a 60° tilted surface are shown with a friction coefficient of 0.0 and 0.5, with the implementation of the 'no-separation' settings. The 'no-separation' condition allows the sliding fluid to spread on the surface while the coefficient of friction, along with the fluid viscosity, controls the sliding velocity.

to detect them at longer simulation times. This process required far more computational resources than having a sliding velocity to compare, being also time consuming. Further investigation in this area is therefore advised.

5.3.3 Cartridge-Shave prep shearing interaction models

The cartridge-shave prep shearing interaction models account for the dynamic shearing conditions the shave prep is subject to during rheological testing or a shaving stroke. Similar to the shear models described in **Section 5.2.3.1**, the fluid is contained between two surfaces, subject to shear due to motion of one of the surfaces. Unlike the shear models, where the velocity was applied as a boundary condition to the Eulerian domain, the surfaces containing the fluid were included in the cartridge-shave prep models as solid parts, and the velocity of these surfaces was transmitted to the fluid through the fluid-solid contact interaction. As a rough tangential friction behaviour is not feasible for the fluid interactions with the skin, the contact interaction was described in terms of coefficient of friction for the evaluation of slip for different test fluids. These two-component interaction models were also built in the radial and planar conditions, as described next.

5.3.3.1 Taylor-Couette flow model (TCF)

The TCF model comprises the simulation of radial shearing of a fluid representing the flow phenomena found in concentric cylinders rheological tests. The model geometry was defined by a $d = 0.375$ mm gap containing the fluid between a 5 mm radius

rotating inner cylinder and a static outer one. Both cylinders were represented as 0.1 mm thick solid rings. The first drafts of the model considered the complete circumference of the cylinders, with similar mesh quality to the one used in the shear models. However, this mesh was not able to capture the solid-fluid interaction. Thus, only a 10° section of the fluid with a finer mesh was modelled in contact with a 12° section of the outer cylinder, and larger 33° section of the inner cylinder providing enough extension for its estimated rotation. The accounting of gravity forces was required in this simulation to induce the initial fluid-contact interaction. See **Figure 5.19**.

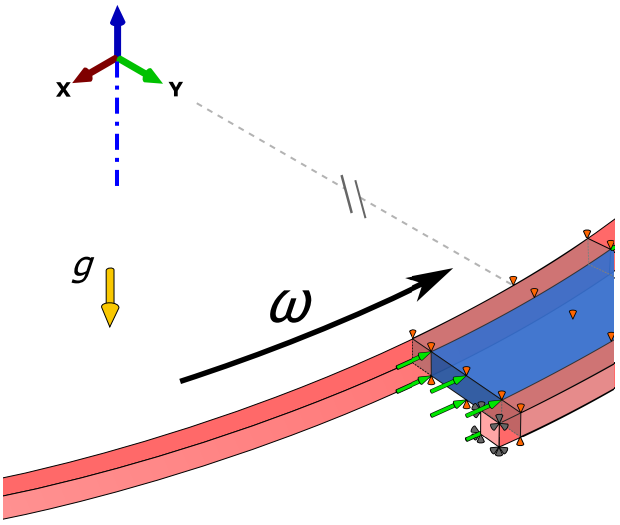

Figure 5.19: Taylor-Couette flow model. The Taylor-Couette flow model comprises a section of fluid (blue) contained between two concentrical cylinders of which the outer one is fully constrained (grey) and the inner one that rotates on its axis (blue line) at a ω angular velocity, applying shearing forces to the fluid. Only a section of the concentric cylinders is modelled to ensure faster runtimes. Therefore, the fluid is constrained by setting velocity in z direction to zero in the faces normal to the axis (orange), and a free inflow and outflow at the faces normal to the flow direction (green arrows). The Eulerian domain (gray shade) extends over the fluid gap, overlapping the cylinders' structure to enhance the solid-fluid contact interaction.

The cylinders' global seed size was set to 0.01 mm, with a variation of 0.03-0.01 mm in the radial direction (with finer mesh towards the fluid contact surface), generating 14,250 and 5,700 linear hexahedral elements (C3D8R) for the inner and outer cylinders, respectively. For the fluid, the global seed size was set to 0.02 mm with a variation of 0.03-0.0075 mm in the radial direction, refining the mesh towards each of the contact surfaces, generating 13,050 linear hexahedral Eulerian elements (EC3D8R). Overlap between the Eulerian domain and the cylinders was specified to maintain a solid-fluid interface throughout the simulation, but only the elements in between the solid surfaces were set to be filled with fluid. The fluid was constrained between the cylinders by setting the velocity in the width direction to zero in the free surfaces. In order to ensure a constant flow, free inflow and outflow was specified at the surfaces normal to the flow. The outer cylinder was fully constrained to prevent any motion, while the inner one was set to gradually reach an angular velocity of 150 rad/s (i.e. $V_T = 750$ mm/s, $\dot{\gamma} = 2000$ s^{-1}), at 0.005 s. The simulation step was set to 0.025 s.

Water, corn syrup, PEG 4MM 1% solution, and shaving foam A fluids (see **Table B.2** for properties) were tested under these shearing conditions. For these fluids, laminar flow was expected along the simulation, with the exception of water, which reaches $Re > 107$ after 0.002 s of simulation (see **Figure 5.20**). At such Re a vortex flow is expected (instead of laminar flow) (Andereck et al., 1986). A friction coefficient of 1.0, allowing 'no-separation' between the fluid and the cylinders was defined for the fluid-solid contact interaction, for the evaluation of 'slip' effects at the fluid-solid interface.

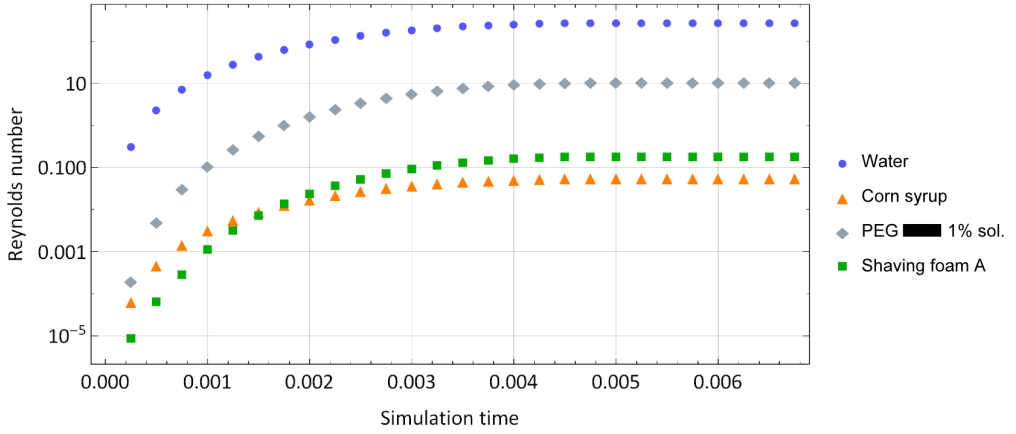

Figure 5.20: Reynolds number analysis of the Taylor-Couette flow models. With the exception of water after 0.002 s simulation time, the flow is maintained within the Couette flow (laminar) with a $Re < 107$ (Andereck et al., 1986).

A big concern was raised by noting that within 150 hours runtime, only 7-8% of the simulation had been completed (with a maximum simulation time of $2{\times}10^{-3}$ s, at which $V = 238$ mm/s), even with the use of 48 parallel processors. Improvement of the runtime could be achieved by redefining the mesh dimensions. However, in these shearing conditions, lower quality of the mesh caused artefacts in the simulation that introduced 'void' values in the fluid, while the mesh described above proved to appropriately capture the solid-fluid interaction. For this reason, no further simulations were run with the TCF model, which showed to be too computationally expensive. Therefore, the analysis of results was focused on those obtained in the transient state.

As shown in **Figure 5.21**, the laminar flow condition was met for all the fluids. In the transient flow, the velocity profile was expected to reflect the changes in velocity through the fluid, showing a soft reduction of velocity in the cross section from the moving inner boundary to the static outer one. However, such a condition seems to be highly affected by slip. In order to analyse slip at the fluid-solid interfaces, the relative velocities between the fluid and the cylinders at the fluid-solid interface were compared.

Taking a cross section of the fluid model (section C-C' in **Figure 5.21**), the average velocity of the nodes in contact with the cylinders was subtracted from the velocity on the cylinder's surfaces. In 'no-slip' conditions, the relative velocity is zero. Different levels of slip were observed at the two interfaces. At the inner cylinder, where V_T was applied, low slip was observed for all the fluids up to $1.5{\times}10^{-3}$ s, where the slip of corn

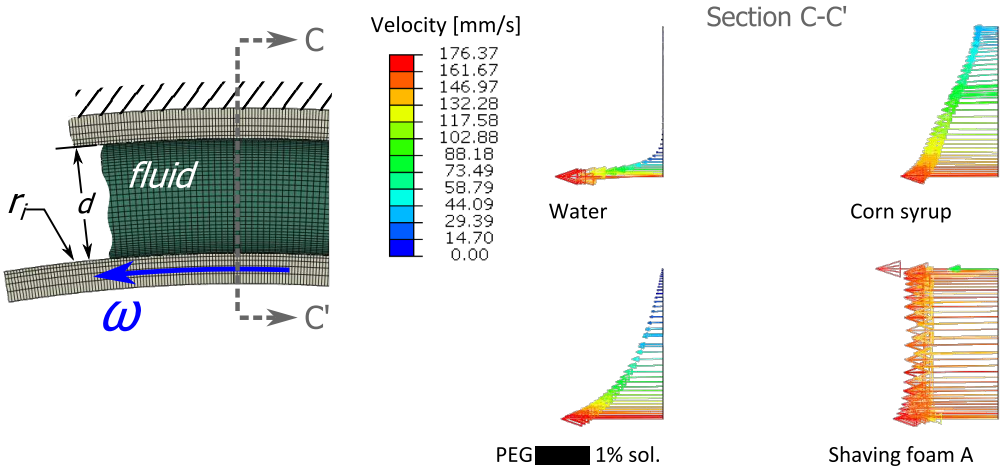

Figure 5.21: Taylor-Couette flow model velocity profiles. Shearing of the fluid contained in the gap d between the concentric cylinders is caused by the rotation of the inner cylinder of radius r_i at an angular velocity ω. The velocity profiles at section C-C', as indicated in the model diagram (left), are shown for the simulation time 1.75 $\times 10^{-3}$ s, with transient flow (ω is increasing at this stage of the simulation) and tangential velocity at the inner ring contact interface $V_T = \omega \cdot r_i = 211.31$ mm/s. The difference in fluid velocity at this interface indicates slip effects for the specified coefficient of friction of 1.0.

syrup showed higher magnitude than the other fluids. At the outer cylinder, water and PEG solution showed a relative velocity close to zero, while higher slip was observed for corn syrup and shaving foam A as a result of higher viscous drag. See **Figure 5.22**. Although the level of slip seems related to the mechanical properties of the fluids, no direct relation of these properties with the slip was found.

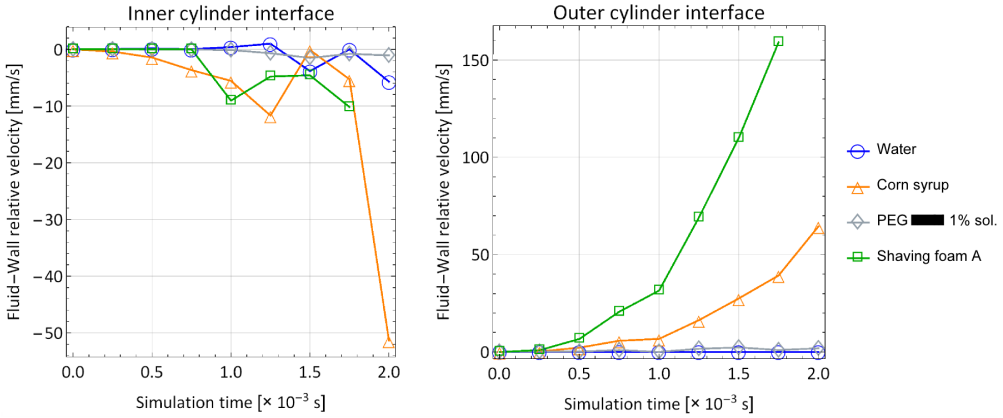

Figure 5.22: Slippage measurements in Taylor-Couette flow model. The plots show the relative velocity between the fluid and cylinders. At the inner cylinder surrface (left), where maximum velocity is expected, the negative values show a slower velocity of the fluid compared to that of the cylinder wall. At the outer cylinder surface (right), where the cylinder is static, the positive value show a speed up of the fluid, driven by viscous drag.

5.3.3.2 Laminar flow model (LF)

The LF model provides a fluid-structure interaction version of the planar shear model, consisting on the simulation of planar shearing of a fluid, simplifying the features of the channel created between the skin and the cartridge blade/guard into a fluid been sheared between two parallel plates. The model assembly included a static plate providing a 2.0×0.1 mm^2 contact surface to the fluid, a longer moving plate applying the shearing velocity, and a $1.6 \times 0.475 \times 0.1$ mm^3 Eulerian domain. Like in the TCF model, overlapping the solid plates with the Eulerian domains was specified to maintain the fluid-solid interface for the contact interaction). The moving plate was set ten times longer to the static one to ensure shear throughout the simulation time. Only the Eulerian elements in-between the plates were filled with fluid material. Once more, gravity forces were accounted for to ensure the first contact between the fluid and the plates. See **Figure 5.23**.

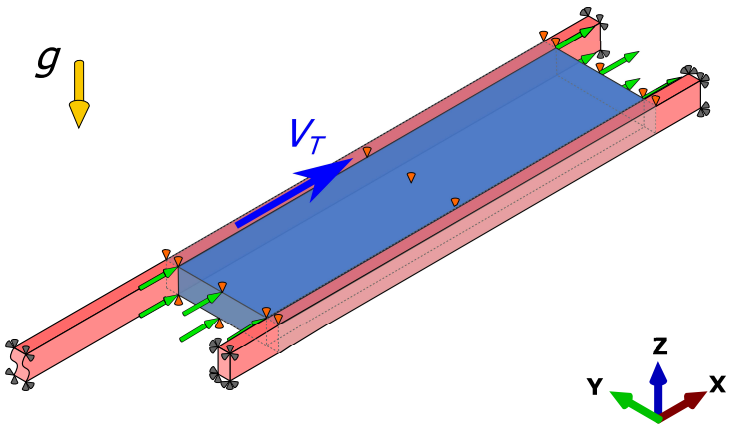

Figure 5.23: Laminar flow model. The Laminar flow model comprises a section of fluid (blue) contained between two parallel plates of which the bottom one is fully constrained (grey) and the top one that moves in the flow direction at V_T velocity, applying shearing forces to the fluid. The fluid is constrained by setting velocity in z direction to zero in the faces normal to the axis (orange), and a free inflow and outflow at the faces normal to the flow direction (green arrows). The Eulerian domain (gray shade) extends over the fluid gap, overlapping the plates' structure to enhance the solid-fluid contact interaction.

The same meshing approach used in the TCF model was applied, generating 80 and 800 linear hexahedral elements for the static and moving plate, respectively, and 13,440 linear hexahedral Eulerian elements. Likewise, the same velocity constraints were applied to contain the fluid in the space between the plates. In order to ensure a constant flow, free inflow was specified at the inlet surface, and zero pressure outflow was enforced at the outlet surface. The static plate was fully constrained to prevent any motion. The moving plate was allowed to move in only one direction, at a gradually increasing velocity $V_T = 800$ mm/s (i.e. $\dot{\gamma} = 2133.33$ s^{-1}), reaching a steady state at 0.005 s. The simulation step was set to 0.025 s.

The simulations were performed with the same test fluids of the previous model. Under these conditions, a maximum Reynolds number range between 600 (for water) and 0.122 (for corn syrup), maintaining the simulations within the laminar flow regime. The contact interaction between the fluid and the cylinders was defined by a friction coefficient of 1.0, allowing 'no-separation' between the parts.

The geometry of the LF model provided better runtime performance. In this case, most of the simulations reached a steady shearing velocity, with the exception of the shaving foam A one, which only reached up to 1.75 $\times 10^{-3}$s after 20 hrs runtime with 32 parallel processors. Although the Reynolds number doubles the one on TCF model, the velocity profiles patterns of water, corn syrup, and PEG solution show some similarities up to this point (see **Figures 5.21** and **5.24**). Like the TCF model, slip measurements were taken from the average velocity of the nodes at the plates interfaces, across a section of fluid (section D-D' in **Figure 5.24**).

Like the slip results of the TCF model, lower slip was observed for water followed by the PEG solution, while higher slip was show for corn syrup and then the shaving foam A, driven by the viscous drag. In the LF model, slip at the moving plate for all fluids and slip closed to zero for water and PEG solution at the static plate only, was also registered in the transient state. The changes in slip throughout the simulation appear to reflect the effects of acceleration of the moving part. At the moving plate interface, these effects are more noticeable at the transient state, as higher slip occurs at the start of the simulation, when the plate starts to move, and then the fluid slip reduces as the acceleration is reduced, with more immediate effects in the less viscous fluids. At the static plate interface, initial acceleration has a larger effect in the corn syrup and shaving foam A as higher viscous drag is transmitted. Further inertial effects in fluid slip were observed at the transition to the steady state. These effects are captured in the plots shown in **Figure 5.25**.

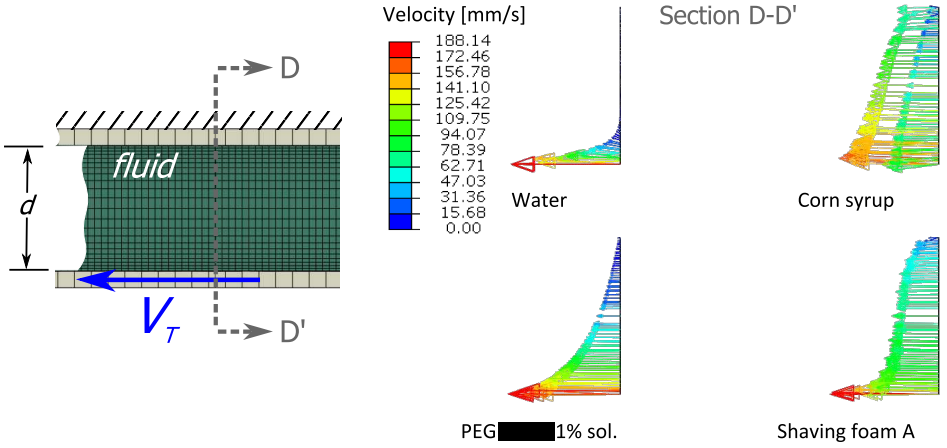

Figure 5.24: Planar shear model profiles. The fluid is contained in the gap d formed between two plates. The boundary conditions are set to allow the fluid flow in the velocity direction, but preventing the flow in the z direction by setting the normal velocity at faces normal to z as zero. The top plate is fixed while the bottom plate shears the fluid by moving at a velocity V_T. The figure plots the velocity profiles obtained at section D-D' for different fluid models at simulation time 1.75×10^{-3} s, where the current plate velocity is transient at $V_T = 188.14$ mm/s.

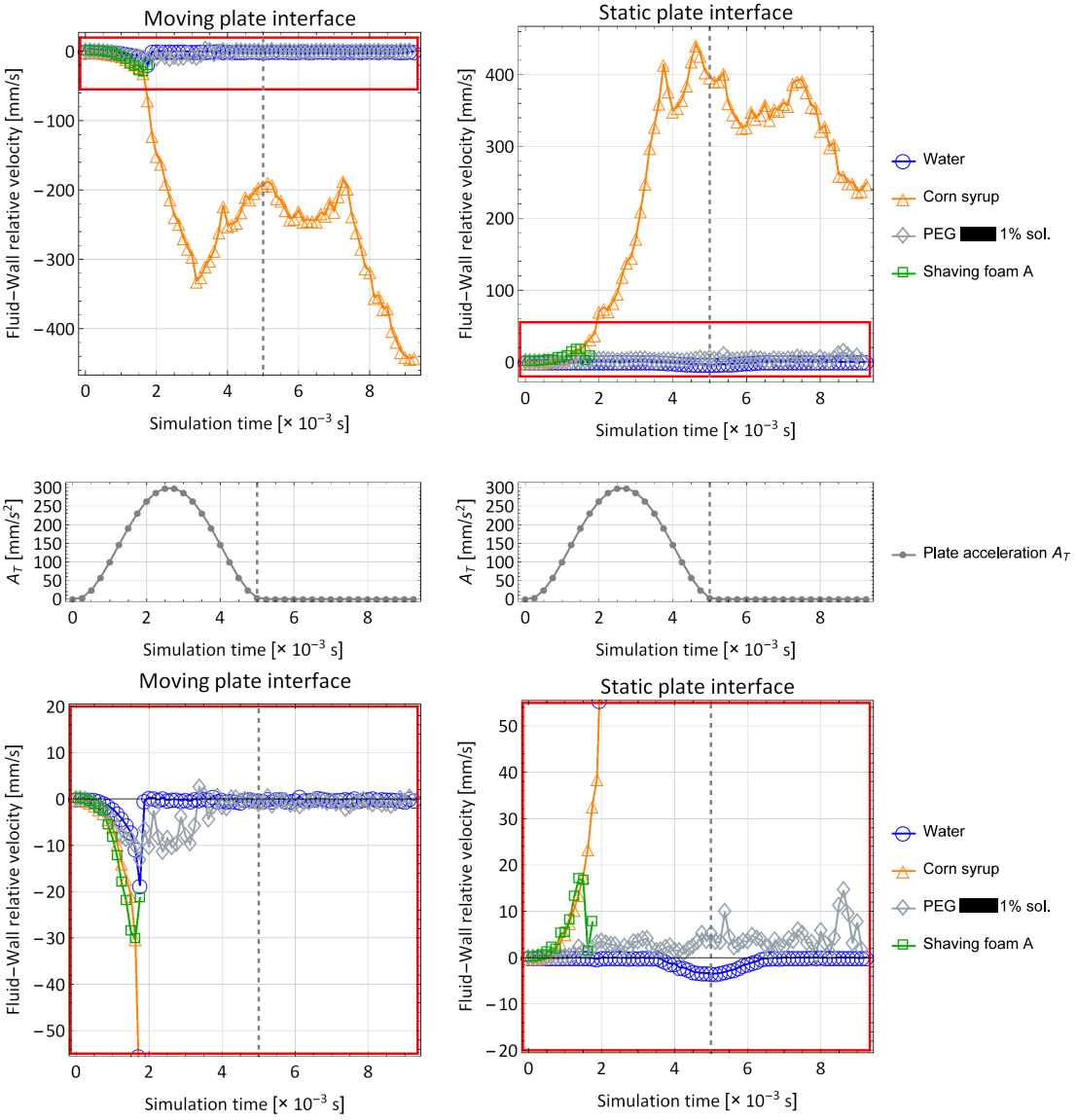

Figure 5.25: Slippage measurements in Laminar flow model. The plots (top) show the relative velocity between the fluid and plates surfaces. At the moving interface (left), where maximum velocity is expected, the negative values show a slower velocity of the fluid compared to that of the plate. At the static plate interface (right), the positive value show a speed up of the fluid, driven by viscous drag. The dotted line indicates the start of the steady state of the simulation, corresponding to the stage at which the plate acceleration plot (centre) reaches zero at 0.005 s. A zoomed area of the slip plots is shown to highlight the slip behaviour of water and PEG solution (bottom).

5.4 Modelling framework development, stage III: Three- component contact interactions

Taking the knowledge provided for the two-component interaction models, the skin-solid-fluid interaction was assessed in terms of the contact parameters, considering the fluid adhesion to the skin prior, during and after shearing, in the **solid-rigid skin-shave prep (SRS)** model, incorporating the skin large deformations in the **skin-guard-shave prep (SGS)** model. These two models show the initial stages of the **multi-physics modelling framework** developed in this PhD project.

5.4.1 Skin-solid-fluid interaction

The three-component interaction incorporates the two-component interaction models into a simulation of the interaction of a free surface fluid with both, the surface it rests on, and the solid part than deforms it by applying the characteristic forces exerted by a cartridge during a shaving stroke. The skin-solid-fluid interaction models built up on the acquired knowledge during the development of the previous two-component models, starting from simpler to more complex, as explained in the following sections, providing the bases for the **multi-physics modelling framework**.

5.4.1.1 Solid-rigid skin-shave prep model (SRS)

The SRS model, built as a 'step' model towards the **multiphysics modelling framework**, comprises the simulation of a shaving stroke motion by an indenter on a rigid skin substrate, that allows the analysis to focus on the deformation of a portion of shave prep lying on its surface. The basic geometrical features of the DRS model (**Section 5.3.1.1**) were used, setting the indenter as a rigid body, the skin with mechanical properties similar to iron, and the shave prep with the properties of fluid SP01 (see **Table B.1**). On top of the epidermal surface, a $8 \times 3 \times 6$ mm^3 fluid droplet within a $2 \times 5 \times 10$ mm^3 Eulerian domain was placed in front of the indenter. At this stage, no overlap between the fluid and the contact surface was considered. See **Figure 5.26**.

Like in the DRS model, the indenter was set as a shell rigid part with a global mesh seed size of 1 mm, generating 468 mixed triangular and quadrilateral linear elements (R3D3 and R3D4). Due to the rigid structure of the skin, its mesh was much coarser, with a global seed size of 3 mm generating 60 linear hexahedral elements (C3D8R). For the fluid, the global seed was set to 1 mm, refining the area around the droplet to half the size, generating 4,480 linear hexahedral Eulerian elements (EC3D8R). The motion of the indenter was set by applying a constant velocity vector of 40 mm/s, constraining the motion to the stroke direction. With the exception of the top surface, the

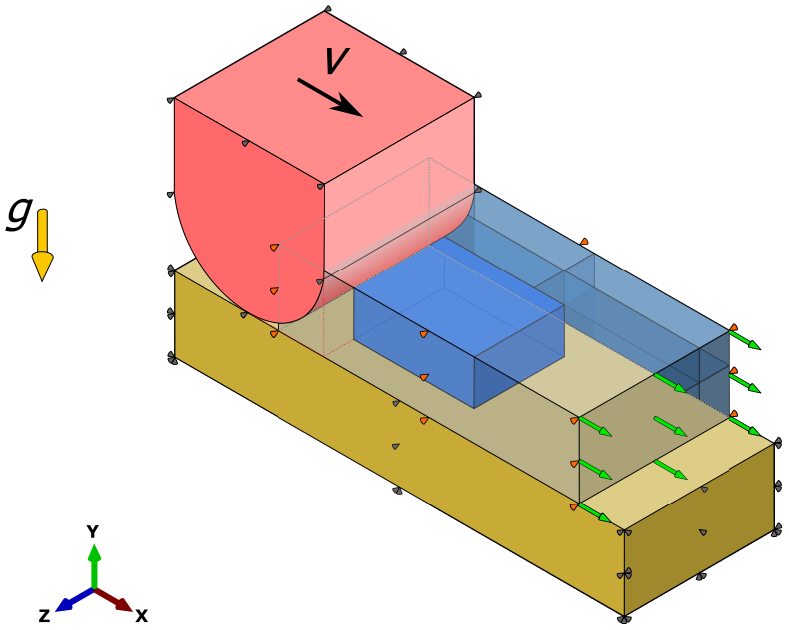

Figure 5.26: Solid-rigid skin-shave prep model. The Solid-Rigid skin-Shave Prep model comprises a fluid droplet (blue) lying on a solid stiff skin (yellow) deformed by the sliding motion of a rigid indenter (pink) travelling at a rectilinear speed V. The fluid droplet is allowed to flow outside the Eulerian domain (gray shade) in the x direction (green arrows), but is constrained in the z direction by setting the velocity normal to this surfaces as zero (orange). The displacement of the skin non-contact surfaces is also restrained (grey) by applying symmetry boundary conditions. Gravity forces are accounted for to ensure the contact of the fluid with the skin.

skin surfaces were constrained by symmetry boundary conditions. The fluid was constrained within the Eulerian domain by setting the velocity normal to the surface, at lateral walls, as zero. The interaction properties between the solid and the skin were set as frictionless while the skin-fluid and solid-fluid interaction was defined with an infinite coefficient of friction (indicated as 'rough' contact within the Abaqus environment), for the assumption of 'no-slip' conditions. At this stage, the 'no-separation' settings used to capture adhesion of the fluid to the surface of contact, had not been implemented. As explained in the following section, this interaction does not work appropriately when applied to soft materials, so specific coefficient of friction of the shave prep-skin interaction should be assigned. Gravity forces were accounted for to ensure initial contact of the fluid with the skin. The simulation step was set to take 0.3 s.

As shown in **Figure 5.27**, the model captured how the fluid deforms and adapts to the loading feature. It was later discovered that the default boundary conditions (free in-flow/outflow) in the top surface of the Eulerian domain was not adequate for the simulation, as the fluid leaving this surface was replaced by more fluid. This model set the basis for the next stage of the skin-solid-fluid interaction model where the deformation of the skin was taken into account.

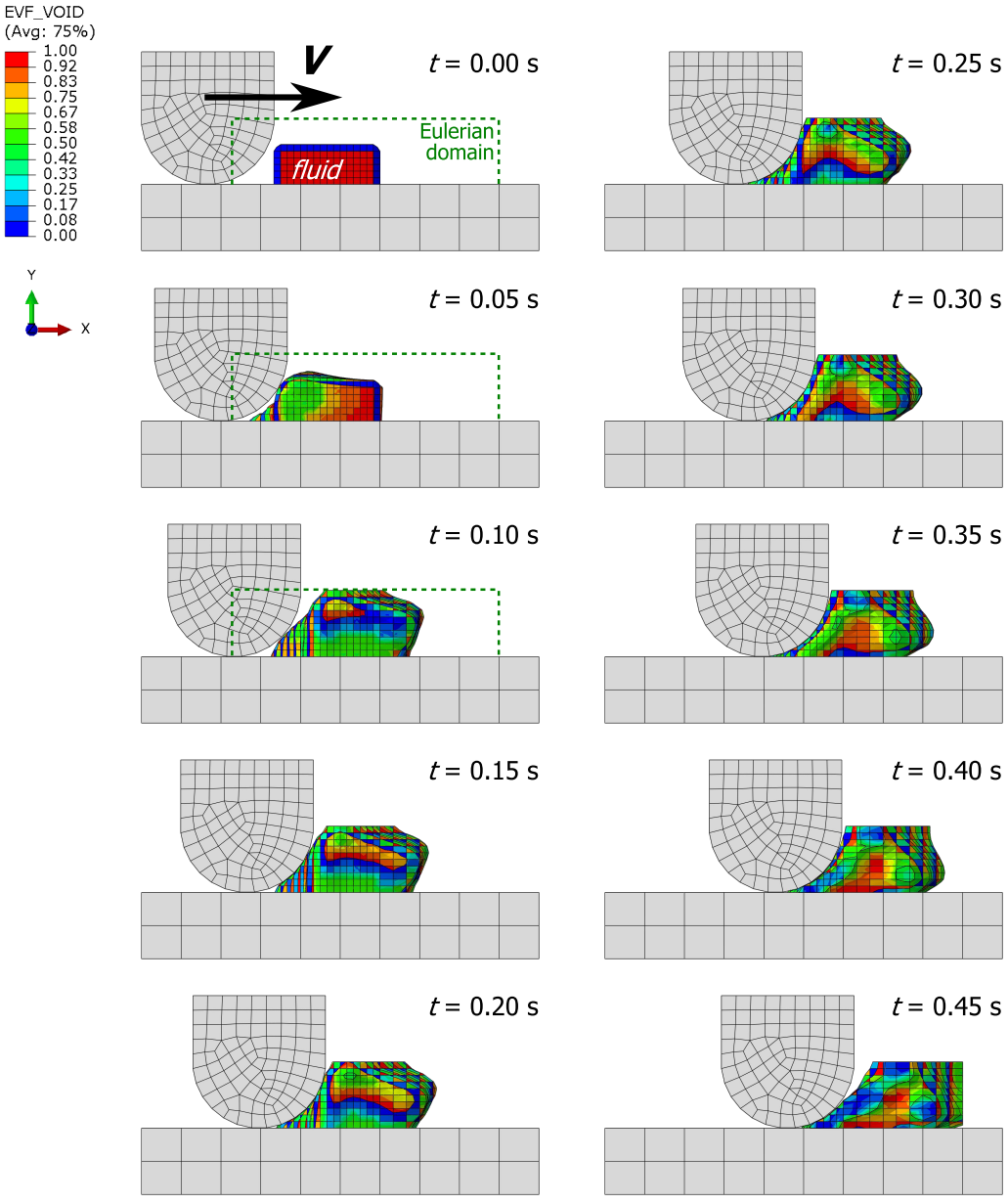

Figure 5.27: Solid-rigid skin-shave prep model. In this fluid-structure interactions (FSI) model, a fluid lying on an horizontal surface is deformed by a rigid body moving at a velocity V parallel to the surface. The boundary at the top surface of the Eulerian domain is set by default to replace the fluid leaving this surface by more fluid. This condition (not desired in the final model) is observable by the apparent additional fluid after the fluid touches the top surface of the Eulerian domain, at simulation time 0.10 s.

5.4.1.2 Guard-skin-shave prep model (SGS)

The SGS model comprises the simulation of a shaving stroke motion, with a section of a cartridge guard as an indenter, on a soft bi-layer skin that is deformed along with a shave prep droplet that lies on top of the skin. The geometrical features of the SG model (**Section 5.3.1.2**) were used, setting the guard as a rigid body, the skin with the hyperelastic, viscoelastic, properties of the dermis and epidermis (O'Callaghan and Cowley, 2010), and the shave prep with the properties of the test fluids (water, corn syrup, PEG 4MM 1% solution and shaving foam A —see **Table B.2**). A 2.5×0.8×0.5 mm^3 fluid droplet within a 12×3.5×0.5 mm^3 Eulerian domain was specified on the skin surface 2.5 mm from the surface edge where the shaving stroke starts. On top of this area, at a 0.08 mm, the comb guard was positioned 1 mm away from the shave prep droplet. The Eulerian domain overlapped the whole skin part and most of the guard in order to account for the fluid and skin deformation around the guard. See **Figure 5.28**.

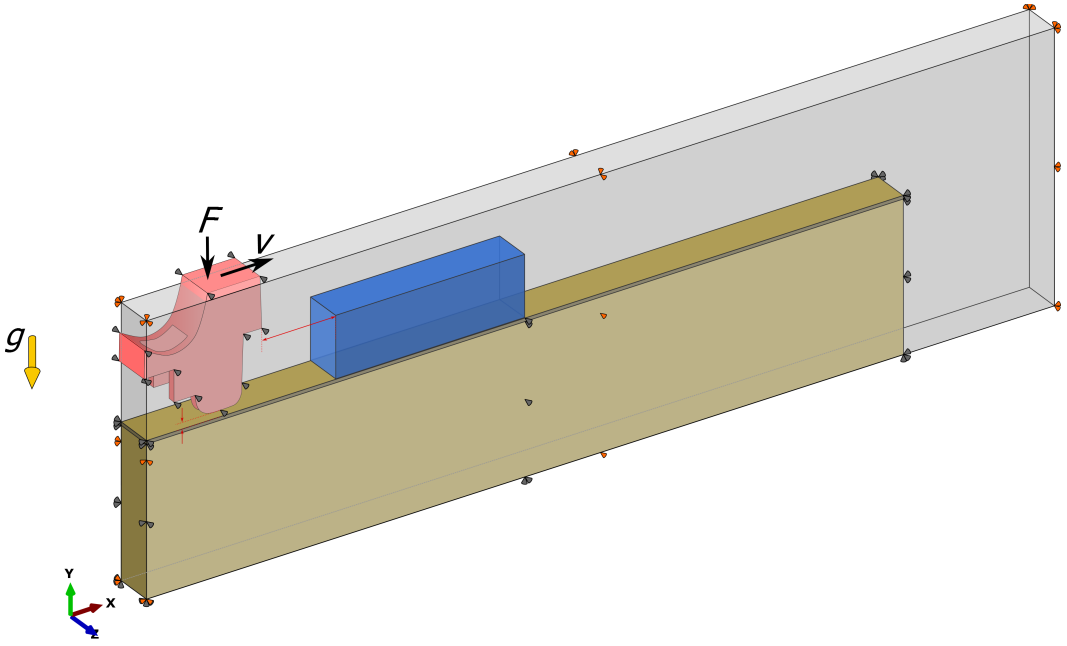

Figure 5.28: Skin-guard-shave prep model. The skin-guard-shave prep model comprises a fluid droplet (blue) lying on a soft bi-layer skin (yellow) to be deformed by the action of a normal force of magnitude F and lateral velocity of magnitude V applied to the comb guard (pink). The motion of which is constrained to align with the stroke direction (grey). The fluid droplet is constrained within the Eulerian domain by setting velocity normal to surfaces as zero (orange) in all the surfaces but the bottom one. The displacement of the skin non-contact surfaces is also restrained (grey) by applying symmetry boundary conditions. Gravity forces are active to ensure the contact of the fluid with the skin.

The skin and guard were meshed with the same parameters than the ones used in the SG model, providing 4,795 linear hexahedral (C3D8R) and 978 quadratic tetrahedral elements (C3D10M), respectively. The shape prep global seed size was set to 0.005 mm, generating 138,600 linear hexahedral Eulerian elements (EC3D8R). The motion of the guard was set as in **Section 5.3.1.2** by a 30 mN normal load and 10-20 mm/s

velocity, gradually applied, reaching its maximum value at 0.2 s. With the exception of the top surface, the skin surfaces were constrained by symmetry boundary conditions. The fluid was constrained within the Eulerian domain by setting the normal velocity to zero in all the surfaces except the bottom one. Gravity forces were included in the model to ensure the initial contact of the fluid with the skin. The simulation step was set to represent a physical time of 0.5 s.

An early version of this model setting rough friction interaction between the skin and the shave prep showed that the fluid adhesion was so strong that the skin elements were dragged and deformed to the point of reaching the locking stretch of the skin tissue (see **Section 2.4.2**), causing simulations to fail. Therefore, the contact interactions were defined individually in terms of the coefficient of friction and the separation/no separation conditions. The contact pairs and their corresponding coefficient of friction are identified as: *a*) skin-cartridge interaction, μ_{sc}; *b*) fluid-cartridge interaction, μ_{fc}; and *c*) fluid-skin interaction, μ_{fs}.

In the cartridge-shave prep shearing interaction models (**Section 5.3.3**), it was shown that equal interaction properties had different effects in the slip of different fluids. These effects were visually inspected for the test fluids, under shaving stroke conditions, considering $\mu_{sc} = 0.0$, $\mu_{fc} = 0.3$, and $\mu_{fs} = 0.7$. The 'no-separation' condition was applied only to the fluid-skin interaction.

The spreading behaviour of the fluids was evident in the simulations, where water deforms on the skin surface due to gravity forces, and it is easily splashed by the action of the cartridge guard movement. Higher adherence was observed for the corn syrup and the PEG solution, allowing the fluid to go through the channel in the comb guard geometry. With lower viscosity than the corn syrup, the simulation showed that more of the PEG solution fluid was allowed to enter the channel, leaving a thicker 'tail' of fluid behind. Different effects were observed for the shaving foam A, which showed low adhesion and, with its high viscosity, how it was pushed by the solid guard allowing only a small amount of fluid to go through the guard channel. See **Figure 5.29**. These results confirm that the specific adhesion conditions cannot be characterised equally for different fluids, as indicated in the previous analysis.

The test fluid simulations were run with 48 parallel processors. However, analysis was computationally expensive, requiring exceptionally low time increments for reaching convergence, as the estimated completion time ranged between 140 and 230 hours, having lower runtimes with the PEG 4MM 1% solution. Taking into account the sensitivity analysis, where the longitudinal wave propagation velocity (sound speed) was directly correlated with the simulation runtimes (**Section 5.2.4.1**), this simulation was repeated selecting the fluid with better performance with a reduced value of longitudinal wave propagation velocity. The fluid with these characteristics is fluid SP04 (see

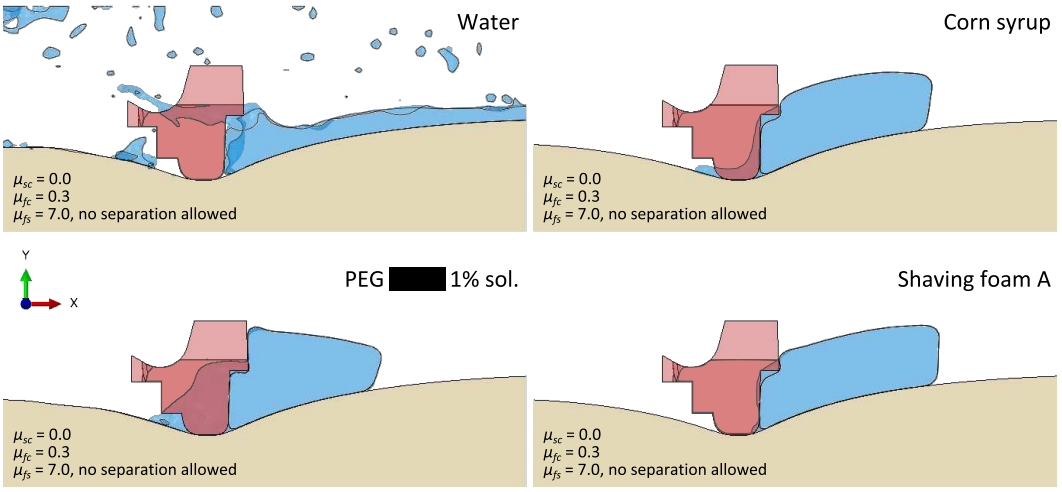

Figure 5.29: Evaluation of the deformation of test fluids with the SGS model under shaving stroke conditions. With identical interaction properties (coefficient of friction for each contact pair: skin-cartridge μ_{sc}, fluid-cartridge μ_{fc} and fluid-skin μ_{fs}), different spreading, sliding and trace-leaving behaviour was observed for four test fluids.

Table B.1), which showed a speed up in the simulation with four times better performance in terms of runtime than the observed for the PEG solution. The effects in the fluid behaviour caused by the modification of the longitudinal wave propagation velocity values were evaluated in terms of deformation and shear stresses with the SGS model, also accounting for any deformation effect on the skin material. Further analysis considered the evaluation of shear stresses and velocity profile, using the TCF and LF models.

Great similarities were observed between the deformation of the fluid ahead and though the guard part in the SGS model simulations, leaving similar traces of fluid behind. However, the distribution of shear stresses was different, showing a smoother distribution of stress across the fluid with lower wave propagation velocity. This resulted in reduced unrealistic splashing effects observed in the PEG solutions model, capturing a more appropriate behaviour of the fluid. By reducing this parameter, the compressibility of the fluid increases, providing more stable conditions for the finite element analysis. Negligible differences were observed in the skin deformation. See **Figure 5.30**.

Capturing the appropriate viscous behaviour is of great relevance in the simulation of shear thinning fluids. For this reason, the effects of a reduced wave propagation velocity were evaluated in the TCF and LF models, under shearing conditions. Fluid SP04 showed great similarities in distribution of shear stress, but higher slip was observed in the contact interaction. Such slip is within 4% of the observed for PEG solution in the moving interface, but up to 4.45 times higher at the static interface of the LF model, and 15 times higher in the TCF one (see **Figure 5.31**). By specifying the interaction with a coefficient of friction, the stresses normal to the contact surface determine the critical tangential stress required to allow slip between the surfaces (Aba,

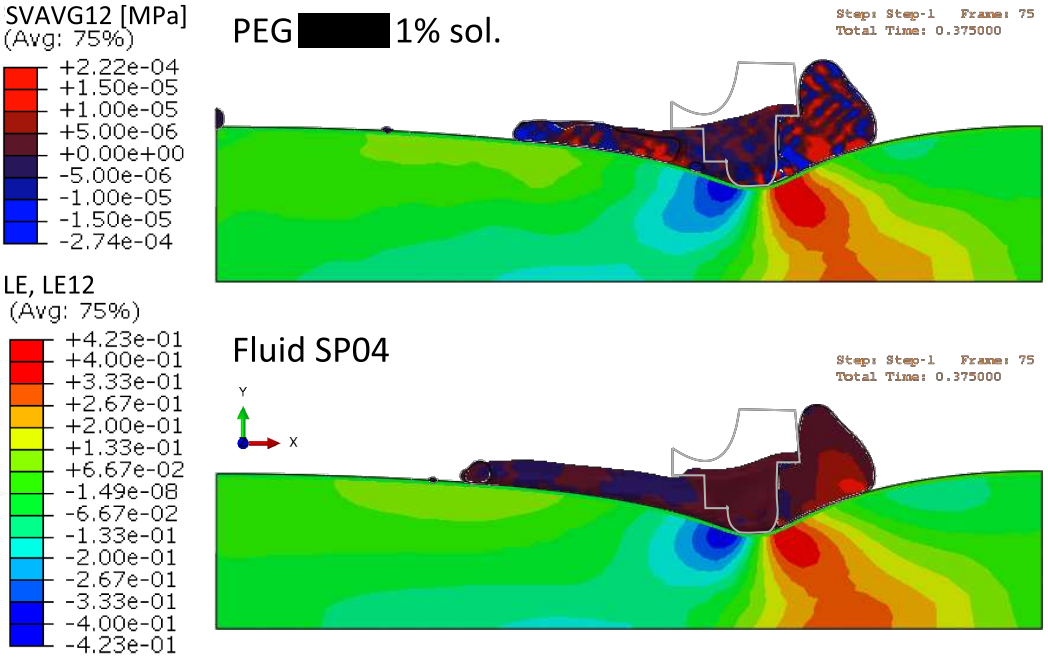

Figure 5.30: Effects on deformation and shear stress distribution in the fluid, by reducing the longitudinal wave propagation velocity (sound speed). The results of the simulation of PEG 4MM 1% solution in the SGS model were compared with those of fluid SP04, whose wave propagation velocity is two orders of magnitude lower. Similar deformation is observed for the two fluids, but the shear stresses (SVAVG12) in fluid SP04 showed a smoother transition throughout the material. Negligible effects were observed in the skin deformation, as shown in the plot for logarithmic shear strain (LE12).

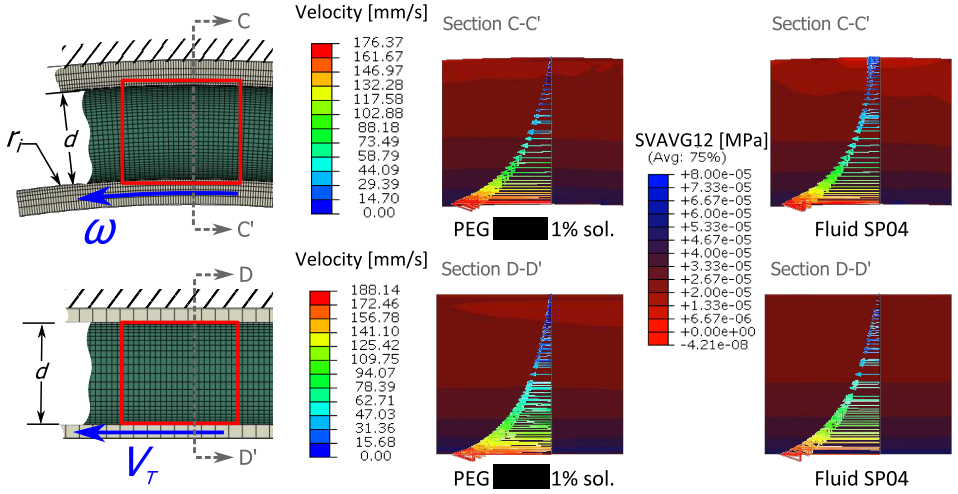

Figure 5.31: Comparison of the viscous response and contact interactions of PEG 4MM solution (centre) and fluid SP04 (right) under pure shear simulations, with the TCF (top) and LF (bottom) models. The velocity profiles of the two fluids are shown across section C-C' and D-D' as indicated in the models diagrams (left), superimposed to the close up of the area marked in red, showing the distribution of shear stresses across the gap between the two solid interfaces.

2014c). Therefore, it is likely that by changing the fluid compressibility, the fluid pressure (and thus the normal stress on the contacting surface) is modified affecting the wall slip. As mentioned in **Chapter 3**, capturing the appropriate wall slip is a complex task. So, any modification in the wall slip behaviour would require to be compensated by adjusting the coefficient of friction at the fluid-solid interaction. Although further investigation of these effects is required, doing so is worth the effort, especially after a four times improved performance was observed.

The SP04 fluid was used for the analysis of the contact interactions effects in the simulation of the shaving stroke with the SGS model. The effects of the application of 'no-separation' condition to the fluid-skin interaction was evaluated at different interaction conditions in the whole system. The simulations showed that when 'no-separation' was enforced, the combined effects of the coefficient of friction and adhesion was able to capture a larger fluid trace, longer than if 'separation' was allowed. A higher coefficient of friction between the skin and the fluid, drove more fluid into the guard channel than a lower one. The coefficient of friction between the fluid and the cartridge, coupled with the effects of the deformation on the skin (caused by the skin-cartridge interaction definition), have a direct effect with ploughing of the shave prep ahead the guard. These results are shown in **Figure 5.32**.

The effects of the shaving stroke velocity were also compared along with the characteristics of the fluid-cartridge interactions. The analysis considered the variation of the stroke velocity from 10 to 20 mm/s, and variation of μ_{fc} from 0.0 to 0.3, while the interactions of the skin with the cartridge and fluid remained unchanged, with $\mu_{sc} = 0.3$ and $\mu_{fs} = 0.7$ with no separation allowed. In this test, it was shown that with higher velocity a longer trail of fluid is left but, although more fluid enters the channel, this effect can be counteracted by the fluid-cartridge friction forces, pushing the fluid ahead of the guard, as shown in **Figure 5.33**.

Gathering the knowledge obtained in the development process of the multi-physics modelling framework, the following recommendations are made for the characterisation of the interactions with open surface fluids.

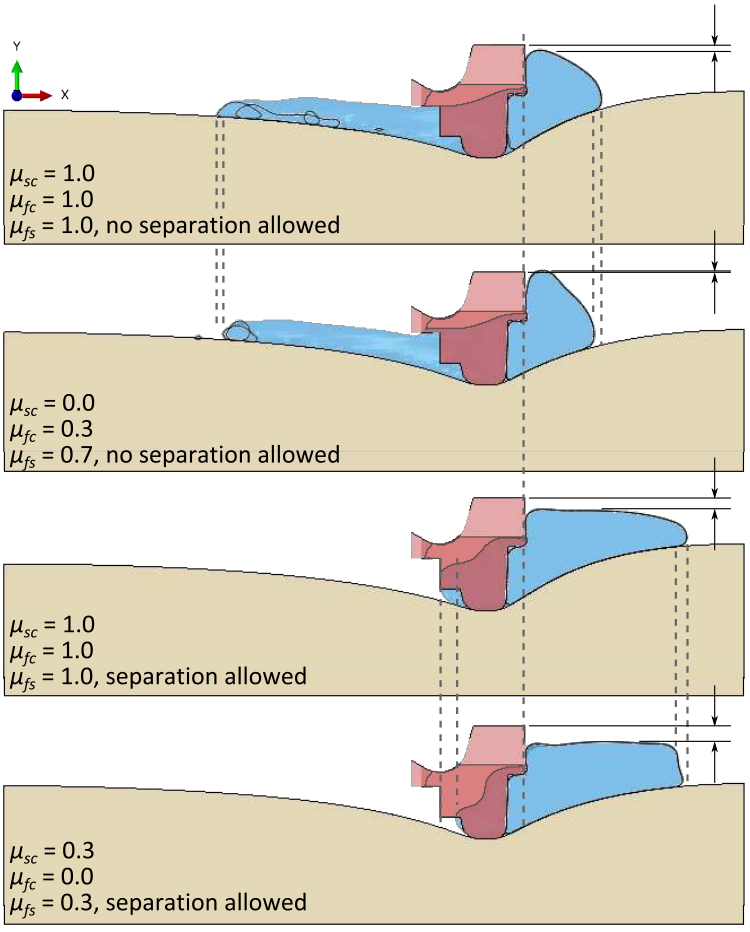

Figure 5.32: Coupled effects of the two-component interactions on the fluid deformation in the SGS model. The deformation of the SP04 showed high dependency on the characteristics of the three contact interactions. Higher friction between the fluid and skin (μ_{fs}), implicitly accounts for adhesion forces, while a higher coefficient of friction between the fluid and the cartridge (μ_{fc}), coupled with the deformation in the skin caused by the skin-cartridge friction (μ_{sc}), has an impact on the shape of the plough of foam ahead of the guard. All images are at the same scale.

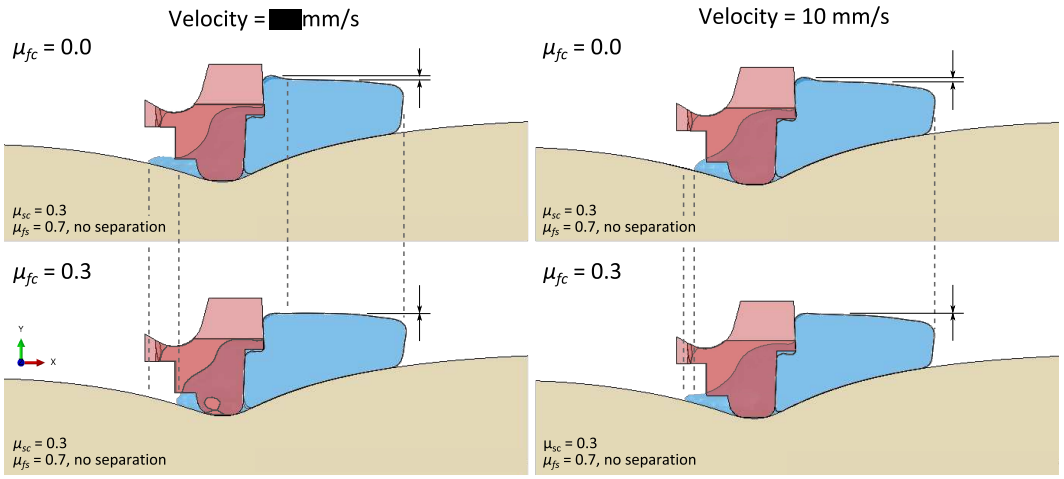

Figure 5.33: Evaluation of fluid deformation effects with a stroke velocity of 20 mm/s (left) and 10 mm/s (fight), with frictionless interaction between the fluid and the guard ($\mu_{fc} = 0.0$, top) and a coefficient of friction $\mu_{fc} = 0.3$, (bottom). The skin-cartridge and fluid-skin contact interaction are identical in the four cases shown. The stroke velocity can favour the formation of a fluid trail as the grooved guard deforms. However, these effects can be counteracted by the friction forces between the guard and fluid. All images are at the same scale.

5.5 Modelling recommendations for the characterisation of interaction with open surface fluids

The development of the multi-physics modelling framework in stages, to characterise the interactions of skin and wet shaving products, has provided detailed and essential knowledge to be used for the modelling of interactions of deformable and rigid solids with open surface fluids. From this process, the following modelling recommendations can be highlighted:

Eulerian domain. The dimension of the Eulerian domain should include all the space where the fluid can exist. In order to ensure the interaction with other solids is captured, the Eulerian domain should overlap the elements of the parts in which the fluid is in contact.

Eulerian boundaries. The Eulerian domain should be built considering that inflow of fluid can be modelled when dragged by the cohesion forces of the existing fluid (specifying free inflow at the boundary), but that the fluid leaving the Eulerian limits cannot be recovered. Therefore, the following consideration should be taken for modelling the interaction of the fluid with the Eulerian boundaries:

1. Specifying 'none' inflow at a boundary will create an adhesive interaction with the fluid, if it is in contact with the surface in the reference configuration. This effect can be avoided by specifying 'void' inflow boundary condition.
2. Specifying a zero velocity normal to the surface, the model provides a frictionless interaction that mimics the fluid laminar behaviour when applied to surfaces parallel to the flow.
3. For fluids leaving the Eulerian domain, specifying a 'zero pressure' condition at the boundary ensures the fluid outflow does not generate undesired effects.

Fluid-solid interactions. For fluid-solid interactions, the experimentally obtained coefficient of friction for the specific fluid and solid should be used. The adhesive behaviour of a fluid can be implicitly accounted for by a large coefficient of friction and the 'no-separation' condition.

Runtime performance. Higher performance is achieved with the use of lower wave propagation velocity to characterise the compressibility of the fluid, and minimising the number of elements in the Eulerian mesh.

5.6 Application of the multi-physics modelling framework to the design of wet shaving products

The recommendations above have been applied for the completion of the **multi-physics modelling framework**. In this framework, the parts are interchangeable for more complex geometries or assemblies, and the outputs can be adapted for the requirements of the analysis, providing a modular tool that can aid to the analysis of lubrication performance of different cartridge designs and shave prep formulations.

The **multi-physics modelling framework** was applied, in a job requested by P&G, for the assessment of shave prep 'flow' towards the blades for two elastomer guard designs in development. For faster simulations, some simplifications of the geometries were applied. The effectiveness of the designs were evaluated in terms of the relative velocity of the fluid with respect to the velocity of the razor cartridge, as an indication of flow. The new guard designs were compared to the results obtained with the simplified Gillette Fusion® cartridge, shown in **Figure 5.34**.

In this job, the modularity of the modelling framework was put into test, showing its capability for the consideration of different shave prep properties and razor cartridge components. These and some other applications of the multi-physics modelling framework are shown in **Figure 5.35**, in which different geometries and fluids are applied in on a thin slice of fluid or at a larger scales.

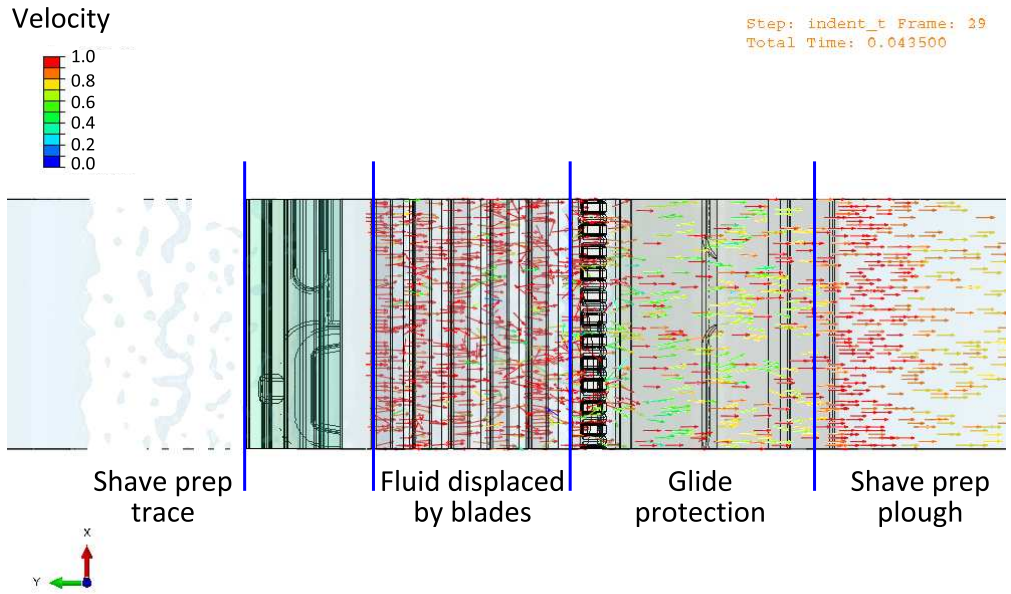

Figure 5.34: Application of the **multi-physics modelling framework** for evaluation of guard design, evaluating the velocity (normalised) of the fluid. The simulation captured the trail of fluid left behind the shaving stroke, the displacement of shave prep in between the blades, the glide protection layer under the elastomer guard, and ploughing of the shave prep ahead the cartridge. Simplified version of Gillette Fusion® cartridge shown. **Proprietary data (P&G). Do not disclose**.

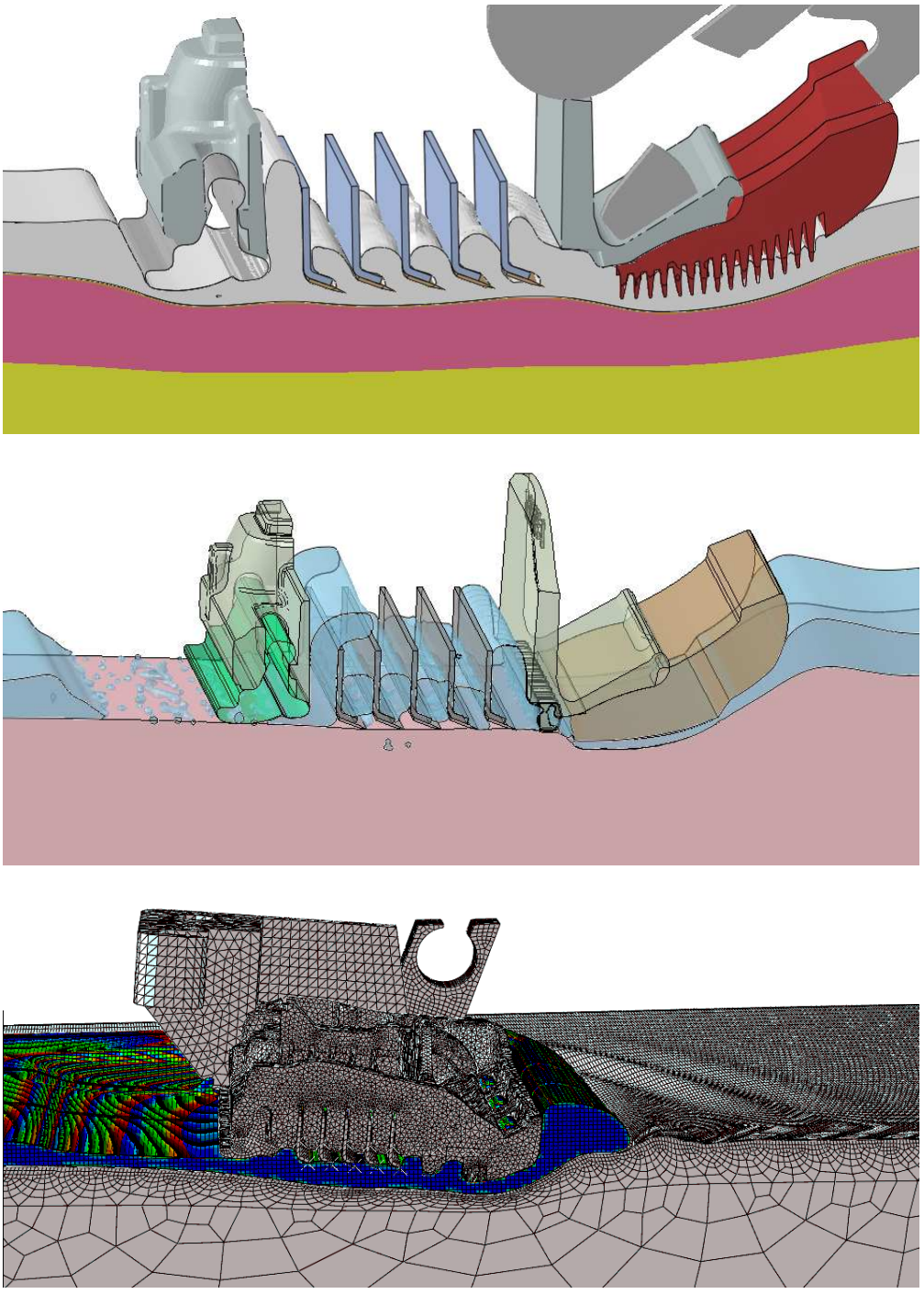

Figure 5.35: Other applications of the **multi-physics modelling framework**. **Proprietary data (P&G). Do not disclose.**

5.7 Limitations and further work

The **multi-physics modelling framework** was built on an existing model of facial skin, developed and validated by O'Callaghan and Cowley (2010), being a crucial step the implementation of the shave prep model. In every step of the development of the shave prep model for its implementation in the modelling framework, a several analyses were performed to verify that the viscous behaviour of shave preps was appropriately captured. However, due to the complexity of the fluid-solid contact interactions, the model could not be appropriately validated.

In the experimental characterisation of the fluid-structure contact interactions, the adhesive behaviour between PEG solutions (interstitial fluid in a shave prep foam) and cartridge materials (i.e. blades and guard elastomer) was captured. However, limitations in the surface size of the solid materials did not allow the characterisation of their interactions in sliding conditions. Reasonable assumptions were taken in terms of the coefficients of friction used for the implementations of fluid-solid contact interactions in the modelling framework, indicating a high coefficient of friction for the skin-shave prep interaction, and low one for the guard-shave prep one, in both cases accounting for the adhesion effect by specifying 'no-separation' allowed at the contact. However, due to high sensitivity of the fluid-structure interactions simulations to the specified contact interactions conditions, it was not possible to determine the accuracy of the simulations rather than by visual inspection (qualitative assessment).

In order to address this limitation, a combined experimental-computational analysis was proposed for future work, under the framework of a fluid droplet sliding over a slanted surface. This analysis involves the use of larger fluid droplets and larger contacting surfaces samples in the experimental tests, so the droplet is forced to slide on the surface under the action of gravity, as the contacting surface is rotated. Once the sliding of the droplet is captured, an iterative simulation processes could be implemented aiming the tuning of the fluid-surface coefficient of friction to the sliding captured in the experimental test.

5.8 Summary

The development of the **multi-physics modelling framework** has been performed focusing on the characterisation of, first, the individual shaving stroke components, and second, the individual interactions between the three contact pairs. These three components were joined together for the evaluation the effect each interaction has in the whole simulation of a shaving stroke, when acting simultaneously. Once these effects

were understood, a more complex model was assembled in the finite element environment, involving the interaction of skin, cartridge and shave prep, setting the basis of the **multi-physics modelling framework**.

While the skin and cartridge models used in these simulations have been previously validated by P&G, the shave prep model was fully characterised, taking into account the viscous properties measured in the experimental tests, and through verification of its spreading and viscous behaviour. As part of the optimisation process, the sensitivity of the simulation runtimes to the mechanical properties defining the fluid showed that the longitudinal wave propagation velocity (sound speed) is the parameter that most influences the runtime performance. The sensitivity of the runtimes performance is also affected by the characteristics of the fluid mesh and the level of parallelisation. The performed analysis showed that, excluding the obvious influence of the mesh size (which dimensions depend directly on the simulated problem), an area of best performance was reached, for pure fluid problems, when the simulations were run with between 50-100 elements per parallel processor. The analysis also showed that the performance of the simulations was independent of the fluid-void ratio contained in the Eulerian space, for which the appropriate setting of the Eulerian domain contributes to higher performance.

Two-component interaction models were developed for the individual analysis of each contact pair involved during a shaving stroke. While the coefficient of friction between the skin and the cartridge ha a direct influence on the skin deformation —which was also transmitted to the shave prep on the skin surface—, the shave prep was subjected two different conditions when in contact with the skin or the razor cartridge: adhesion and shearing conditions. In the characterisation of adhesion, low or no shear stresses were imposed on the fluid, meaning that the viscosity of the shear-thinning fluids remains unchanged. However, under shearing conditions, the viscosity of shave preps was altered, having an effect on its final deformation. It was shown that when shear was imposed on the Eulerian boundaries, the simulation captured the fluid behaviour with a coarse mesh. However, when shear was driven by the interaction with a solid surface, a finer mesh was required for appropriate capture of the fluid response.

The fluid-solid contact interactions were defined by a coefficient of friction and allowing or not separation of the fluid from the surface. It was found that these properties do not produce the same adhesion behaviour in different fluids; although no relation between the observed slip and mechanical properties of the fluid was found. Therefore, for the appropriate implementation of the contact interactions an iterative process relating the sliding behaviour with experimental response is required for each fluid-solid contact pair.

In order to characterise the skin-solid-fluid interaction, where the fluid was sheared and deformed by the action of the solid parts, a first model has been developed focusing on the deformation of the free surface fluid only and then including the skin deformation and geometrical features characteristics of the razor cartridge (**Section 5.4.1**). In this model, the influence of the interaction properties between the fluid and the skin and guard were simultaneously assessed, noticing the large influence in the overall deformation of the shave prep.

The three contact interactions were joined together in a model simulating a shaving stroke at a small scale, for the evaluation of their simultaneous effects to the fluid deformation on the skin surface. It was shown that the 'no-separation' condition was essential to capture the spreading of shave prep on the skin surface, while the skin deformation, caused by the skin-cartridge interaction, contributed along with the coefficient of friction between the cartridge and shave prep, to the shape of the shave prep ploughing ahead the guard.

In this model, the performance of the simulation was limited by the required mesh quality and mechanical properties of the modelled fluid. However, it was shown that further improvement in the runtime performance can be achieved by reducing the longitudinal wave propagation velocity (sound speed) of the fluid, providing improvement of the fluid deformation behaviour and no effects on its viscous response. With this alteration, the fluid contact interaction response is affected, but this effect can be counteracted by modifying the coefficient of friction between the fluid and the surface.

The models and analyses described above led to the construction of the **multi-physics modelling framework**, in which the shave prep, skin and cartridge parts can be replaced for the analysis of specific shaving conditions and lubrication performance of prototype cartridge designs. Its development required sound experimental techniques, and a mindful step by step modelling approach. This modelling framework goes beyond the state-of-the-art, providing a modular interface for the study of multi-physics fluid-structure interactions.

This framework has been already implemented for different applications and projects within P&G. In these simulations, the models were able to capture formation of the lubrication film under the cartridge. With the aim of providing a skin model able to capture the multi-physics interactions at a blade tip scale, the human skin topography features have been characterised in a 2D image based model of the skin as a complement for this project. The development of this model and how it can be related to the multi-physics interactions of wet shaving is described in the following chapters.

Chapter 6

Micromechanical modelling of skin mechanics I - mechanistic insight into the material and structural role of the *stratum corneum* on skin mechanics

This chapter presents an adaptation to the thesis format of the work co-authored with Anton Page, Neil W. Bressloff and Georges Limbert, published in the *Journal of the Mechanical Behavior of Biomedical Materials*, doi:10.1016/j.jmbbm.2015.05.010. See (Leyva-Mendivil et al., 2015).

The study of skin biophysics has largely been driven by consumer goods, biomedical and cosmetic industries which aim to design products that efficiently interact with the skin and/or modify its biophysical properties for health or cosmetic benefits. Up to now, no computational models of the skin have simultaneously accounted for the geometrical and material characteristics of the skin microstructure to study its complex biomechanical interactions under particular macroscopic deformation modes.

The goal of this study was, therefore, to develop a robust methodology combining histological sections of human skin, image-processing and finite element techniques to address fundamental questions about skin mechanics and, more particularly, about how macroscopic strains are transmitted and modulated through the epidermis and dermis.

A sample of fresh human mid-back skin was processed for wax histology. Sections were stained and photographed by optical microscopy. The multiple images were stitched together to produce a larger region of interest and segmented to extract the geometry of the

stratum corneum, *viable epidermis and dermis. From the segmented structures a 2D finite element mesh of the skin composite model was created and geometrically non-linear plane-strain finite element analyses were conducted to study the sensitivity of the model to variations in mechanical properties.*

The hybrid experimental-computational methodology has offered valuable insights into the simulated mechanics of the skin, and that of the stratum corneum *in particular, by providing qualitative and quantitative information on strain magnitude and distribution.*

Through a complex non-linear interplay, the geometry and mechanical characteristics of the skin layers (and their relative balance), play a critical role in conditioning the skin mechanical response to macroscopic in-plane compression and extension. Topographical features of the skin surface such as furrows were shown to act as an efficient means to deflect, convert and redistribute strain —and so stress—within the stratum corneum, *viable epidermis and dermis. Strain reduction and amplification phenomena were also observed and quantified.*

Despite the small thickness of the stratum corneum, *its Young's modulus has a significant effect not only on the strain magnitude and directions within the* stratum corneum *layer but also on those of the underlying layers. This effect is reflected in the deformed shape of the skin surface in simulated compression and extension and is intrinsically linked to the rather complex geometrical characteristics of each skin layer. Moreover, if the Young's modulus of the viable epidermis is assumed to be reduced by a factor 12, the area of skin folding is likely to increase under skin compression. These results should be considered in the light of published computational models of the skin which, up to now, have ignored these characteristics.*

6.1 Introduction

In the last few decades, the study of skin biophysics has largely been driven by pharmaceutic, cosmetic and consumer goods industries which aim to offer solutions to reduce the effects of intrinsic and extrinsic ageing factors on skin health and appearance (e.g. using topical agents) and to design products that efficiently interact with the skin (e.g. razors). The surface of the human skin is characterised by ridged features, or skin furrows (*sulci cutis*), varying in length between 70 and 200μm for the main furrows and 20 and 70μm for the superficial furrows (Piérard et al., 2003; Shimizu, 2007). These furrows, which represent the natural microrelief of the skin, along with natural or muscle-induced wrinkles, are thought to deflect tensional forces thus providing

mechanical advantages to the skin (Pedersen and Jemec, 2006). As skin deforms under macroscopic loads it is unclear whether the *stratum corneum* experiences significant local strains (change of length) or simply unfolds/folds during skin extension/-compression as suggested by Geerligs (2010). Providing a mechanistic quantitative insight into this question constitutes the main objective of the present study for which an image-based anatomical modelling approach is developed. Understanding the role of the skin microstructure on its response to deformations has the potential to shed light on fundamental questions such as evolutionary aspects concerning the advantages provided by certain skin characteristics or functional abilities. For example, it was recently demonstrated that water-induced finger wrinkles in humans improved the handling of submerged objects (Kareklas et al., 2013), therefore confirming a possible evolutionary mechanical advantage for manipulating objects in submerged conditions (Changizi et al., 2011). An in-depth understanding of the structure-function relationship of the skin also presents many opportunities for practical applications in the aforementioned industrial sectors besides the obvious applications in biomedical and health sciences where the coupling between mechanics and biology (i.e. mechanobiology) is particularly relevant (Brand, 2006).

The anatomy and physiology of the skin has been previously discussed in **Chapter 2**, describing the complex structure of the different skin layers. Within the epidermis, the *stratum corneum* provides the prime line of defence against environmental threats. However, as described in **Section 2.3**, it is highly sensitive to environmental conditions. Such sensitivity of the mechanical characteristics of the *stratum corneum* to environmental conditions, particularly relative humidity, is well established by Levi and Dauskardt (2010); Levi et al. (2010b, 2011); Pailler-Mattei et al. (2007); Wu et al. (2002, 2006b) and references therein. This phenomenon results in significant intra-sample variability of its mechanical properties. Typically, the Young's modulus of the *stratum corneum* decreases with relative humidity because of the water-induced plasticisation effect affecting its "brick and mortar" structure. Moreover, differences in experimental measurement techniques, testing conditions, inter-and intra-subject variability are translated into a wide range of mechanical properties found in the literature (**Table 6.1**) and this variability must be considered in models if one wants to obtain more universal results. In a finite element modelling context, it implies that using a single set of mechanical properties for the *stratum corneum* would limit the domain of validity of the simulation results to specific conditions.

A wide array of experimental and clinical measurement techniques are used to characterise particular aspects of skin biology and biophysics (Alexiades-Armenakas, 2012; Batisse et al., 2002; Bellemère et al., 2009; Delalleau et al., 2006; Diridollou et al., 2000; Gunner et al., 1979; Hendriks et al., 2006; Jor et al., 2013; Limbert and Simms, 2013; Tonge et al., 2013a,b; Wan Abas and Barbenel, 1982). Nevertheless, complementary approaches based on mathematical and computational modelling techniques

Table 6.1: Linear elastic and corresponding neo-Hookean constitutive parameters for skin layers obtained trough experimental tests or used in finite element (FE) models (SC - *stratum corneum*, VE - viable epidermis, D - dermis). Parameter values which were not in the original paper reference and that were derived for our study (e.g. calculation of neo-Hookean parameters from Young's modulus and Poisson's ratio and vice-versa, see **Equation 6.2**) are indicated in bold characters. The parameter D_1 is related to the bulk modulus κ_0 as $D_1 = 2/\kappa_0$.

Layer	Linear elastic		Neo-Hookean		Test	Ref
	E [MPa]	υ	C_{10} [MPa]	D_1 [MPa^{-1}]		
SC	0.6	0.3†	0.115	4	Human skin, *ex vivo* indentation	1
	1.2	0.3†	0.231	2	Human skin, *ex vivo* indentation	1
	6	0.5	1.003	0.01	FE model	2
	8.87	0.3†	1.706	0.271	Murine skin, tensile test	3$^{\ddagger a}$
	10	0.3	1.923	0.24	FE model	4$^{\ddagger h}$
	12	0.5	2.007	0.005	FE model	5§
	13.5	0.3†	2.596	0.178	Human skin, *ex vivo* out of plane test	6
	13	0.3†	2.5	0.185	Human skin, *in vivo*	3$^{\ddagger b}$
	57.8	0.3†	11.115	0.042	Human skin, *in vivo* sonic propagation	3$^{\ddagger c}$
	100	0.3†	19.231	0.024	Human skin, *in vivo* indentation	3$^{\ddagger d}$
	175.3	0.3†	33.712	0.014	Human skin, in-plane tensile test	6
	240	0.48	40.535	1010	Porcine skin, rheological test	7$^{\ddagger e}$
	1000	0.3†	192.308	0.002	Human skin, *in vivo* indentation	3$^{\ddagger d}$
VE	0	0.3†	0	4195.804	Human skin, *in vivo* suction test	8
	0.05	0.3	0.01	48	FE model	4 $^{\ddagger h}$
	0.05	0.5	0.008	1.2	FE model	5
	0.05	0.5	0.008	1.2	FE model	5§
	0.6	0.3†	0.115	4	Human skin, *ex vivo* indentation	1
	7.8	0.3†	1.5	0.308	Human skin, *in vivo* indentation	3$^{\ddagger f}$
DE	0.01	0.3†	0.001	480	Human skin, *in vivo* indentation	3$^{\ddagger g}$
	0.6	0.3	0.115	4	FE model	4$^{\ddagger h}$
	0.6	0.5	0.1	0.1	FE model	5
	0.83	0.3†	0.16	2.885	Human skin, suction test	8
	1	0.5	0.167	0.06	FE model	5§
	1.61	0.3†	0.31	1.489	Human skin, *in vivo* indentation	3$^{\ddagger f}$

§ Values for aged skin. † Estimated value.

References:
1-Geerligs et al. (2011a)
2-Magnenat-Thalmann et al. (2002)
3-Delalleau (2007)
4-Lévêque and Audoly (2013)
5-Magnenat-Thalmann et al. (2002)
6-Wu et al. (2006b)
7-Flynn and McCormack (2009)
8-Hendriks et al. (2006)

‡ **Originally published by:**
a -Papir et al. (1975)
b -Pannisset et al. (1994)
c -Dahlgren (1984)
d -Pailler-Mattéi and Zahouani (2004)
e -Park (1972)
f -Tran et al. (2005)
g -Lanir et al. (1990)
h -Serup et al. (1995)

offer promising avenues to further our understanding of the skin (Areias et al., 2003; Bischoff et al., 2000; Boissieux et al., 2000; Buganza Tepole et al., 2011; Cavicchi et al., 2009; Duan et al., 2000; Evans, 2009; Flynn and McCormack, 2008a, 2010, 2008b, 2009; Hendriks et al., 2006, 2003; Kuwazuru et al., 2008; Larrabee, 1986; Larrabee and Galt, 1986a,b; Larrabee and Sutton, 1986; Lévêque and Audoly, 2013; Tepole and Kuhl, 2014; Tepole et al., 2014a,b; Zöllner et al., 2013). These methods have the potential to provide a mechanistic insight into the role and interplay of the material and structural properties of the different skin constituents, albeit in simplified idealised conditions. A microstructural outlook on the mechanics of skin can be exploited to design innovative cosmetic and consumer good products. For example, by locally controlling the stiffness of skin layers using targeted nanoparticles one could ultimately modify the skin topography (wrinkles) and therefore its appearance (Limbert, 2014). Moreover, modelling approaches can be used to complement physical and clinical experiments by guiding their design (Hendriks et al., 2006, 2003). Intra-individually, the biological and mechanical characteristics of skin, considered either as a material or a composite structure, are also known to vary with age (Waller and Maibach, 2005, 2006), environmental conditions (Wilhelm, 1991), hormonal changes (Bolognia et al., 1989) and exposure to specific chemical agents (Levi et al., 2010a, 2011; Matts et al., 2006). The experimental characterisation of mechanical strains inside and at the external surface of the *stratum corneum* is a tremendous technical challenge due to its sensitivity to environmental conditions, size, limitations of existing metrology technologies, experimental measurement errors and issues of repeatability. The approach proposed in this chapter is a prime example of where a physics-based modelling study can address simple fundamental questions unavailable by other means. To reach this goal, what is required is basic information about the geometry, mechanical properties and loading/boundary conditions of what is effectively a multi-component structure. Naturally, in the modelling process, and by definition, a number of simplifying assumptions and discretisation errors are introduced. However, even in the absence of experimental validation, mathematical and computational simulation tools are well suited to provide *relative* answers-the so-called 'what if scenarios': how one or several parameters of the system can affect its output response.

The central focus of the present study is to test the hypothesis that, in a 2D modelling context, as skin deforms under macroscopic loads, the local strains experienced by the *stratum corneum* are modulated by the effect of its geometry and material properties. We propose to identify and quantify potential mechanisms by which strains in the *stratum corneum* are reduced or amplified with respect to global macroscopic strains. This aim is achieved through the key objective of assessing the magnitude and distributions of strains induced in the *stratum corneum*, viable epidermis and dermis in a simplified anatomically-based 2D model as a result of simulated in-plane compression and extension of the skin. Particular attention was paid to evaluating the interplay between the mechanical properties of each layer and the relationship between macroscopic

and local strains. The study provided an opportunity to highlight potentially important anatomical structural effects that are missed by idealised multi-layer models of the skin.

In order to capture a wider range of conditions the finite element analyses presented in this study consider extreme values for the mechanical properties of the *stratum corneum*. In the next section, a methodology combining histology, image processing and finite element modelling to analyse the mechanical behaviour of a three-layer model of the skin (*stratum corneum*, viable epidermis and dermis) is described. This approach brings a new level of anatomical fidelity which is a stepping stone in the state-of-the-art modelling of human skin. To indirectly account for the sensitivity of the *stratum corneum* to relative humidity, a series of parametric finite element analyses varying the properties of the *stratum corneum* are conducted. Results of the analyses are presented in the **Section 6.3** and discussed in **Section 6.4**.

6.2 Materials and methods

6.2.1 Skin histology and imaging

A fresh mid-back skin sample was obtained from a 30 years-old healthy white Caucasian female patient following biopsy. The specimen was processed, sliced, stained (haematoxylin and eosin) and stored by the Biomedical Imaging Unit (BIU) at Southampton General Hospital under given consent for its use for research by the patient. The use of images obtained from the histology sections for the development of this model was ethically approved by both the Research Governance Office at the University Hospital Southampton NHS foundation Trust, Research and Development department (ID: RHM MISC0014, December 6th, 2013), and the Ethics and Research Governance at University of Southampton (ID: 6751, October 10th, 2013). A microscope adapted with a Nikon E950 camera (Nikon UK Ltd, Kingston Upon Thames, UK) was used to obtain the images of the histology sections. A series of images (1600 x 1200 pixels, JPG format with maximum quality settings) was taken for each section at automatic aperture and exposure time, ISO-80 speed, no flash, at both 4X and 10X magnifications, including the images of the scale bar which were later used for dimensioning the model. For better resolution of the skin topography, only the 10 X magnification images of each section were manually stitched together in a software environment (GIMP, www.gimp.org) by aligning each image with the next one, ensuring the overlapping parts correctly matched, forming a single PNG image (**Figure 6.1**).

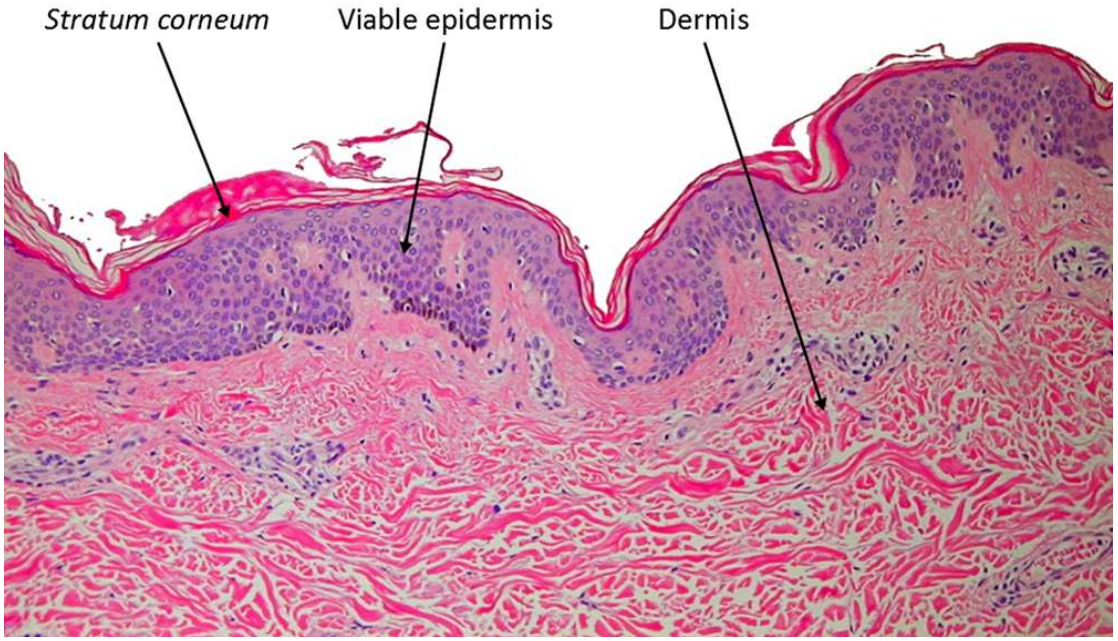

Figure 6.1: Histological section of human middle back skin, haematoxylin and eosin stained, showing several skin furrows. The *stratum corneum* (SC), viable epidermis (VE) and dermis (D) are clearly visible.

6.2.2 Image processing and finite element meshing

The single PNG image of the combined skin histological sections was processed in order to develop a 2D anatomical model of the skin capturing not only the skin topography but also the epidermal-dermal junction and the interface between the viable epidermis and the papillary dermis. The image was processed in the open-source software ImageJ 1.47v (Wayne Rasband, National Institutes of Health, USA) to enhance its contrast and then transferred into the image-processing software application ScanIP^{TM} 6.0 (Simpleware Ltd, Exeter, UK) for segmentation. Image segmentation involved extracting the regions corresponding to the 2D boundaries and inside of each skin layer phase. This process was semi-automatically performed by a human operator using a threshold filtering algorithm which allowed segmentation of regions of interest according to pixel intensity. The clarity and contrast of the photograph was pivotal in distinguishing the different skin structures. In order to limit the model to only three phases, namely the *stratum corneum*, viable epidermis and dermis, threshold filtering was complemented by "manual" painting of the region of interest, therefore ignoring heterogeneities within each phase. A 1.93 mm long section of the skin was selected to build a representative composite model of the skin. Within the same software environment, this section was subsequently meshed into bilinear triangular finite elements. An adaptive mesh refinement algorithm was used to accurately capture the complex geometry of the skin substructures whilst minimising the total number of elements. A mesh sensitivity analysis was performed. The best compromise between accuracy of results and computing time was found for characteristic element lengths ranging from 2

to 150 μm, resulting in a total of 173,929 elements. The adaptive meshing algorithm preserves the topology of surfaces and creates a smooth mesh with low element distortion regardless of the complexity and aspect ratios of the underlying 2D structures (**Figure 6.2**). The overall segmentation and meshing procedure is conceptualised in **Figure 6.3**. The finite element mesh was then exported to the finite element analysis package Abaqus 6.13 (Simulia, Dassault Systèmes, Providence, RI, USA) for preparation of the finite element models described in **Section 6.2.3**.

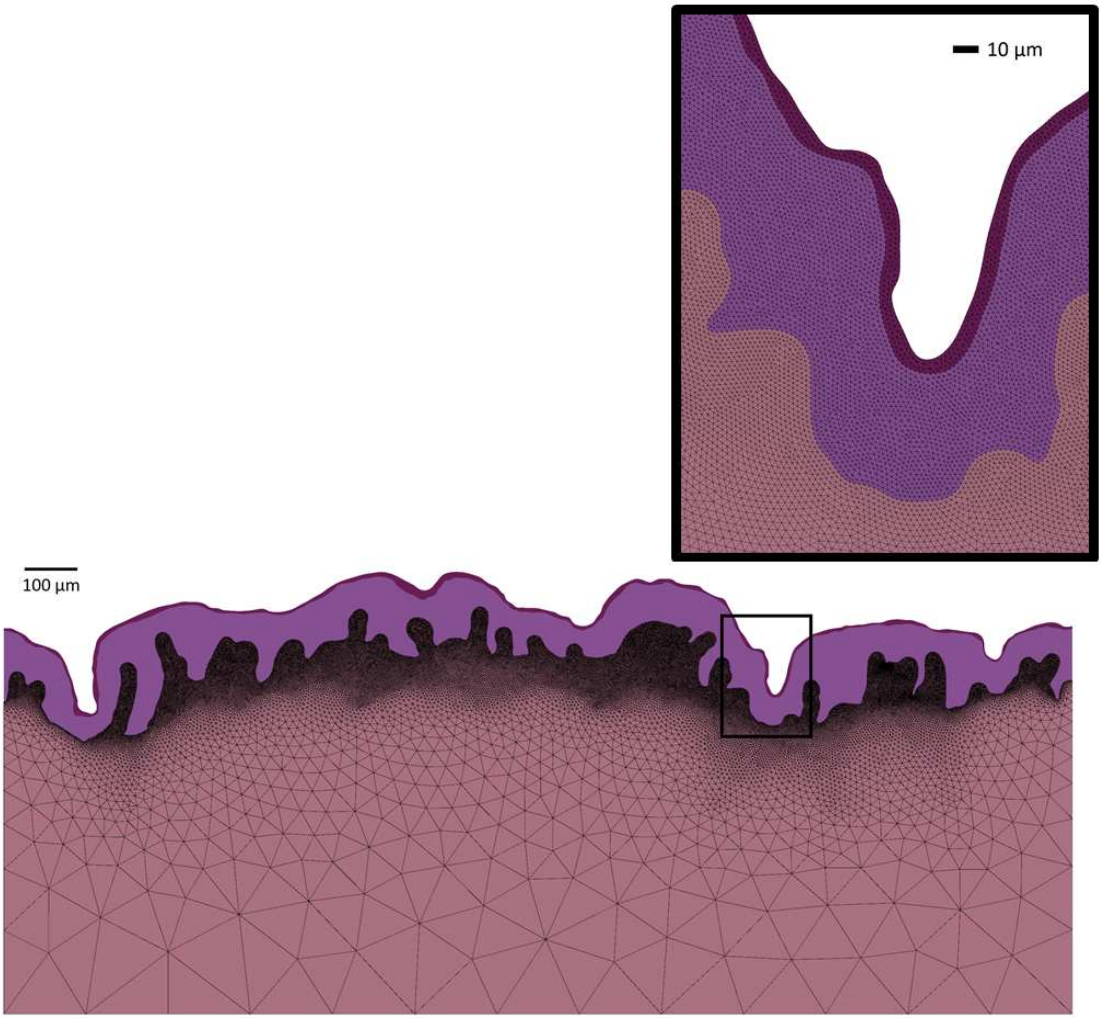

Figure 6.2: Two-dimensional finite element mesh of the skin histological section with zoomed-in view at the top. For sake of clarity, the edges of the finite elements constituting the *stratum corneum* and viable epidermis are not displayed in the bottom picture.

6.2.3 Finite element models and analyses

Preparation of the finite element model comprised definition of the material properties of each sub-structure (that is, the *stratum corneum*, viable epidermis and papillary dermis), assignment of the boundary and loading conditions and specification of potential self-contact interaction for the *stratum corneum* due to surface folding. Perfect

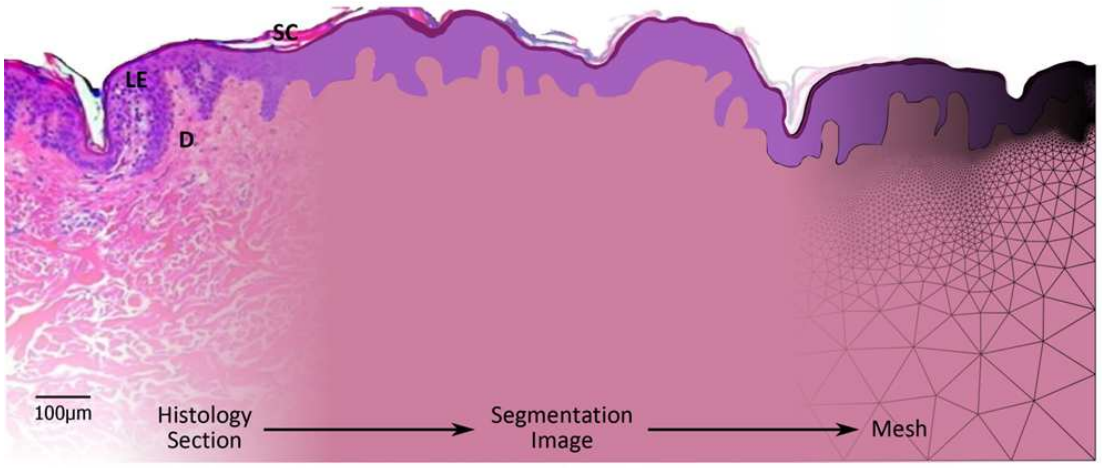

Figure 6.3: Illustration of the image-based finite element model generation process from histology, image segmentation and mesh generation.

bonding was assumed between adjacent layers. Symmetry boundary conditions were enforced at the bottom (horizontal) and left (vertical) edges of the skin model (**Figure 6.4**). Static finite element analysis was conducted wherein no time-dependent effects such as inertia or viscoelasticity were considered. A series of finite element models featuring distinct combinations of mechanical properties of the *stratum corneum* and/or the viable epidermis was devised. The characteristics of these models are presented in the next section. For each finite element model two analyses were considered. In-plane 20% compression and extension of the skin surface was replicated in the finite element model by applying a lateral displacement on the free edge on the vertical right side of the model (**Figure 6.4**). An hybrid plane-strain 3-noded element formulation was used (CPE3H element in Abaqus) to cope with the nearly incompressible behaviour of the materials (when the Poisson's ratio is close to 0.5) which would result in locking of elements (Belytschko et al., 2000).

6.2.4 Mechanical properties of skin

The mechanical properties of the different skin layers have been reported by numerous authors with a wide range of variation depending on body location, hydration, age and testing techniques (**Table 6.1**). In most of these studies, each skin layer or the entire skin-considered as a homogeneous material-is assumed to obey an isotropic Hookean elasticity law. For example, Geerligs et al. (2011a) have determined the Young's modulus of the *stratum corneum* to be 0.6 MPa while Lévêque and Audoly (2013) and Magnenat-Thalmann et al. (2002) have used values of 1-12 MPa for the Young's modulus of the *stratum corneum*, 0.05 MPa for that of the viable epidermis and 0.6 MPa for the modulus of the dermis in mathematical and computational models of skin wrinkles. With increased hydration, the elastic modulus of the *stratum corneum* can vary from about

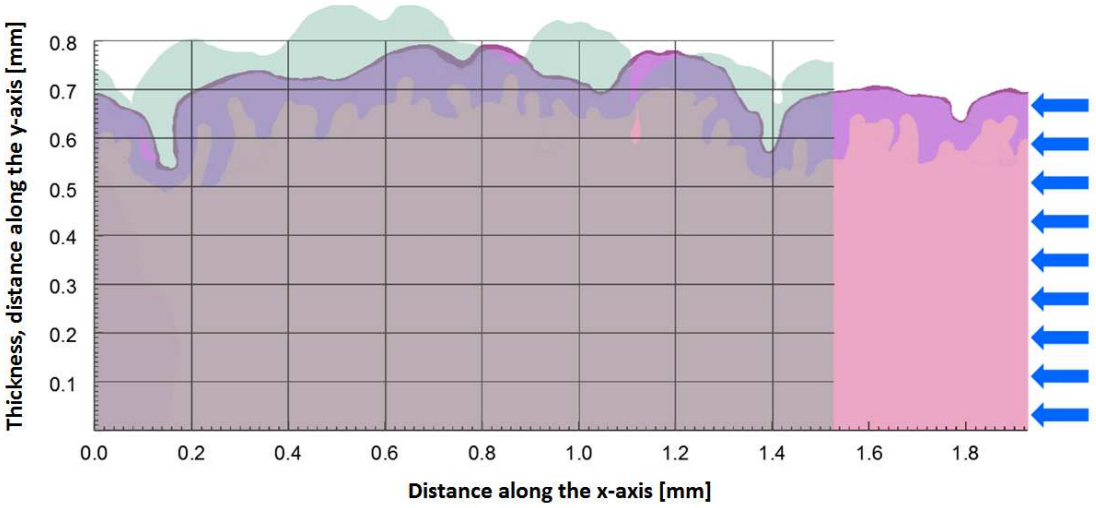

Figure 6.4: Illustration of the macroscopic loading condition of skin for the compression case (indicated by blue arrows). Vertical displacements are fixed at y = 0 and horizontal displacements are fixed at x = 0. The transparent overlay corresponds to the deformed 2D skin structure after 20±1% deformation.

5 MPa to 1000 MPa in the in-plane direction (parallel to the skin surface), and from about 1 MPa to 25 MPa in the out-of-plane direction. Wu et al. (2006b) reported a tensile Young's modulus of 3 MPa at 100% RH to 370 MPa at 30% RH. Although some authors have developed computational models of the skin (Groves et al., 2013; Limbert, 2011; Ní Annaidh et al., 2012a) or the dermis (Flynn and McCormack, 2010, 2009) which account for the anisotropic properties induced by the presence of collagen fibres, this approach is not followed in the current research for two main reasons. The first reason is motivated by the decision to keep the model as simple as possible to facilitate the interpretation of results and to focus on structural rather than material effects. Secondly, the use of a continuum fibre-reinforced hyperelastic model (Holzapfel et al., 2000; Limbert, 2011; Limbert and Taylor, 2002; Weiss et al., 1996) entails the definition of a unit vector field corresponding to the local orientation of collagen fibres. It is possible to extract this information from histological sections by statistical analysis of pixels (Elbischger et al., 2004) but, in the absence of accurate structural information, any deviation from the real collagen bundle orientations might lead to very different results. In the present 2D case, any out-of-plane fibre orientation would not be captured. In order to account for a wider range of conditions, the finite element analyses presented in this study consider extreme values for the mechanical properties of the *stratum corneum* (**Table 6.2**).

One of the key objectives of the present study is to assess strain magnitudes in the skin layers as a result of simulated in-plane compression and extension (apparent macroscopic strain of the whole skin composite structure of up to 20%). It is therefore critical to account for potentially large strains in each of these structures. Hookean elasticity is not appropriate for materials undergoing large deformations and the simplest

Table 6.2: Design of computational experiment. Mechanical properties of the skin layers implemented in the eight cases/finite element models considered in this study.

Analyses		***Stratum corneum***		**Viable epidermis**			**Dermis**	
		E [MPa]	υ	E [MPa]		υ	E [MPa]	υ
				A	**B**			
A1	B1	0.6	0.3	0.6	0.05	0.3	0.6	0.3
A2	B2	370	0.3	0.6	0.05	0.3	0.6	0.3
A3	B3	0.6	0.45	0.6	0.05	0.3	0.6	0.3
A4	B4	370	0.45	0.6	0.05	0.3	0.6	0.3

alternative constitutive law valid for finite deformations is the so-called neo-Hookean elasticity. It is based on the definition of a strain energy function depending on invariants of a deformation tensor which is chosen here as the right Cauchy-Green deformation tensor $\mathbf{C}$ (Ogden, 1984). The neo-Hookean hyperelastic strain energy potential Ψ is defined with the first deviatoric invariant of $\mathbf{C}$, $\bar{I}_1 = J^{-2/3}\,(\mathbf{C} : I_1)$ where $J = \sqrt{\det \mathbf{C}}$ (varying between 0 and 1) provides a measure of material compressibility (see **Section 2.4.2**). When $J = 1$, the material is fully incompressible which implies that no change of volume is allowed and the material can only change its shape by shear deformations.

$$\Psi = C_{10}\left(\bar{I}_1 - 3\right) + \frac{\kappa_0}{2}\,(J-1)^2 \tag{6.1}$$

The constitutive parameters C_{10} and κ_0 correspond, respectively, to half the shear modulus and bulk modulus of an isotropic linear elastic material because linearised neo-Hookean elasticity is equivalent to isotropic linear Hookean elasticity (Ogden, 1984). One can therefore express C_{10} and κ_0 as functions of the initial Young's modulus E and Poisson's ratio υ:

$$C_{10} = \frac{E}{4\,(1+\upsilon)} \qquad \text{and} \qquad \kappa_0 = \frac{E}{4\,(1-2\upsilon)} \tag{6.2}$$

A finite element model considering the skin as a monolayer material (the three layers have the same material properties) was implemented in order to serve as a reference for subsequent comparison purposes, thus highlighting potential structural effects arising only from the surface topography. The effect of varying the *stratum corneum* properties (to simulate property variability or change in relative humidity) was addressed by two cases: **A)** the viable epidermis and dermis have identical mechanical properties; and **B)** the viable epidermis is much softer than the underlying dermis (**Table 6.2**). For each loading case (20% compression and 20% extension), a total of eight finite element analyses were run. For further analyses, the geometry of the skin composite model was virtually split into zones of interest corresponding to particular topographic features (**Figure 6.5**) which will be discussed later in the manuscript (**Section 6.3.4**).

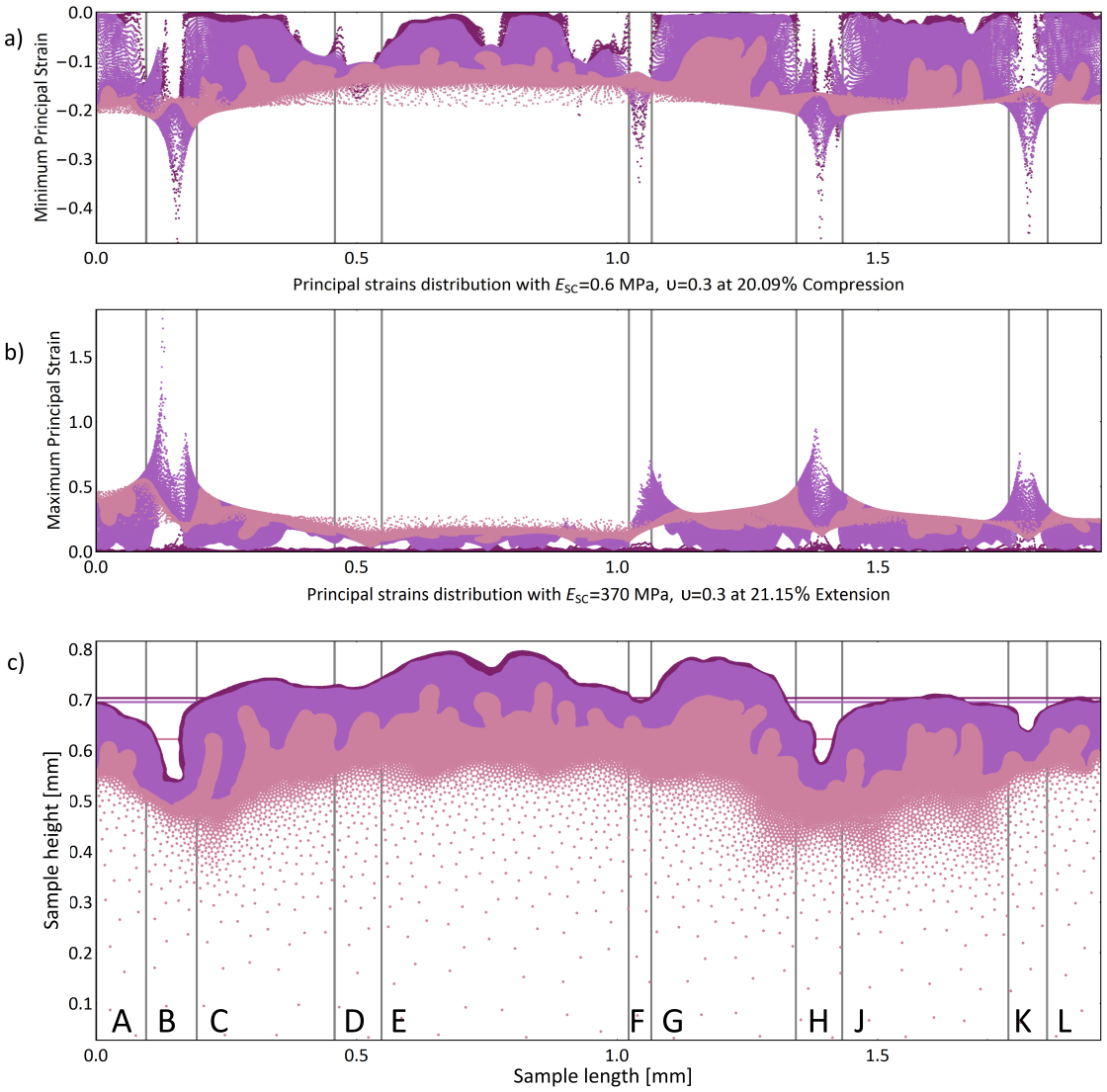

Figure 6.5: Topographic features of the anatomical multi-layer skin model. These region of interest were selected according to their geometrical characteristics and the magnitude of principal strains for case A1 and A2: (a) in **compression** (A1) and (b) in **extension** (A2). These features, which were identified by the letters A-L (omitting letter I), distinguish areas with high strain peaks (skin furrows) from those with small peak strains (crests); (c) plot of the finite elements' centroids in the *stratum corneum* (SC, plum colour), viable epidermis (VE, purple) and dermis (DE, pink). The horizontal lines indicate the mean value of the location of the layer interfaces.

6.3 Results

Colour plots of *minimum* principal strains distributions in the skin composite model are provided in **Figure** 6.6 and **Figure** 6.7, respectively for cases A and B in compression whilst **Figure** 6.8 and **Figure** 6.9 depict the *maximum* principal strains for the *extension* case (also for cases A and B). Complex non-uniform strain distribution patterns are observed for all analyses (compression and extension), thus highlighting the importance of the geometrical characteristics of each skin layer in combination with their

respective mechanical properties. It is worthy to highlight that for the four cases A1-A4, the mechanical properties of the viable epidermis and dermis remained identical ($E_{VE} = E_D = 0.6$ MPa, $\upsilon_{VE} = \upsilon_D = 0.3$), only the mechanical properties of the *stratum corneum* were varied. For the four cases B1-B4, the Young's modulus of the viable epidermis was changed from 0.6 to 0.05 MPa and the mechanical properties of the *stratum corneum* were varied in the same way as they were for cases A1-A4.

6.3.1 Effects of mechanical properties on skin surface topography

For a fixed Poisson's ratio of the *stratum corneum*, the surface topography of the skin is clearly affected by change in stiffness of this layer. In compression, it has the effect of reducing the self-contact area of the *stratum corneum* as two cavities resulting from the closure of the deep furrows can be observed in **Figure 6.6** and **Figure 6.7** (these deep furrows correspond to zones B and H depicted on **Figure 6.5**). Compared to cases A1-A4, an increase in the folding-induced contact area is observed by reducing the Young's modulus of the viable epidermis (case B, shown in **Figure 6.7**). In extension, the effects are particularly visible on the deformed deep furrows which take a sharper angular shape when the highest Young's modulus is considered (**Figure 6.8** and **Figure 6.9**). The outer geometry of the skin gets softer by reducing the Young's modulus of the viable epidermis (case B, shown in **Figure 6.9**), provided the *stratum corneum* has its lowest stiffness ($E_{SC} = 0.6$ MPa). Varying the Poisson's ratio of the *stratum corneum* for a given Young's modulus does not have a major effect on the geometry of the deformed skin model in neither cases A and B.

6.3.2 Strain distribution and magnitude in the skin layers for the compression case

For a given Poisson's ratio, increasing the elastic modulus of the *stratum corneum* induces a significant redistribution of principal strains in the underlying layers: larger compressive strains are observed under compression in the viable epidermis and dermis (**Figure 6.6** and **Figure 6.7**). The effect is less apparent in the dermis when the Young's modulus of the living epidermis is about an order of magnitude smaller than that of the *stratum corneum* (cases B1-B4, **Figure 6.7**). However, for these cases, and as expected, the tensile strains in the viable epidermis are an order of magnitude higher. Approximately 30% compressive strains are produced in the viable epidermis zones interdigitating with the papillae of the papillary dermis, mainly in areas surrounding and beneath skin furrows. For cases A (**Figure 6.6**), the area of high compressive strains extends laterally while for case B (**Figure 6.7**), high compressive strains are produced in the viable epidermis with further concentrations in the dermis beneath deep furrows. The difference observed between high strain levels at the bottom of furrows and

low strain levels at the top of the surrounding crests reveals a potentially interesting strain deflection mechanism that could occur as a result of stiffening of the *stratum corneum* (e.g. drying stress, (Levi and Dauskardt, 2010; Levi et al., 2010b)).

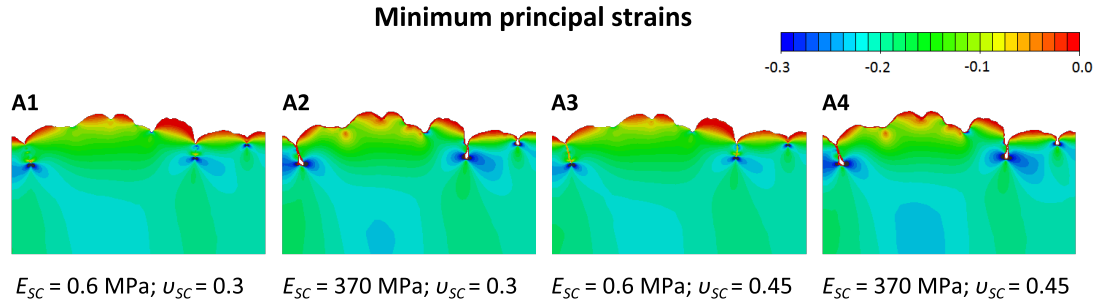

Figure 6.6: Colour plot of minimum principal strains in the skin for analysis cases A1, A2, A3 and A4 ($E_{LE} = E_D = 0.6$ MPa and $\upsilon_{LE} = \upsilon_v = 0.3$) under simulated **compression**.

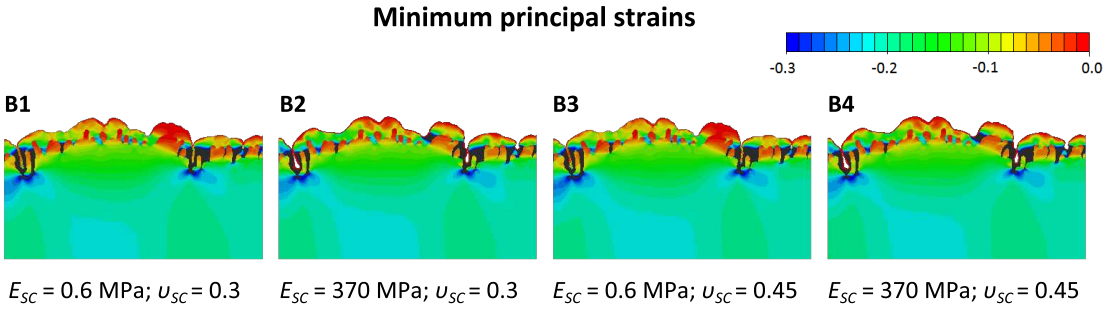

Figure 6.7: Colour plot of maximum principal strains in the skin for analysis cases B1, B2, B3 and B4 ($E_{LE} = 0.05$ MPa,$E_D = 0.6$ and $\upsilon_{LE} = \upsilon_v = 0.3$) under simulated **compression**.

6.3.3 Strain distribution and magnitude in the skin layers for the extension case

Increasing the Young's modulus of the *stratum corneum* from 0.6 to 370 MPa has the effect of significantly altering the distribution of tensile strains in the skin in the vicinity of furrows. Higher strain levels are observed in the viable epidermis, but the effect is less apparent in the dermis when the Young's modulus of the viable epidermis is about an order of magnitude smaller than that of the *stratum corneum* (case B, **Figure 6.9**), showing no significant effect in the rather homogeneous tensile strain distribution and magnitude in the dermis. In contrast, tensile strains above 50% are produced in the viable epidermis zones interdigitating with the papillae of the papillary dermis. Altering the Poisson's ratio of the *stratum corneum* has a minimal effect on the strain distribution and magnitude in the viable epidermis and dermis (compare cases B1/B3 and B2/B4, **Figure 6.9**).

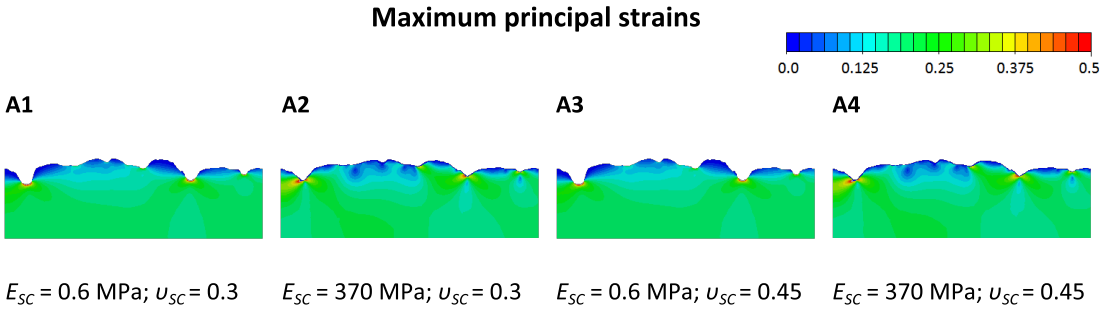

Figure 6.8: Colour plot of maximum principal strains in the skin for analysis cases A1, A2, A3 and A4 ($E_{LE} = E_D = 0.6$ MPa and $\upsilon_{LE} = \upsilon_v - 0.3$) under simulated **extension**.

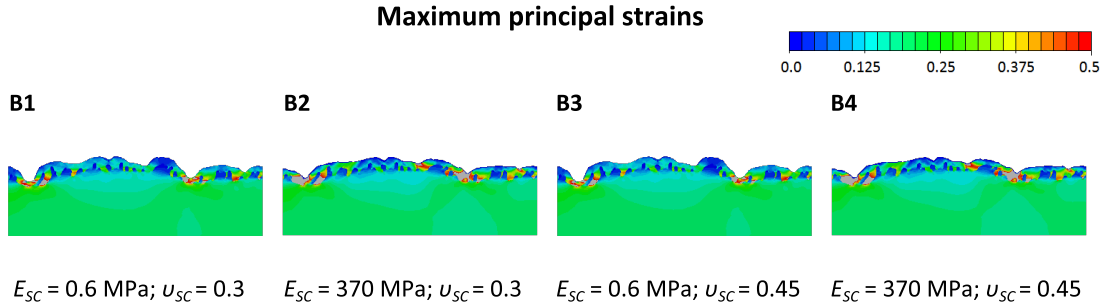

Figure 6.9: Colour plot of maximum principal strains in the skin for analysis cases B1, B2, B3 and B4 ($E_{LE} = 0.05$ MPa,$E_D = 0.6$ and $\upsilon_{LE} = \upsilon_v - 0.3$) under simulated **extension**.

6.3.4 Quantitative analysis of strains in the *stratum corneum*

The distribution of strain within the composite model of skin is intrinsically conditioned by the specific geometry of each layer of the skin sample used in this study as well as their respective mechanical properties. In order to make the analysis of results more universal, the geometry of the skin composite model was virtually split into zones of interest corresponding to characteristic surface topographic features which can be found on any human skin sample (**Figure 6.5**-c). These zones were selected based on geometrical features (**Figure 6.5**-c) but also according to trends in the distribution of principal strains in the three layers along the skin sample (**Figure 6.5**-a-b). The crests and furrows were identified with the labels A-L, omitting intentionally the letter I to prevent any typographic confusion. **Crests** are labelled as A, C, E, G, J and L. The dimensions of the skin furrows were measured using the image processing software application ImageJ (U. S. National Institutes of Health, Bethesda, Maryland, USA) by measuring the distance between the deepest point in the furrow and the midpoint located between the furrow boundaries (**Figure 6.10**). Furrows were classified according to their depth as **deep** (B, H), **superficial** (F, K) and **wide furrows** (D) (Piérard et al., 2003; Shimizu, 2007).

The median values of the principal strains of the finite elements (evaluated at their centroid) **contained in each of the topographic regions of the *stratum corneum***

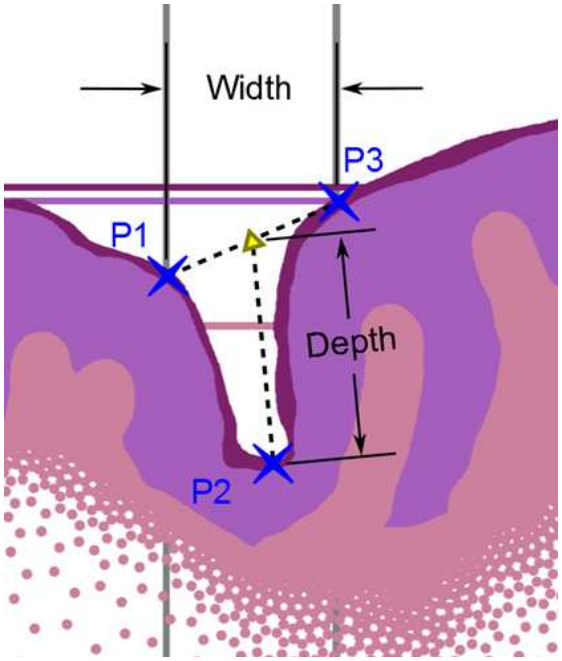

Figure 6.10: Schematic illustrating the characteristic dimensions of a skin furrow (depth and width). By selecting three points defining the location of the furrow edges (P1, P3) and the deepest point (P2) of the furrow (blue crosses), the width was determined by the horizontal distance between P1 and P3, and the depth as the distance between the midpoint between P1 and P3 and P2.

were extracted from the results of the finite element analyses. These metrics are defined as **local median strain (LMS)**, local because they are specific to each topographical zone (**Figure 6.5**-c). A **global median strain (GMS)** is also defined as the median value of the strains of all of the finite elements of the *stratum corneum* layer. The rationale for defining these measures was to look at how certain topographic features of the skin surface (**Figure 6.5**) might amplify or reduce local strains in the *stratum corneum* in response to macroscopic deformations such as those applied during in-plane extension/compression of the skin. GMS values are explored in **Figure 6.11**-**Figure 6.14** while **Figure 6.16**-**Figure 6.19** report LMS values.

Figure 6.11 and **Figure 6.12** show the **median minimum principal strains** for cases A and B, respectively, **in compression**. Likewise, **Figure 6.13** and **Figure 6.14** report the median values for the **maximum principal strains** in **extension**. For a fixed Poisson's ratio, increasing the Young's modulus of the *stratum corneum* from 0.6 to 370 MPa (this is an increase by approximately a factor of 617) reduces strain levels in the *stratum corneum* by about one order of magnitude. This suggests that non-linear effects are at play here and the geometrical characteristics of the topographic features may play a significant role on strain distribution. While most of the crests show similar strain levels, the distribution of median strains in the skin furrows is not uniform. Furthermore, the level of strain across the topographic features is also affected by the stiffness of the *stratum corneum*: when the Young's modulus of the *stratum corneum* is minimal a broader strain range is observed.

6.3.5 Global and local strains in the *stratum corneum* for the compression case

Under **compression**, for case A, compressive strains (minimum principal strains) of maximum magnitude are observed in the superficial furrow zone F. The maximum magnitude is 19.18% (9.85% GMS) for case A1 ($E_{SC} = E_D 0.6$ MPa, $\upsilon_{SC} = 0.3$) (**Figure 6.11**-a). For a stiffer *stratum corneum* (**Figure 6.11**-b), the LMS level in zone F peaks at about 1%. Similar strain levels can be observed in furrow zones B, D and H for a soft *stratum corneum* (cases A1 and A3), but for a stiffer *stratum corneum* intermediate values between the GMS and furrow F LMS are observed in furrow zones D, H and K. Lower magnitude of LMS levels are observed in crest features for all cases (A1, A2, A3 and A4) (**Figure 6.11**). Under **compression**, variation of the Poisson's ratio of the *stratum corneum* has a small effect on the overall median strains. However, its effect is not evenly distributed along the topographic features (zones A to L). It was found that in **all crests** the strain magnitude is higher when the Poisson's ratio is maximum ($\upsilon = 0.45$). For the **deep furrows zones** (B and H), the effect is reversed (the strain magnitude is lower for maximum Poisson's ratio). For **smaller furrows**, their behaviour is dependent on the *stratum corneum*'s stiffness. An inversely proportional strain-Poisson's ratio relationship for superficial furrows (F and K) and a proportional one for the shallow furrow (D) are observed for a low stiffness *stratum corneum* (**Figure 6.11**-a) while this behaviour is reversed in the case of a stiffer *stratum corneum* (**Figure 6.11**-b). For case B, where the viable epidermis is the softest (E_{VE} = 0.05 MPa), compressive strains are maximum in the deep furrow zone H, with a LMS=-6.3% for the soft *stratum corneum* (2.46% GMS) (**Figure 6.12**-a) and -0.55% for the stiffer one (2.72% GMS) (**Figure 6.12**-b). Similarly to case A (**Figure 6.12**-b), higher levels of strain are observed in the crests when the Poisson's ratio of the *stratum corneum* is increased from 0.3 to 0.45. For the furrows, it is observed that for the case of a soft *stratum corneum*, most of the furrows (with the exception of superficial furrow K) show a reduction in LMS as the *stratum corneum*'s Poisson's ratio increases, while for a stiffer *stratum corneum*, LMS increase with Poisson's ratio. For the stiffest *stratum corneum* (**Figure 6.11**-b, **Figure 6.12**-b), the overall strain levels (GMS and LMS, defined across skin layers) measured in cases B are lower than those obtained for cases A. This would suggest that that the structural and mechanical effects of a soft viable epidermis ($E_{VE} = 0.05$ MPa) are a reduction in the strain levels across skin layers.

6.3.6 Global and local strains in the *stratum corneum* for the extension case

In simulated extension, for case A, maximum tensile strains (maximum principal strains) are observed for the soft *stratum corneum* (cases A1 and A3) in the superficial furrow zone F with LMS of 36% (9.6% GMS) and the shallow furrow zone D with LMS of

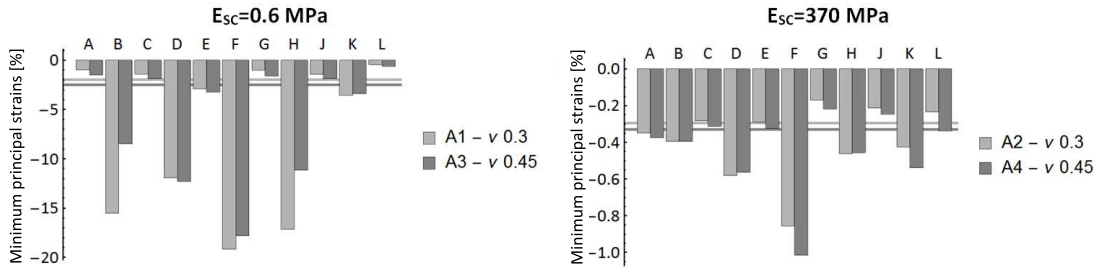

Figure 6.11: Bar chart representing local median minimum principal strain (LMS) values in the *stratum corneum* at each characteristic skin topographic zone (A, B, C, D, E, F, G, H, J, K and L, **Figure 6.5**) for cases A1, A2, A3 and A4 (in **compression**). The horizontal lines correspond to the global median principal strain values (GMS) of the whole *stratum corneum* (GMS).

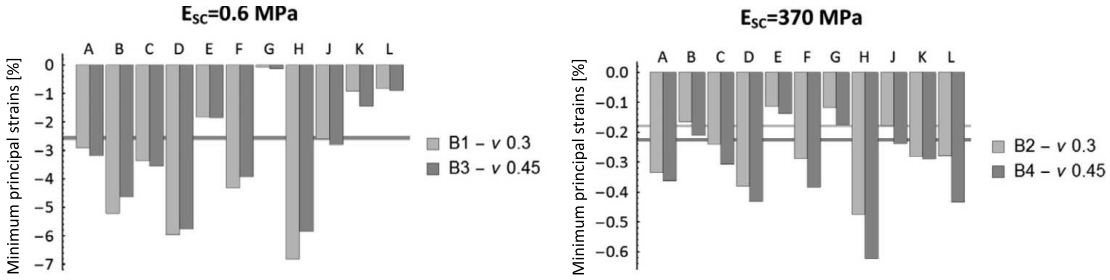

Figure 6.12: Bar chart representing local median minimum principal strain (LMS) values in the *stratum corneum* at each characteristic skin topographic zone (A, B, C, D, E, F, G, H, J, K and L, **Figure 6.5**) for cases B1, B2, B3 and B4 (in **compression**). The horizontal lines correspond to the global median principal strain values (GMS) of the whole *stratum corneum* (GMS).

17.8% (4.75% GMS). Theses strain magnitudes are significantly higher than in the other zones (**Figure 6.13**-a). Zone G experiences a 0.2% LMS. For a stiffer *stratum corneum*, differences in LMS between anatomical zones are less pronounced (**Figure 6.13**-b). Zone F still experiences maximum strain levels, closely followed by zones K, H and D. Naturally, the GMS values are much smaller (0.76% compared to the soft *stratum corneum* case of 3.76%). For all cases (E_{SC} = 0.6 MPa and E_{SC} = 370 MPa, cases A and B, **Figure 6.13**, **Figure 6.14**), higher tensile LMS is produced in the furrow zone compared to the surrounding crests (e.g. LMS for furrow B is 71% while crest A and C show LMS of 33% and 48%, respectively, **Figure 6.13**-b). For cases B and low stiffness of the *stratum corneum* (cases B1 and B3), furrow zones D, F and H exhibit the highest LMS values (LMS=13.6%; 2.5% GMS) while the lowest LMS are found in zone G (LMS 2.16%; 0.39% GMS) (**Figure 6.14**-a). When the Young's modulus of the *stratum corneum* is increased from 0.6 MPa to 370 MPa, (cases B2 and B4), higher LMS values are found in case B4 at furrow zones F, H and K, with maximum values in zone F with LMS of 1.44% (2.93% GMS) and zones H and K with LMS of 1.01% (2.07% GMS) (**Figure 6.14**-b). If Poisson's ratio of the *stratum corneum* is reduced from 0.45 to 0.3 (case B2), strain levels in zones F are reduced to 1.08% LMS (2.66% GMS) and zones H and K to 0.84% LMS (2.08% GMS). All of the crests show similar values of LMS ranging from 0.36% to 0.53% (0.48 to 1.10% GMS) for case B4 and from 0.26% to 0.46% (0.65 to 1.14% GMS) for case B2. For both cases A and B, variations in the

Poisson's ratio of the *stratum corneum* did not lead to significant differences in the GMS of the whole skin model under extension.

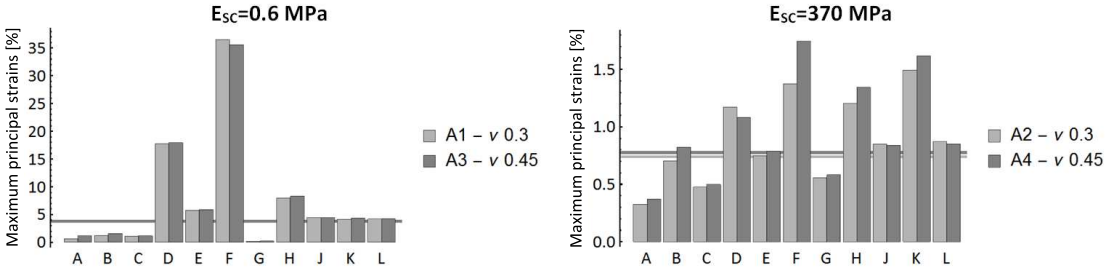

Figure 6.13: Bar chart representing local median maximum principal strain (LMS) values in the *stratum corneum* at each characteristic skin topographic zone (A, B, C, D, E, F, G, H, J, K and L, **Figure 6.5**) for cases A1, A2, A3 and A4 (in **extension**). The horizontal lines correspond to the global median principal strain values (GMS) of the whole *stratum corneum* (GMS).

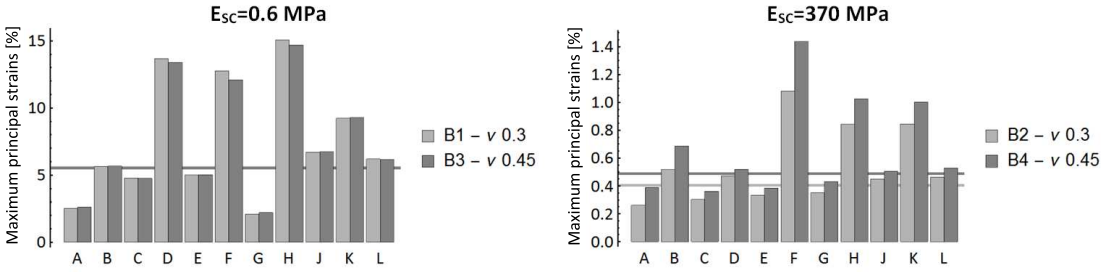

Figure 6.14: Bar chart representing local median maximum principal strain (LMS) values in the *stratum corneum* at each characteristic skin topographic zone (A, B, C, D, E, F, G, H, J, K and L, **Figure 6.5**) for cases B1, B2, B3 and B4 (in extension). The horizontal lines correspond to the global median principal strain values (GMS) of the whole *stratum corneum* (GMS).

6.3.7 Influence of the viable epidermis stiffness on the strain magnitude in the *stratum corneum*

To assess the sensitivity of the principal strains in the *stratum corneum* to the mechanical properties of the viable epidermis at each of the characteristic topographic locations (**Figure 6.5**), box plots of the minimum and maximum principal strains were used for the case of compression (**Figure 6.16** and **Figure 6.17**) and extension (**Figure 6.18** and **Figure 6.19**), respectively, for each value of the Young's modulus of the viable epidermis (case A, $E_{VE} = 0.6$ MPa; case B, $E_{VE} = 0.05$ MPa). For each zone, the principal strains of each finite element of the *stratum corneum* layer were evaluated at the centroid of the element and accounted for in the distribution evaluation. Each particular zone's response is described in terms of the median value (50^{th} percentile of the distribution), the statistical dispersion defined by the interquartile range (IQR) (i.e. range of values between the first (25%) and third quartiles (75%)) and the peak value range (PVR) (range between the minimum and maximum values). Within data sets, data points located in the tail of the distribution curves are classified as near or far outliers according to the following criteria (Wolfram Research, 2014):

$$\begin{aligned} Q_1 + 1.5\,(\text{IQR}) < \text{near outlier} < Q_1 - 1.5\,(\text{IQR}) \\ Q_3 + 3\,(\text{IQR}) < \text{far outlier} < Q_1 - 3\,(\text{IQR}) \end{aligned} \tag{6.3}$$

Here Q_1 and Q_3 are respectively the first (25^{th} percentile) and third (75^{th} percentile) quartiles of the distribution. Although still accounted for in the PVR, the outliers are ignored in the figures for better visualisation. The range bars indicate values of the extreme data points that are not classified as outliers. The deformed geometry of the *stratum corneum* was nearly identical in both cases A (where viable epidermis and dermis feature the same material properties) and B (where the three layers' properties are distinct) when subjected to compressive or extensive deformation (**Figure 6.6**-**Figure 6.9**). However, when considering the strain magnitude in the *stratum corneum* a different picture emerges.

Under skin compression, median values for the minimum principal strains in the *stratum corneum* can reach 19.2% (case A1, **Figure 6.16**) and 6.8% (case B1, **Figure 6.16**) depending on the anatomical locations, showing lower dispersion levels for case B1. Increasing the Young's modulus of the *stratum corneum* from 0.6 to 370 MPa (**Figure 6.17**, cases A2 and B2) has a drastic effect on the median and peak values of the minimum principal strains which are reduced in amplitude and exhibit lower variations across the anatomical zones considered. These median values do not exceed 1%.

For the case of skin extension, there is a wide distribution of maximum principal strain values reaching up to 50% in the interquartile range (**Figure 6.18**, cases A1 and B1) with a very heterogeneous response when considering each anatomical zone. The median values are predominantly lower in case A1, while the amplitude of dispersion is substantially reduced in case B1. For a stiffer *stratum corneum* (E_{SC} = 370 MPa), the maximum principal strain ranges in the *stratum corneum* are significantly reduced (**Figure 6.19**). Median values lie within the 0-1.5% range. Lower median strains and dispersion levels are observed in case B2.

It was found that the principal strain PVR representing the maximum dispersion was correlated to the geometry at the furrow. This was established by conducting a regression analysis (**Figure 6.15**) using a logarithmic form $f\,(d_f) = m_f \cdot \ln\,(d_f) + b$, where $f\,(d_f) =$ PVR and d_f is the furrow depth. **Table 6.3** lists the parameters m_f and b of the regression function corresponding to each of the tests and their respective coefficient of determination, R^2. The coefficients of determination between the simulation results and the values estimated by the logarithmic regression were $R^2 >$ 0.69 for compression and $R^2 >$ 0.81 for extension.

Under macroscopic compressive load the *stratum corneum* exhibits the following mechanical response at the characteristic anatomical locations:

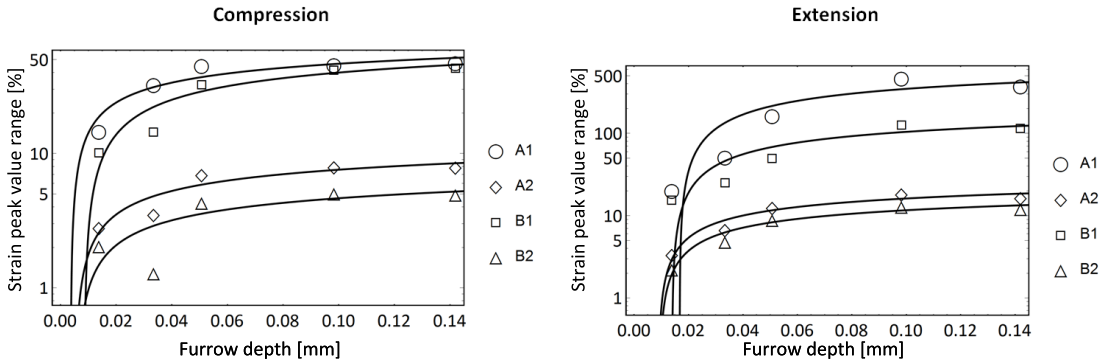

Figure 6.15: Plot representing the regression analysis between furrow depth and the principal strain peak value range (PVR) experienced by the *stratum corneum* layer under compression (left) and extension (right). The continuous lines represent the best fit using a logarithmic regression.

Table 6.3: Fitting function parameters obtained from the logarithmic regression of the furrow depth-strain PVR data. Quality of the correlation is indicated by the coefficient of determination R^2.

Analysis type	**Case**	**m**	**b**	R^2
Compression	A1	14.06	78.94	0.87
	A2	2.52	13.38	0.86
	B1	16.28	77.51	0.91
	B2	1.6	8.33	0.69
Extension	A1	194.19	794.4	0.81
	A2	6.7	31.59	0.91
	B1	53	226.33	0.85
	B2	4.91	22.94	0.93

- **Crests (A, C, E, G, J, L):** The LMS lie in the same respective range for each specific case (A1, A2, B1, B2) with average minimum principal strains from -0.08% to -3.37% when the Young's modulus of the *stratum corneum* is minimal (**Figure 6.16**) and do not exceed -0.35% when it is maximal (**Figure 6.17**). Lower dispersion levels (IQR) are observed in the more protruding crests.

- **Deep furrows (B, H):** The intensity of the LMS is significantly reduced by the presence of a soft viable epidermis and the stiffening of the *stratum corneum*, showing average minimum principal strain of -16.34% and -6.02% for Cases A1 and B1 (**Figure 6.16**), and -0.43% and -0.32% for cases A2 and B2 (**Figure 6.16**). These values are significantly higher in magnitude than the ones observed for the crests. The IQR is similarly affected.

- **Superficial furrows (F, K):** The LMS is -11.37% and -2.62% minimum principal strain in cases A1 and B1, respectively (**Figure 6.16**), while it reduces to -0.64% and -0.28% for cases A2 and B2 (**Figure 6.17**). The dispersion levels are similar to the ones observed for the deep furrows.

- **Wide furrow (D):** LMS values of minimum principal strain lie between those of the crests and deep furrows showing a reduction from -11.94% to -5.97% for a soft *stratum corneum* (**Figure 6.16**), and from -0.58% to -0.38% for a stiff *stratum corneum* (**Figure 6.17**), due to the presence of a soft viable epidermis. The dispersion levels (IQR) in this area are similar to those observed in other furrows.

Higher LMS are observed in the shallower superficial furrow F for case A, shifting to the shallower deep furrow H for case B. The higher IQR dispersion values were found among furrows H and K (next to each other in terms of depth, but classified as deep and superficial, respectively). Correlation between principal strain PVR of all furrows and their respective depth are: for A1, R^2= 0.87; A2, R^2=0.86; B1, R^2=0.91; B2, R^2=0.69), showing higher overall dispersion in the deep furrows (**Table 6.3**).

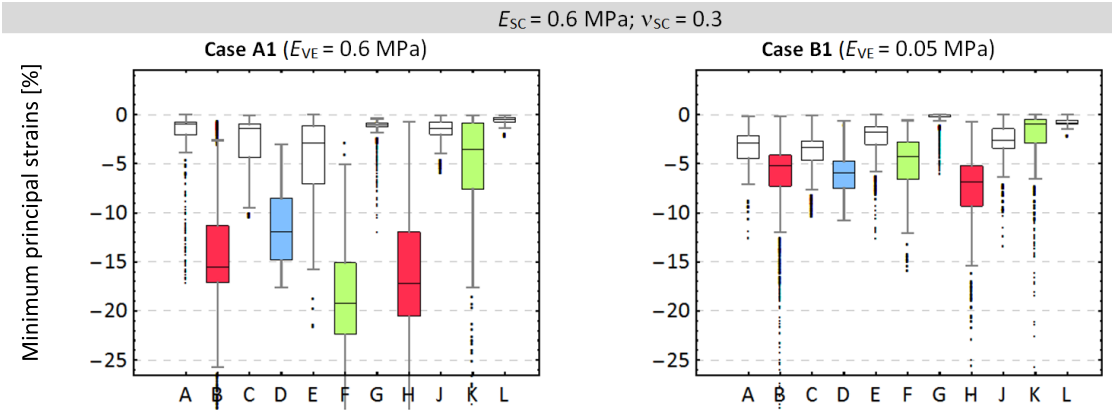

Figure 6.16: Box plot representing the minimum principal strains distributions in the *stratum corneum* across the different topographic features of the skin (zone A to L, **Figure 6.5**) under **compression**. Minimum principal strains are presented for cases A1 (where the viable epidermis and dermis share the same mechanical properties) and B1 (where the viable epidermis is 12 times softer than the dermis).

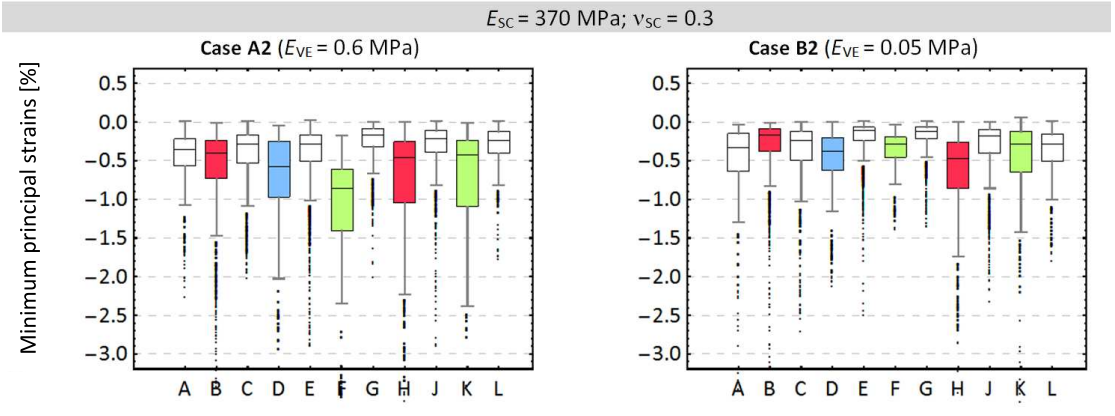

Figure 6.17: Box plot representing the minimum principal strains distributions in the *stratum corneum* across the different topographic features of the skin (zone A to L, **Figure 6.5**) under **compression**. Minimum principal strains are presented for cases A2 (where the viable epidermis and dermis share the same mechanical properties) and B2 (where the viable epidermis is 12 times softer than the dermis).

Under macroscopic tensile load the *stratum corneum* exhibits the following mechanical response:

- **Crests (A, C, E, G, J, L):** The LMS lie in the same respective range for each specific case (A1, A2, B1, B2) with average maximum principal strains varying from 2.73% (case A1) to 4.56% (case B1) when the Young's modulus of the *stratum corneum* is minimal (**Figure 6.18**). When the Young's modulus of the *stratum corneum* is increased from 0.6 to 370 MPa these LMS are within 0.64% and 0.36% (**Figure 6.19**). Low dispersion levels (IQR) are observed in the more protruding crests (e.g. crests G and A had the lowest LMS for soft and stiff *stratum corneum*, respectively).
- **Deep furrows (B, H):** The intensity of the LMS is significantly amplified by the presence of a soft viable epidermis when the *stratum corneum* is soft, but this trend is reversed when the *stratum corneum* is much stiffer (E_{SC} = 370 MPa), showing average maximum principal strain of 4.55% and 10.35% for cases A1 and B1 (**Figure 6.18**), and -0.95% and 0.68% for cases A2 and B2 (**Figure 6.19**). These values are significantly higher in magnitude than the ones observed for the crests. The IQR are reduced by the presence of the soft viable epidermis, having a larger effect (i.e. more reduction) in the furrows showing larger dispersion in case A1. The opposite reaction is observed, at a lower scale, for a stiff *stratum corneum* (cases A2 and B2).
- **Superficial furrows (K):** The LMS is about 20.30% and 10.98% maximum principal strain in respectively cases A1 and B1 (**Figure 6.18**) while it goes down to 1.43% and 0.96% in cases A2 and B2 (**Figure 6.19**). The dispersion levels are similarly affected to the ones observed for the deep furrows, showing larger amplification due to the presence of the soft living epidermis and stiff *stratum corneum*.
- **Wide furrow (D):** LMS values of minimal principal strain lie between those of the crests and deep furrows showing a reduction from 17.71% to 13.67% for a soft *stratum corneum* (**Figure 6.18**), and from 1.16% to 0.47% for a stiff *stratum corneum* (**Figure 6.19**), due to the presence of a soft viable epidermis. Dispersion levels (IQR) observed in furrow D are as low as the ones witnessed in the crests, unlike what is observed in compression.

Higher LMS are observed in the superficial furrows F and K, and in the shallower deep ridge H. The higher IQR dispersion values were found mainly at deep furrow H. Correlation between principal strain PVR of all furrows and their respective depth are: for A1, R^2= 0.81; A2, R^2=0.91; B1, R^2=0.85; B2, R^2=0.91), showing higher overall dispersion in the deep furrows (**Table 6.3**). Generally, **Figure 6.16**-**Figure 6.19** show that, for the **compression** case, the LMS and IQR of principal strain magnitude

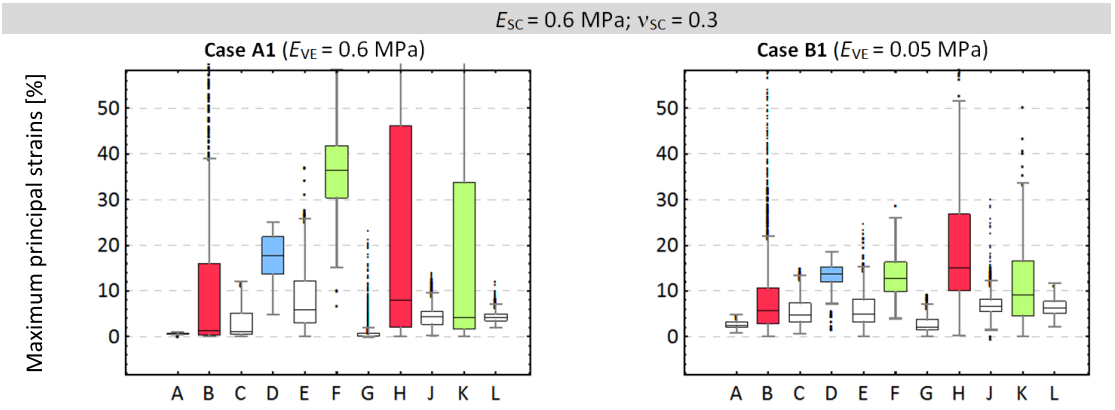

Figure 6.18: Box plot representing the maximum principal strains distributions in the *stratum corneum* across the different topographic features of the skin (zone A to L, **Figure 6.5**) under **extension**. Maximum principal strains are presented for cases A1 (where the viable epidermis and dermis share the same mechanical properties) and B1 (where the viable epidermis is 12 times softer than the dermis).

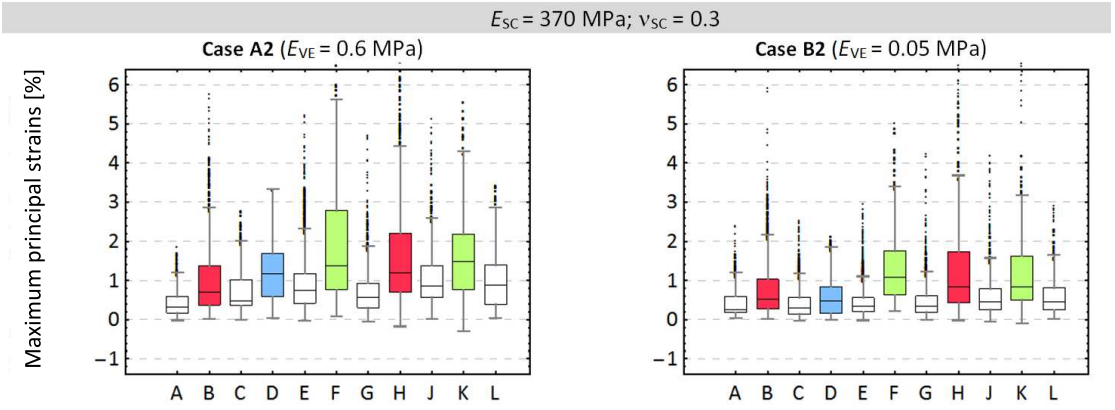

Figure 6.19: Box plot representing the maximum principal strains distributions in the *stratum corneum* across the different topographic features of the skin (zone A to L, **Figure 6.5**) under **compression**. Maximum principal strains are presented for cases A2 (where the viable epidermis and dermis share the same mechanical properties) and B2 (where the viable epidermis is 12 times softer than the dermis).

and directions in the *stratum corneum* can be significantly affected by the value of the Young's modulus chosen for the viable epidermis provided that the Young's modulus of the *stratum corneum* is approximately an order magnitude greater. These effects are more or less pronounced depending on the topographical features of the *stratum corneum* (zones A-L). When considering the **extension** case, significant difference exists between the case of E_{VE} = 0.6 MPa and E_{VE} = 0.05 MPa (cases A and B). There appears to be much more significant change in LMS and IQR of strain in specific topographic zones compared to the compression case. Moreover, for the case when E_{SC} = 370 MPa (cases A2 and B2), lowering the Young's modulus of the viable epidermis from 0.6 to 0.05 MPa has the effect of reversing the direction of principal strains in some of the features.

The effect caused by the presence of a lower stiffness viable epidermis is a major result to consider in the light of all multi-layer finite element models of the skin found in the literature which typically assume flat interface between layers. These models are unlikely to capture these effects even by varying the Young's modulus of the viable epidermis.

6.3.8 The role of structural features of the skin and *stratum corneum* stiffness in strain reduction/amplification

One of the key objectives of this study was to assess the level of strain in the *stratum corneum* during simulated in-plane compression and extension of the skin. An important aspect to consider concerns the possible variations of the *stratum corneum* stiffness as a function of environmental or ageing conditions which, in turn, are likely to affect strain magnitude in the *stratum corneum*. To assess the effect of variations of the Young's modulus of the *stratum corneum* and also that of the viable epidermis a strain ratio metric was defined. The strain ratio metric R was defined as the ratio of principal strains (i.e. minimum and maximum principal strains respectively for compression and extension) of the compared model (models A2, B2, E_{SC} = 370 MPa) over those of the reference model (models A1, B1, E_{SC} = 0.6 MPa) at each of the elements composing the skin model. $R = 1$ indicates that strain levels remain the same, $R > 1$ indicates an amplification of strains, $0 < R < 1$ a reduction in the strain levels. A negative value for R implies a change in the principal direction of strain (from compressive to tensile and *vice versa*). Distribution of ratios of principal strains in the compression and extension cases are respectively depicted in **Figure 6.20** and **Figure 6.21** for models A1, A2, B1 and B2 and described in the following section. For each of the topographical zones, the median value of the strain ratio metric distribution $\tilde{R}$ is taken to represent the ratio of amplification or reduction while the IQR for these distributions is a measure of dispersion.

6.3.8.1 Compression

As intuitively expected, increasing the Young's modulus from E_{SC} = 0.6 MPa to E_{SC} = 370 MPa significantly reduces the principal strains in the *stratum corneum* (**Figure 6.20**) for all characteristic anatomical zones, with a GMS ratio (i.e. the median ratio observed for the whole *stratum corneum* elements) of $R \approx 0.1$. The minimum principal strains are mostly reduced in deep furrows with an average median value of $R \leq 0.05$ for both cases A and B. The wide furrow D and the shallower superficial furrow F follow close with $R < 0.06$ and $R < 0.075$ for cases A and B, respectively. With respect to dispersion, most of the furrows show a rather homogeneous reduction of strains with IQR <0.075 except for furrow K (IQR $\leq$ 0.50). Minimum reduction is found in crest L

as R is 0.45 for both cases. The most remarkable result is shown in the most protruding crest G, as while $R = 0.15$ with a dispersion ratio of 0.21 is found in case A, the resulting ratios for case B shows an amplification of $R = 1.57$ and IQR of 3.37. These results show how heterogeneous the effect is in the elements contained in this crest. In general, greater R values are observed in the crests, and lower ones in the furrows.

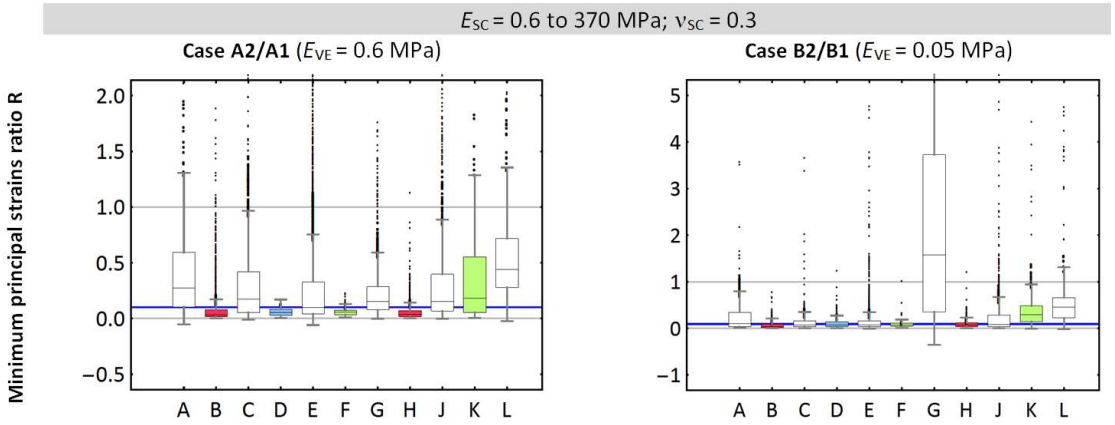

Figure 6.20: Box plot representing the distribution of ratio of minimum principal strains from analysis A2 (E_{SC} = 370 MPa, υ = 0.3) over those of analysis A1 (E_{SC} = 0.6 MPa, υ = 0.3) in the *stratum corneum* across the different topographic features of the skin (zone A to L, **Figure 6.6**) under **compression**. The same ratio of strains from analysis B2 over those of analysis B1 when the Young's modulus of the viable epidermis is 0.05 MPa is also plotted. The values between 0 and 1 (grey lines) represent a reduction in principal strains while the values higher than one represent amplification. The blue horizontal line indicates the median value of the ratio obtained for all the elements of the *stratum corneum* in the skin model (i.e. the general median strain ratio, GMS ratio).

6.3.8.2 Extension

Like in the load case corresponding to in-plane compression of the skin, stiffening of the *stratum corneum* by a factor in excess of a 600 induces a significant reduction in the magnitude of principal strains (**Figure 6.21**) with a GMS ratio $R < 0.20$. However, unlike the case of compression where the GMS ratio was similar between cases A and B, the GMS ratio of case A is larger than the one observed in case B by a factor of about 2. Regardless of that, both cases show particularly different behaviours in terms of the reduction and amplification of strains in each of the topographic features. For case A, the maximum principal strains are mostly reduced in the shallower furrows ($R < 0.08$), but a relevant contrast between the two superficial and the two deep furrows is observed (i.e. a 3 to 5 times larger ratio is observed in the deeper furrow of each category). The ratio in most of the crests ranges from 0.12 to 0.44 with no shape dependency. In contrast, crest G, exhibits a significant amplification factor ($R = 2.20$). For case B, the distribution of R is rather homogeneous across the topographic features, with a range between 0.05 and 0.16 for crests and between 0.04 and 0.11 for furrows. Although a lower ratio is observed in the wide furrow D and a larger ratio at the crest G, no topographic shape dependency is observed.

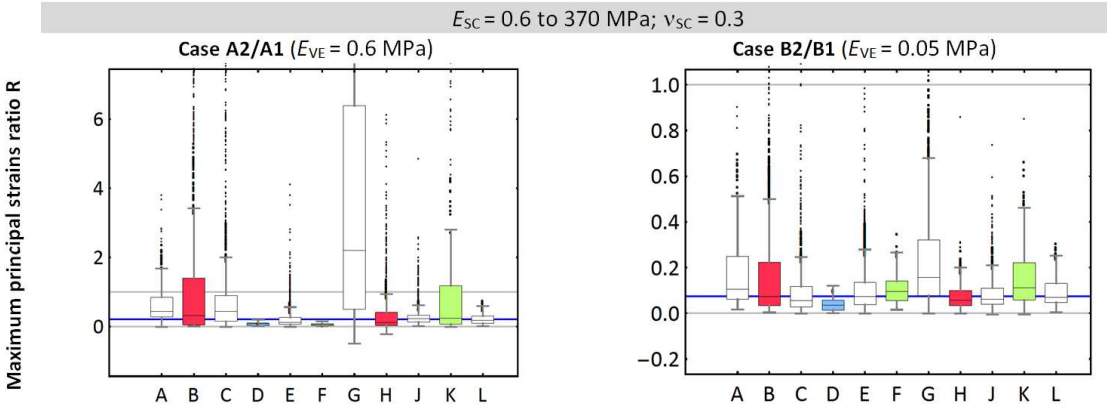

Figure 6.21: Box plot representing the distribution of ratio of maximum principal strains from analysis A2 (E_{SC} = 370 MPa, υ = 0.3) over those of analysis A1 (E_{SC} = 0.6 MPa, υ = 0.3) in the *stratum corneum* across the different topographic features of the skin (zone A to L, **Figure 6.6**) under **extension**. The same ratio of strains from analysis B2 over those of analysis B1 when the Young's modulus of the viable epidermis is 0.05 MPa is also plotted. The values between 0 and 1 (grey lines) represent a reduction in principal strains while the values higher than one represent amplification. The blue horizontal line indicates the median value of the ratio obtained for all the elements of the *stratum corneum* in the skin model (i.e. the general median strain ratio, GMS ratio).

6.3.9 Influence of the skin topography on the distribution and modulation of strains across skin layers

In **Figure 6.22** and **Figure 6.23** the ratio of the strain distribution magnitude of each skin layer (*stratum corneum*, viable epidermis and dermis) over the respective applied macroscopic strain (20%) is reported for each case A1, A2, B1 and B2. This metric expressed in% assess whether the magnitude of applied macroscopic strain is amplified or reduced in the skin layers. A value above or below 100% means that strains are respectively magnified or reduced. This effectively highlights the effect of the structural properties of the skin layers in redistributing strains-and so the stress-within the skin. Even when the skin is modelled as a homogeneous material (case A1) the median proportional strain values of the outer layer are remarkably lower than the ones observed in the layers underneath. For case A, it is observed that strains in the dermal layer are the least attenuated whilst those in the *stratum corneum* experience the largest reduction. For case B, strains in the viable epidermis are the least attenuated. When the Young's modulus of the *stratum corneum* is increased from 0.6 to 370 MPa, the magnitude of strain is obviously reduced and so is the dispersion.

In **compression** (**Figure 6.22**), the proportional median strain levels in cases A and B are respectively 7 and 15 times lower for the stiffer *stratum corneum*, while the dispersion levels are reduced 20 and 12 times for the IQR, and 6 and 9 times for the PVR. The changes in the stiffness of the *stratum corneum* have a marginal effect in the proportion of macroscopic strains transmitted to the viable epidermis and dermis. Between cases A1-A2 and B1-B2, the median values of this proportion are hardly altered in the dermis.

For **extension** (**Figure 6.23**), the change in stiffness of the *stratum corneum* has a relatively different effect as the median proportional strain levels in cases A and B are respectively 5 and 13 times lower as the Young's modulus of this layer increases, while the dispersion levels are reduced 9 and 11 times for the IQR, and 25 and 10 times for the PVR. The stiffening of the *stratum corneum* not only increases the median values of the proportional maximum principal strain distributions in the layers underneath, but also has an important effect on their dispersion parameters. The increase of proportional strain in the viable epidermis is 20% and 40% for cases A and B respectively, and 25% and 4% for the dermis. The interquartile dispersion is augmented on average by 50% for the viable epidermis in both cases, but for the dermis the IQR doubles in case A, while a negligible reduction is observed for case B. In terms of peak values dispersion, the results show negligible variation for the dermis and case A for the viable epidermis, while the PVR of case B2 is 2.5 times larger than the one observed in case B1.

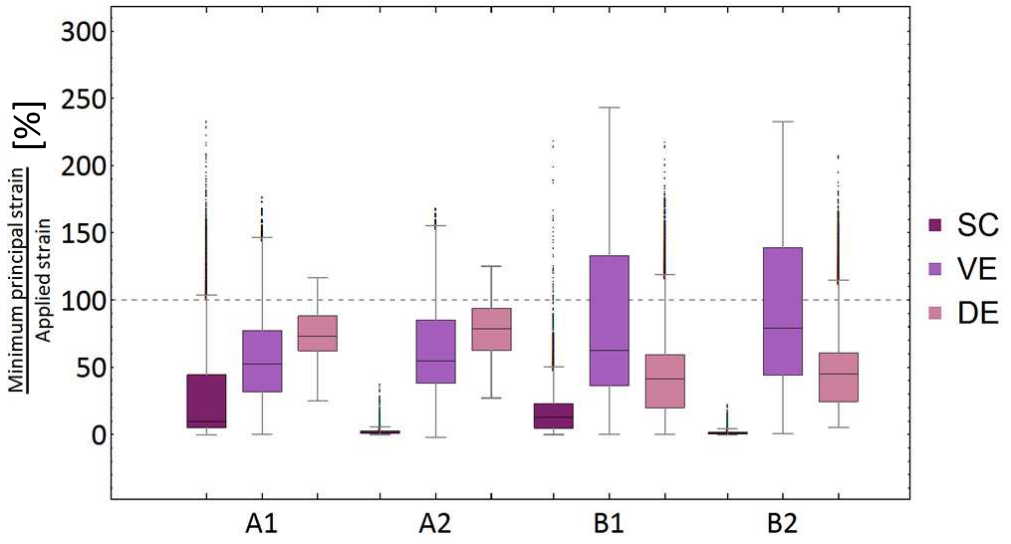

Figure 6.22: Ratio of minimum principal strains in each skin layer (SC - *stratum corneum*, VE - viable epidermis, DE - dermis) over the macroscopic strain applied to the skin composite model (expressed in%) for the **compression** case. The dashed line indicates the limit between strain amplification (> 100%) and strain reduction (< 100%).

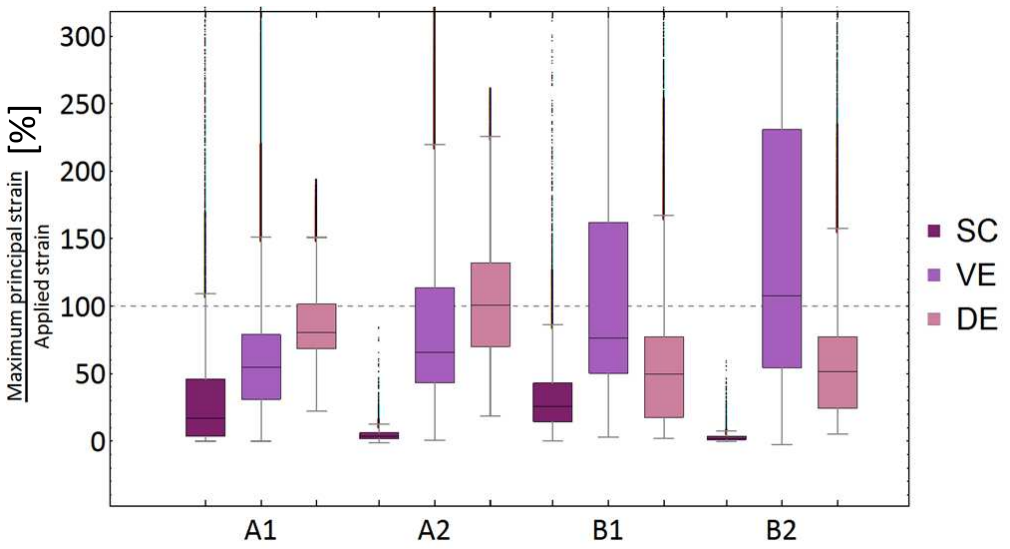

Figure 6.23: Ratio of minimum principal strains in each skin layer (SC - *stratum corneum*, VE - viable epidermis, DE - dermis) over the macroscopic strain applied to the skin composite model (expressed in%) for the **extension** case. The dashed line indicates the limit between strain amplification ($> 100\%$) and strain reduction ($< 100\%$).

6.4 Discussion

The imaged-based computational study presented in this paper has highlighted and quantified the critical role of the structural and mechanical characteristics of the skin layers over their mechanical response under tension and compression as well as on the global response of the skin as a 2D composite structure. Given that the skin is the human body's interface to the external environment, these results have implications for a variety of mechanical and/or mechanobiological processes (Limbert and Simms, 2013) across many domains of application including skin tribology in general (van Kuilenburg et al., 2013a,b; Veijgen et al., 2013b), pressure sores (Brand, 2006) and wound healing (Evans et al., 2013).

Geerligs (2010) stated that, during stretching of the skin, the *stratum corneum* partially unfolds without elongating, but to the best of our knowledge, this had not been previously quantified until now. In our 2D study it was revealed that, for a given imposed in-plane macroscopic deformation of the skin and fixed value of Young's modulus of the *stratum corneum*, the magnitude of strain in the *stratum corneum* tends to be significantly attenuated, particularly at specific topographic locations (crests, see **Figure 6.5** and **Figure 6.11**-**Figure 6.14**). When all layers have identical mechanical properties (case A1), this phenomenon is still present. There is, therefore, evidence that the convoluted geometry of the *stratum corneum*, in its own, is a contributor to this effect. When each skin layer features different mechanical properties, in addition to the *stratum corneum*, the contribution of the viable epidermis and dermis to these structural effects is modulated by the balance of mechanical properties between these

three layers. When the viable epidermis is 12 times softer than the dermis this strain reduction effect in the *stratum corneum* is even stronger (cases B1-B4). In all the cases considered in the computational analyses, the strain deflection mechanism provided by the topographical features of the *stratum corneum* and underlying layers is clear. In all cases the 75th percentile of the *stratum corneum*'s finite elements experience a strain lower than half of the applied macroscopic strain. Similarly, in most of the results, more than 75% of the finite elements contained in the deeper layers sustain less than the total applied macroscopic strain. For case B, results show that the viable epidermis is the most strained layer, experiencing 2.5 to 3 times more strain than those that are macroscopically applied.

It was shown that the stiffness of the *stratum corneum* plays a critical role in conditioning the folding characteristics of the skin surface in both simulated in-plane (parallel to the outer surface of the skin) compression and extension of the skin (**Figure 6.6**-**Figure 6.9**). When the *stratum corneum* tends to stiffen —for example, as a result of a dryer external environment —cavities are likely to form in deep furrows, between skin folds, in compression while, in extension, the bottom surface of furrows experience limited rotation and significant strains. In this latter case, the base of a deep furrow acts like the fixed axis of a hinge mechanism in which the surrounding "vertical walls" of the furrow undergo large rotations with minimal straining. This observation suggests that, for the simulated 2D loading conditions, deep furrows convert in-plane deformations into out-of-plane deformations. In compression, this is very similar to the buckling of a column where compressive loads are converted into bending loads. Moreover, this functionality creates concentrated high strain zones in the deeper layers of the epidermis and dermis. Interestingly, dermal papillae tend to be very small or non-existent immediately under deep furrows and there might be a causal correlation here which could be relevant to the mechanobiology of skin.

With the image-based modelling approach, the *stratum corneum* structure was captured 'as is', so the thickness of this layer was fixed according to the pixel information available in the skin histological images. In order to investigate the role of *stratum corneum* thickness in the distribution of strain within the skin, the anatomical skin model can be modified so the *stratum corneum* geometry is modelled as a shell structure. Such model, in which bending of outer shell could be related to the levels of strain beneath this layer, could be applied to investigate coupled effects of humidity in the *stratum corneum* thickness and stiffness.

The surface topography of the skin and how it deforms under loads are critical factors to consider for applications where the skin undergoes contact interactions with external devices like consumer good products (e.g. for dry and wet shaving the skin interacts with metal and polymer components, water, body secretions, gel or foam) or cosmetic agents (e.g. moisturiser). The aforementioned strain reduction and amplification mechanisms are therefore potentially very important to consider. Depending

on the initial stiffness of the *stratum corneum* and its structural geometry, the skin will produce certain types of mechanical response, particularly if one considers the presence of a liquid thin-film (e.g. shave preparation) which introduces additional complex tribophysical phenomena (Israelachvili, 1991; Pailler-Mattéi and Zahouani, 2004, 2006; Pailler-Mattei et al., 2007). The application of water-based agents to the skin has a plasticising effect on the *stratum corneum* which drastically reduces its Young's modulus (Wu et al., 2002, 2006b). In these conditions, where friction forces tend to increase, rubbing of hard or softer surfaces against the skin can generate significant local strains which, in turn, can lead to important strain and stress redistribution in the underlying skin layers. The 2D computational study presented in this paper demonstrated the complex interplay between the material and structural properties of the skin layers during simulated compression and extension of the skin and therefore highlighted the importance of faithfully capturing these characteristics for reliable numerical analyses, especially when they are used to assist design decisions in industrial applications.

The numerical analyses showed that, for a given imposed macroscopic deformation of the skin, increasing the Young's modulus of the *stratum corneum* from 0.6 to 370 MPa led to higher strains in the deeper layers of the skin (viable epidermis and dermis). Drying stresses arising as a result of water loss in the *stratum corneum* (Levi et al., 2010b) are generally perceived through the feeling of skin "tightness". Given that the *stratum corneum* has no mechanoreceptors capable of sensing changes in the homeostatic state of stress and/or strain, the computational results are consistent with this observation, namely that stiffening of the *stratum corneum* in combination with in-plane loads increases the depth of influence of mechanical stress/strain which reaches deeper in the viable epidermis and dermis where free nerve endings, Merkel cells, Meissner's, Ruffini's and Pacinian corpuscules are located (Shimizu, 2007).

As in any computational model, a number of limiting assumptions had to be made. The major limitation of the present model concerns its restriction to 2D geometry, boundary and loading conditions. The computational model was restricted to 2D due to the imaging technique used in this study and a desire to focus on the simplest modelling approach that would facilitate interpretation of results. An extension to 3D, straightforward in principle, would likely affect the results. However, based on the 2D results, one would also expect a strong influence of the structural and material properties of each skin layer on strain/stress magnitude and distribution as well as on surface topography. The 2D model is already a significant addition to what has been proposed in the literature so far. To the best of the authors' s knowledge, the proposed micromechanical model is the first to account for such a level of structural details for the skin (high-fidelity anatomical geometries for the *stratum corneum*, living epidermis and papillary dermis) and the objectives were to assess how such structural features play a role in transforming macroscopic strains and redistribute loads. The emphasis was

on identifying structural effects on a 2D model and use that to suggest potential deformation mechanisms occurring in real skin structures. The simulations highlighted potentially important effects that are missed by idealised multi-layer models of the skin. The present study is a first attempt to pave the way for more advanced 3D microstructural models of the skin. The complex 3D patterns of sulci and how they might control deformations of the upper part of the epidermis should be explored in future studies.

The constitutive models used for the skin layers were based on isotropic neo-Hookean elasticity and ignored viscoelasticity. There is evidence that the *stratum corneum* possesses anisotropic properties (Geerligs et al., 2011a). Due to its high content of collagenous fibres, the dermis also has directional properties. As reviewed in **Chapter 2**, under compression, the collagen fibres do no take any load, and the skin mechanical response is regarded to the compression of the bulk material of the fibres and the ground substance. In extension, the level of deformation defines whether the fibre orientation is relevant or not for the analysis. In the present model, the level of deformation was kept under 20% macroscopic strain, which is within the toe region of the stress-strain curve observed in collagen fibrils (Graham et al., 2004). In this region, the skin mechanical response is determined by the elastic fibres which, unlike collagen fibre bundles, do not show a preferred direction (Ní Annaidh et al., 2012b), rather than parallel to the skin surface (Shimizu, 2007). With the range of deformation explored in this study, the strain field in the dermis is not related to any fibrous response nor the specific deformation of cells in the viable epidermis. The reported strains are rather significant for the instantaneous deformation skin experiences in normal conditions, highlighting the importance of the skin microstructure on its mechanical response.

It should be taken into account that, although the skin is naturally in a pre-tensed state, this condition was not taken into account in the present model. Thanks to the work of the Austrian anatomist Karl Langer (Lan, 1978; Langer, 1861) it has been known since the 19th century that the skin is in a state of residual tension *in vivo*. Flynn et al. (2013, 2015) determined a relation between the *in vivo* the relaxed skin tension lines (RSTL) on a human face and the directional dependency of the skin stiffness using a combination of contact measurement techniques and inverse finite element methods. These authors demonstrated the need to account for these tension lines in the characterisation of the anisotropic properties of the human skin. It is noteworthy that mechanical anisotropy of the skin is due to the combined effects of the presence of Langer lines and to the anisotropy induced by the structural characteristics of the skin layers and their sub-structural components. In-plane anisotropy of the skin is correlated with Langer lines Ní Annaidh et al. (2012b) while out-of-plane (or across-the-thickness) anisotropy is due to the distinct mechanical properties and complex 3D structure of the skin layers. In the dermis, the organisation of collagen changes from loose and tortuous fibres in the papillary dermis to large dense stratified fibre bundles in the reticular dermis (Shimizu, 2007). The inclusion of such features (residual

strains and fibrous microstructure) in a microstructural finite element model of the skin, although possible in principle, would only make sense in a 3D setting at larger deformation, and would require significantly more information on skin microstructure, data on the level and 3D directions of pre-strain in the specific skin sample (i.e. consistent with anatomical location) and may likely require higher resolution imaging modalities. In a 3D finite element context, the question of reliably applying pre-strains with regards their non-uniform distributions and directions would present technical challenges (Limbert, 2004; Rausch and Kuhl, 2013; Weiss et al., 1995). The aforementioned observations provide justification to the choice of using initially stress-free 2D computational multi-layer skin models.

The composite skin model did not account for the full thickness of the dermis and its underlying hypodermis. Addressing this limitation would likely affect the results by reducing the effect of imposed boundary conditions, particularly the symmetry boundary. Future computational analyses should also include skin appendices such as hair follicles and pores which could play a mechanical role in redistributing strain and stress in the skin as well as in stopping fracture propagation in the (drying) *stratum corneum*.

All skin layers were assumed to be perfectly bonded to each other without the presence of any intermediary interface. This simplifying assumption was deemed necessary to focus on other factors, namely, the geometrical and material properties of each layer. It was also necessary due to the significantly higher computing power that this would have required because of the level of mesh refinement needed. The living epidermis is connected to the underlying dermis through a 3D interlocking wavy interface called the dermal-epidermal junction (DEJ) or *basal lamina* which is effectively a 0.5-1 μm thick basement membrane (Chan, 1997). In the epidermis, the basal cells of the *stratum basale* are connected to the basement membrane by anchoring filaments of hemidesmosomes while the cells of the papillary dermis connect to the basement membrane through type VII collagen fibrils. The geometry and material properties of these structural elements are likely to play a critical role in load transmission between layers, particularly in 3D. Future studies should investigate this further but are likely to require a multiscale approach given the large span of spatial dimensions involved.

As is always the case with mathematical and computational models, a critical step, before relying on the predictive capabilities of these models, is to validate them-even partially-using physical experiments. This is currently very challenging but there are very promising emerging approaches in skin research. For example, using digital image correlation techniques it is possible to obtain full (strain) field measurements (Tonge et al., 2013a,b). The modelling approach adopted here is a first step towards models to assess, understand and control the effects of the structural properties of skin in medicine, biology and industrial applications.

In the last few years, the concept of skin microclimate has been in the spotlight with regards to pressure ulcer research (Gefen, 2011). Skin microclimate encompasses a number of physical factors such as temperature, humidity and air flow at the skin surface. These interacting factors are believed to play a critical role in compromising skin integrity by reducing its natural barrier function. These effects are amplified when the skin acts as a load-bearing surface, particularly when subjected to shear loads (Zhong et al., 2006). There is evidence that the skin surface topography changes during loading but it is unclear whether these changes are purely driven by mechanics or partly induced by microclimate factors such as temperature and moisture (Kottner et al., 2013; Veijgen et al., 2013b). The models developed in our study offer the potential to address these questions by either focusing on the mechanics only or by considering coupled thermo-mechanical effects combined with moisture absorption or exudation. Our study showed that, during in-plane compression of the skin, if the Young's modulus of the *stratum corneum* and the viable epidermis are both 0.6 MPa (low end of the spectrum for the *stratum corneum*) maximum strains are located in the dermis and lower regions of the viable epidermis rather than branching from the skin surface (**Figure 6.6**). When considering the viable epidermis with a Young's modulus 12 times lower, strains are intensified in these regions (**Figure 6.7**). This effect increases the likelihood of compromising the integrity of the dermal-epidermal junction (DEJ) which is believed to play a major role in the chemo-mechano-biology of the skin. Indeed, the DEJ controls the transit of molecules between the dermis and epidermis according to their dimension and charge. It allows the passage of migrating and invading cells under normal (i.e. melanocytes and Langerhans cells) or pathological (i.e. lymphocytes and tumour cells) conditions (Burgeson and Christiano, 1997). However, it is important to reiterate that the results were obtained for a 2D setting and, that future 3D studies may unravel more complex structural effects.

After an injury, the folding/unfolding or straining of the skin furrows may play an important role during the scar formation process by controlling the mechanical environment around a wound (Wong et al., 2012). This environment has been clinically shown to be of the utmost importance for conditioning scar tissue formation (Gurtner et al., 2011). Using an external device to mechanically shield a wound, Gurtner et al. (2011) showed that creating a mechanical equilibrium state around the wound would in turn lead to homeostasis (biological equilibrium), effectively inhibiting the production of new scar tissue with undesirable structural and mechanical characteristics (e.g. fibrosis). There is evidence that mechanical tension can induce phenotypic alteration in fibroblasts during wound healing under the form of altered collagen network characteristics (Dunn et al., 1985). These effects lead to hypertrophic scar tissue formation where the new tissue features a reduced extensibility rather than an increased stiffness. Compared to normal skin, scar tissue loses the uncrimping phase of the typical J-shape of the tensile stress-strain curve (Fung, 1981). Recently, using a 3D in vitro tissue engineered model, Suarez et al. (2014) demonstrated that skin tension

up-regulates tension-related gene expression in keloid fibroblasts thus confirming the role of mechanics as a regulator of the scarring process. There have been few computational studies in the literature examining the mechanical or chemo-bio-mechanical environment around a wound or skin suture. In a recent computational study examining the mechanics of local skin flaps after tissue expansion, Tepole et al. (2014b) suggested a direct correlation between regions of maximum stress and tissue necrosis. Their model considered the skin as a mono-layer transversely isotropic hyperelastic structure. Cerda (2005) developed a mechanical model of wound contraction in skin with special focus on wrinkles induced by the existence of residual tension in the skin. To analyse stress and displacement distributions produced by different wound shapes and suture patterns, (Chaudhry et al., 1998) established a 2D mathematical model of the skin. Skin was assumed to be a linear orthotropic elastic material. Following a similar motivation, Flynn (2010) developed a series of finite element models featuring different types of wound shapes and compared the distribution and magnitude of stress. The skin was modelled as an orthotropic hyperelastic material (Bischoff et al., 2002).

In all these numerical studies the skin was assumed to be either a 2D or 3D homogeneous structure. There was no account of realistic anatomical skin topography or geometry of the *stratum corneum*, living epidermis and dermis. It is often assumed that the collagen-rich dermis is the main mechanical contributor to the macroscopic response of the skin, particularly under finite extension. However, under surface loads or loads applied in the upper strata of the skin like in the present study, there is a complex mechanical interplay between these layers. If one considers these purely mechanical phenomena in combination with the presence of a wound it is straightforward to anticipate that the coupled mechanobiological processes involved in epidermal and dermal wound healing (Vodovotz, 2010) would be affected by the microstructural response of the skin. In the light of the computational results obtained in the present study, it is suggested that past computational studies should be revisited by incorporating anatomical geometries into skin models, ideally in 3D, in order to provide additional insight.

6.5 Conclusion

The study presented in this paper has introduced a 2D image-based finite element modelling approach, with special emphasis on anatomical realism, to study the microstructural and mechanical interplay of the *stratum corneum*, viable epidermis and dermis layers of the human skin under simulated in-plane compression and extension. The hybrid experimental-computational methodology has proven to be robust and has offered valuable insights into the simulated 2D mechanics of the skin, and that of the *stratum corneum* in particular, by providing qualitative and quantitative information on strain magnitude and distribution. The implications of this study are many-fold across

a wide range of sectors where simulating the mechanics of the skin is relevant, particularly in biomedical, consumer goods, cosmetics, sport equipment and computer graphics. Based on 2D finite element simulations, it appears that the geometry of the skin layers (together with their material properties) could play a significant role in controlling the local mechanical environment at the surface and within the skin.

The series of finite element analyses has highlighted and quantified the following key points

- Through a complex non-linear interplay, the geometry and mechanical characteristics of the skin layers (and their relative balance), play a critical role in conditioning the 2D skin mechanical response to macroscopic in-plane compression and extension. Topographical features of the skin surface such as furrows were shown to offer an effective means to deflect, convert and redistribute strain- and so stress-within the *stratum corneum*, viable epidermis and dermis. This is achieved through geometrical features and structural effects that energetically favour certain deformation modes like bending. A corollary consequence of these phenomena is that strains can be amplified or reduced in certain locations of the skin structure. This confirms the work hypothesis of the present study although these conclusions are based on a 2D approach and it is therefore important to exercise caution in the interpretation of the results, particularly with regards to the real 3D characteristics of the human skin (e.g. material and structural properties as well as residual tension lines). Extension of the model to 3D is likely to highlight comparable structural effects in terms of deformation mechanisms (i.e. local modulation of macroscopic strains) but potentially different in terms of spatial distributions and orientations. Future studies should investigate these questions.
- Despite the small thickness of the *stratum corneum*, its Young's modulus has a significant effect not only on the magnitude and directions of the strains it experiences but also on those of the underlying layers. This effect is reflected in the deformed shape of the 2D skin surface in simulated compression and extension and is intrinsically linked to the rather complex geometrical characteristics of each skin layer. Moreover, if the Young's modulus of the viable epidermis is assumed to be reduced by a factor 12, the area of skin folding is likely to increase under skin compression. These results should be considered in the light of published computational models of the skin which, up to now, have ignored these characteristics.
- Stiffening of the *stratum corneum*, for example, as a result of a dryer environment, has consequences not only for its own mechanical response but also for the underlying viable epidermis and dermis because of the intimate mutual structural relations between these layers.

Chapter 7

Micromechanical modelling of skin mechanics II - structural and material aspects of skin contact mechanics

In the previous chapter, it has been demonstrated that the skin microstructure, its geometry and mechanical properties, play an important role in the distribution of principal strains within the skin during compressive and tensile deformation. In solid contact interactions, it is known that the surface micro-structure can significantly influence the friction response; however, the few publications investigating the contribution of skin microstructure to its macroscopic friction response show mixed results. This chapters describes a computational analysis performed, taking the ***anatomical model*** *described in* ***Chapter 6*** *as a base for the simulations, to evaluate the effects the skin topography and microstructure have on the skin macroscopic friction response. The simulations involved pure indentation and sliding contact of the skin with a rigid indenter, at various local coefficients of friction. The scale of the contact interaction was considered with variation of the indenter radius from 0.1 mm to 0.5 mm for microscopic scale interactions, and an infinite radius (flat indenter) for macroscopic scale ones. This study compared the results of the anatomical model with those o an idealised flat skin model, in terms of relative contact area, global and local friction response, and the distribution of shear stresses within the skin layers. The results showed that the relative contact area is highly sensitive to the contact interaction scale, being much lower in macroscopic scale interactions. The skin topography showed to be a dominant factor in the friction response, regardless of the scale of interactions. Further results revealed the effects of the skin topography and microstructure in the distribution and propagation of shear stresses in the periphery of the contact area, and*

how these stresses are much higher than those assumed by modelling the skin as a flat tissue.

The human skin is the first line of defence against environmental hazards. Its mechanical integrity relies on a complex microstructure that provides the skin with high elasticity and strength, while maintaining a 15-20 cell-thick self-renewable layer of keratinised epithelial cells (Hendriks, 2005), the *stratum corneum*, that provide a strong interface for contact interactions. With the *stratum corneum* as an interface, contact interactions transmit vibration and deformation to the mechano-receptors in the skin, providing the sense of touch (Shimizu, 2007). If the interaction causes significantly high deformation or damage to the skin structure, the 'pain' signal pathway of the nociceptors is activated (Shimizu, 2007). This results, in most cases, in an uncomfortable experience to the person (Gerhardt et al., 2008). This phenomenon is of great interest to the industry of consumer goods such as wet shaving products, skin care, clothing and sport equipment, who share a vital interest on ensuring that, when interacting with the consumer's skin, their products provide a comfortable experience.

As reviewed in **Section 2.3**, skin is very sensitive to the biophysical effects of environmental conditions and ageing that can alter the microstructure and stiffness of the *stratum corneum* and other skin layers (Geerligs et al., 2011a; Kwiatkowska et al., 2009; Wu et al., 2006b). High humidity levels, for example, can significantly reduce the stiffness of the *stratum corneum*, and produce a considerable increase the friction forces at the skin contact interface (Gefen, 2011; Hendriks and Franklin, 2010; Zhong et al., 2006). This effect can lead to a greater likelihood of mechanical damage to the skin (Derler and Gerhardt, 2012; Sopher and Gefen, 2011).

Experimental characterisations of the skin friction response, often report values of macroscopic friction, involving the reaction force obtained from relative motion of a surface with respect to the skin (Masen, 2011). In contrast, only few studies report the skin friction response at a microscopic scale (Pailler-Mattei et al., 2007; Tang and Bhushan, 2010). To the best of the author's knowledge, there are no current studies comparing the relation between the microscopic friction response, here referred as **local friction**, and the macroscopic one (**global friction**), with the same contacting materials and environmental conditions. However, a computational study from Stupkiewicz et al. (2014), recently quantified that for a given local coefficient of friction for the simulations, the topography of the material can influence the global friction response, particularly with regards to anisotropic friction.

The friction responses of soft materials involve the contribution of both an adhesion and a deformation component. The adhesion component is driven by real area of contact (sum of micro-asperity contacts), while the deformation component is directly represented by physical obstacles (i.e. asperities) that oppose the relative motion of the

contacting surfaces. Although in solid mechanics the surface microstructure of the materials provides the principal source of friction (Stachowiak and Batchelor, 2013), only a few studies have investigated the contribution of the skin topography to its global friction response (Egawa et al., 2002; Nakajima and Narasaka, 2010). These studies showed contradicting or inconclusive results. In most of the studies found in the literature, the topographic features of the skin are assumed to provide no contribution to the skin global friction response, because of the high compliance of the skin compared to that of the indenter (Adams et al., 2007; Derler and Gerhardt, 2012; Gerhardt et al., 2008). However, it is reasonable to assume that the compression and distortion of the skin topographic features during sliding contact, as documented by Koudine et al. (2000), can significantly contribute to the skin global response. The topography of the skin is dependent on age and body location (Derler and Gerhardt, 2012; Gerhardt et al., 2009a; Zahouani et al., 2011), but so are its mechanical and bio-physicochemical properties. It might be the case that the effects of the skin topographic features on its friction response have been overlooked due to the inherent complexity and multi-factorial nature of skin friction, which requires a step-by-step simplified approach focusing on a very limited factors at a time (Gerhardt et al., 2009a; Nakajima and Narasaka, 2010).

In the present study, the effect of the skin topography and microstructure on the global friction response of human skin was explored. The simulations consisted of pure indentation and sliding of a rigid indenter on a previously developed 2D **anatomical model** of human skin (**Chapter 6**, Leyva-Mendivil et al. (2015)), and a counterpart **idealised skin model**, based on the average thickness of the layers in the anatomical one. The analysis considered the effect of different interaction scales through variation of the indenter radius, and the effects of humidity conditions by varying the stiffness of the *stratum corneum*. The effects of the skin microstructure in contact interactions were evaluated in terms of real contact area and comparison of the statistical distribution of the global coefficient of friction and the specified (local) one. Due to their implication in the mechanism of damage in the inner skin layers (Derler and Gerhardt, 2012; Sopher and Gefen, 2011), the effect of the surface topography on the distribution of shear stress throughout the dermal tissue was also analysed, by considering pure indentation (e.g. pressure ulcers) and sliding conditions (e.g. friction blisters).

7.1 Physics of friction and contact mechanics

Although it is known that the fundamental source of friction forces between two contacting body remains in their electromagnetic forces, the “concept of friction” has been developed for a mechanical interpretation of the factors contributing to a resistance to relative motion between contacting bodies (Persson, 2000). The friction response

can be classified into two categories: **local friction**, involving the micromechanical interactions at a single-asperity level; and **global friction**, referring to the macroscopic friction response, as the sum of the contribution of those micromechanical interactions (Stupkiewicz et al., 2014). This can be explained within the context of a 2D multi-asperity contact system. Taking a coordinate system (x, y), consider the contact of an solid indenter into a nominally flat material. The mean contact surface is parallel to the x direction, and sliding contact between the two bodies is imposed by the application of an indenting force of magnitude P, parallel to the y direction, and a displacement u_x, parallel to the mean contact surface, as illustrated in **Figure 7.1**.

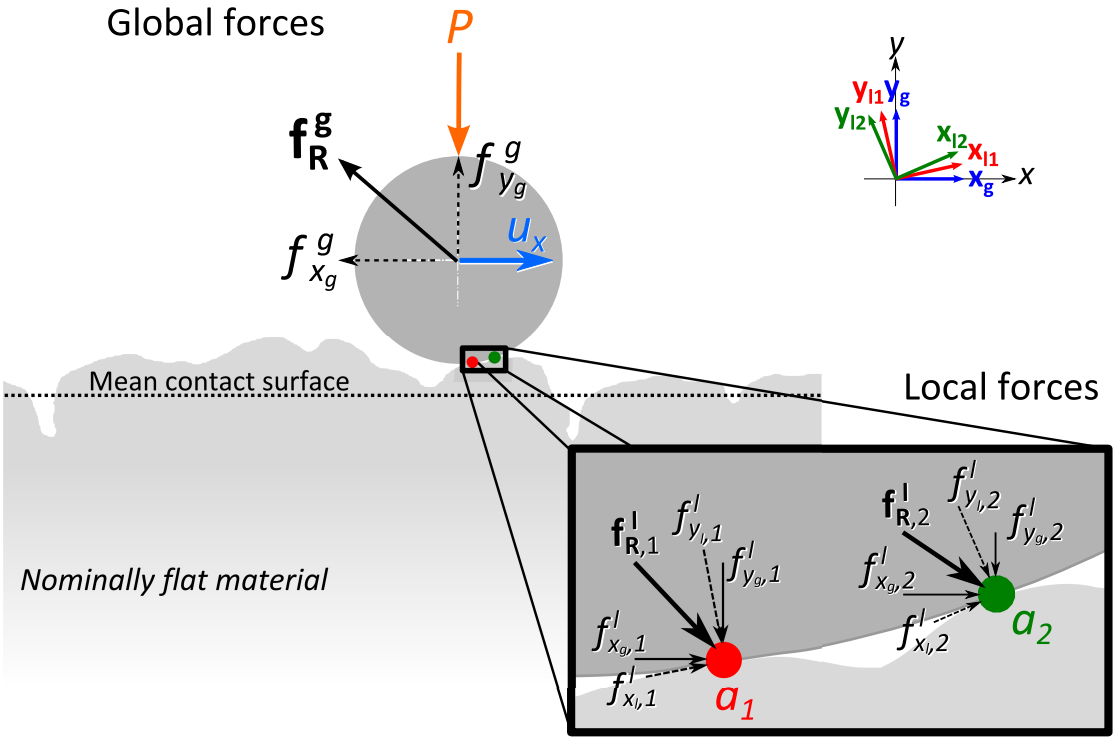

Figure 7.1: Contact system determined by a nominally flat surface and an indenter, subject to an indenting force of magnitude P and imposed displacement u_x, normal and parallel to the mean contact surface. The global forces involve the reaction force $\mathbf{f^g_R}$ at the indenter, which components in the global coordinate system defined by the unit vectors $(\mathbf{x_g}, \mathbf{y_g})$ are used for the estimation of the global coefficient of friction. At a micro-asperity contact a_i, the local reaction forces $\mathbf{f^l_{R}}_i$ can be derived in their normal and tangential components defined by the local coordinate systems $(\mathbf{x_{li}}, \mathbf{y_{li}})$ for the determination of the local coefficient of friction. The components of the local reaction forces in the global coordinate system (e.g. $f^l_{x_g,1}$ and $f^l_{y_g,1}$ for a_1), are related to the global friction response as $f^g_{x_g} = \sum_{i=1}^{n_a} f^l_{x_g,i}$ and $f^g_{y_g} = \sum_{i=1}^{n_a} f^l_{y_g,i}$. For the case represented here, $n_a = 2$ number of asperities.

The global friction response is measured in with respect to the global unit vectors $(\mathbf{x_g}, \mathbf{y_g})$, coincident with the x and y directions of the coordinate system, where a global reaction force $\mathbf{f^g_R}$ is generated at the indenter as a reaction of the multi-asperity contact. Considering n_a number of asperities in contact, a system of local unit vectors $(\mathbf{x_{li}}, \mathbf{y_{li}})$ can be used to define the tangent and normal directions of each contact point i. The local reaction forces $f^l_{R,i}$ generated at each of these contact points can then be expressed with respect to the local coordinate system $(x_{l,i}, y_{l,i})$, or the global one (x_g, y_g)

as:

$$\mathbf{f}^{\mathbf{l}}_{\mathbf{R}i} = f^{l}_{x_l,i}\mathbf{x_{li}} + f^{l}_{y_l,i}\mathbf{y_{li}} \tag{7.1}$$

$$\mathbf{f}^{\mathbf{l}}_{\mathbf{R}i} = f^{l}_{x_g,i}\mathbf{x_g} + f^{l}_{y_g,i}\mathbf{y_g} \tag{7.2}$$

Then, the local coefficient of friction for a given contact point, as per **Equation 2.30**, is given by:

$$\mu_{l,i} = \frac{f^{l}_{x_l,i}}{f^{l}_{y_l,i}} \tag{7.3}$$

Like in **Equation 7.2**, the global reaction force can be described in the global coordinate system as:

$$\mathbf{f}^{\mathbf{g}}_{\mathbf{R}} = f^{g}_{x_g}\mathbf{x_g} + f^{g}_{y_g}\mathbf{y_g} \tag{7.4}$$

where

$$f^{g}_{x_g} = \sum_{i=1}^{n} f^{l}_{x_g} \tag{7.5}$$

This value represents the magnitude of the global friction force, as reported in the experimental context (e.g. friction tests):

$$f_\mu = f^{g}_{x_g} \tag{7.6}$$

In order to preserve the equilibrium of forces in the y direction, the component of the global reaction force, normal to the mean contact surface, is considered to be $P = f^{g}_{y_g}$, where

$$f^{g}_{y_g} = \sum_{i=1}^{n} f^{l}_{y_g} \tag{7.7}$$

Then, the global coefficient of friction is given as per **Equation 2.30**, by:

$$\mu_g = \frac{f^{g}_{x_g}}{f^{g}_{y_g}} \tag{7.8}$$

In the 3D context, the friction force $\mathbf{f}_\mu$ is composed by the sum of forces within the plane of contact.

Elastomer friction theory has been widely applied for the study of skin tribology (Derler et al., 2009a; Gerhardt et al., 2008, 2009a). In this theory, the friction force is the result of the summed contribution of an adhesion and a deformation component:

$$\mathbf{f}_\mu = \mathbf{f}_\mu{}^{\text{adh}} + \mathbf{f}_\mu{}^{\text{def}} \tag{7.9}$$

The adhesion component is dependent on the contact area (Wolfram, 1983), while the deformation contribution to friction depends on the presence of micro-asperities (Persson, 2000) and peripheral deformation around the area of contact (Greenwood and Tabor, 1958). In the analysis of contribution of these two components to the global

friction response of human skin, many studies have concluded that the adhesion component is the dominant source of friction on human skin (Adams et al., 2007; Derler et al., 2009a,b; Kwiatkowska et al., 2009). However, these results have been called into question by van Kuilenburg et al. (2013a) in which, accounting for the real area of contact between a fingerpad and a contacting surface with a controlled topography showing a uniform pattern of micro-asperities, concluded that the deformation component provides a higher contribution to friction at higher contact loads. In addition, Gerhardt et al. (2009a) found that on aged skin, the deformation component provides a higher contribution than the adhesive one, while the opposite response is observed in younger skin. It seems that these two effects balance themselves as Gerhardt et al. (2009a) found no significant difference in the skin friction response between young and aged skin.

In the present study, local and global friction were compared to reveal the contribution of the skin topography to the deformation friction component. This was achieved by using an anatomically-based and geometrically-idealised multi-layer finite element model of skin, subjected to indentation and indentation-sliding. The effects of softening of the *stratum corneum* due to high humidity, and the influence of contact interactions at microscopic and macroscopic scales were also evaluated.

7.2 Materials and methods

In this study, finite element methods where applied for the computational simulation of skin contact interactions with rigid bodies. This approach allowed to quantify of the contribution of the skin topography and microstructure to the global friction response, in different contact scenarios. The application of various coefficients of friction at a local scale was used for the representation of different contacting materials. Variation of the *stratum corneum* stiffness, was applied to simulate different humidity conditions. Furthermore, it was possible so estimate the effects of different indenter dimension, to identify particular structural effects of contact interactions at a micro and a macroscopic scale.

7.2.1 Skin models

The skin was modelled in 2D using a plain strain assumption based on histological sections of a mid-back skin sample obtained from a healthy 30 years old Caucasian female with no known medical conditions. The procedures for sample preparation, image acquisition, image segmentation and meshing are provided in **Chapter 6** (Leyva-Mendivil et al., 2015). The model considered the intricate geometry of the skin topography and that of the different layer interfaces, identifying the *stratum corneum*, viable epidermis, and dermis. The area comprising the previously developed anatomical model, was set as the **area of interest** of the present study. Nevertheless, the dimensions of skin model were expanded outside this area to meet the recommendations by Karduna et al. (1997) to avoid boundary effects in the contact simulations. In order to be able to isolate the effects of the skin microstructure, a geometrically idealised skin model was built. This model took into account the mean thickness of the *stratum corneum* and viable epidermis to provide an *idealised* representation of the skin, as a flat multi-layered tissue (see **Figure 7.2**).

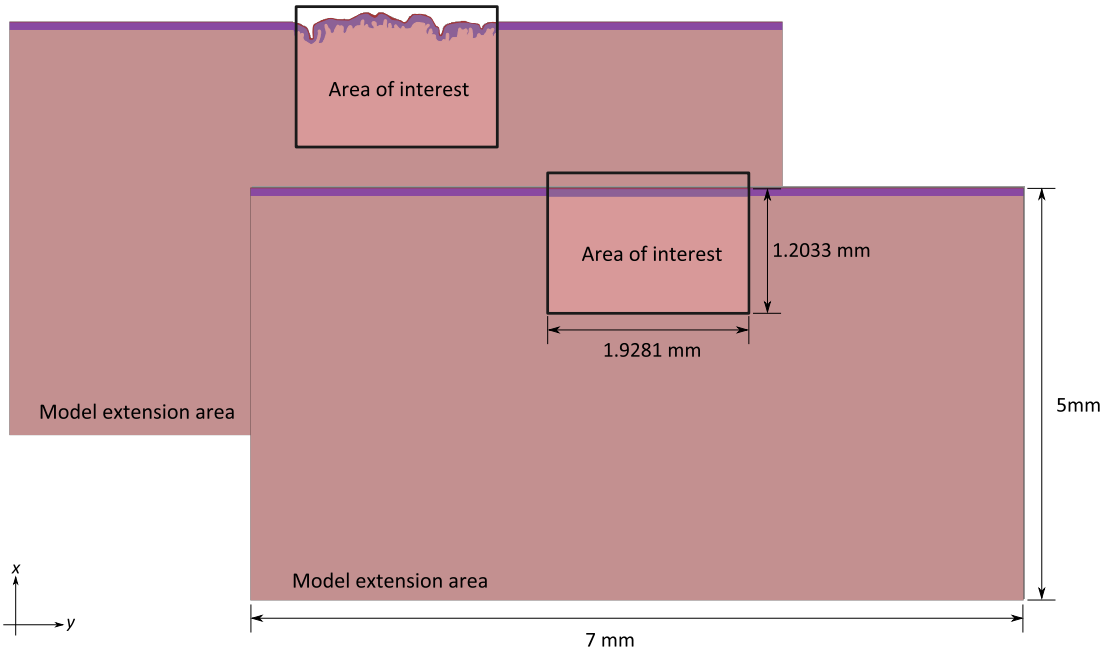

Figure 7.2: Extension of the skin model for indenting conditions was performed in order to avoid boundary effects in the results, according to the recommendations by Karduna et al. (1997). The topographic features present in the original skin anatomical model, as described in **Chapter 6**, was set as the **area of interest** for the analyses, and extension of the model was made in the lateral and depth directions. The mean height of the topographic features were used to define the layers dimensions for the extension of the anatomical model and those of the idealised skin model.

The finite element meshes of the idealised and anatomical models were generated within the finite element environment of Abaqus 6.14 (Simulia, Dassault Systèmes, Providence, RI, USA). This software package was used for the simulation of contact

interactions at a macroscopic scale, and meshes were exported to the AceGen/AceFEM package integrated within Mathematica (Wolfram Research, Inc., Champaign, IL, USA.) for the simulation of microscopic contact interactions.

Following the approach taken in **Chapter 6** (Leyva-Mendivil et al., 2015), the skin layers were represented as neo-Hookean materials (see **Section 2.4.2**), representing the viable epidermis and dermis with a Young's modulus of $E_{VE} = E_{DE} = 0.6$ MPa (Geerligs et al., 2011b; Lévêque and Audoly, 2013; Magnenat-Thalmann et al., 2002). To account for the effects of relative humidity (RH), a variation of *stratum corneum* stiffness considered the cases of 100% and 30% RH. Wu et al. (2006b) reported a Young's modulus of 0.6 MPa and 370 MPa, for these humidity levels. The Poisson's ratio was assumed to be $\upsilon = 0.3$ in all the layers (Serup et al., 1995).

7.2.2 Contact interaction simulations

The simulation of the contact interactions were performed in two steps: pure indentation and sliding contact. The 2D skin models were contained within an xy plane where the x axis is parallel to the mean contact area and the y axis is orthogonal to it. For the contact interactions, a rigid indenter was located on top of the centre of the area of interest, so indentation was performed along the y direction, and sliding along the x direction (see **Figure 7.3**). The base of the skin models were allowed to displace only in the x direction, while the side edges were allowed to freely displace during the interaction simulations.

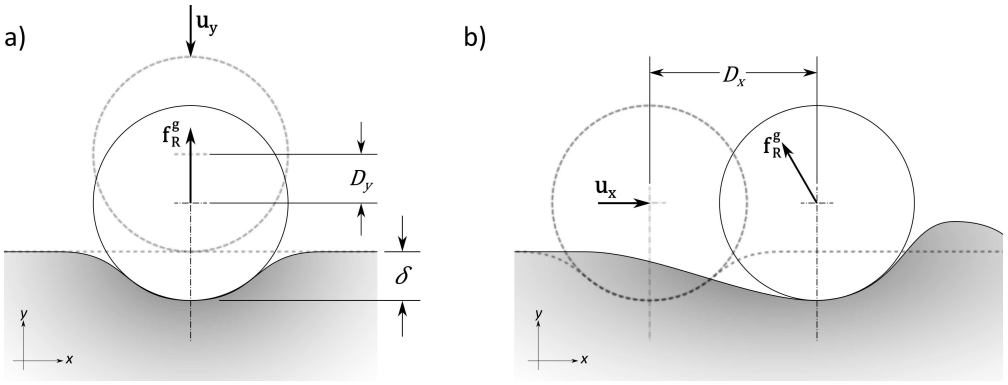

Figure 7.3: Description of the simulation steps. *a*) Indentation is simulated with the application of a vertical displacement $\mathbf{u_y}$ of magnitude D_y, resulting in skin deflection δ and a global reaction force $\mathbf{f^g_R}$ in the y direction. *b*) Sliding is simulated with the application of an horizontal displacement $\mathbf{u_x}$ of magnitude D_x, resulting in a global reaction force $\mathbf{f^g_R}$ which components in the x and y directions are used to calculate the global coefficient of friction. The images shown in dashed lines indicate the initial conditions of each simulation step, and the solid one the completed step.

The indenter was defined as a discoidal body. In order to represent various contact interaction scales, four indenter dimensions were considered. For microscopic scale interactions, the radius of the indenter R_1 was set to 0.1, 0.25 and 0.5 mm. For macroscopic scale interactions, R_1 was set to an infinite radius, thus representing the indenter as a flat contacting surface.

The indentation step was defined by imposing a D_y displacement to the indenter along the y direction. In order to avoid boundary effects, the indenter displacement was set to $D_y = R_1/2$ for micro-scale contact (Karduna et al., 1997), and a maximum of 0.25 for the macro-scale contact. The pure indentation simulation required a preceding step to achieve the first contact, so the skin deflection $\delta \leq D_y$. To enforce stability of the contact, small damping effects were added to the simulation (Vad et al., 2010). For this reason, once D_y was reached a stabilisation period was allowed prior to the beginning of the sliding step. The sliding motion was set towards the edge of the model, up to a distance equivalent to R_1 (or 0.25 mm for the macroscopic scale simulations) from the model edge. However, the results discussed in this study are limited to the measurements taken within the area of interest only.

The contact interactions were enforced using an augmented Lagrangian method and were defined by a local coefficient of friction μ_l. For the comparison of the local and global friction responses with different local coefficients of friction, μ_l was set to 0.0, 0.1, 0.2 and 0.3. All the variables considered in our computational study are summarised as follows:

- **Skin geometry:** Idealised, anatomical
- **Mechanical properties of the skin layers:**
  Stratum corneum: $E_{SC,1} = 0.6$ MPa, $E_{SC,2} = 370$ MPa, $\upsilon_{SC} = 0.3$
  Viable epidermis: $E_{VE} = 0.6$ MPa, $\upsilon_{VE} = 0.3$
  Dermis: $E_{VE} = 0.6$ MPa, $\upsilon_{VE} = 0.3$
- **Indenter radius:**
  Microscopic interaction scale: $R_{1,1} = 0.10$ mm, $R_{1,2} = 0.25$ mm, $R_{1,3} = 0.50$ mm
  Macroscopic interaction scale: $R_{1,4} = \infty$ mm
- **Interaction conditions**: Pure indentation, sliding contact
- **Local coefficient of friction:** $\mu_{l,1} = 0.0$, $\mu_{l,2} = 0.1$, $\mu_{l,3} = 0.2$, $\mu_{l,4} = 0.3$

7.2.3 Analytical validation of the finite element models

The finite element models were validated, by comparing the contact area and deflection parameters against the relevant analytical models describing the contact conditions applied in the simulations. The 2D conditions of the models relate to plane strain

conditions equivalent to a cylinder in contact with a half space (i.e. discoidal indenter on skin). Considering the skin as a flat homogeneous material, its representation as a half-space is equivalent to an infinitely long cylinder of radius $R_2 = \infty$ mm. Therefore, the relevant contact models for this study correspond to the representation of contact between two cylinders with parallel axes. The contact of cylinders with parallel axes, is described as 'line contact', because it depicts a contact area of width $2b$ with length L, as shown in **Figure 7.4**, for which the half width b is the most representative parameter of the contact area.

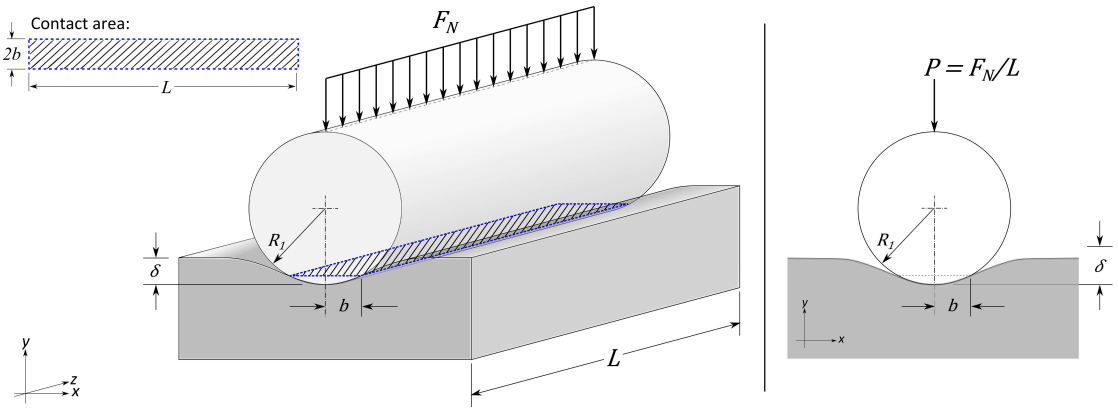

Figure 7.4: Line contact between a cylinder and a flat surface. The contact between a cylinder of radius R_1 and a half-space providing a flat surface, both of length L in the x direction, under indentation force of magnitude F_N, equally distributed along the cylinder length, causes the flat material to deflect a distance δ, resulting in a contact area of $2b \times L$, where b is the half width of the line contact area. This system can be simplified in 2D under the assumption of plane strain (infinitely long cylinders), where indentation in caused by a punctual load of magnitude P (right).

The relevant analytical contact models describing the contact interaction of cylinders with parallel axes are reviewed in **Section 7.3**. The validation of the finite element model was performed with the use of the idealised skin model under micro-indentation conditions (AceGen/AceFEM software package). The contact area and deflection responses were registered at each converged time increment of the simulations. The validation process consisted of the evaluation of sensitivity of contact area and deflection parameters, to the variation of stiffness of the half-space material, indenter radius and indenter displacement. The results of the finite element models were compared against those of the analytical models.

For the validation of the macroscopic interaction models implemented in the Abaqus software package, micro-scale frictionless indentation was implemented in this software for the comparison of the results obtained in AceGen/AceFEM. The measurements of the contact area and deflection response in both software packages, taken at each converged times steps of the simulations, were compared to one another and to the analytical models results.

7.2.4 Analysis of the results

The evaluation of the contribution of skin topography and microstructure to its global friction response was evaluated considering:

a) **contact area:** comparison of the real and apparent contact area, under pure indentation;

b) **friction response:** comparison of the global friction response with respect to the specified local coefficient of friction; and

c) **distribution of shear stress:** evaluation of the shear stress distribution throughout the skin layers.

The analysis of the results was performed by comparing the results of the idealised skin model with those of the anatomical one, whilst the effects of the interaction scale, local coefficient of friction and humidity conditions were accounted for. The procedures followed for the analysis of the results are described next.

7.2.4.1 Contact area

The area of contact, related to the adhesive component of friction (Wolfram, 1983), was evaluated in terms of the *relative contact area*, described as the ratio of the real contact area A_r with respect to the apparent (or projected) one A_p. These metrics are given by $A_r = 2b_rL$ and $A_p = 2b_pL$, where b_r is the real half width of the contact area, calculated as the half of the sum all regions in contact, and b_p is the apparent (also mentioned as projected) half width of the contact area.

The relative contact area is then represented by:

$$\frac{A_r}{A_b} = \frac{2b_rL}{2b_pL} = \frac{b_r}{b_p} \tag{7.10}$$

where the b_r/b_p is referred as the **half-width ratio**.

In the finite element simulations, b_p was measured as half of the distance projected on the mean contact surface (x direction), between the first and last nodes in contact. b_r, otherwise, was measured with the following algorithm, implemented in the AceGen/AceFEM models:

1. Detection of the nodes in contact n_i ($i = 1, 2, ..., N_n$), and their location in the current configuration in the coordinates given by (x_{n_i}, y_{n_i});

2. identification of the initial and final nodes in contact (n_1 and $n_f = n_{N_n}$) for the calculation of b_p:

$$b_p = \left(x_{n_f} - x_{n_1}\right)/2; \tag{7.11}$$

3. calculation of the projected distance d_{n_i} between each of the nodes in contact, parallel to the skin surface plane:

$$d_{n_i} = x_{n_i} - x_{n_{i-1}}, \quad 2 \leq i \leq f \tag{7.12}$$

4. identification of the median projected distance $\tilde{d_{n_i}}$; the use of the median value of d_{n_i} for the estimation of the real contact area, instead of a mean one, was implemented in order to prevent effects caused by the larger distances observed for nodes located at the furrows periphery in the anatomical models;

5. calculation of the real half width as:

$$b_r = \frac{N_n \tilde{d_{n_i}}}{2} \tag{7.13}$$

where N_n is the total number of nodes in contact.

This procedure, illustrated in **Figure 7.5**, is mesh-dependent. A word of caution is advised in the interpretation of the half width ratio at the smaller areas of contact.

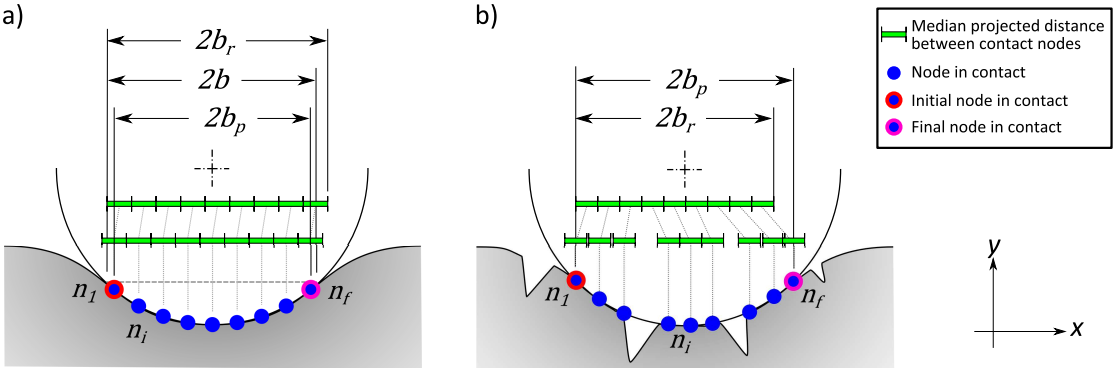

Figure 7.5: Procedure for the measurement of the projected and real half width. The projected contact area width $2b_p$ is estimated by accounting for the distance between the initial node in contact n_1 and the final node in contact n_f. The real contact width $2b_r$ is estimated by multiplying the amount of nodes in contact n_i by the median projected distance between the contact nodes. For *a)* idealised skin model, it is expected that the total width $2b$ has similar values than $2b_p$ and $2b_r$, while in *b)* the anatomical skin model, $2b_r < 2b_p$.

For the macro-scale models, the same procedure for the measurement of b_p was followed. However, the b_r algorithm was not implemented in Abaqus, and the measurements were performed using the distance measuring tools provided by the software from the output results.

In the conditions provided by the smooth surface of the idealised model, it is expected that $b_p \approx b_r$ (while in the anatomical model $b_r < b_p$). For this reason, the idealised

model was used for the verification of the b_r calculation algorithm. With an homogeneous skin material, it was confirmed that $b_r \approx b_p \approx b$. However, with a stiffer *stratum corneum*, the contact area was much smaller, so the algorithm was unable to capture b_r, confirming the mesh sensitivity of the algorithm.

In a linear regression of the measurements obtained for the homogeneous model, a slope of 0.9988 was found for the projected and real half width values, within a relative error of 0.2% of the ideal fit. Furthermore, a correlation of $R^2 = 0.99978$ was observed between the b_p and b_r, showing that for these conditions (homogeneous skin model, with $E_{SC} = E_{VE-DE} = 0.6$ MPa, the use of the projected half width is reliable to represent the ideal conditions of contact. **Figure 7.6** shows the effectiveness of the algorithm for half width values larger than 0.06 mm, but mesh sensitivity of the algorithm was observed for half width values lower than 0.06 mm. For $b_r < 0.06$ mm, the mean relative error of b_r with respect to b_p was of 8.8%, while for larger deflection the relative error was of 2.7%.

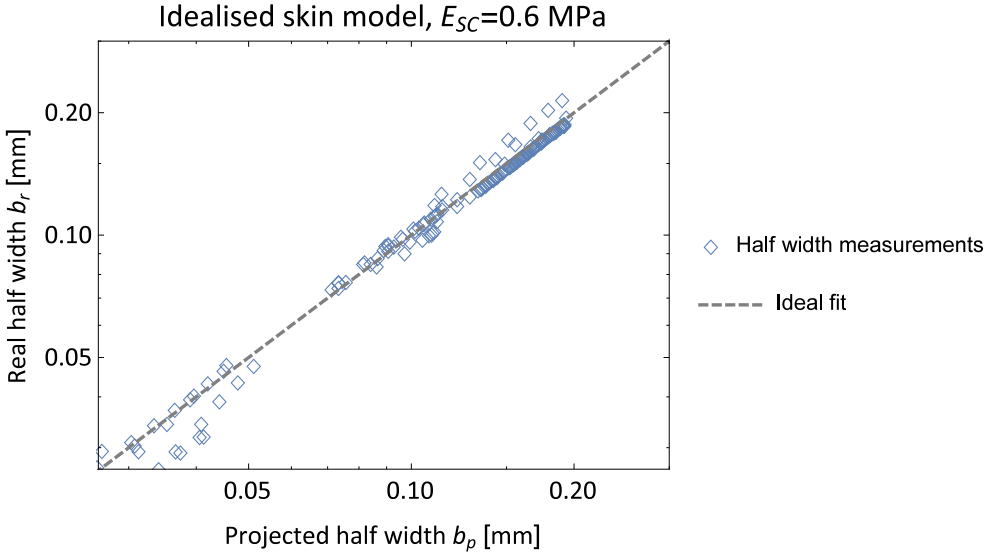

Figure 7.6: Fit of projected and real half width measurements for idealised homogeneous conditions. The real half width values were compared against the projected half width measurements in the simulation of micro and macro indentation, under idealised homogeneous conditions (ideal skin model, with $E_{SC} = 0.6$ MPa). The results showed good correlation, with a close fit to the ideal conditions, so $b_p \approx b_r$. The dashed line represents the ideal fit for $b_p = b_r$.

7.2.4.2 Friction response

The analysis of the **global friction** was performed by measuring the components of the reaction force at the indenter, normal and tangential to the mean contact surface, at each converged increment of the sliding simulations. The ratio between the magnitude of these components was taken as a measurement of the global coefficient of friction (**Equation 7.8**). These measurements were analysed by reporting their probability

distribution, which was analysed with respect to the specified local coefficient of friction considering all the interaction scales. A second analysis evaluated the contribution of each interaction scale to the global friction response, to investigate the interaction scale dependency of the global response. A third analysis considered the evaluation of the global friction response with respect to the indenter lateral displacement, for the evaluation of the global friction sensitivity to the topographic features of the skin model.

7.2.4.3 Shear stress distribution

The analysis of shear stress distribution was performed with three different approaches, during both pure indentation and sliding contact simulations. The first approach involved the analysis of shear stress distribution throughout the whole area of interest, allowing to observe the effects of geometry, stiffness of the *stratum corneum* (to indirectly represent relative humidity) and interaction scale throughout the whole area of interest. The second approach involved the evaluation of shear stress magnitude and distribution with respect to the geometrical location of the skin topographic features; this analysis was performed for specific skin layers, in order to capture the contribution of the skin microstructure on the transmission and concentration of shear stress. In the third analysis, only performed in pure indentation, compared the direction of the third stress eigen vectors at each node, throughout the area of interest, providing an insight to the influence of the skin topography in the compressive response of skin (due to indentation).

7.3 Analytical validation of the finite element models: relevant analytical models validation procedure

Under the action of an indenting load of magnitude F_N, equally distributed along the length L of a cylinder, the Hertz theory of contact, defines the half width the contact area (i.e. contact radius) between two cylinders with parallel axes as:

$$b = \sqrt{\frac{4R^* F_N}{\pi L E^*}} \tag{7.14}$$

where R^* and E^* are the reduced radius and reduced Young's modulus respectively. The reduced radius is defined in terms of the radii of the contacting parts:

$$\frac{1}{R^*} = \frac{1}{R_1} + \frac{1}{R_2} \tag{7.15}$$

which, considering $R_2 \rightarrow \infty$, results in $R^* = R_1$. The reduced Young's modulus is defined in terms of the elastic properties of the materials in contact as:

$$\frac{1}{E^*} = \frac{1-\upsilon_1^2}{E_1} + \frac{1-\upsilon_2^2}{E_2} \tag{7.16}$$

where subindexes 1 and 2 refer to the indenter and flat materials, respectively. Assuming that $E_1 \rightarrow \infty$ for a rigid indenter,

$$E^* = \frac{E_2}{1-\upsilon_2^2} \tag{7.17}$$

Although the Hertz theory is widely accepted to estimate the half width of the contact area between a cylinder in contact with a flat surface, no common consensus has been reached for the analytical estimation of the surface deflection. The application of the Hertzian theory for cylinders with parallel axes does not not capture δ when one of the cylinders is represented with an infinite radius (i.e. a half-space) (Puttock and Thwaite, 1969), as $\lim_{R_2 \rightarrow \infty} \delta = \infty$. A great variety of models have been proposed in the literature for the estimation of δ, for which a review is presented next, identifying each model with a Roman number subindex. Norden (1973) provided an in-depth review of various models for contact of cylinders with a half-space. One of these models corresponds to the expression obtained from the work of Thomas and Hoersch (1930) and Love (1942):

$$\delta_I = \frac{F_N}{L\pi E^*}\left[1 + \text{Ln}\left(\frac{L^3\pi E^*}{F_N R^*}\right)\right] \tag{7.18}$$

which, although expressed in a different arrangement of parameters, is coincident with the work of Lundberg (1939) and Puttock and Thwaite (1969). Another model corresponds to the work of Ferguson (1957), considering an elliptical distribution of pressure on the plane surface:

$$\delta_{II} = \frac{F_N}{L\pi E^*}\left[-0.608205 + 1.5\ \text{Ln}\left(\frac{L^3\pi E^*}{F_N R^*}\right)\right] \tag{7.19}$$

From the formulation for deflection of one half of a cylinder compressed by two diametrical forces (Johnson, 1985), the deflection between two parallel cylinders can be derived as:

$$\delta_{III} = \frac{F_N}{L\pi E^*}\left[\text{Ln}\left(\frac{4R^* L\pi E^*}{F_N}\right) - 1\right] \tag{7.20}$$

which is equivalent to the solution presented by Nakhatakyan (2011). Johnson (1985) also presented a model for 2D contact between a cylinder and a half-space, estimating the deflection of a plane surface with respect of a point located directly underneath the indenter contact point at a distance ζ as:

$$\delta_{IV} = \frac{F_N\left(1-\upsilon_2^2\right)}{L\pi E_2}\left[2\ \text{Ln}\left(\frac{2\zeta}{b}\right) - \frac{\upsilon_2}{1-\upsilon_2}\right] \tag{7.21}$$

which, assuming the indenter is much stiffer than the half-space material (i.e. $E_1 >> E_2$), is equivalent to the total deflection. It was indicated that ζ can be used to indicate the depth h_s of the half-space in the model, as it does affect the contact interaction. Considering the thickness of the flat material, Johnson (1985) reviewed the Wrinkler *elastic foundation* model. This model represents the flat material as an elastic foundation resting on a rigid surface instead of a half-space. The elastic response of this material is dependent on the displacement normal to the surface and excludes any shear response. Such behaviour is analogous to a mattress whose deformation is given by the resistance of its springs. With the Wrinkler model, the 2D contact between a cylinder and the 'mattress' material can be approximated as:

$$\delta_V = \frac{3F_N}{4L\left(1.18E^*\right)} \tag{7.22}$$

The last model presented in this section, applied in the analysis of contact in roller bearings, reviewed by Harris and Kotzalas (2007), accounts for the models from Lundberg (1939) for line contact with semi-cylindrical stress distribution at the contact area:

$$\delta_{VI} = \frac{2F_N\left(1-\upsilon_2^2\right)}{L\pi E_2}\,\mathrm{Ln}\left[\frac{L^2\pi E_2}{F_N\left(1-\upsilon_2^2\right)}\right] \tag{7.23}$$

All these models (**Equations 7.14, 7.18-7.23**), were developed under the assumptions of Hertzian theory (Harris and Kotzalas, 2007; Johnson, 1985; Norden, 1973; Puttock and Thwaite, 1969):

a) the materials are linear elastic;

b) the contacting surfaces are perfectly smooth and frictionless;

c) loading is applied normal to the contact surface, neglecting shear effects;

d) the area of contact is much smaller than the surface dimensions of both contacting bodies; and

e) strain levels are small and within the elastic regime.

The **validation of the computational model** was performed using the idealised skin model, with homogeneous mechanical properties, under micro-scale indentation. By varying the stiffness of the flat material (i.e. skin) E_2, the indenter radius R_1 and displacement of the indenter D_y, three sampling sets of 25 experiments were generated by following the procedure for the sensitivity analysis presented in **Section 5.2.4.1**. Each set of experiments, identified as a sensitivity analysis (SA), was set within different ranges of parameters, considering the effects of different levels of indentation and stiffness of the flat material, as listed in **Table 7.1**.

Table 7.1: Parameter limits for the analyses of sensitivity of half width and deflection sensitivity of the analytical models, with the use of the idealised skin contact model. E_2 - Young's modulus of the flat material.

Analysis	Limits	E_2 [MPa]	R_1 [mm]	D_y [mm]
SA 1: Large indentation	min	0.01	0.05	0.01
	max	400.0	0.5	**1.0**
SA 2: Small indentation	min	0.01	0.05	0.01
	max	400.0	0.5	**0.05**
SA 3: Low stiffness of flat material	min	0.01	0.05	0.01
	max	**1.0**	0.5	0.5

Given the variety of models proposed for the analytical description of deflection δ, the first analysis was performed for determining which of these models could appropriately capture the skin deflection, assuming it could be represented as the idealised model. Despite the imposed indenter displacement, the maximum deflection captured in the sensitivity analysis simulations was $\delta = 0.42$ mm. The deflection results were compared against the six analytical models reviewed (**Equations 7.18** to **7.23**). Models δ_{III} and δ_V showed a large difference from the simulations results, while higher agreement was shown for models δ_I, δ_{II}, δ_{IV} and δ_{VI}, especially for $\delta < 0.1$ mm (**Figure 7.7**). At such a small deflection ($\delta < 0.1$ mm), model δ_{IV} showed a mean and median error of 5.43% and 5.48%, respectively, and an interquartile range of 0.007. This model was of higher accuracy (lower error and lower dispersion) for the conditions applied in these simulations. **Table 7.2** shows the relative error comparison between the six models here evaluated and the finite element results for $\delta \leq 0.1$ mm.

The variation observed among the analytical deflection models results reflect the different conditions considered in their development. In these simulations, where the height of the skin model was considered to be $h_s = 5$ mm, the analytical model δ_{IV} showed higher correspondence with the finite element model results. However, further analysis is required to evaluate the role of the parameter h_s has on the simulation results, and how it would compare with the different analytical deflection models.

Table 7.2: Error analysis between the analytical deflection models and the finite element (FE) results. Mean and median values of the relative error distribution for deflection $\delta < 0.1$ mm are compared, showing the interquartile range (IQR) as a measure of error dispersion. Lower error and dispersion was found in model δ_{IV}, as marked in bold font.

Model	Mean error [%]	Median error [%]	IQR
FE	0.0	0.0	0.0
δ_I	23.05	23.17	0.0315
δ_{II}	6.30	5.92	0.0672
δ_{III}	53.05	52.88	0.1056
δ_{IV}	**5.43**	**5.48**	**0.0070**
δ_V	80.35	80.25	0.0273
δ_{VI}	10.78	9.26	0.1032

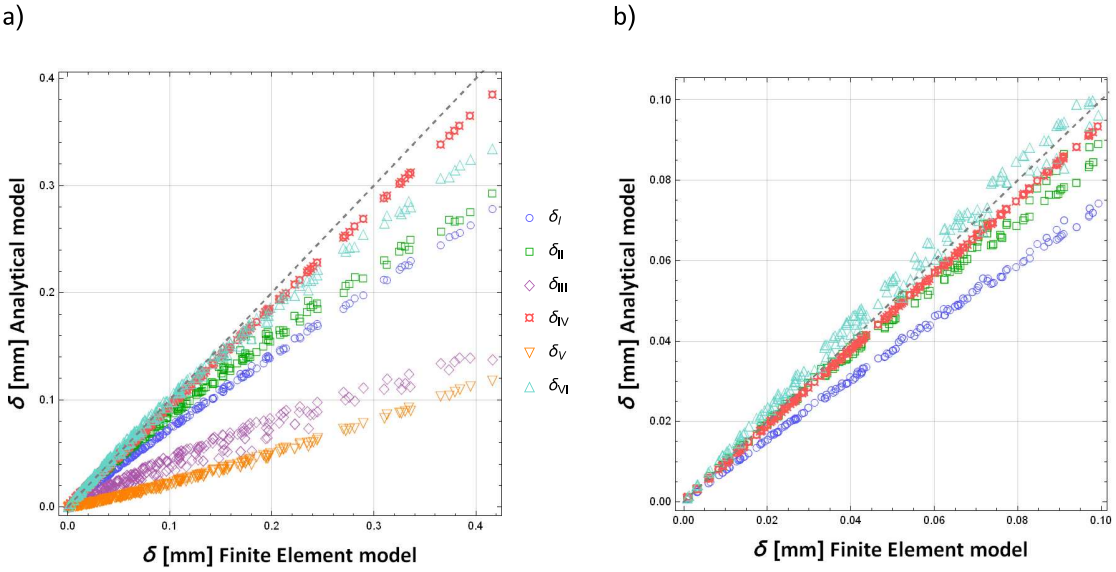

Figure 7.7: Analysis of the analytical deflection models. The deflection results of the finite element (FE) model simulations were compared against the results of the analytical models δ_I to δ_{VI} for *a*) the full range of deflection observed in the simulations, and *b*) for $\delta < 0.1$ mm, focusing on the models with closer match to the ideal fit (dotted line), indicating a perfect fit between the theory and computations.

In order to complete the validation analysis, both analytical models for half width (**Equation** 7.14) and deflection (δ_{IV} -**Equation** 7.21) where compared against the measurements performed in the finite element models. The summary of the results of the sensitivity analyses is displayed in **Figure** 7.8. These results show good agreement between the analytical and FE solutions, completing the validation of the model. Furthermore, it was shown that the effects of damping, implemented for the stabilisation of the contact, were minimal.

The previous analysis was performed for micro-indentation simulations, where the results provide validation of the AceGen/AceFEM model (Mathematica —Wolfram Research, Inc., Champaign, IL, USA.). For the validation of the macroscopic model developed in Abaqus (Simulia, Dassault Systèmes, Providence, RI, USA) the idealised micro-scale homogeneous conditions were implemented, and the skin deflection and half width values were compared against the analytical models (**Equations** 7.14 and 7.21). Both software packages showed similar results, and the measurements of half width and deflection were in agreement with the analytical models, as shown in **Figure** 7.9. The results of these preliminary validation steps indicate that the modelling strategy proposed in this study is based on a sound assumptions and numerical methods. This indicates that both microscopic and macroscopic interaction simulations are compatible for the analysis of the effects of interaction scale in the skin tribological response.

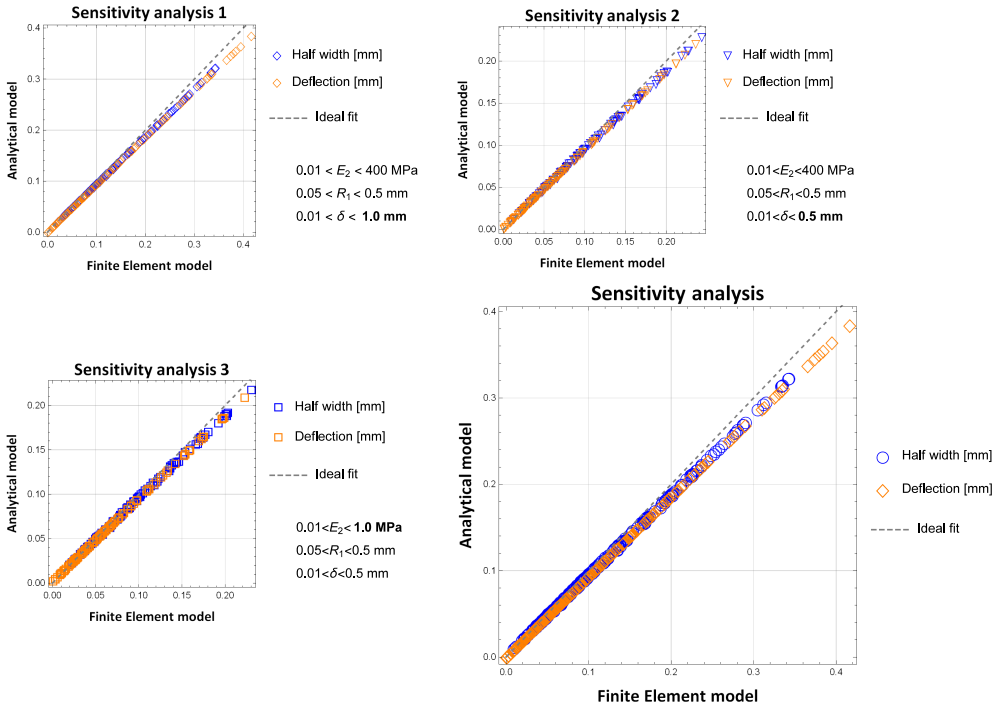

Figure 7.8: Fitting of the sensitivity analysis results with the analytical models for the calculation of half width, using the Hertz model described in **Equation 7.14**, and deflection, calculated with model δ_{IV} given in **Equation 7.21**. The small plots show the results of the individual sensitivity analyses, with all the results gathered in the large plot (bottom right).

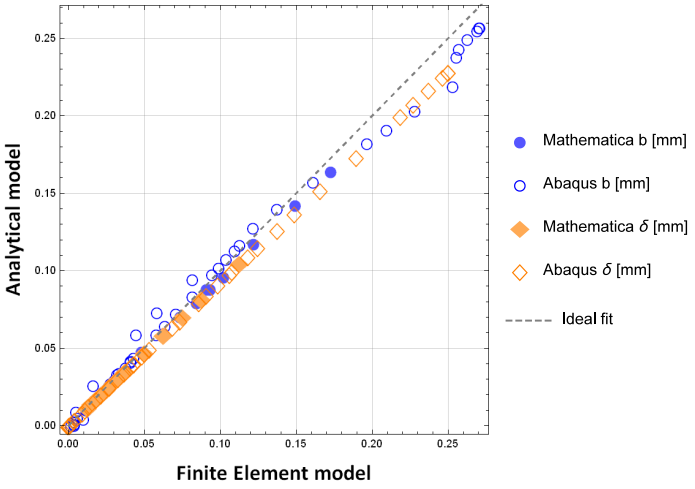

Figure 7.9: Congruency of the results in Mathematica and Abaqus FEA software packages was confirmed by good agreement in the results, compared here against the analytical model of half width b (**Equation 7.14**) and deflection δ (using model δ_{IV} in **Equation 7.21**).

7.4 Results

7.4.1 Contact area

The analysis of the contact area was focused on the comparison of the real and apparent contact area, under pure indentation. The ratio between these parameters represents the relative contact area, which was evaluated in terms of the half-width ratio b_r/b_p described in **Section 7.2.4.1** (**Equation 7.13**).

Figure 7.10 shows the half-width ratio measurements of the idealised (grey markers) and anatomical (coloured markers) models, with respect to the skin deflection, captured a the node with higher displacement in the indentation direction. Due to difficulties for capturing b_r in stiff materials (much smaller contact area), the results showed here are limited to the models assuming high humidity conditions, where $E_{SC} = 0.6$ MPa. Each plot compares the half width ratio observed at the different contact scale, for each specified local coefficient friction μ_l. In **frictionless conditions** (top left plot), it is observed that for the **idealised model** $b_r \approx b_p$ for all indentation scales, which confirms the accuracy of the algorithm developed for the calculation of b_r; the **anatomical model**, as expected, showed considerably lower half-width ratio with high dependency on the indentation scale. **Increase of the local coefficient of friction** have low effects in the **idealised model**, where the effects of the mesh-dependency of the half-width ratio measurements becomes obvious for $\delta < 0.05$ mm; nevertheless, ignoring the results obtained with $R_1 = 0.1$ mm (where the mesh-dependency effects are higher), the half-width ratio measurements of the idealised model showed a mean value of 1.0114, within a range between 0.884 (for $R_1 = 0.5$ mm at $\mu_l = 0.3$) and 1.0913 (for $R_1 = 0.25$ mm at $\mu_l = 0.1$). In the **anatomical model**, the results showed to high sensitivity to the interaction scale, showing lower half-width ratio for greater indenter radii; however, the effects of the local coefficient of friction on the relative contact area are not clear in these plots.

The effects of the local coefficient of friction on the relative contact area, at the different interaction scale, are shown in **Figure 7.11**. The plots compare side by side the results of the idealised and anatomical models. The sensitivity of the measurements to the mesh size are more obvious in these plots, for $\delta < 0.05$ mm, showing great dispersion in the idealised model for $R_1 = 0.1$ mm, and the anatomical one for $R_1 = 0.25$. For $R_1 = 0.5$ mm, more consistent results are shown for $\delta > 0.05$ mm. For this indenter size, it is apparent that with local frictionless conditions the half with ratio is higher. However, the results do not show an obvious trend between the local coefficient of friction and the relative contact area for $\mu_l > 0.0$, neither for the idealised nor the anatomical model. For macroscopic scale interactions ($R_1 \to \infty$), the half-width ratio showed no sensitivity to the local coefficient of friction.

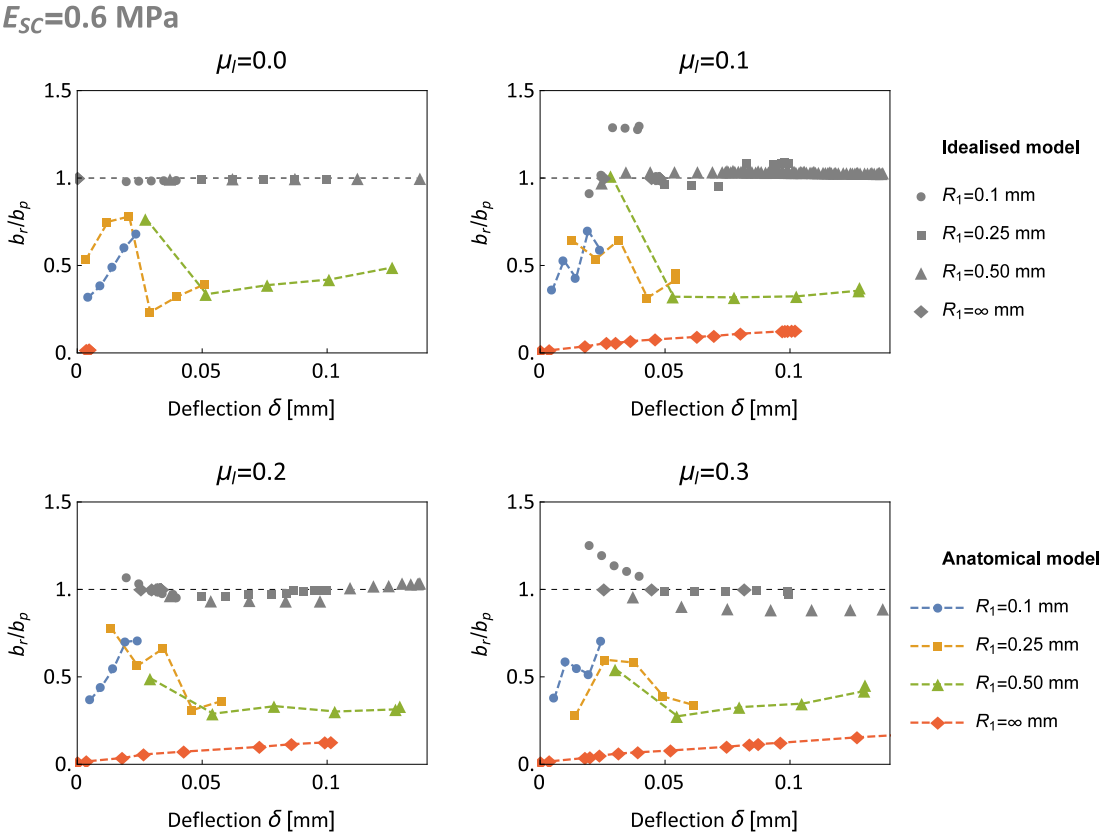

Figure 7.10: Effects of the skin microstructure and indentation scale in the half width ratio measurements at different skin deflection values. While the ideal model results (grey markers) show a constant trend of the ratio between the real and project half width of $b_r/b_p = 1.0$, with dispersion in the results for all radii caused by higher coefficient of friction, different trends of b_r/b_p were observed for the anatomic model (coloured markers) at each indentation scale: highest slope in the half width ratio trend was observed for the smaller indenter radius $R_1 = 0.10$ mm, and lower for the the macroscopic indentation scale where $R_1 = \infty$. See **Figure 7.5** for the description of the procedure for calculation of b_r and b_p.

For the **anatomical model**, an apparent correlation between the half-width ratio and the level of deflection was observed in **Figure 7.11**. In order to analyse the effects of high deflection in the relative contact area, larger deflection was implemented in the macroscopic indentation simulation. By establishing a non-frictionless interaction at the indenter-skin interface, the contact instabilities in the simulation are reduced. This was reflected in the simulations with higher coefficient of friction, which showed better convergence in the results, thus reaching higher deflection levels. Considering that the half-width ratio showed not sensitivity to this parameter, this analysis was performed for $\mu_l = 0.3$. In order to increase the level of compression on the skin, this analysis was performed with a mean skin thickness of 4 mm, where 20% compression, in the direction normal to the skin surface, was applied.

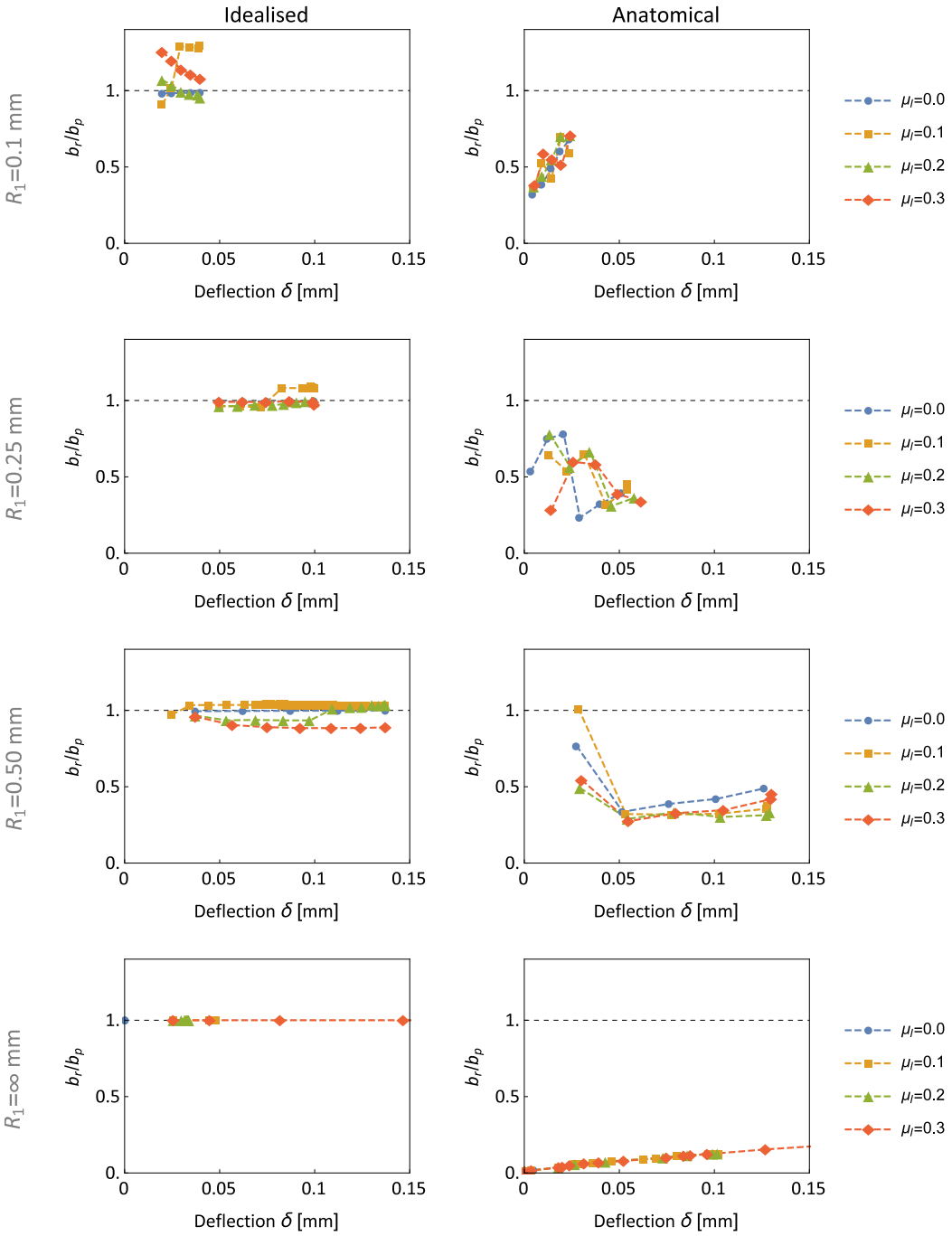

Figure 7.11: Analysis of the friction effects on the half width ratio at each indentation scale. No specific link between the local coefficient of friction μ_l and the half width ratio (comparing the real and projected half width measurements b_r/b_p) was found at the different indenter radii R_1. However, at macroscopic indentation ($R_1 = \infty$) the results showed no sensitivity to μ_l.

Figure 7.12 shows the half-width measurements taken throughout each of the converged time increments of the simulation. These measurements were compared with respect to a function derived from a quadratic regression of the measured values with respect to the deflection level. With a correlation of $R^2 = 0.998$, the half-width ratio appears to plateau with higher deflection, not reaching a full contact area (where $b_r/b_p = 1.0$), as commonly assumed in the literature.

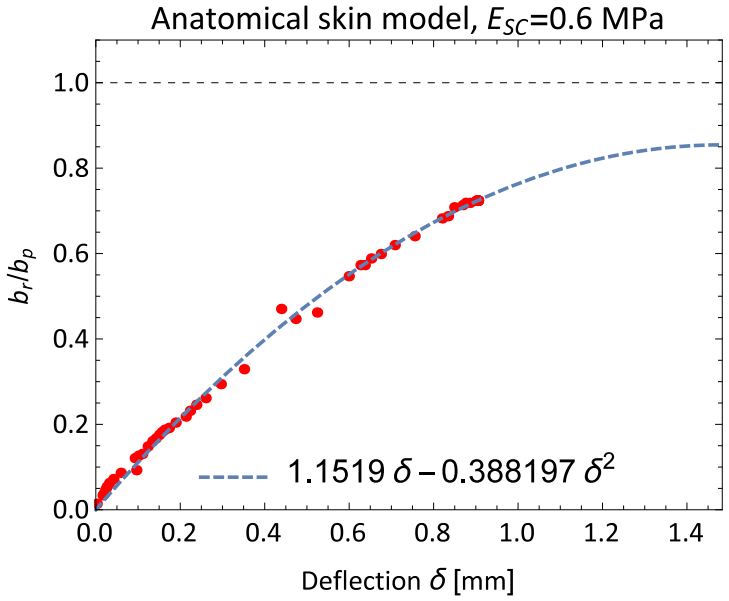

Figure 7.12: Half width ratio behaviour at high deflection in macro-indentation. The ratio between the real and projected half width (representing the ideal contact conditions, with a flat surface), b_r/b_p shows a parabolic trend with the increment of deflection imposed by the indenter.

7.4.2 Friction response

In the analysis of the friction response, the distribution of the global coefficient of friction measurements with respect to the specified local coefficient of friction was compared. In these results, the evaluation considered the effects of humidity (through variation of the *stratum corneum* stiffness E_{SC}) and interaction scale during sliding contact. The measurements were taken at each converged time increment of the simulations, while the centre of the indenter was located within the area of interest (as indicated earlier in **Figure 7.2**).

The **first analysis** considered the global response at all interaction scales. **Figure 7.13** shows the probability distribution of the measurements of the global coefficient of friction. The lines plotted indicate the location of the top centre of the probability histogram distributions (being dependent the bandwidth of the histograms bins). On top the histogram lines, a box plot indicates the median value of the coefficient of friction $\tilde{\mu_g}$ (darker line), the interquartile range (IQR) (coloured box) and the total range of

values (horizontal coloured line). The values of the local coefficients of friction μ_l analysed are indicated with the grey dashed line.

Figure 7.13 shows that for the idealised model (left), in frictionless conditions (blue), the global coefficient of friction was coincident to the local one with almost no variation; a median value of approximately 0.0003 was found in both cases (this is more clear on the box plot). As the local coefficient of friction increased, a shift between the global and local friction (i.e. $|\tilde{\mu_g} - \mu_l|$) was observed, showing that $\mu_g < \mu_l$. Nevertheless, such shift was less pronounced in the idealised model with stiffer *stratum corneum*. This was shown by shift values ranging from 0.017-0.031 for $E_{SC} = 0.6$ MPa, and 0.004-0.006 for the stiffer $E_{SC} = 370$ MPa. In all the ideal cases, low dispersion in the μ_g results was observed with IQR values lower than 0.018.

A completely different picture was observed for the **anatomical skin model** (right), where higher dispersion of the values was observed in all the cases, where the IQR depicted ranged from 0.16-0.33 for soft *stratum corneum*, and 0.23-0.28 in the stiff one. Given the response of the idealised model where no shift of the global response was observed in the frictionless conditions (blue), the distribution of global friction measurements in the anatomical model for $\mu_l = 0.0$ reflects the pure effect of the skin topography. This was reflected in both frictionless cases of the anatomical model, where the global response was $\tilde{\mu_g} = 0.184$ with IQR$= 0.243$ for the soft *stratum corneum*, and $\tilde{\mu_g} = 0.168$ with IQR$= 0.228$ for stiff one. With $\mu_l > 0.0$, the global friction response was increased with higher shift of global friction for higher values of μ_l in the low stiffness model (top), but no clear trend between the $\tilde{\mu_g}$ and μ_l was observed. A striking result was provided from the anatomical model with stiff *stratum corneum*, which showed low sensitivity to μ_l, where the values of $\tilde{\mu_g}$ showed and approximate value of $\tilde{\mu_g} \approx 0.224$ with an average IQR of 0.257, with values similar to those observed for the two frictionless cases.

In **Figure 7.13**, the results showed the combined response of all the interaction scales. In order to isolate the effects of the interaction scale from those measurements in the anatomical models, the **second analysis** compared the global friction distribution for each μ_l, with respect to the indenter size. Due to convergence problems in the macroscopic scale interactions, these results were omitted from the analysis. The curves, like in the previous figure, describe the location between the centre of the top of the probability histogram bars. These results are presented in **Figure 7.14**.

In frictionless conditions, no sensitivity of the global coefficient of friction distribution to the indenter size was observed for $E_{SC} = 0.6$ MPa; however, a clearly higher probability was found for the larger indenter for $E_{SC} = 370$ MPa, with a $\tilde{\mu_g} = 0.133$ and IQR of 0.12 (the IQR of the smaller indenters was of 0.24 and 0.28). With larger values of μ_l, specific indenter radii showed low-dispersion in the distribution of global friction

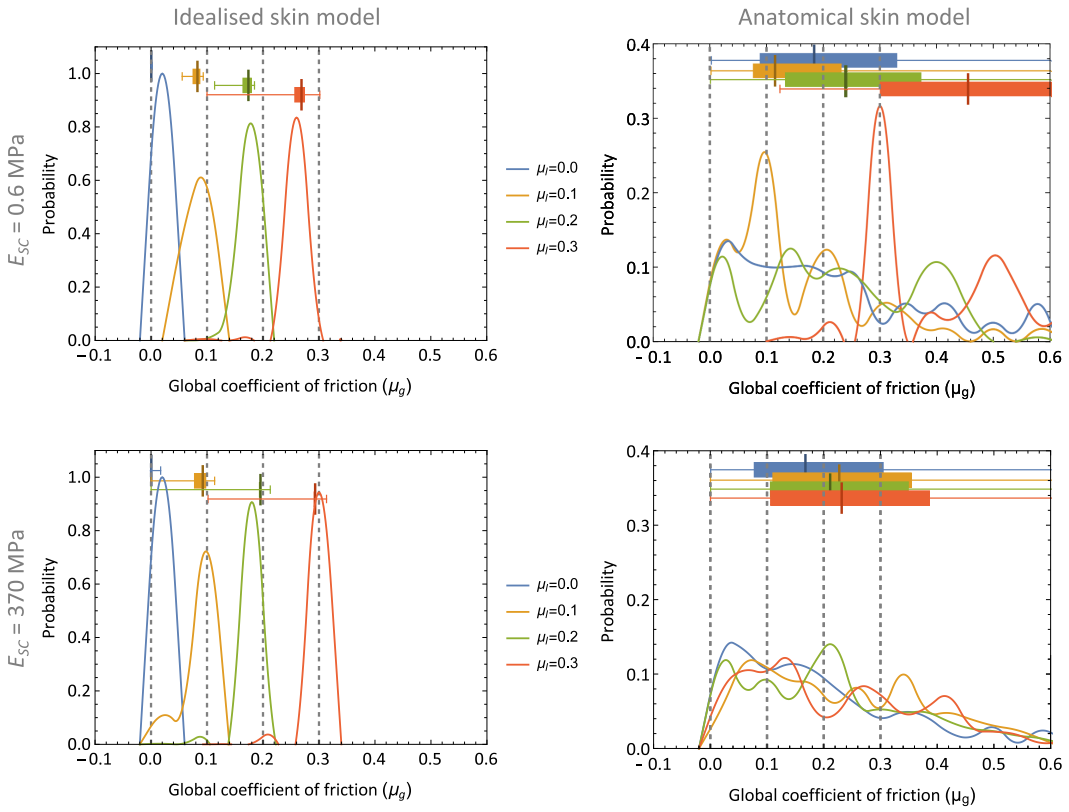

Figure 7.13: Probability distribution of global coefficient of friction in sliding simulations. During the sliding friction simulations, the reaction forces in the indenter were recorded along the lateral displacement on top of the area of interest. These measurements were used for the calculation of the global coefficient of friction μ_g, plotted here in where the graphs locate the top centre of the histogram bars for the ideal skin model (left) and the anatomic one (right), considering a soft stratum corneum (top) and the stiffer one (bottom). The median value and interquartile range is highlighted by the box plots on the top of each graph.

measurements, but no specific trend between the indenter size and global friction response was observed. An eye-striking result was found for the stiffer *stratum corneum*, under a local friction defined by $\mu_l = 0.3$ where, noting the difference scale in the chart frame, where a $\tilde{\mu_g}$= 1.59 with an IQR of 0.005 was found for $R_1 = 0.1$ mm. The analysis of the simulations raw data indicated that this was a case where the indenter lateral displacement reached only 8.8% of the intended displacement before the simulation stopped as no converged solution was found. Such displacement corresponds to the location of one crest of the skin topography, providing high resistant to motion due to micro-asperity interlocking (considering the 1 mm radius indenter as a single asperity).

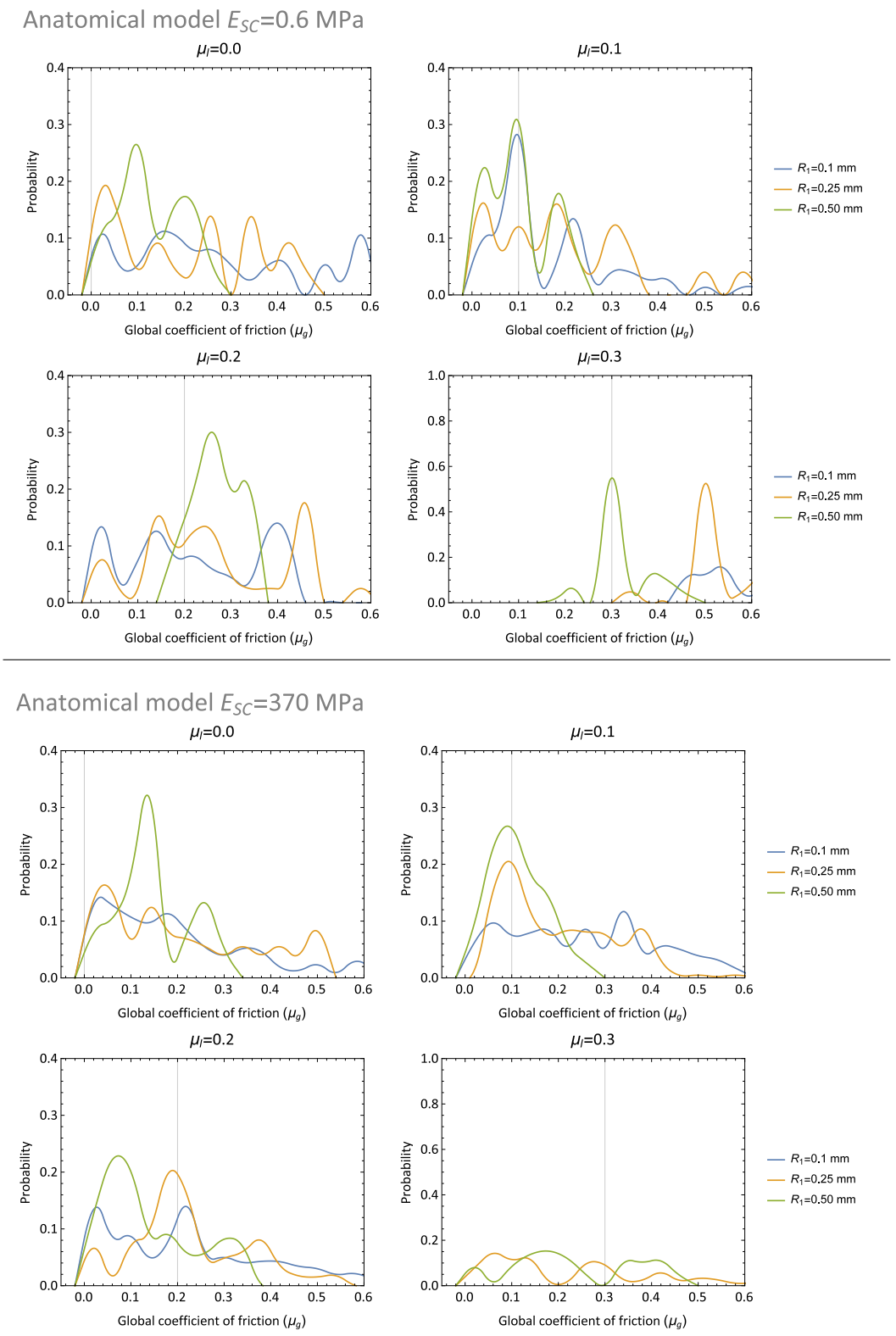

Figure 7.14: Probability distribution of global coefficient of friction in sliding simulations—interaction scale analysis. Each graph compares the distribution of global coefficient of friction measurements obtained for different indenter radius R_1, at different imposed local coefficient of friction μ_l (indicated with the grey vertical line). Only the results for micro-scale interactions were evaluated.

The **third friction analysis** consisted in the evaluation of the global friction response with respect to the indenter lateral displacement, showing the sensitivity of the global friction response to the topographic features of the skin model. The global friction response was evaluated in the idealised and anatomical models, for different specified local coefficients of friction. The idealised model results provided required contrast to isolate the effects of the skin topography and microstructure on the anatomical model results. Like in the previous analyses, only the global friction measurements taken within the models's area of interest were considered.

Figure 7.15 shows the geometry of the *stratum corneum* corresponding to the idealised (left) and the anatomical (right) skin models, with respect to the models coordinate system (x, y). Each of the global friction measurements taken during sliding contact, were plotted according the location of the indenter centre in the sliding direction. The effects of sensitivity of the *stratum corneum* to relative humidity were also considered in the analysis.

Under the idealised conditions, most of the global coefficient of friction measurements were maintained under their respective specified local friction. These effects were more significant in the soft *stratum corneum* simulations, indicating the contribution of local deformation. In the idealised simulation results, it is apparent that the dispersion observed for the idealised models with $\mu_l > 0.0$ (**Figure 7.13**) could be caused by stick-slip phenomena, as reported in the experiments by Pailler-Mattei et al. (2007). In the simulations performed with the anatomical models, the magnitude of the global friction response was considerably higher than the local one. With the stiffer *stratum corneum* ($E_{SC} = 370$ MPa), the effects where scaled up approximately 30%. The pattern of the measurements indicated high resistance when the centre of the indenter was located on top of the skin furrows, where the skin crests provide resistance in the form of asperity interlocking. Similar patterns of global friction response were observed across the skin surface, independently of the specified local coefficient of friction.

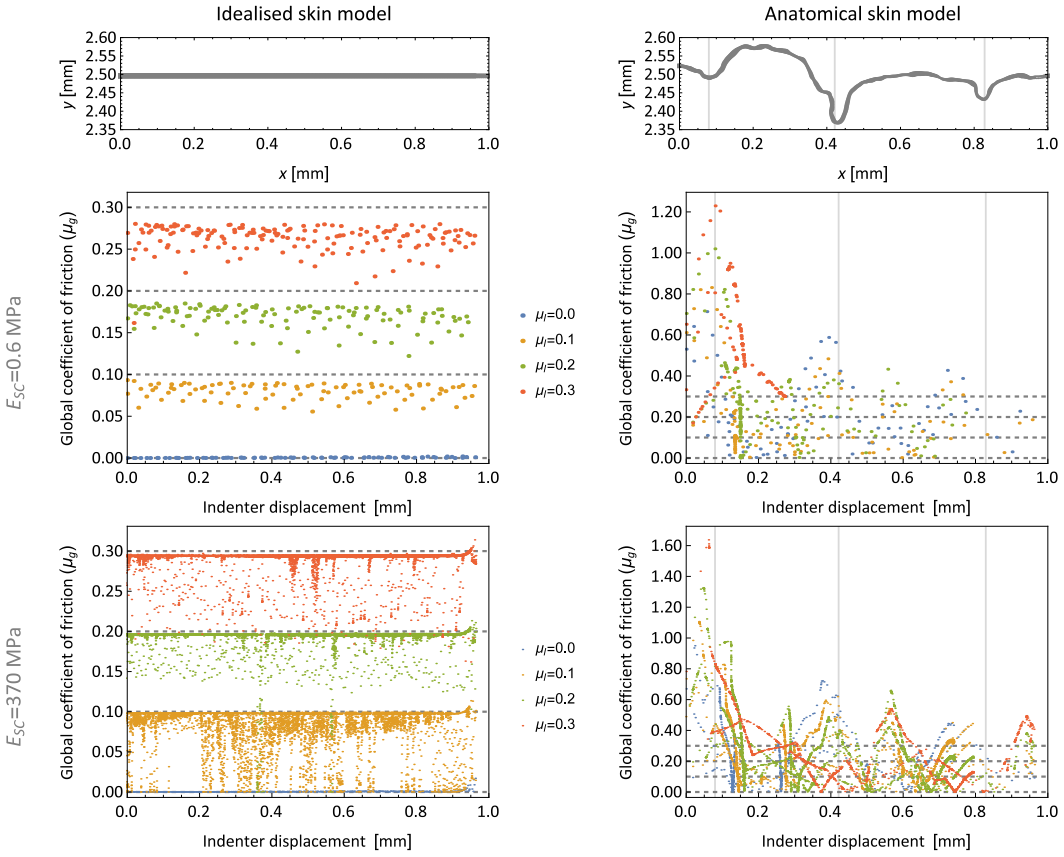

Figure 7.15: Global friction response across the skin surface. The geometry of the skin models (grey) is provided with respect to its location in the model coordinate system (x, y) for the identification of the effects of skin geometry on the global friction response. The idealised model results are shown on the left, and those of the anatomical model on the right, showing the location of the skin furrows with the vertical gridlines. The colour plots show the measurements of the global coefficient of friction across the skin surface, resulting from the lateral displacement of the indenter, for different local coefficients of friction μ_l. The colour plots in the top show the results obtained for the simulations with soft *stratum corneum* ($E_{SC} = 0.6$ MPa); those of the simulations with stiffer *stratum corneum* ($E_{SC} = 370$ MPa are shown in the bottom).

7.4.3 Shear stress distribution

The evaluation of shear stress distribution within the area of interests was done for both pure indentation and sliding contact. In the idealised homogeneous model, the shear distribution was expected to reveal a scaled pattern for the different indenter radius $R_1 \leq 0.5$. Using this pattern as a reference, the effects caused by having a stiffer *stratum corneum* and the effects of a higher local coefficient of friction were identified from the ideal model. These single-asperity effects contacts, were compared with those observed in the macro-scale contact interactions. In the anatomical model, these effects were observed at each asperity contact, showing an alternation of shear stress direction for the contiguous contact points. Furthermore, the effects of transmission and deflection of shear stresses across topographic features were identified.

The shear stress distribution in the viable epidermis was analysed under pure indentation because of the relevance of this layer in the formation of superficial pressure ulcers. During sliding contact, the analysis was extended to both the *stratum corneum* and viable epidermis, to relate the effects of shear stress distribution to the risk of tissue damage due to abrasion (failure of the *stratum corneum*) or the formation of friction blisters (de-bonding of the epithelial cells).

7.4.4 Shear stress distribution during pure indentation

In order to aid the interpretation of subsequent results, **Figure 7.16** provides an overall view of the boundary conditions of the complete anatomical and idealised models. In this figure, the area of interest is highlighted showing a contour plot for the indentation simulations, equivalent to the area shown in **Figures 7.17** and **7.20**. Only the shear stress results within this area were analysed in this study. Outside this region, the results were considered to be influenced by the boundary conditions, and discarded.

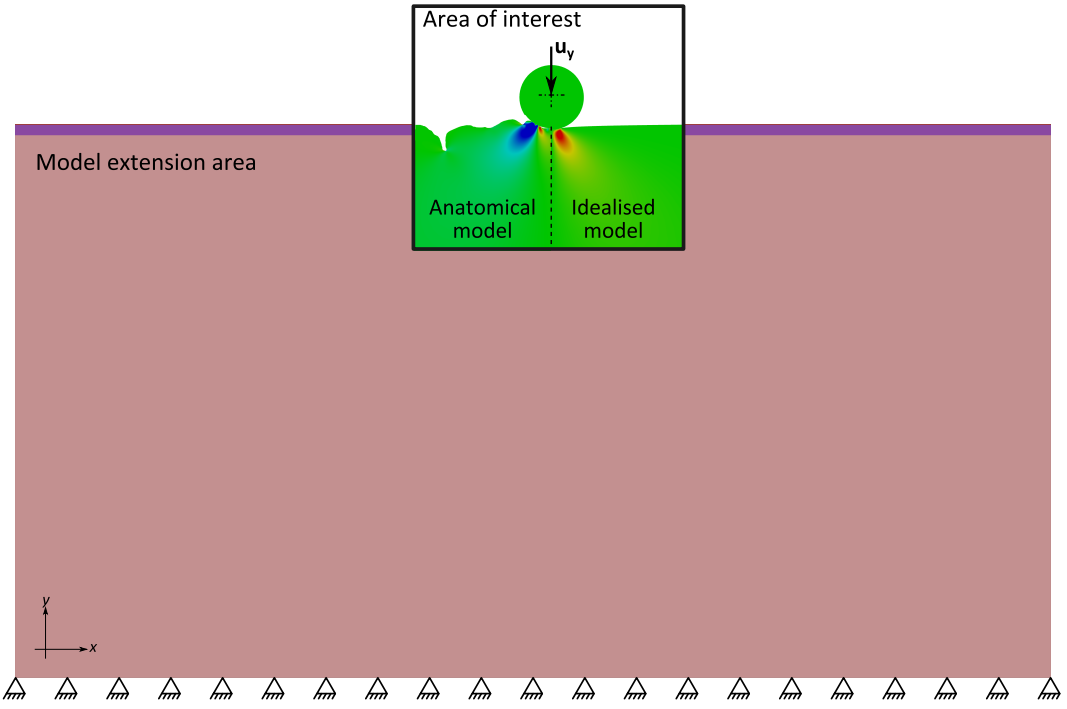

Figure 7.16: The full model for the simulations considering the area of interest and model extension area. The base of the full model is fully constrained and indentation is applied directly over the area of interest (indenter displacement $\mathbf{u_y}$). The area of interest is highlighted the contour plots of the anatomical (left) and idealised (right) models, indicating that only the results in this area were taken into account for this study.

The analysis of the stress distribution in the idealised homogeneous model ($E_{SC} = 0.6$ MPa), under frictionless contact conditions, revealed the typical shear stress distribution of single-asperity contact in the **microscopic interaction** scale models ($R_1 \leq 0.5$

mm). The patter reveals symmetric shear stress distribution with respect to vertical plane passing though the centre of the indenter; near the skin surface, higher concentration of shear stress were observed in the limits of the area of contact; the shear stresses propagate diagonally towards the deeper dermis. Due to the symmetry of the patter, where shear stress showed equal magnitude but opposite direction, a small area of low shear was identified directly underneath the indenter. These effects are illustrated in the contour plot of the shear stress distribution, left hand side of **Figure 7.17**.

As expected, the shear stress distribution pattern was scaled with the larger indenter radii in the micro-scale. Considering changes in the stiffness of *stratum corneum* due to lower humidity conditions ($E_{SC} = 370$ MPa), the contact area was reduced so shear stress was transmitted to the viable epidermis and dermis by the bending response of the outer layer. With the same symmetry observed before, larger areas of high shear stress were observed in the viable epidermis, directly under the area of contact, compare to those observed with the soft *stratum corneum* conditions. This effect was observed for larger skin deflection, while for the smaller deflection (as shown for the smaller indenter radius) the shear stress distribution appeared rather diffused. The effect of the ratio of indenter size with respect to the thickness of the *stratum corneum* was not explored in this study.

In the **macroscopic interaction scale**, the skin was assumed to be under pure compression so the shear stress pattern of single asperity contact was, as expected, not observed. However, some boundary effects were observed at the edges of the skin model. In the bottom row of **Figure 7.17**, it can be observed that those boundary effects were minimum within the area of interest. This is a clear example of why only the results within this area were considered in this study. Due to the convergence issues in the macroscopic scale interaction models under larger indentation, the shear stress distribution was analysed only in the simulations with $\mu_l = 0.3$.

Considering the region of the viable epidermis underneath the indenter in the ideal homogeneous skin model, the shear stress at each node was plotted according to their location in the x direction, for the quantification of the shear stress sensitivity to the coefficient of friction and stiffening the *stratum corneum* in **Figures 7.18** and **7.19**.

As the different simulation did not converged at exactly the same levels of indentation, it was required to identify the effects caused purely by skin deflection from those caused by the different friction conditions. As expected for the linear elastic response of neo-Hookean materials at low deformation, the displacement and shear stresses in the viable epidermis scaled up as further deflection was imposed to the skin surface as shown for frictionless indentation with $R_1 = 0.25$ mm in the left hand side of **Figure 7.18**. With the imposition of a coefficient of friction $\mu_l > 0.0$ (right), similar scale up was experienced. However, the shear stress distribution pattern in the region between

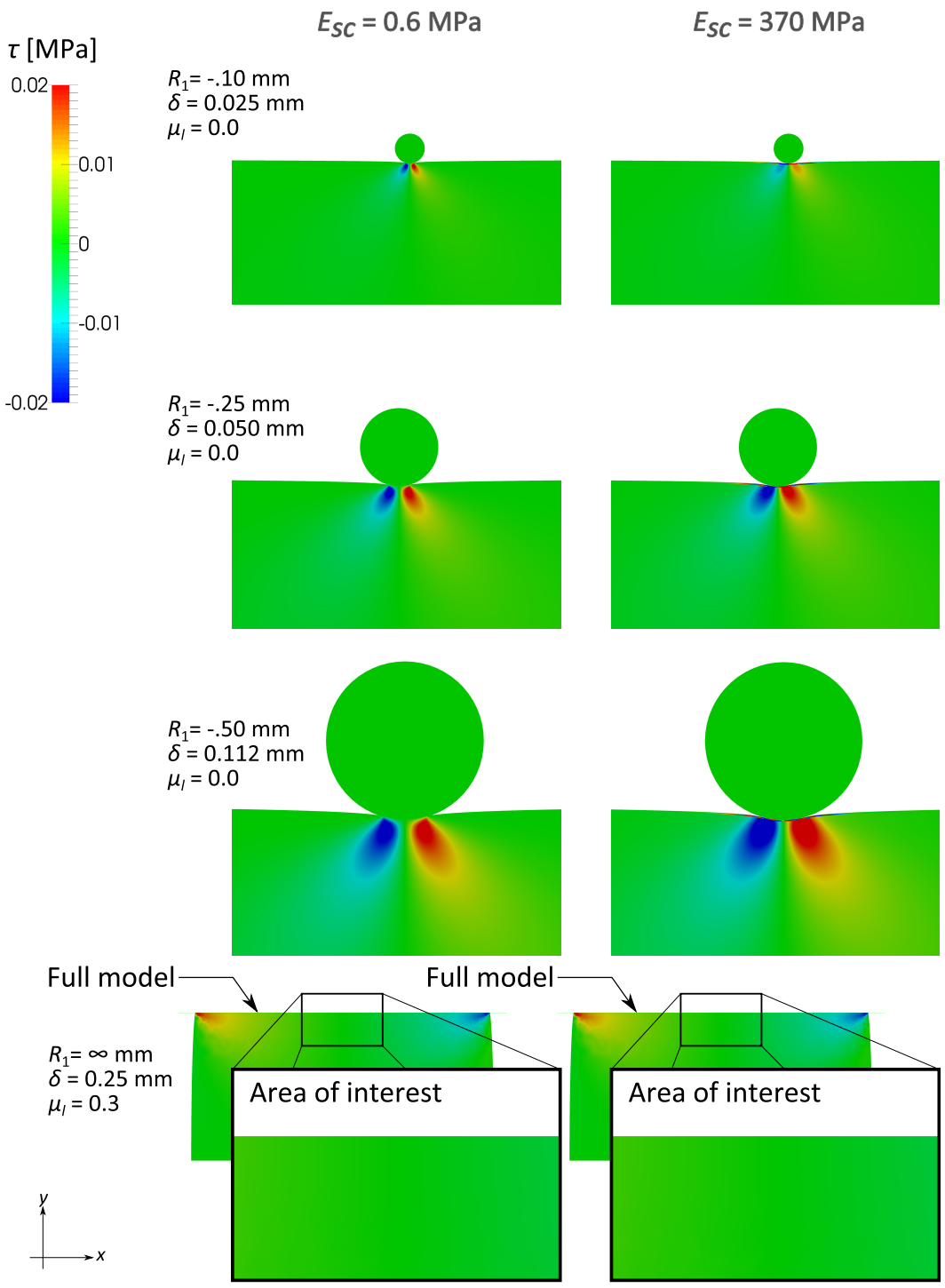

Figure 7.17: Effects of stiffer *stratum corneum* in shear stress τ distribution in pure indentation ideal conditions. The shear stress distribution in the area of interest of the ideal model is shown for the different indenter dimensions (from top to bottom, with smaller indenter at the top), at high humidity conditions with $E_{SC} = 0.6$ MPa (left) and dry conditions where $E_{SC} = 370$ MPa (right). For microindenation ($R_1 <= 0.5$ mm), the graphic show the results of frictionless indentation ($\mu_l = 0.0$); for macroscopic indentation ($R_1 = \infty$ mm), the results show pure indentation with local coefficient of friction $\mu_l = 0.3$, for which better convergence was obtained in the simulations at higher deflection (δ). For macroindentation, the graph included the full model with a zoom into the area of interest for visualisation of the observed boundary effects.

the contact area limits was narrowed, showing a more homogeneous response in comparison with the frictionless simulation.

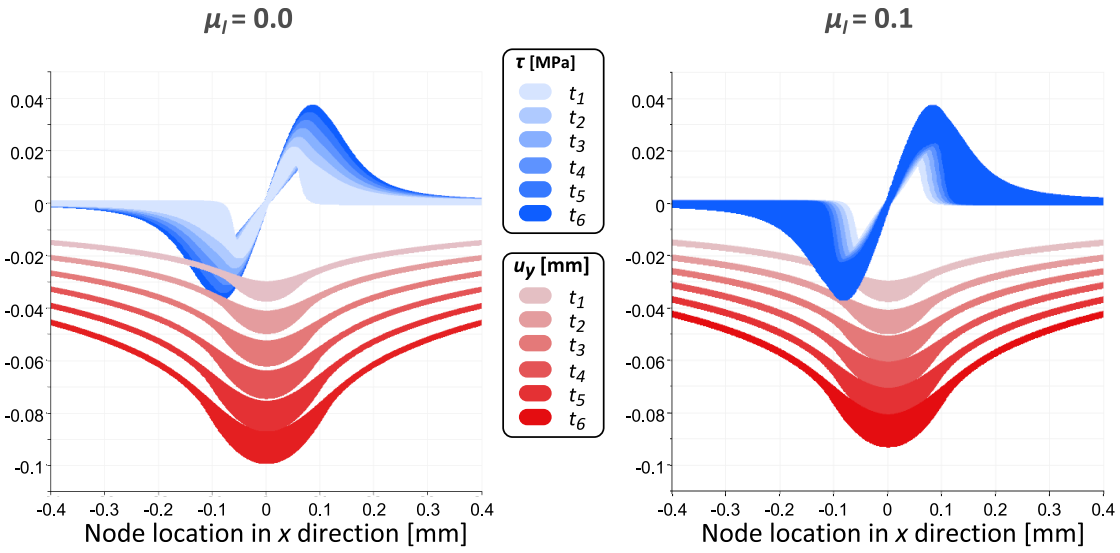

Figure 7.18: Shear stress and deformation scale up at indentation. The values of shear stress τ (blue) and displacement u_y (red) at the different nodes located in the viable epidermis are plotted with respect to the node location in the x direction. The gradient in colour shows the evolution of the parameters distribution from times t_1 to t_6, showing a scale up of the shear stress and deformation patterns. The results shown correspond to pure indentation with and indenter of radius $R_1 = 0.25$ mm.

This effect is highlighted in **Figure 7.19** (left-hand-side graph), comparing the shear stresses experienced with $\mu_l = 0.0$ and $\mu_l = 0.3$ at similar deformation levels. Similar analysis was performed for the non-homogeneous ideal skin model, in which $E_{SC} = 370$ MPa, showing that under these conditions, the shear stress distribution in the viable epidermis was unaffected by the local coefficient of friction (right hand side graph).

The shear stress distribution in the anatomical model involves multi-asperity contact. **Figure 7.20** shows the contour plot of the distribution shear stress throughout the area of interest of the skin models in frictionless conditions for the micro-scale interactions. Like in the idealised skin model analysis, due to the convergence issues in the macroscopic scale interaction models under larger indentation, the shear stress distribution was analysed only in the simulations with $\mu_l = 0.3$.

The results show the combined action the multiple single-asperity contact effects observed earlier in **Figure 7.17**. At each contact point, two high-shear stress regions are separated by a low-shear stress area underneath the centre of the contact point. However, the presence of multiple contact points causes a more complex distribution of the shear stresses as each the high-shear stress regions overlap across the projected contact area. Furthermore, the topographic features appeared to deflect the shear stresses, propagating its effects further sideways in the viable epidermis, affecting mainly the skin furrows. With stiffer *stratum corneum*, further propagation was observed, causing

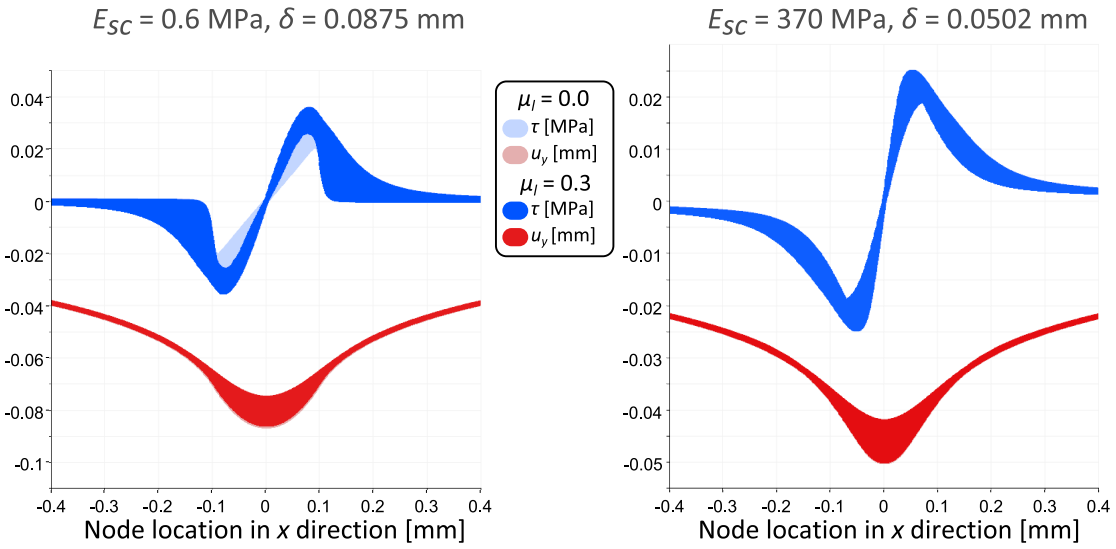

Figure 7.19: Effects of local coefficient of friction in the shear stress distribution pattern in the viable epidermis at pure indentation. The values of shear stress τ (blue) and displacement u_y (red) at the nodes located in the viable epidermis are plotted with respect to the node location in the x direction. At similar states of deformation, shear stress and deformation patters are compared for frictionless conditions $\mu_l = 0.0$ (light colour) and an imposed local coefficient of friction $\mu_l = 0.3$ (darker colour). The results shown correspond to pure indentation with and indenter of radius $R_1 = 0.25$ mm.

connection between the high shear stress areas across the viable epidermis from one skin protrusion to another. See **Figure** 7.20.

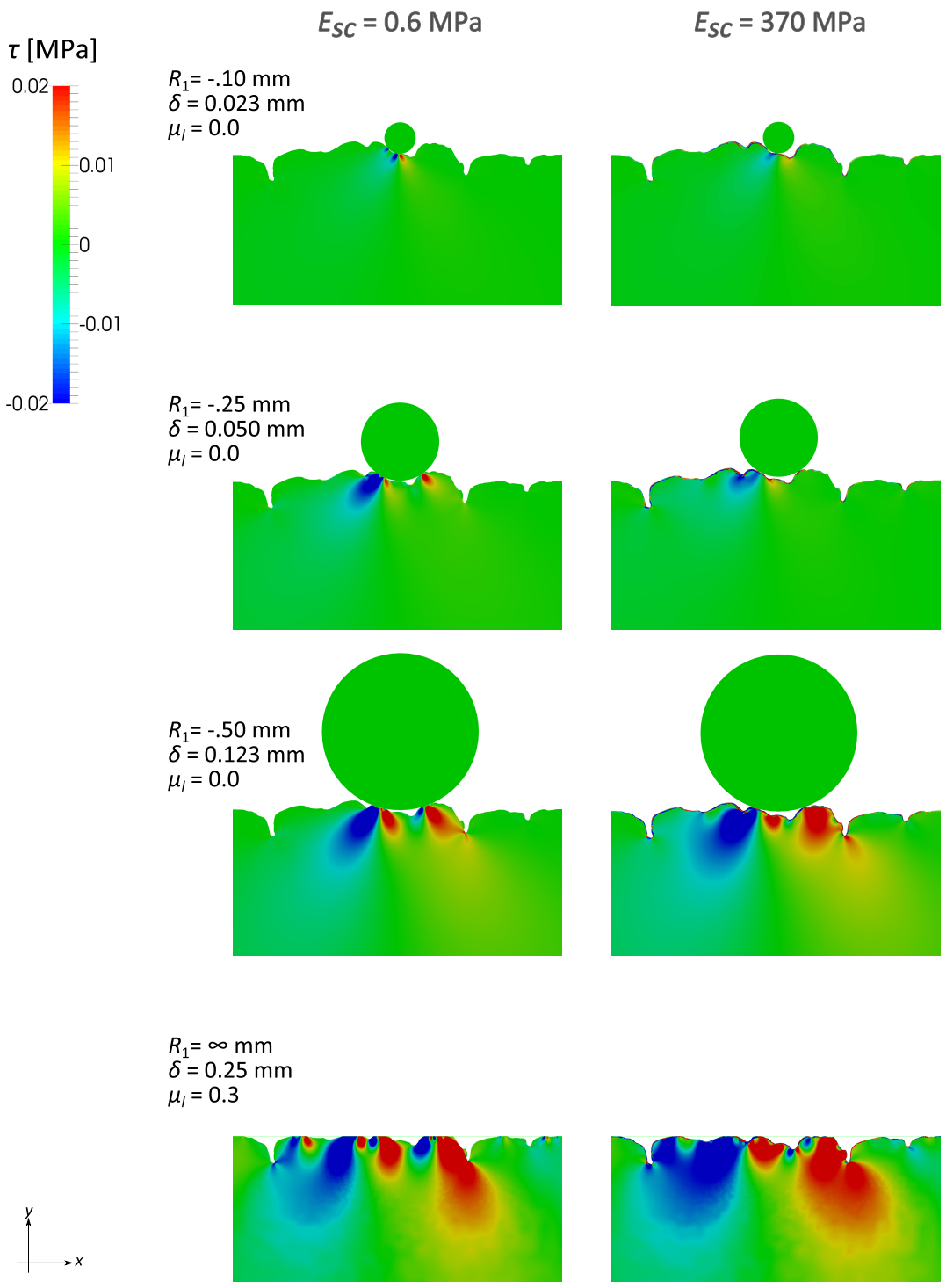

Figure 7.20: Shear stress distribution in pure indentation with the anatomical skin model. The shear stress τ distribution in the area of interest of the anatomical model is shown for the different indenter dimensions (from top to bottom, with smaller indenter at the top), at high humidity conditions with $E_{SC} = 0.6$ MPa (left) and dry conditions where $E_{SC} = 370$ MPa (right). For microindenation ($R_1 <= 0.5$ mm), the graphic show the results of frictionless indentation ($\mu_l = 0.0$); for macroscopic indentation ($R_1 = \infty$ mm), the results show pure indentation with local coefficient of friction $\mu_l = 0.3$, for which better convergence was obtained in the simulations at higher deflection (δ).

A more interesting result was observed in the macroscopic scale interaction simulations, where the multi-asperity contact provide multiple areas of high stress. This finding shows a great contrast with respect to the shear stress distribution results found in the idealised model.

The analysis of the shear stress distribution along the viable epidermis was performed by comparing, at each interaction scale, the magnitude of shear stress experienced by the different model configurations, for similar skin deflection. Like in the previous models, the results showed are limited to the area of interest of the skin models. **Figures 7.21** to **7.24** show the shear stress distribution at each interaction scale with respect to the node location in the x direction, comparing the results obtained from the idealised and anatomical models, under both high and low humidity conditions (captured with variation of the *stratum corneum* stiffness). In these figures, the geometry of the anatomical model with respect to its location in the xy plane was shown for the identification of topography-driven effects.

For the analysis of micro-indentation, the contact of the smaller indenter ($R_1 = 0.1$ mm, shown in **Figure 7.21**) with the anatomical skin model showed similar behaviour than that of the idealised one. However, higher levels of shear stress where observed in the anatomical model, regardless of the *stratum corneum* stiffness. In homogeneous conditions, peaks of shear stress were at each asperity contact, maintaining the areas of high magnitude shear stress within the same region. For the stiffer *stratum corneum* ($E_{SC} = 370$ MPa), where the are of contact was smaller, a wide range of shear stress was observed in the anatomical model, compared to the shear stress pattern observed in the idealised one. In both skin models, it was observed that the total range of experienced shear stresses where lower with a stiffer *stratum corneum*, though this might be an effect of the low indentation level for these simulations. Despite of the low indentation level, shear stresses were transmitted across the skin to the contact periphery, affecting mostly the areas located under the skin furrows.

Similar effects were observed between the simulations with indenter radii of $R_1 = 0.25$ mm (**Figure 7.22**) and $R_1 = 0.50$ mm (**Figure 7.23**). Higher levels of shear stress were observed in the anatomical models, propagating further away from the area of contact, in comparison with the idealised models. However, with the presence of multi-asperity contact, each one altering the direction of the shear stresses, the shear stress distribution patterns observed in the anatomical model significantly differ from the idealised ones. With respect to changes in the *stratum corneum* stiffness, the idealised model show similar shear stress intensity within the same distance from the indenter centre; in contrast, further propagation of shear stress was observed for the anatomical model with $E_{SC} = 370$ MPa. With the higher indentation levels and larger indenter sizes, these effects where also observed in the nodes around the skin furrows away from the area of contact, with higher shear stress levels in for the stiffer *stratum corneum*.

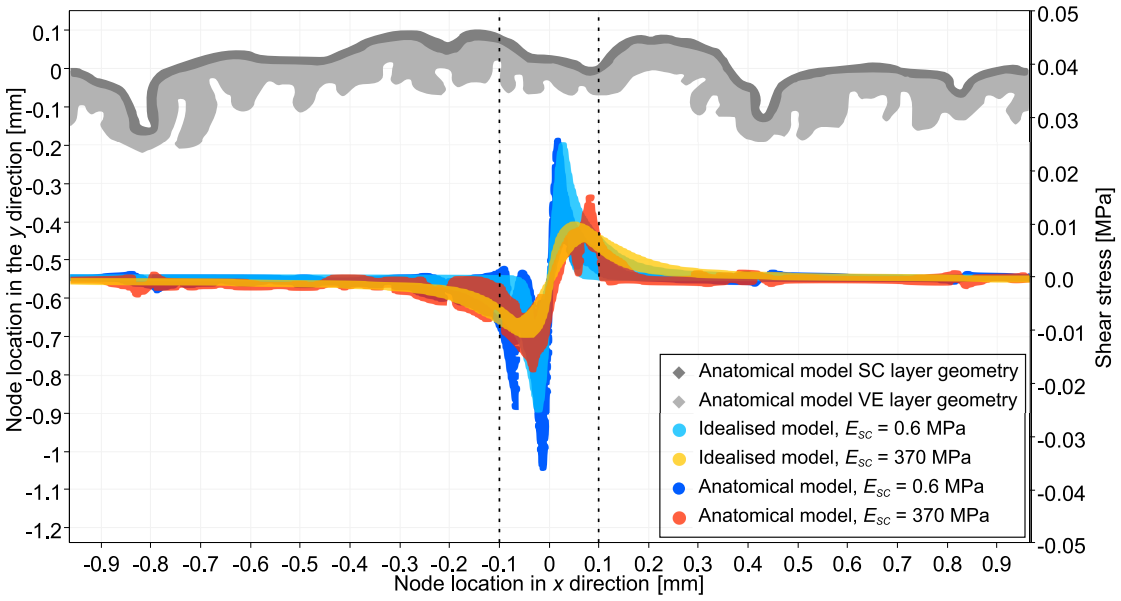

Figure 7.21: Shear stress distribution under pure indentation for $R_1 = 0.1$ mm, at $\delta = 0.023$ and $\mu_l = 0.0$, for the nodes of the viable epidermis contained within the area of interest (grey). The result compare the shear stress distribution of the anatomical model (dark blue and orange) and ideal model (light blue and yellow). The dotted lines indicate the dimensions of the indenter.

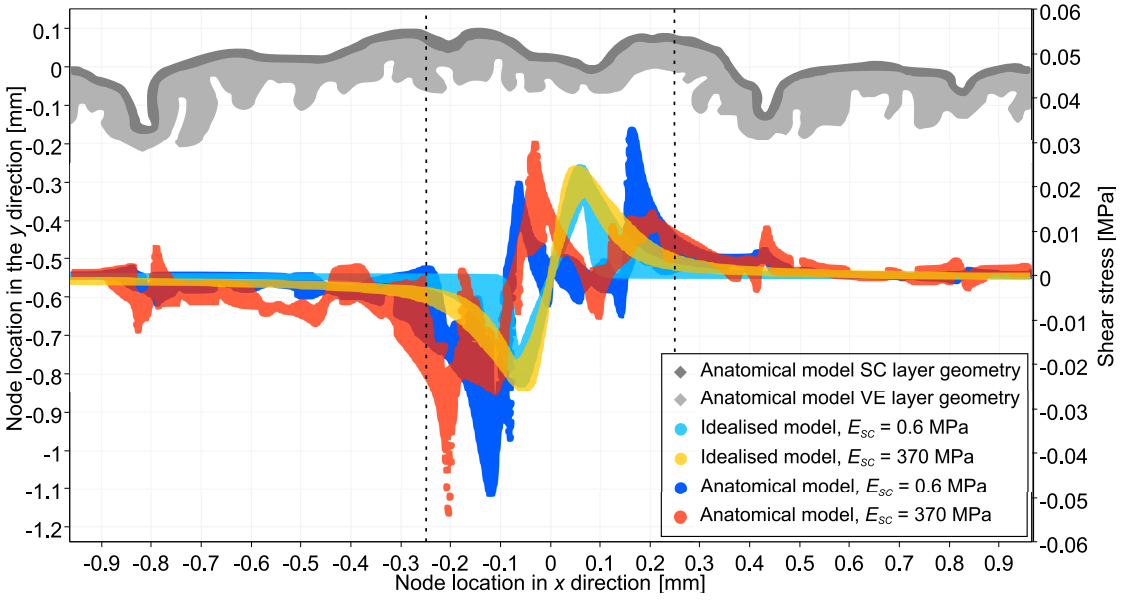

Figure 7.22: Shear stress distribution under pure indentation for $R_1 = 0.25$ mm, at $\delta = 0.05$ and $\mu_l = 0.0$, for the nodes of the viable epidermis contained within the area of interest (grey). The result compare the shear stress distribution of the anatomical model (dark blue and orange) and ideal model (light blue and yellow). The dotted lines indicate the dimensions of the indenter.

The striking differences previously observed between the idealised and anatomical models in **Figure 7.20**, were quantified in **Figure 7.24**. The idealised model showed a shear stress range of ± 0.003 MPa for $\delta = 0.25$ mm in the viable epidermis across the whole area of interest, for the two cases of E_{SC}, barely distinguishable in the plots. In contrast, the mixed effects of the local micro-asperity contacts and transmission of shear stress depicted shear stress values in the anatomical models ranging between

-0.07 and 0.1 MPa, for the same skin deflection (i.e. >300% larger). With respect to the *stratum corneum* stiffness, the anatomical models showed similar intensity, but the simulation with $E_{SC} = 0.6$ MPa showed higher sensitivity to the characteristics of the topographic features. While for this case the areas of high stress seem related to the skin crests, in the case of stiffer *stratum corneum* higher shear stresses where observed in the nodes located at the skin furrows.

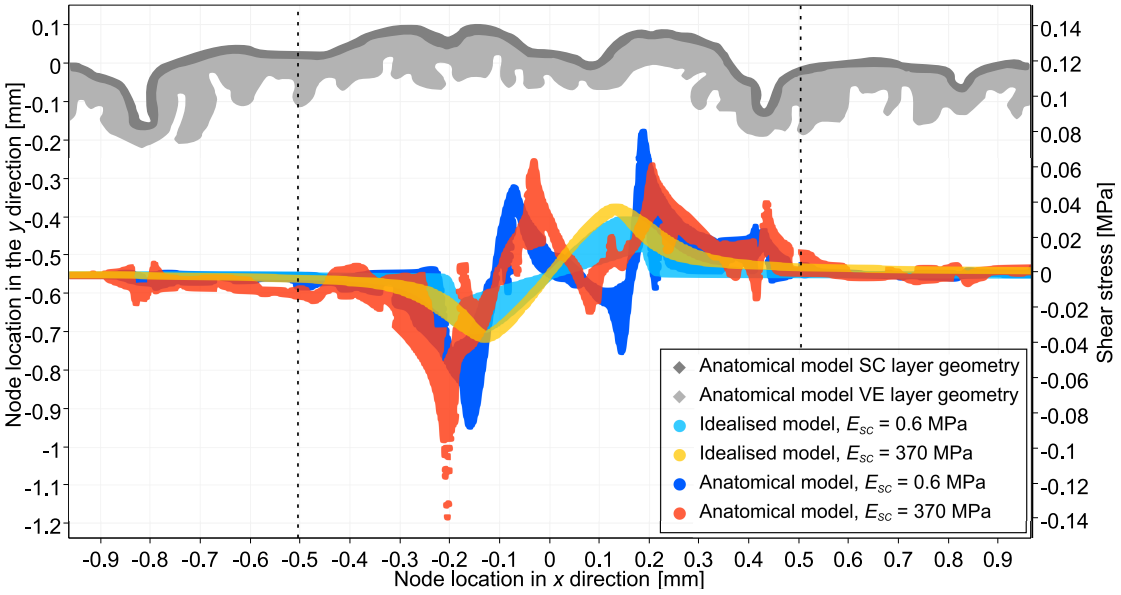

Figure 7.23: Shear stress distribution under pure indentation for $R_1 = 0.50$ mm, at $\delta = 0.12$ and $\mu_l = 0.0$, for the nodes of the viable epidermis contained within the area of interest (grey). The result compare the shear stress distribution of the anatomical model (dark blue and orange) and ideal model (light blue and yellow). The dotted lines indicate the dimensions of the indenter.

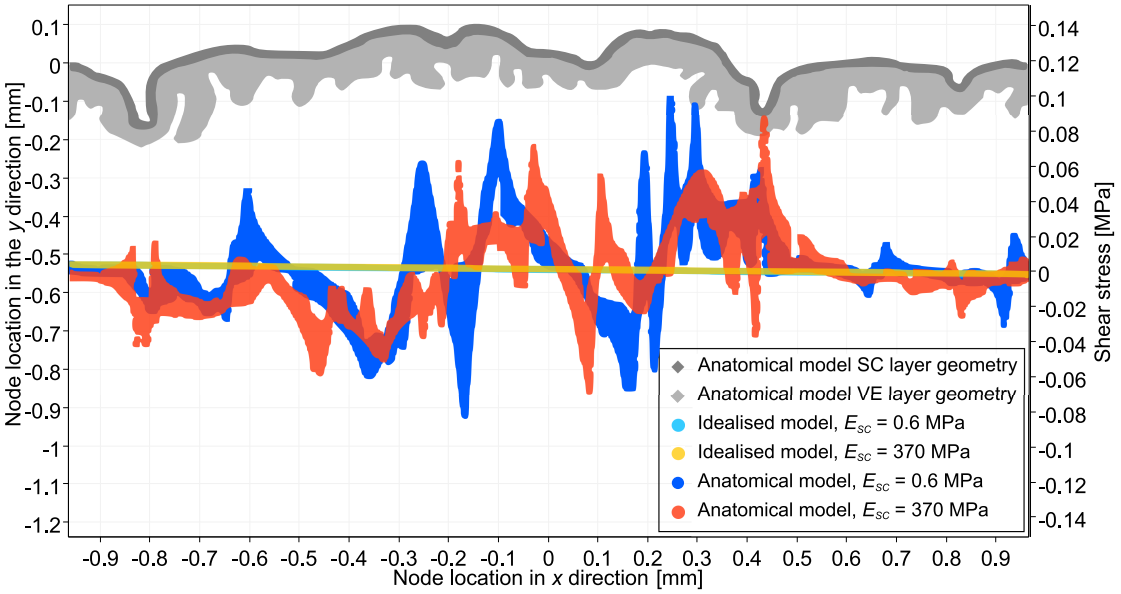

Figure 7.24: Shear stress distribution under pure indentation for $R_1 = \infty$ mm, at $\delta = 0.25$ and $\mu_l = 0.3$, for the nodes of the viable epidermis contained within the area of interest (grey). The result compare the shear stress distribution of the anatomical model (dark blue and orange) and ideal model (light blue and yellow). The dotted lines indicate the dimensions of the indenter.

For the evaluation of the influence of the skin topography in the compressive response of skin (under indentation), the direction of the third stress eigen vectors at each node, was analysed throughout the area of interest in the skin models. The directions of these eigen vectors were traced and interpreted as streamlines, referred as *compression streamlines* in this study. This analysis compared the idealised and anatomical models, considering only the cases of homogeneous skin (E_{SC}) $= 0.6$ MPa), for the micro and macroscopic contact interactions during pure indentation.

Figure 7.25 shows the compressive streamlines observed for the contact interaction simulations, indicating the different levels of shear stress. On the top right corner, a the geometry of the full skin model is presented, showing the area of interest for which the compressive streamlines were analysed. On the top left corner, a representative example of the compressive streamlines observed in idealised conditions is provided —this pattern was repeated in all of the homogeneous, frictionless, idealised simulations. The other plots show the compressive streamlines observed for the different indentation scales in the anatomical model.

In ideal conditions, the compressive streamlines formed a 'bell-shape' as the streamlines diverged from the area of contact towards the skin depth, indicating principal direction of compressive stress in the nodes. The 'bell-shape' was symmetrically aligned to the direction of the indentation load (i.e. normal to the flat skin surface). In the periphery of the contact area, the compressive streamlines follow a vertical path in the compression-free areas, that deflect to incorporate to the 'bell-shape' area subject to compression.

In the anatomical models, each micro-asperity contact replicated the 'bell-shape' observed in the idealised model, rotated with respect to reaction force component, normal to the asperity geometry (see **Figure 7.1**). For bigger indenter sizes depicting multi-asperity contact, the contiguous bell-shaped compressive stream lines appeared to be squeezed one next to the other, in a composite 'bell-shape'. In the path of the compressive streamlines, the load-free topographic features were by-passed showing similar behaviour to that observed in the periphery of the idealised model. In the macroscopic interaction scale, the compressive streamlines appear to 'by-pass' the less-loaded topographic located in between two areas under higher compression.

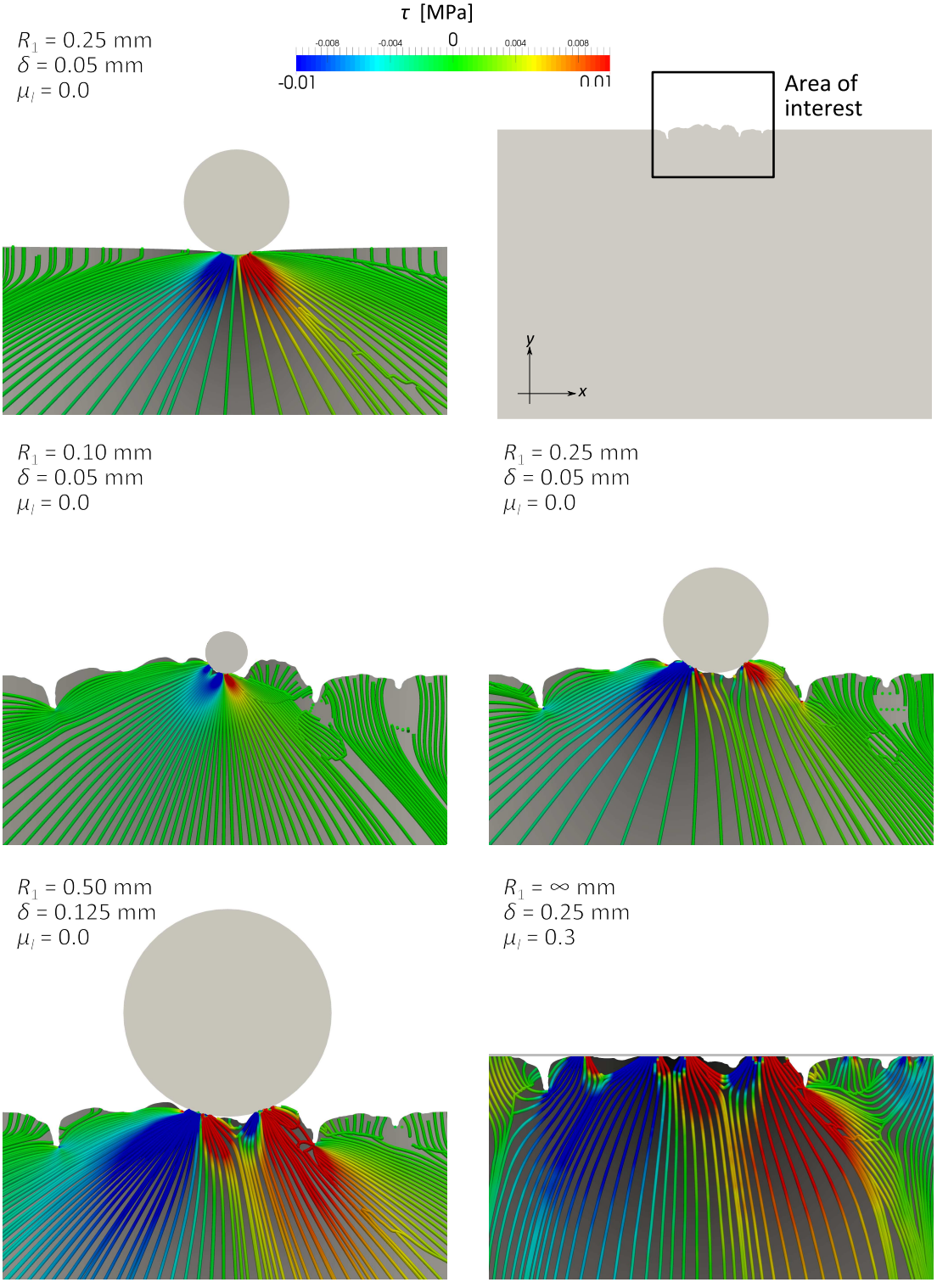

Figure 7.25: Shear stress distribution overlaid with the compressive streamlines. Comparison between the ideal (top left) and anatomical skin models at different indentation scales (microindentation with indenter radius $R_1 \leq 0.5$ mm, and macro indentation with $R_1 = \infty$ mm), in homogeneous conditions for $E_{SC} = 0.6$ MPa. With except for the macroindentation simulation where the local coefficient of friction is $\mu_l = 0.3$, the microindentation simulations show the results with frictionless ($\mu_l = 0.0$) conditions.

7.5 Shear stress distribution during sliding contact

Under sliding conditions, the analysis was performed only in the idealised skin model simulations, as it was observed how the shear stress response of a single-asperity contact can be put into context of the multi-asperity ones. This analysis included the evaluation of shear stress distribution throughout the area of interest with a contour plot, and their quantification with respect to the location of the nodes in the direction of sliding (x direction) for specific skin layers. The analysis was focused in the effects for the viable epidermis and *stratum corneum* with respect to the local coefficient of friction, for two different humidity conditions affecting the stiffness of the *stratum corneum*.

Figures 7.26 and 7.27 show two examples of the sliding simulations for the soft and stiff *stratum corneum*, respectively. On the top part of the figures, the contour plot of the shear stress distribution shows the changes in symmetry of the high shear stress areas (in comparison with the pure indentation results, showed in **Figure** 7.17). Each plot indicates the level of skin deflection and lateral displacement of the indenter. The plots at the bottom part of the figures show the isolated shear stress response of the *stratum corneum* (left) and viable epidermis (right) with respect of the location of the nodes in the x direction.

In high humidity conditions, simulated with a *stratum corneum* stiffness of $E_{SC} = 0.6$ MPa, a larger region of high shear stresses was depicted in the contour plot ahead the indenter, propagating towards the deeper dermis. Furthermore, the area of low shear stress (mainly compressive behaviour) observed in pure indentation conditions directly under the indenter was not longer observed. Analysing these effects on the isolated measurements in the *stratum corneum*, the magnification of the shear stresses with higher local coefficient of friction was clearly observed. In contrast to the low-shear stress observed at the area of contact for frictionless conditions, a maximum shear stress value of 0.03 MPa was depicted for $\mu_l = 0.2$; this represents a magnification of 30% from the maximum values captured in the *stratum corneum* for $\mu_l = 0.0$. In the viable epidermis, the maximum shear stress at this area was of 0.026 MPa; however, this was only 62% of the maximum shear stress observed ahead of the indenter. The magnitude of the shear stresses ahead of the indenter increased with the larger μ_l, while that of the shear stresses behind the indenter were reduced; however, no significant variation was observed with respect to the frictionless conditions in comparison to the effects observed in the *stratum corneum*. See **Figure** 7.26.

In dryer conditions, simulated with a *stratum corneum* stiffness of $E_{SC} = 370$ MPa, the magnification of high shear stress region, propagating towards the deeper dermis ahead of the indenter was also captured in the contour plot. However, the section of

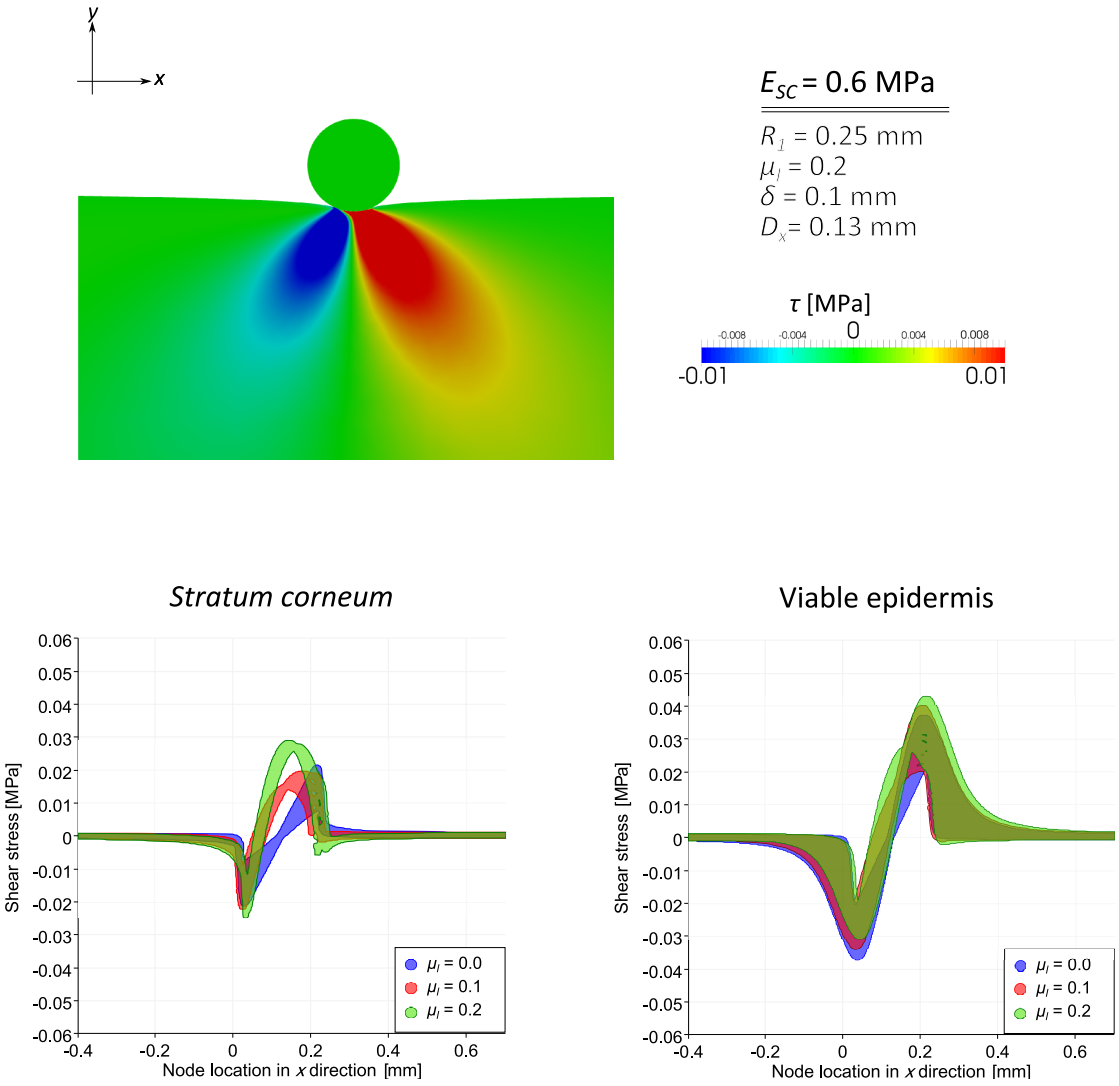

Figure 7.26: Shear stress τ distribution under sliding contact with $E_{SC} = 0.6$ MPa. The contour plot (top) shear stress distribution in the area of interest of the idealised skin model, under sliding contact. The interaction conditions corresponding to this plot are provided (indenter radius R_1, local coefficient of friction μ_l, maximum skin deflection δ, and lateral displacement of the indenter D_x). At similar deflection and indenter lateral displacements, the plots in the bottom illustrate the sensitivity of the *stratum corneum* (left) and viable epidermis (right) layers to changes in the local friction conditions, showing the shear stress levels observed the nodes of each layer, across the node location in the x direction.

low shear stresses directly under the indenter was still obvious in the viable epidermis. The shear stress response of the *stratum corneum* and viable epidermis were captured with respect to the location of its nodes in the x direction. In the stiffer *stratum corneum*, the simulations captured an alternation in shear stress direction caused by the bending of this layer under the contact interactions, but no significant sensitivity of the shear stress to larger local friction conditions was observed. In the viable epidermis, despite the asymmetry shear stress distribution observed in the contour plot, the shear stress distribution was similar to that observed in the for pure indentation (see **Figure** 7.19). Likewise, no significant sensitivity to larger local friction conditions was observed. See **Figure** 7.27.

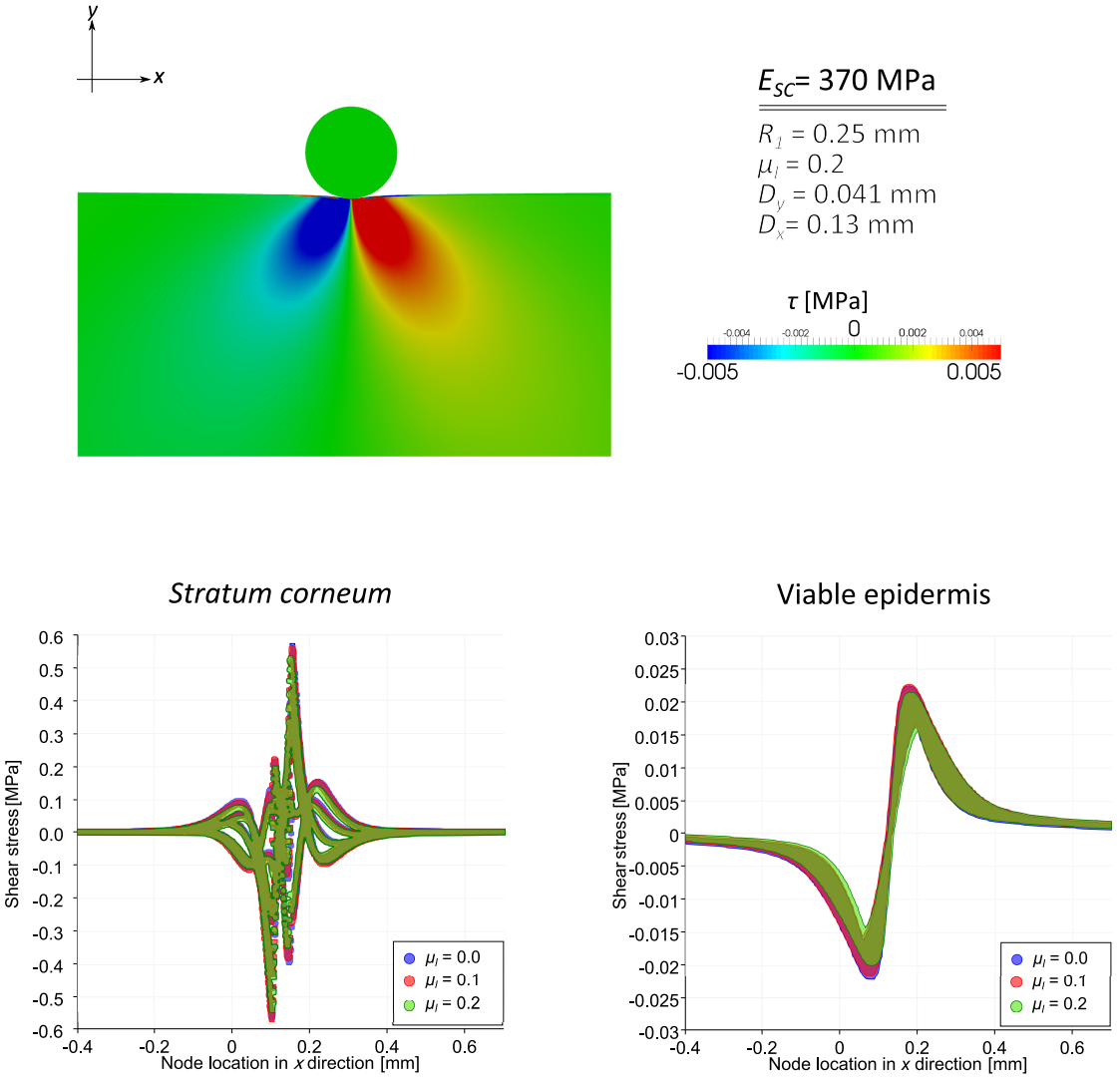

Figure 7.27: Shear stress τ distribution under sliding contact with $E_{SC} = 370$ MPa. The contour plot (top) shear stress distribution in the area of interest of the idealised skin model, under sliding contact. The interaction conditions corresponding to this plot are provided (indenter radius R_1, local coefficient of friction μ_l, maximum skin deflection δ, and lateral displacement of the indenter D_x). At similar deflection and indenter lateral displacements, the plots in the bottom illustrate the sensitivity of the *stratum corneum* (left) and viable epidermis (right) layers to changes in the local friction conditions, showing the shear stress levels observed the nodes of each layer, across the node location in the x direction.

7.6 Discussion

This study was based on the simulation of skin **contact interactions** at microscopic and macroscopic interaction scales. The contact was simulated as pure indentation and sliding contact (combination of indentation and lateral displacement), for the analysis of the contribution of the skin topography to the macroscopic friction response of this tissue, comparing the results to those obtained with an idealised flat skin model. The study comprised the analysis of relative contact area, comparison of the global and local friction response of skin, and distribution of shear stress throughout the skin layers. Multiple scenarios were considered, accounting for variation of stiffness of the *stratum corneum*, and various local coefficients of friction at the contact interface. The principal findings of this study are:

Contact area:

The real contact area between the skin and the contacting material can have significant influences on the skin friction response, especially under larger loading conditions (van Kuilenburg et al., 2013a). In the simulations of pure indentation, it was noted that the real contact area in the anatomical model is inversely proportional to the scale of the interaction (larger relative area as observed for smaller indenter radius). This was observed for small skin deflections (with deflection equivalent to half of the indenter radius). It is expected that in a micro-scale contact with larger skin deflection the real and apparent contact areas might be the same. However, in the simulation of macro-scale indentation, a relative contact area of 72% was found for up to 20% compression of the skin (indentation). These results were obtained with a soft *stratum corneum* stiffness corresponding to high humidity conditions, so for a stiffer *stratum corneum*, this measurement is expected to be lower. Most of the experimental techniques exploring the contribution of adhesive and deformation effects to the skin friction response, relate the adhesive contribution to the skin contact area, and deformation contribution to the ploughing or 'bow-wave' effects in the contact periphery (Kwiatkowska et al., 2009). However, the contribution of the skin topography to the deformation friction is often overlooked under the assumption that the real contact area is similar to the apparent one. Nevertheless, the contact area results obtained in this study suggest that this is not the case. This has further implications in the skin friction response and the distribution of shear stresses within the skin layers, as explained below.

Friction response:

The global friction response obtained in the simulations of sliding contact was analysed with respect to the applied (input) local coefficient of friction. The friction response of the anatomical model was contrasted with that of the idealised model.

- Despite of the small thickness of the *stratum corneum*, the contact simulations showed that its mechanical properties have a significant effect on the skin global friction response, as it alters the peripheral deformation at the contact area. With a lower stiffness, the contact area increased and larger 'bow-wave' or ploughing was observed. Many studies consider that the contribution to friction due to peripheral deformation is relatively small (Kwiatkowska et al., 2009), attributing the friction response to be largely dominated by adhesion and the contact area (Gerhardt et al., 2008). The study presented in this chapter, analysed the effects of peripheral deformation and contact area in sliding contact with use of the idealised skin model. In these simulations, the specification of a local coefficient of friction implicitly accounted for the adhesion effects. In these idealised conditions, the 'bow-wave' peripheral deformation effects behind the indenter provided a 'push forward' force causing the reduction of the global friction response —effect that was not observed with a stiffer *stratum corneum*. This suggests that even though ploughing contributes to the resistance to motion, the mechanical deformation behind the indenter provide a counteracting effect, reducing its total response.

- In comparison with the friction response observed in idealised conditions (flat surface of contact), the global friction response of the anatomical skin model was dominated by the skin topography. Comparing the results to the specified local coefficient of friction, the simulations performed with a soft *stratum corneum* showed significant increase of the global friction response, as a result of the combined peripheral deformation effects and the resistance provided by the skin topographic features. In contrast, for a stiffer *stratum corneum* where the no 'bow-wave' effects were observed in ideal conditions, similar global friction response was registered for all the simulations, regardless of the specified local coefficient of friction or indenter radius. These results strongly suggest that the contribution to friction at the area of contact in soft materials, is a combined response of the adhesive effects and the deformation due to multi-asperity contact at the microscopic scale. Despite the fact that the simulations accounted for a 1 mm sliding distance, they provided enough information about the influence of the skin topography and microstructure on its global friction response. In order to isolate the specific contribution each topographic feature to the skin global friction, the skin model should include a significant number of topographic features with similar characteristics, identified as in **Chapter 6** (Leyva-Mendivil et al., 2015). This could also provide a more generalised understanding of the global friction response and how the geometrical characteristics (e.g. skin furrows, size of crests) of the skin topography can influence this response. So far, not many studies have considered the skin topography as a contributing factor to the skin friction response. With the evidence provided in this study, it is implied that this factor should not be longer overlooked in the study of skin friction.

Shear stress distribution:

The shear stress distribution within the skin layers showed a complex multi-asperity response under contact interactions. In comparison with the shear stress distribution for a single-asperity contact in the idealised model, the skin topography and microstructure can significantly alter the distribution of shear stress:

- The multi-asperity contact in the anatomical model, with lower contact area than in idealised conditions, results in higher concentration of stress at each localised contact. This was observed regardless of indentation scale. However, this is of higher relevance in the macroscopic scale, where in idealised conditions the skin is assumed to be in pure compression (in the direction normal to its surface). The results of macroscopic indentation showed that the shear stresses in the viable epidermis were in the range of ± 0.003 MPa in the idealised model, while reaching values 300% larger when the micro-asperity contact is considered. These results are of great implication for the study of the mechanism of formation of superficial pressure ulcers due to constant application of pressure on the skin surface.

  Shear stress provides an indication of potential damage of the skin tissue (Goldstein and Sanders, 1998; Sopher and Gefen, 2011). For this reason, it is crucial that the computational models investigating the mechanism of skin damage (e.g. for superficial pressure ulcers and friction blisters) take into consideration the microstructure of the skin.

- Once more, the stiffness of the *stratum corneum* depicted an important role in the propagation of shear stresses within the viable epidermis. Although similar levels of maximum shear stresses were observed with a stiff and soft *stratum corneum* (accounting for the Young's modulus of this layer for 30% and 100% RH (Wu et al., 2006b)), a stiffer *stratum corneum* produces higher propagation effects around the area of contact in comparison to the soft one. This is caused by the peripheral deformation: with a soft *stratum corneum*, this layer is both, subject to displacement and deformation, while a stiff *stratum corneum* is less subject to deformation, so it is only displaced on the skin surface, causing the propagation of shear stresses further away. Under the 'hinge-like' mechanism observer for the in-plane deformation of skin (**Chapter 6**), further strains/stresses concentrate at the areas of the skin furrows, away from the area of contact.

7.7 Conclusion

The topography and microstructure of the skin play a crucial role in its tribological interactions, widely overlooked by the assumption of the tissue as a flat material. The

simulations of pure indentation and sliding contact with the 2D anatomical skin model showed that the skin topography provides a multi-asperity contact that dominates the skin global friction response, regardless of the contact area. The multi-asperity contact results in higher concentrations of shear stress at each contact point, in comparison to the levels expected with an idealised (flat) skin model. However, the skin furrows provide a mechanism of shear stress propagation along the outer layers of the skin, not observed in idealised conditions. Furthermore, the *stratum corneum* proved once more that, despite of its small thickness, has a significant effect in the skin tribological interactions. Its stiffness is key in the characteristics of contact area and peripheral deformation, affecting directly the distribution of shear stresses within the skin. In addition, a stiffer *stratum corneum* results on further propagation of shear stress, away from the contact area.

7.8 Limitations and further work

The anatomical skin model comprises the geometry of the skin layers obtained from histological sections of a specific sample of human skin. The preparation of the histological sections allows the preservation of the skin anatomical features, but in order to preserve these features in an un-loaded state or damaged stare, the sample cannot be used for experimental testing. Although a different part of the sample could have been tested for experimental characterisation of the mechanical properties of the skin layers, such procedure was not contemplated in this project. Without these 'patient-specific' parameters, it is impossible to validate our results against experimental evidence.

Given the factors involved in the variation of mechanical properties and topography of the skin layers, a more meaningful application of this model has been provided by the exploration of different 'what if' scenarios. The relevance of capturing a patient-specific skin geometry is not that of providing specific answers, but exploring the insights of the role of the skin microstructure on its mechanical response, and any potential implications it might have in the skin care research (either for consumer products, or health care). However, capturing in detail the complex geometry of the skin in finite element models requires a fine mesh resolution that results in a great demand of computational resources. In order to reduce the computational cost, the anatomical model was developed in plane strain (2D), and the mechanical properties of its layers where represented with the use of the isotropic neo-Hookean constitutive model.

Future work involves the representation of the skin layers in the anatomical model with their anisotropic time-dependent mechanical properties and expansion of the model in 3D. As mentioned before, this would result in high computational cost, for which the 2D model provides a tool to explore a wide range of scenarios in order to isolate a specific conditions to be implemented in the 3D computational analysis.

Chapter 8

Conclusions and future work

The goal of this PhD project, the development of a ***multi-physics modelling framework*** *for the characterisation of the complex wet-shaving interactions has been achieved. For the development of this project, it was necessary to experimentally characterise not only the mechanical properties of shave preps (density, compressibility, non-linear viscosity), but also their contact interactions with the cartridge materials. Its implementation in the multi-physics modelling framework required multiple verification steps in order to ensure that its viscous and contact response were appropriately captured. During this process, some of the key multi-physics interactions taking place between the skin, shave prep (gel/foam) and razor have been established, paving the road for further multi-physics simulations. Beyond the original purpose of this project, an image-based* ***anatomical skin model*** *was developed for further investigation of the tribological interactions of skin. This 2D finite element model was implemented for the study of the effects of the skin topography and microstructure on its deformation and contact interaction response. These studies revealed important implications about the role of the skin microstructure with respect to the micro and macroscopic mechanical response, as well as mechano-biological implications derived from the distributions of strain/shear within the skin layers. In this chapter, the conclusion of this PhD thesis is provided, highlighting the key findings of this project and their implications, discussion of the project limitations and recommendations for further work.*

Many of the interactions the human skin is subjected to, involve complex multi-physics phenomena. This is the case of wet-shaving interactions, where the human skin deforms by the combined action of the loads applied through the razor cartridge and the pressures and stresses experienced by the shave prep as a lubricating media. Understanding the complex multi-physic phenomena taking place on the surface of the skin, is of high relevance for the development of high performance consumer products that provide comfort to the consumer and ensures a safe interaction with the skin.

In the study of the lubrication phenomena in wet shaving interactions, three main aspects have been historically considered for the delivery of a close shave that prevents damage of the skin: *a*) pressure distribution on the skin surface; *b*) lubrication at the guard-skin; and *c*) lubrication at the blade tip. These three factors are inter-connected, requiring deep understanding of the mechanical behaviour of skin (O'Callaghan and Cowley, 2010), lubrication theory (Moir and Craig, 2010) and fluid dynamics (Lawler, 2001), as it was reviewed in **Chapters 2** and **4**. Furthermore, understanding of the complex non-linear behaviour of shave preps (**Chapter 3**), is crucial for the study of wet shaving interactions.

Until now, the study of the wet shaving interactions required major assumptions. The skin model developed by O'Callaghan and Cowley (2010) has been used in P&G for the investigation of skin deformation, considers the complex 3D geometry of the razor cartridge, but the lubrication factor was accounted for as a reduced coefficient of friction. In the analyses of Lawler (2001) and Moir and Craig (2010), the lubrication phenomena as been studied into a 2D analysis approach at a microscopic scale, considering simple linear elastic response of the skin and highly simplified geometries representing the cartridge parts. With latter improvements in the technology where finite element techniques are more accessible and capable to capture the fluid-structure interactions and non-linear viscous fluids, an opportunity was provided for this project with the following objective:

> *the development of a **multi-physics modelling framework** for the characterisation of the interactions between the skin, razor and shave preps in shaving stroke simulations.*

The completion of this project opens further opportunities for the study of shaving interactions, providing a modular tool that can aid to the analysis of lubrication performance of different cartridge designs and shave prep formulations.

This project was taken beyond its original purpose, expanding the analysis of the skin contact interactions to a micro-mechanics perspective. The objective of these side studies was the investigation of the role of the skin topography and microstructure on the macroscopic response to deformation and contact interactions. The development of an image-base anatomical skin model, accounting for its topography and microstructure with high geometrical fidelity, provided a tool for the investigation of the link between the microscopic and macroscopic mechanical response of this tissue. Furthermore, this model opens the door to the investigation of the mechano-biological implications derived from the distribution of stress and strain within the skin layers, in a variety of 'what-if' scenarios. The anatomical skin model is unique on its type, comprising a state-of-the-art model with great potential for its application in the field of interactions with consumer products, prevention of skin damage (e.g. pressure ulcers, friction blisters) and skin health care.

8.1 Principal findings

The development of the **multi-physics modelling framework** required the experimental characterisation of the non-linear viscous behaviour of shave preps and their contact interactions with the cartridge materials. Through the implementation of the shave prep within the modelling framework it was essential the careful evaluation of the effects of the fluid mechanical properties, its contact interactions and mesh characteristics on *a*) the simulation runtimes performance; and *b*) the behavioural response of the simulation. From this process, the principal findings are summarised next.

The **simulation runtime performance** is highly affected by the mechanical properties of the fluid, the fluid mesh characteristics, and level of parallelisation of the calculations. The sensitivity analyses performed through the simulation provided the following findings:

- **Shave prep mechanical properties.** The analysis of the mechanical properties of the shave prep indicated that he runtime performance is highly sensitive to the longitudinal wave propagation velocity (i.e. sound speed), related with the compressibility of the fluid. This finding was applied for the optimisation of the simulation, where the reduction of 50% of this value in a lubricant fluid resulted in 4 time faster simulations. The effects of this change were evaluated in the lubricant fluid. In the open fluid configuration (i.e. the simulation of a shaving stroke), previous un-realistic splashing effects were reduced —improving the behavioural response of the fluid. Under pure shear, no significant effects were observed in the fluid viscous behaviour, but higher slip at the fluid-solid interface was observed. This meant that the fluid contact interaction response was reduced, but such effect can be easily accounted for with the modification of the friction parameters. This provides an example of significant optimisation of the simulation runtime performance, without compromising the behavioural performance of the shaving stroke simulation.

- **Fluid mesh characteristics and parallelisation level.** The analysis of the shave prep deformation in a shaving stroke requires a fine fluid mesh to capture the fluid-structure interactions at the detailed geometry of the cartridge (e.g. small features such as the grooved surface of the elastomer guard). Furthermore, the Eulerian space, where the fluid mesh is defined, requires to be large enough to contain the space where the shave prep can exist. That is, that it should account for the skin deformation and the shave prep ploughing ahead of the razor. This results in a large fine Eulerian mesh. With these mesh characteristics, it is advised that parallelisation methods are applied to faster computation of the analysis.

The sensitivity analysis was performed for the evaluation of the effects of the mesh characteristics and parallelisation level on the simulation runtime performance. The analysis compared the effects of the element size, Eulerian space volume or fluid-void ratio within the Eulerian space at different parallelisation levels. The results showed that the most relevant parameter for the estimation better performance was the parameter 'number of elements per processors'. This indicated that the simulation performance can be improved by optimising the dimensions of the Eulerian space (e.g. running a 'dry' simulation to estimate the maximum deformation of the skin) to adjust the number of elements to the parallelisation capabilities available.

The analysis of **qualitative performance** of the shaving stroke simulation involved constant verification of the viscous fluid response and fluid-solid contact interactions at the different stages of development of the model, providing the following conclusion:

- In the different stages of development of the modelling framework, the shave prep non-linear viscous response was appropriately captured, showing no concern for the simulations: the shear stress experienced at specific shear strain rates was in agreement with the specified non-linear viscosity (input) with a relative error lower than 2%. However, in the context of the shaving stroke, the behavioural response of the multi-physics interaction was highly conditioned by the **fluid-solid contact interaction properties**.

  The experimental characterisation of the fluid-solid contact interactions required the identification of the adhesion forces between the fluid and solids, and the forces required to produce sliding of the fluid on the contact surface. These properties require a mechanical interpretation for its implementation in the modelling framework in the form of a coefficient of friction (sliding resistance) and a condition to allow or not separation of the fluid from the surface (adhesion). However, there is no direct link between such mechanical interpretation and the adhesion response for fluid-solid contact interactions. For this reason, empirical estimation of these contact parameters through combined experimental and computational analysis, was proposed.

The **development of the anatomical skin model** resulted in a robust methodology in which the combination of histological sections of human skin, image-processing and finite element techniques were applied to address fundamental questions about skin mechanics: *a*) what is the role of the skin microstructure in the mechanism of transmission and modulation of macroscopic strains through the epidermis and dermis; *b*) how does the skin microstructure contribute to the macroscopic friction response of skin in contact interactions. These questions where addressed in two studies in which the anatomical model was subjected to in-plane deformation and multi-scale contact

interactions. These studies accounted for multiple scenarios affecting the mechanical properties of the skin and contact interaction properties, providing the following findings.

- A complex non-linear interplay between the geometry and mechanical characteristics of the skin layers, plays a critical role in conditioning the 2D skin mechanical response to macroscopic in-plane compression and extension. The skin topographic features provide a 'hinge-like' mechanism that effectively deflects and redistributes the strain (and so stress) within the skin layers. This resulted in substantially lower strains in the *stratum corneum*, below 50% of the macroscopic strain applied as a result of purely geometrical implications (considering the skin as a homogeneous tissue). These results indicate that the topography of the skin has a strain modulating role, protecting the epidermis under large deformations.

- In contact interactions, the simulations showed that the skin topography has a great influence in the global friction response, from the micro-asperity contact point of view. This aspect is often overlooked under the assumption of skin as a flat material. In the contact interaction simulations performed with the anatomical model, it was shown that the contact interaction is highly influenced by the resistance provided by the topographic features, and the deformation around the contact area. In the simulations with a stiff *stratum corneum*, where the such deformation was minimal, all of the simulations showed closely similar results in the measurements of global friction. With these results, the computational analysis strongly suggests that, in tribological interactions of the skin, its topography dominates the friction interaction response.

- The intensity of the shear stresses observed in the multi-asperity contact of the skin is of higher relevance in the macroscopic scale. In idealised conditions the skin is assumed to be in pure compression (in the direction normal to its surface). The results of macroscopic indentation showed that the shear stresses in the viable epidermis were in the range of ± 0.003 MPa in the idealised model, while reaching values larger than 300% when the micro-asperity contact is considered. These results are of great implication for the study of the mechanism of formation of superficial pressure ulcers due to constant application of pressure on the skin surface. Shear stress has been used as a mechanical measure to account for potential skin damage (Sopher and Gefen, 2011), therefore, the results of this study imply that capturing the effects of the skin topography in the distribution of shear stress is crucial to evaluate such potential damage.

- Despite the small thickness of the *stratum corneum*, its mechanical properties have a significant effects not only on the magnitude and directions of the strains and stresses it experiences, but also on those of the underlying layers. In the simulation of contact interactions, changes in the mechanical properties of this

layer had significant effects, not only in the dimension of the area of contact, but also in the mechanism of shear stress propagation in the viable epidermis, further away from the contact area. With a soft *stratum corneum* (representative of high humidity conditions), the skin furrows deflect route of propagation of shear stresses sideways, further away from the area of contact, affecting mainly the viable epidermis. With a significant increase in the stiffness of the *stratum corneum* (representative of low humidity conditions), similar levels of stress were observed in the viable epidermis, but the mechanism of shear stress propagation was modified. As a result of the peripheral deformation around the contact area, the stiffer *stratum corneum* is displaced, causing higher propagation of shear stresses. With the presence of the 'hinge-like' mechanism mentioned above, higher stress concentration in the skin furrows located further away from the area of contact.

From the mechano-biological perspective, the strains in the underlying skin layer can affect the tactile sensation (Van der Heide et al., 2013), so the results of this study imply that the mechanical properties of the *stratum corneum* can considerably affect the sensation in the skin. This implication is consistent with the aims of the skin cosmetic industry, where a softer moisturised skin provides comfort to the individual, a relieves itching sensation caused by a dry skin (Shai et al., 2009). In terms of the distribution of shear stresses, the mechano-biological implication resides on the potential risk of skin damage (Goldstein and Sanders, 1998).

8.2 Recommendations for further work

The knowledge generated throughout this project, can be combined by the implementation of the anatomical model in the computational modelling framework, for the benefit on the industry of consumer products. In the area of wet-shaving research, the following recommendations for further work are proposed:

Analysis of the micro-mechanical interactions of wet shaving:

The development of the anatomical model emerged with the aim of capturing the formation of the protection layer under the cartridge blade. With the extension of the anatomical model in 3D, the modularity of the multi-physics modelling framework can be exploited to investigate the wet-shaving lubrication phenomena in microscopic scale —without the simplification of the skin nor the fluid-structure contact interactions.

Analysis of comfort perception:

The mechano-receptors and nociceptors of the skin (providing the sense of touch and pain) are activated by the deformation caused within the skin. Complementary to the proposal above, the study of the shear stress and strain distribution within the viable epidermis, can be applied for the assessment of the 'comfort perception'. The implementation of this idea would require further knowledge in the biological aspect of the skin sensation, application of wider ranges of loading conditions, and interaction with the consumers for the evaluation of their comfort perception.

The implementation of the anatomical model has proven the importance of the skin topography in the micro-mechanical response of the skin. This model provides the opportunity to explore many other scenarios where the skin microstructure is key on its mechanobiological response. Some examples include:

Development of permanent wrinkles:
The concentration of strains in the skin furrows directly affects the viable epidermis and the basal layer of the skin. A combination of the anatomical model with adaptive computational methods as applied by Buganza Tepole et al. (2011), could result in the analysis of the development of permanent skin wrinkles.

Development of superficial pressure ulcers:
It is thought that ischemia is the principal cause of superficial pressure ulcers, as compression of the dermal papilla prevents the flow of blood to the skin capillaries during prolonged compression of the skin. In the studies presented here, it was demonstrated that a complex shear response also takes place in the upper dermis and viable epidermis. Time-dependent effects can be implemented in the simulation of macro-scale compression of the skin for the investigation of 'ischemic damage'.

Investigation of the damaging mechanism of friction blisters:
Friction blister are caused by de-bonding of the epithelial cells in the viable epidermis, as a result of mechanical fatigue. The sliding contact simulations have shown that the propagation of shear stresses towards this layer. The anatomical skin model could be combined with analysis of fatigue and crack propagation. With further implementation of pro-elasticity or bi-phasic materials could capture the formation and filling of the friction blisters in a fluid-structure interaction model.

Mechanical effects of the alteration of the skin microstructure:
The thickness and mechanical properties of the *stratum corneum* can be considerably altered by the micro-climate conditions. Further changes in the skin microstructure can be produced by ageing, UV damage, and inflammatory skin conditions. The techniques and methods developed in the course of this PhD project

can be also applied for the investigation of how these structural changes affect the skin mechanical response. In the case of skin conditions such as eczema, further efforts can be applied for the investigation of mechanisms triggering the itch response, and how the (tribological) reponse to scratching can be linked to further inflammation.

8.3 Conclusion

A new approach for the modelling of multi-physics fluid-structure interactions has been proposed with the development of the **multi-physics modelling framework**. The implications of the characteristics of the fluid mechanical properties, its mesh and the parallelisation level required for best simulation runtime performance have been unravelled. Furthermore, the methods for the representation of the fluid-solid contact interactions have been challenged. The characterisation of the fluid-solid contact interactions requires hybrid experimental-computational methodologies to remove simple assumptions of 'slip' or 'no-slip' conditions, investigating different methods for the mechanical representation of these complex interactions. With these findings, the way has been paved for future implementations of multi-physics modelling of fluid-structure interactions.

Going beyond the interest of capturing the skin tribological interactions on the surface, this project has gone further, investigating the effects of these interactions within the skin. With the development of the **skin anatomical model**, a new perspective on the modelling of human skin has been provided. This model has excelled the common practices in the computational modelling of skin with the implementation of the complex geometry of the skin. This project has captured the relevance of the skin microstructure, not only in its macroscopic mechanical response, but also in its internal response to deformation and contact interactions, providing great potential in the investigation of skin biomechanics.

Appendix A

Shave Prep Rheological Testing Protocol

Rheological test of Shave preps in ARG2 rheometer (TA Instruments Ldt. New Castle, Delaware, U.S.). SAFETY GLASSES SHOULD BE WORN AT ALL TIMES IN THE LAB AREA.

Materials:
- Shave prep sample(s)
- Beaker (0.5-1 L capacity)
- Stirrer
- Minimum 3 glass slides and glass slide covers per test.
- 10 ml Beaker
- 10 ml syringes. At least one for foams and another for pre-canned fluids.
- Cutter
- Four digit precision balance
- Microscope (10x, 20x)
- Paper tissue
- Ethanol (for cleaning rheometer parts)
- Chronometer

Procedure:

1. ARG2 Set up: Set the geometry (concentric cylinders for interstitial fluid, either concentric cylinders or cone and plate geometries - to be confirmed). Set the test Flow Procedure under the following recommended values:

   (a) Conditioning Step:

      i. Temperature: 25°C

      ii. Perform equilibration: 0:00:00

i. Flow Step:
   A. Test type: steady state flow
   B. Ramp: Shear rate (1/s). Set values as required for the test.
   C. Mode: log
   D. Points per decade: 5
   E. Sample period: 0:00:01
   F. Percentage tolerance 3%; Consecutive within tolerance: 3; max point time 0:05:00

ii. Minimum shear strain rate.

iii. Maximum shear strain rate.

2. Prepare sample. See **Section A.1** for different procedure for interstitial fluid and foams. Set the chronometer on when the sample is ready. The test time should be less than 20 minutes, prior the foam starts coarsening.

3. Take a sample to the microscope to capture the foam structure (foams only). Using the stirrer to apply a tiny amount of foam on the glass slide. Measure film thickness and average bubble radius.

4. Measure the sample specific gravity. In case of foams, compare their weight with the interstitial fluid weight to obtain the volume fraction.

   (a) Weight the small beaker. Empty 10 ml beaker weight =

   (b) Fill the beaker to the top with water (Volume > 10 ml).

      i. Water+beaker weight=

      ii. Water weight = Water+beaker weight - beaker weight =

   (c) Dry perfectly the beaker. Measure the weight and make sure it has not changed.

   (d) Fill the beaker to the top with the interstitial fluid. In case of canned gels, use the pure gel (non-lathered); for canned foams, use the pre-can fluid if available.

      i. Interstitial fluid+beaker weight:

      ii. Interstitial fluid weight = Interstitial fluid + beaker weight − beaker weight =

   (e) Clean and dry perfectly the beaker. Measure the weight and make sure it has not changed.

   (f) Fill the beaker to the top with the foam sample (Volume > 10 ml).

      i. Foam+beaker weight =

      ii. Foam weight 1 = Foam+beaker weight − beaker weight =

      iii. Foam gas volume fraction 1 = 1 - (Foam weight 1 / Interstitial fluid weight) =

iv. Foam specific gravity 1 = Foam weight 1 / Water weight =

5. Load the sample into the rheometer geometry.
   (a) For concentric cylinders geometry: Once the inner cylinder has been placed in the test height, the fluid should be covering completely the inner cylinder without over-flowing.
   (b) For cone and plate geometry: Once the cone has been placed in the test height, the foam sample should go slightly out of the cone diameter. Too little foam will not provide full contact area, while too much foam will alter the torque forces.
6. Run the test.
7. Take the sample out of the rheometer. In case of foams, take a sample to the microscope to capture the foam structure (as in step 3).
8. Measure the after-test sample specific gravity as in step 4. No difference should be observed in testing of the interstitial fluid. *This step might be omitted if there is no enough sample to perform the measurement.
   (a) Foam+beaker:
   (b) Foam weight 2 = Foam+beaker weight − beaker weight =
   (c) Foam gas volume fraction 2 = 1 - (Foam weight 2 / Interstitial fluid weight) =
   (d) Foam specific gravity 2 = Foam weight 2 / Water weight =
9. Repeat steps 7 for the aged sample (for reference and comparison of sheared vs. aged foam). Step 8 might be omitted if value for after-test sample was not taken. Foams only.
   (a) Foam+beaker 3 =
   (b) Foam weight 3 = Foam+beaker weight − beaker weight =
   (c) Foam gas volume fraction 3 = 1 - (Foam weight 3 / Interstitial fluid weight) =
   (d) Foam specific gravity 3 = Foam weight 3 / Water weight =
10. Clean the rheometer parts and repeat the procedure for next sample.

A.1 Sample preparation

This procedure is to ensure consistency of the samples for test repeatability.

INTERSTITIAL FLUID (PRE-CANNED FOAM SOLUTION).

1. Use the syringe to place the fluid into the rheometer outer cylinder. Once the inner cylinder has been placed in the test height, the fluid should be covering completely the inner cylinder without over-flowing.

FOAM OR LATHERED GEL.

1. Disassemble the syringe and cut the syringe nozzle. This will be used to load the sample into the rheometer geometry. The nozzle is cut to avoid extra shearing of the sample.
2. Alternative lathering processes:
   (a) In a large beaker apply approximately 10 ml of gel or 50 ml of foam. Stir during 50 s until the sample has been completely lathered (no gel is observed within the sample). For this sample, either 'cup and bob' or plate and cone could be used.
   (b) Apply the foam or gel on the palm of the hand. Rub for 10 s. Repeat until a proper amount of foam is collected for the density test and rheometry.
   (c) Wet the hands. Apply the foam or gel on the palm of the hand. Rub for 10 s. Repeat until a proper amount of foam is collected for the density test and rheometry.
3. Measure the sample density. In case of foams, compare it with the interstitial fluid density to obtain the volume fraction.
   (a) Weight of the empty 10 ml beaker:
   (b) Fill the beaker with 10 ml of the sample. Weight of the sample and beaker:
4. Analyse a sample within the microscope for bubble homogeneity and bubble size.
5. Assure the conditions obtained in steps 3 and 4 are met in every prepared sample (error within 5%).

Appendix B

Mechanical properties of fluid models

The mechanical properties required for the computational modelling of Eulerian materials in the Abaqus environment require complete sets of properties consisting on: Density ρ, Sound propagation velocity c_0 (also mentioned as 'sound speed'), and Viscosity η. With these properties, the mass and volume occupied by the fluid are accounted by ρ, the compressibility by c_0 and the viscous behaviour is accounted as a function of the shear rate (i.e. $\eta(\dot{\gamma})$). The list of fluid properties explored in this project are included in two sections, providing the list of fluid models used for the selection of the most viable constitutive model to represent the viscous behaviour of the shave prep in **Table B.1**, and the properties used for the validation and interaction models in **Table B.2**. These sets of properties where gathered as follows. The values shown for shave prep fluids are property of P&G.

B.1 Fluid models analysed for the selection of the shave prep constitutive model

Fluid SP00

This fluid was built as a reference inviscid fluid for performance comparison against non-linear viscous fluids, using the density of water, the wave propagation velocities of fresh Gillette® regular foam (Mujica and Fauve, 2002).

Fluid SP01

This fluid was characterised with the density of water, wave propagation velocities of aged Gillette® regular foam (Mujica and Fauve, 2002), and viscous

properties of shaving foam (Moir and Craig, 2010), represented by the Herschel-Bulkley constitutive model, under the assumption that the yield stress occurs at a shear rate of 0.05 s^{-1}.

Fluid SP02

This fluid was characterised with the density of water, wave propagation velocities of fresh Gillette® regular foam (Mujica and Fauve, 2002), and viscous properties of PEG 4MM (Polyox™ WSR-301) 0.15% solution in water, represented by the Carreau-Yasuda constitutive model.

Fluid SP03

This fluid shows the same characteristics of Fluid SP02, for a concentration of 0.2% in water, represented by the Power Law constitutive model.

Fluid SP04

This fluid shows the same characteristics of Fluid SP02, for a concentration of 1.0% in water, represented by the Power Law constitutive model.

Fluid SP05

This fluid was built with the same density and wave propagation velocities as Fluid SP02, for PEG 8M (Polyox™ WSR-303) 0.2% solution in water (Lawler, 2001), represented by the Power Law constitutive model, represented by the Power Law constitutive model.

Fluid SP06

This fluid shows the same characteristics of Fluid SP05, for a concentration of 1.0% in water, represented by the Power Law constitutive model.

Fluid SP07

Fluid SP07 was built with the preliminary results obtained from the rheological test, for lathered Gillette® Series Sensitive shave gel with 0% water inclusion, assuming the wave propagation velocities of fresh Gillette® regular foam (Mujica and Fauve, 2002), represented by the Power Law constitutive model.

Table B.1: Summary of properties for fluid models for the selection of the constitutive model to represent the shave prep viscous behaviour. N, H-B and C-Y stand for Newtonian, Herschel-Bulkley and Carreau-Yasuda parameters. **Proprietary data (P&G). Do not disclose**..

	Fluid	**Density [Ton/mm^3]**	**Sound speed [mm/s]**	**Viscosity**
N	Fluid SP00	1.000×10^{-9}	6.500×10^{4}	η =0.000 MPa·s
H-B	Fluid SP01	1.000×10^{-9}	4.500×10^{4}	η_0 =1.000×10^{-3} MPa·s τ_0 =5.000×10^{-5} MPa K =1.700×10^{-5} MPa·s^n n =0.550
C-Y	Fluid SP02	1.000×10^{-9}	6.500×10^{4}	η_0 =1.800×10^{-3} MPa·s η_∞ =1.600×10^{-9} MPa·s λ^t =0.010 s n =0.200 a_y =1.500
Power Law	Fluid SP03	1.000×10^{-9}	6.500×10^{4}	K =3.500×10^{-8} MPa·s^n n =0.590 η_{max} =3.800×10^{-8} MPa·s η_{min} =3.000×10^{-9} MPa·s
	Fluid SP04	1.000×10^{-9}	6.500×10^{4}	K =2.700×10^{-6} MPa·s^n n =0.390 η_{max} =2.706×10^{-6} MPa·s η_{min} =6.000×10^{-9} MPa·s
	Fluid SP05	1.000×10^{-9}	6.500×10^{4}	K =9.400×10^{-8} MPa·s^n n =0.490 η_{max} =9.720×10^{-8} MPa·s η_{min} =3.200×10^{-9} MPa·s
	Fluid SP06	1.000×10^{-9}	6.500×10^{4}	K =5.000×10^{-6} MPa·s^n n =0.350 η_{max} =5.005×10^{-6} MPa·s η_{min} =5.000×10^{-9} MPa·s
	Fluid SP07	8.968×10^{-11}	6.500×10^{4}	K =4.036×10^{-5} MPa·s^n n =0.312 η_{max} =1.966×10^{-4} MPa·s η_{min} =1.052×10^{-6} MPa·s

B.2 Fluid models employed in the simulations

Water

The properties of water have been obtained as an approximate value for a temperature of 20.5°C, from Haynes (2014).

Fluid A

This fluid was built with the density and sound propagation velocity of water, multiplying the viscosity by a factor of 4.

Corn syrup 93% (corn syrup-water dilution, 93-7% by weight)

The density and viscosity were taken from experimental results provided by P&G. The sound propagation velocity was calculated assuming a linear relation between the solid contents and the wave propagation velocity, as follows.

The percent of solid contents S has a direct relation to water content W (portion by weight), as:

$$S(W) = S_0 \cdot (1 - W) \tag{B.1}$$

where S_0 is the solid content for pure corn syrup, which value was taken from Zacharias and Parnell (1972):

$$S(0) = S_0 = 0.785 \tag{B.2}$$

For a dilution with 10% water by weight, were the water-corn syrup proportion is equivalent to 9.09-90.91%, Zacharias and Parnell (1972) repoted:

$$S(0.0909) = S_1 = 0.7136 \tag{B.3}$$

The wave propagation velocity c_0 [m/s] was assumed to be a linear function of the solid content, of the form:

$$c_0(S) = A \cdot S + B \tag{B.4}$$

Given the values publised by Zacharias and Parnell (1972), it is known that:

$$c_0(0.785) = c_{00} = 1.9580 \times 10^6 \text{mm/s} \tag{B.5}$$

$$c_0(0.7136) = c_{01} = 1.8847 \times 10^6 \text{mm/s} \tag{B.6}$$

the slope is defined as:

$$A = \frac{c_{01} - c_{00}}{S_1 - S_0} \tag{B.7}$$

Taking **Equation B.5** and B.6, B is obtained:

$$B = \frac{1}{2}\left[c_{00} + c_{01} - A(S_0 + S_1)\right] \tag{B.8}$$

so the function to estimate the sound propagations velocity was developed as follows:

$$c_0(S) = \frac{c_{01} - c_{00}}{S_1 - S_0} \cdot S + \frac{1}{2}\left[c_{00} + c_{01} - \frac{c_{01} - c_{00}}{S_1 - S_0}(S_0 + S_1)\right]$$

$$= \frac{c_{01} - c_{00}}{S_1 - S_0} \cdot S + \frac{1}{2}\left[\frac{(c_{00} + c_{01})(S_1 - S_0) - (c_{01} - c_{00})(S_0 + S_1)}{S_1 - S_0}\right]$$

$$= \frac{c_{01} - c_{00}}{S_1 - S_0} \cdot S + \frac{1}{2}\left(\frac{c_{00}S_1 + c_{01}S_1 - c_{00}S_0 - c_{01}S_0 + -c_{01}S_0 + c_{00}S_0 - c_{01}S_1 + c_{00}S_1}{S_1 - S_0}\right)$$

$$= \frac{c_{01} - c_{00}}{S_1 - S_0} \cdot S + \frac{1}{2}\left(\frac{2c_{00}S_1 - 2c_{01}S_0}{S_1 - S_0}\right) = \frac{c_{01} - c_{00}}{S_1 - S_0} \cdot S + \frac{c_{00}S_1 - c_{01}S_0}{S_1 - S_0}$$

$$= \frac{c_{01}S - c_{00}S + c_{00}S_1 - c_{01}S_0}{S_1 - S_0}$$

$$c_0(S) = \frac{c_{01}(S - S_0) - c_{00}(S - S_1)}{S_1 - S_0} \tag{B.9}$$

Given viscosity and density values for a corn syrup-water dilution, 93-7% by weight, provided by P&G, the sound propagation velocity for this fluid was calculated as:

$$S(0.07)=0.730, \qquad c_0(0.730)=1.902\times10^6 \text{ mm/s}$$

By mistake the value in the simulation was set as 1.905×10^6 m/s, which is within a 0.2% error, which effect was considered negligible due to the qualitative nature of the **droplet model** simulation.

PEG 1MM (Polyox™ WSR-N-12K) 1%(by weight, dissolved in water)

Density and viscosity-shear rate rheological data were provided by P&G for the PEG 1MM 1% solution.

The viscous behaviour of the PEG solution differs significantly for that of water, but the effects of such small PEG dilution in the wave propagation velocity are still unexplored. In communication with Leighton (2014), from the Institute of Sound and Vibration Research (ISVR, University of Southampton), it was indicated that measuring the wave propagation velocity of this solution was complex problem, unaffordable for this project. Therefore, the sound propagation velocity was assumed to be that of water.

The viscous behaviour data (P&G) was fitted into the Newtonian constitutive model.

PEG 4MM (Polyox™ WSR-301) 1%(by weight, disolved in water)

Density and viscosity-shear rate rheological data were provided by P&Gfor the PEG 4MM 1% solution. The solution density, 0.2% lower than water was rounded

for practical reasons, matching the density of water. The sound propagation velocity was assumed to be that of water. The viscous behaviour data (P&G) was fitted into the Power Law constitutive model.

PEG 5MM (Polyox™ Coagulant) 1%(by weight, disolved in water)

Density and viscosity-shear rate rheological data were provided by P&Gfor the PEG 5MM 1% solution. The sound propagation velocity was assumed to be that of water. The viscous behaviour data (P&G) was fitted into the Power Law constitutive model.

Shaving foam A

The shaving foam was characterised according to the experimental test (**Section 3.7**) for lathered Gillette® Series Sensitive shave gel with 0% water inclusion at 25°C. The density is an average value for five tests. The viscous behaviour was fitted to the Power Law constitutive model, considering the the five tests data at a shear rate range of 0.0001-200.0 s^{-1}. The sound speed is taken from fresh Gillette® regular shaving foam as reported by Mujica and Fauve (2002).

Shaving foam B

The shaving foam was characterised according to the experimental test (**Section 3.7**) for lathered Gillette® Series Sensitive shave gel with 0% water inclusion at 25°C. The density is an average value for five tests. The viscous behaviour was fitted to the Power Law constitutive model, considering the the five tests data at a shear rate range of 0.0001-200.0 s^{-1}. The sound speed is taken from Gillette® 'foamy' at a sound frequency of 670 kHz (pre-resonant) reported by Holt.

Table B.2: Summary of properties for fluid models. N, H-B, C and C-Y stand for Newtonian, Herschel-Bulkley, Cross and Carreau-Yasuda parameters. **Proprietary data (P&G). Do not disclose.**.

	Fluid	**Density [Ton/mm^3]**	**Sound speed [mm/s]**	**Viscosity**
N	Water	1.000×10^{-9}	1.483×10^{6}	$\eta = 1.000 \times 10^{-9}$ MPa·s
	Fluid A	1.000×10^{-9}	1.483×10^{6}	$\eta = 4.000 \times 10^{-9}$ MPa·s
	Corn syrup 93%	1.389×10^{-9}	1.905×10^{6}*	$\eta = 6.849 \times 10^{-6}$ MPa·s
	PEG 1MM 1%	9.981×10^{-10}	1.483×10^{6}	$\eta = 3.32 \times 10^{-8}$ MPa·s
Power Law	PEG 4MM 1%	1.000×10^{-9}	1.483×10^{6}	$K = 2.700 \times 10^{-6}$ MPa·s^n $n = 0.390$ $\eta_{max} = 2.706 \times 10^{-6}$ MPa·s $\eta_{min} = 6.000 \times 10^{-9}$ MPa·s
	PEG 5MM 1%	9.978×10^{-8}	1.483×10^{6}	$K = 3.448 \times 10^{-6}$ MPa·s^n $n = 0.367$ $\eta_{max} = 2.706 \times 10^{-6}$ MPa·s $\eta_{min} = 1.000 \times 10^{-9}$ MPa·s
	Shaving foam A	8.665×10^{-11}	6.500×10^{4}	$K = 5.428 \times 10^{-5}$ MPa·s^n $n = 0.218$ $\eta_{max} = 3.420 \times 10^{-6}$ MPa·s $\eta_{min} = 8.615 \times 10^{-10}$ MPa·s
	Shaving foam B	8.665×10^{-11}	1.200×10^{5}	$K = 5.428 \times 10^{-5}$ MPa·s^n $n = 0.218$ $\eta_{max} = 3.420 \times 10^{-6}$ MPa·s $\eta_{min} = 8.615 \times 10^{-10}$ MPa·s

* Value used in the simulations. Real value should read 1.902×10^{6}.

Bibliography

On the anatomy and physiology of the skin. I. The cleavability of the cutis. (Translated from Langer, K. (1861). Zur Anatomie und Physiologie der Haut. I. Uber die Spaltbarkeit der Cutis. Sitzungsbericht der Mathematisch-naturwissenschaftlichen Classe der. *British journal of plastic surgery*, 31(1):3–8, jan 1978. ISSN 0007-1226. URL http://www.ncbi.nlm.nih.gov/pubmed/342028.

Flexion Reflex Pathways. In Purves, D., Augustine, G. J., Fitzpatrick, D., Katz, L. C., LaMantia, A.-S., McNamara, J. O., and Williams., S. M., editors, *Neuroscience*. Sunderland (MA): Sinauer Associates, 2nd edition, 2001. ISBN 0-87893-742-0. URL http://www.ncbi.nlm.nih.gov/books/NBK11091/.

Rheology Advantage Data Analysis Online Help, 2004. URL www.tainstruments.com.

ANSYS 13 - Documentation. Hyperelastic Material Model, 2010.

Abaqus Analysis User's Guide, version 6.14, 2014a.

Abaqus/CAE User's Guide, version 6.14, 2014b.

Abaqus Theory Manual, version 6.14, 2014c.

Adams, M. J., Briscoe, B. J., and Johnson, S. A. Friction and lubrication of human skin. *Tribology Letters*, 26(3):239–253, apr 2007. ISSN 1023-8883. doi: 10.1007/s11249-007-9206-0. URL http://www.springerlink.com/index/973838UK42723112.pdfhttp://link.springer.com/10.1007/s11249-007-9206-0.

Ahmed, G., Sellier, M., Lee, Y. C., Jermy, M., and Taylor, M. Modeling the spreading and sliding of power-law droplets. *Colloids and Surfaces A: Physicochemical and Engineering Aspects*, 432:2–7, sep 2013. ISSN 09277757. doi: 10.1016/j.colsurfa.2013.05.015. URL http://linkinghub.elsevier.com/retrieve/pii/S0927775713003944.

Ahrens, T. J. Equation of State. In Asay, J. R. and Shahinpoor, M., editors, *High Pressure Shock Compression of Solids*, pages 74–114. Springer-Verlag, NY, 1993.

Alexiades-Armenakas, M. Fractional Laser Skin Resurfacing. *Journal of Drugs in Dermatology*, 11(11):1274–1287, 2012.

Almasi, G. S. and Gottlieb, A. *Highly parallel computing*. The Benjamin/Cummings Publishing Company, Inc., Redwood City, CA, second edition, 1994. ISBN 0805304436.

Andereck, C. D., Liu, S. S., and Swinney, H. L. Flow regimes in a circular Couette system with independently rotating cylinders. *Journal of Fluid Mechanics*, 164(-1):155, apr 1986. ISSN 0022-1120. doi: 10.1017/S0022112086002513. URL http://www.journals.cambridge.org/abstract{_}S0022112086002513.

Areias, P., Jorge, R., Barbosa, J., Fernandes, A., Mascarenhas, T., Oliveira, M., and Patricio, B. Experimental and finite element analysis of human skin elasticity. In *Advances in Bioengineering*, pages 303–304, 2003. doi: 10.1115/IMECE2003-41204.

Arruda, E. and Boyce, M. A three-dimensional constitutive model for the large stretch behavior of rubber elastic materials. *Journal of the Mechanics and Physics of Solids*, 41(2):389–412, 1993. URL http://www.sciencedirect.com/science/article/pii/0022509693900136.

Asserin, J., Zahouani, H., Humbert, P., Couturaud, V., and Mougin, D. Measurement of the friction coefficient of the human skin in vivo. *Colloids and Surfaces B: Biointerfaces*, 19:1–12, 2000. ISSN 09277765. doi: 10.1016/S0927-7765(99)00169-1.

Barnes, H. A. A review of the slip (wall depletion) of polymer solutions, emulsions and particle suspensions in viscometers: its cause, character, and cure. *Journal of Non-Newtonian Fluid Mechanics*, 56(3):221–251, mar 1995. ISSN 03770257. doi: 10.1016/0377-0257(94)01282-M. URL http://www.sciencedirect.com/science/article/pii/037702579401282M.

Barnes, H. A. *A Handbook of Elementary Rheology*. The University of Wales Institute of Non-Newtonian Fluid Mechanics, Department of Mathematics, Aberystwyth, Dyfed, Wales, 2000. ISBN 0-9538032-0-1.

Barnes, H. A. and Nguyen, Q. D. Rotating vane rheometry - a review. *Journal of Non-Newtonian Fluid Mechanics*, 98(1):1–14, mar 2001. ISSN 03770257. doi: 10.1016/S0377-0257(01)00095-7. URL http://linkinghub.elsevier.com/retrieve/pii/S0377025701000957.

Barnes, H. A., Hutton, J. F., and Walters, K. *An Introduction to Rheology*. Elsevier Science, Amstermdam, 1989. ISBN 0444871403.

Batisse, D., Bazin, R., and Baldeweck, T. Influence of age on the wrinkling capacities of skin. *Skin Research and Technology*, 8(3):148–154, aug 2002. ISSN 0909-752X. doi: 10.1034/j.1600-0846.2002.10308.x. URL http://doi.wiley.com/10.1034/j.1600-0846.2002.10308.x.

Bazilevs, Y., Takizawa, K., and Tezduyar, T. E. *Computational Fluid-Structure Interaction: Methods and Applications*. Wiley, Chichester, UK, 1st edition, 2013. ISBN 978-0-470-97877-1.

Bazilevs, Y., Takizawa, K., Tezduyar, T. E., Hsu, M. C., Kostov, N., and McIntyre, S. Aerodynamic and FSI Analysis of Wind Turbines with the ALE-VMS and ST-VMS Methods. *Archives of Computational Methods in Engineering*, 21(4):359–398, 2014. ISSN 11343060. doi: 10.1007/s11831-014-9119-7.

Bellemère, G., Stamatas, G. N., Bruère, V., Bertin, C., Issachar, N., and Oddos, T. Anti-aging action of retinol: From molecular to clinical. *Skin Pharmacology and Physiology*, 22:200–209, 2009. ISSN 16605527. doi: 10.1159/000231525.

Belytschko, T., Liu, W., and Moran, B. *Nonlinear Finite Elements for Continua and Structures*. Wiley, Oxford, 2000. ISBN 978-1-118-63270-3.

Bhushan, B. Nanotribological and nanomechanical properties of skin with and without cream treatment using atomic force microscopy and nanoindentation. *Journal of colloid and interface science*, 367(1):1–33, feb 2012. ISSN 1095-7103. doi: 10.1016/j.jcis.2011.10.019. URL http://www.ncbi.nlm.nih.gov/pubmed/22104280.

Bird, R. B., Armstrong, R. c., and Hassanger, O. *Dynamics of polymeric liquids*. Wiley, New York, NY, 2nd edition, 1987. ISBN 047180245x.

Bischoff, J., Arruda, E., and Grosh, K. Finite element modeling of human skin using an isotropic, nonlinear elastic constitutive model. *Journal of Biomechanics*, 33(6): 645–652, jun 2000. ISSN 00219290. doi: 10.1016/S0021-9290(00)00018-X. URL http://www.sciencedirect.com/science/article/pii/S002192900000018X.

Bischoff, J. E., Arruda, E. a., and Grosh, K. A Microstructurally Based Orthotropic Hyperelastic Constitutive Law. *Journal of Applied Mechanics*, 69(5):570, 2002. ISSN 00218936. doi: 10.1115/1.1485754. URL http://link.aip.org/link/JAMCAV/v69/i5/p570/s1{&}Agg=doi.

Boissieux, L., Kiss, G., Magnenat-Thalmann, N., and Kalra, P. Simulation of Skin Aging and Wrinkles with Cosmetics Insight. In *Computer Animation and Simulation 2000*, pages 15–27, 2000. doi: 10.1007/978-3-7091-6344-3_2.

Bolognia, J., Braverman, I., Rousseau, M., and Sarrel, P. Skin changes in menopause. *Maturitas*, 11:295–304, 1989.

Boyer, G., Laquièze, L., Le Bot, A., Laquièze, S., and Zahouani, H. Dynamic indentation on human skin in vivo : ageing effects. *Skin Research and Technology*, 15(1):55–67, feb 2009. ISSN 0909752X. doi: 10.1111/j.1600-0846.2008.00324.x. URL http://www.ncbi.nlm.nih.gov/pubmed/19152580http://doi.wiley.com/10.1111/j.1600-0846.2008.00324.x.

Brand, P. Pressure sores - the problem. *Journal of Tissue Viability*, 16(2):9–11, may 2006. ISSN 0965206X. doi: 10.1016/S0965-206X(06)62003-2. URL http://linkinghub.elsevier.com/retrieve/pii/S0965206X06620032.

Buganza Tepole, A., Joseph Ploch, C., Wong, J., Gosain, A. K., and Kuhl, E. Growing skin: A computational model for skin expansion in reconstructive surgery. *Journal of the Mechanics and Physics of Solids*, 59(10):2177–2190, oct 2011. ISSN 00225096. doi: 10.1016/j.jmps.2011.05.004. URL http://linkinghub.elsevier.com/retrieve/pii/S0022509611001074.

Burgeson, R. E. and Christiano, A. M. The dermal-epidermal junction. *Current Opinion in Cell Biology*, 9(5):651–658, oct 1997. ISSN 09550674. doi: 10.1016/S0955-0674(97)80118-4. URL http://linkinghub.elsevier.com/retrieve/pii/S0955067497801184.

Burns, T., Breathnach, S., Cox, N., and Griffiths, C. *Rook's Textbook of Dermatology*. Blackwell Science, Oxford, 7th edition, 2004. ISBN 0632064293.

Cantat, I., Cohen-Addad, S., Elias, F., Graner, F., Höhler, R., Flatman, R., Pitois, O., Rouyer, F., and Saint-Jalmes, A. *Foams: Structure and Dynamics*. Oxford University Press, New York, 2013. ISBN 978-0-19-966289-0.

Carreau, P. J., Kee, D. D., and Chhabra, R. P. *Rheology of polymeric systems : principles and applications*. Hanser Publishers, New York, 1997. ISBN 1569902186, 9781569902189.

Catheline, S., Gennisson, J.-L., Delon, G., Fink, M., Sinkus, R., Abouelkaram, S., and Culioli, J. Measurement of viscoelastic properties of homogeneous soft solid using transient elastography: An inverse problem approach. *The Journal of the Acoustical Society of America*, 116(6):3734, 2004. ISSN 00014966. doi: 10.1121/1.1815075. URL http://link.aip.org/link/JASMAN/v116/i6/p3734/s1{&}Agg=doi.

Cavicchi, A., Gambarotta, L., and Massabò, R. Computational modeling of reconstructive surgery: The effects of the natural tension on skin wrinkling. *Finite Elements in Analysis and Design*, 45:519–529, 2009. ISSN 0168874X. doi: 10.1016/j.finel.2009.02.006.

Cerda, E. Mechanics of scars. *Journal of Biomechanics*, 38(8):1598–1603, aug 2005. ISSN 00219290. doi: 10.1016/j.jbiomech.2004.07.026. URL http://linkinghub.elsevier.com/retrieve/pii/S0021929004003793.

Chan, L. S. Human skin basement membrane in health and in autoimmune diseases. *Frontiers in Bioscience*, 2:d343–d352, 1997. ISSN 1093-4715.

Changizi, M., Weber, R., Kotecha, R., and Palazzo, J. Are Wet-Induced Wrinkled Fingers Primate Rain Treads?, 2011. ISSN 00068977.

Chaudhry, H., Bukiet, B., Siegel, M., Findley, T., Ritter, A., and Guzelsu, N. Optimal patterns for suturing wounds. *Journal of Biomechanics*, 31(7):653–662, jul 1998. ISSN 00219290. doi: 10.1016/S0021-9290(98)00069-4. URL http://linkinghub.elsevier.com/retrieve/pii/S0021929098000694.

Clancy, N. T., Nilsson, G. E., Anderson, C. D., and Leahy, M. J. A new device for assessing changes in skin viscoelasticity using indentation and optical measurement. *Skin Research and Technology*, 16(2):210–228, may 2010. ISSN 0909752X. doi: 10.1111/j.1600-0846.2010.00433.x. URL http://www.ncbi.nlm.nih.gov/pubmed/20456102http://doi.wiley.com/10.1111/j.1600-0846.2010.00433.x.

Cohen-Addad, S. and Höhler, R. Bubble Dynamics Relaxation in Aqueous Foam Probed by Multispeckle Diffusing-Wave Spectroscopy. *Physical Review Letters*, 86(20):4700–4703, may 2001. ISSN 0031-9007. doi: 10.1103/PhysRevLett.86.4700. URL http://link.aps.org/doi/10.1103/PhysRevLett.86.4700.

Comaish, S. and Bottoms, E. The skin and friction: deviations from Amonton's laws, and the effects of hydration and lubrication. *British Journal of Dermatology*, 84(1):37–43, 1971. doi: 10.1111/j.1365-2133.1971.tb14194.x.

Cowin, S. C. Bone poroelasticity. *Journal of Biomechanics*, 32(3):217–238, 1999. doi: 10.1016/S0021-9290(98)00161-4.

Crichton, M. L., Donose, B. C., Chen, X., Raphael, A. P., Huang, H., and Kendall, M. a. F. The viscoelastic, hyperelastic and scale dependent behaviour of freshly excised individual skin layers. *Biomaterials*, 32(20):4670–81, jul 2011. ISSN 1878-5905. doi: 10.1016/j.biomaterials.2011.03.012. URL http://www.ncbi.nlm.nih.gov/pubmed/21458062.

Dahlgren, R. M. Measurement of skin condition by sonic velocity. *Journal of the Society of Cosmetic Chemists*, 35(1):1–19, 1984.

Delalleau, A. *Analysis of the Mechanical Behaviour of Skin, in vivo*. PhD thesis, The Jean Monet University of Saint-Etiennne, 2007.

Delalleau, A., Josse, G., Lagarde, J.-M., Zahouani, H., and Bergheau, J.-M. Characterization of the mechanical properties of skin by inverse analysis combined with the indentation test. *Journal of Biomechanics*, 39(9):1603–1610, jan 2006. ISSN 00219290. doi: 10.1016/j.jbiomech.2005.05.001. URL http://linkinghub.elsevier.com/retrieve/pii/S0021929005002162.

Delalleau, A., Josse, G., Lagarde, J.-M., Zahouani, H., Bergheau, J.-M., and Toscano, R. A new stochastic inverse identification of the mechanical properties of human skin. *Engineering Optimization*, 43(1):61–75, jan 2011. ISSN 0305-215X. doi: 10.1080/03052151003739606. URL http://www.tandfonline.com/doi/abs/10.1080/03052151003739606.

Derler, S. and Gerhardt, L. C. Tribology of skin: Review and analysis of experimental results for the friction coefficient of human skin, oct 2012. ISSN 10238883. URL http://www.springerlink.com/index/10.1007/s11249-011-9854-y.

Derler, S., Gerhardt, L.-C., Lenz, a., Bertaux, E., and Hadad, M. Friction of human skin against smooth and rough glass as a function of the contact pressure. *Tribology International*, 42(11-12):1565–1574, dec 2009a. ISSN 0301679X. doi: 10.1016/j.triboint.2008.11.009. URL http://linkinghub.elsevier.com/retrieve/pii/S0301679X0800251X.

Derler, S., Huber, R., Feuz, H.-P., and Hadad, M. Influence of surface microstructure on the sliding friction of plantar skin against hard substrates. *Wear*, 267(5-8):1281–1288, 2009b. ISSN 00431648. doi: 10.1016/j.wear.2008.12.053. URL http://www.sciencedirect.com/science/article/pii/S0043164809000817.

Diridollou, S., Patat, F., Gens, F., Vaillant, L., Black, D., Lagarde, J. M., Gall, Y., and Berson, M. In vivo model of the mechanical properties of the human skin under suction. *Skin Research and Technology*, 6(4):214–221, nov 2000. ISSN 0909-752X. doi: 10.1034/j.1600-0846.2000.006004214.x. URL http://doi.wiley.com/10.1034/j.1600-0846.2000.006004214.x.

Diridollou, S., Vabre, V., Berson, M., Vaillant, L., Black, D., Lagarde, J. M., Gregoire, J. M., Gall, Y., and Patat, F. Skin ageing: changes of physical properties of human skin in vivo. *International Journal of Cosmetic Science*, 23(6):353–362, dec 2001. ISSN 0142-5463. doi: 10.1046/j.0412-5463.2001.00105.x. URL http://onlinelibrary.wiley.com/doi/10.1046/j.0412-5463.2001.00105.x/fullhttp://doi.wiley.com/10.1046/j.0412-5463.2001.00105.x.

Draelos, Z. Male skin and ingredients relevant to male skin care. *British Journal of Dermatology*, 166:13–16, mar 2012. ISSN 00070963. doi: 10.1111/j.1365-2133.2011.10784.x. URL http://www.ncbi.nlm.nih.gov/pubmed/22385030http://doi.wiley.com/10.1111/j.1365-2133.2011.10784.x.

Duan, Z., Tong, B., and Jiang, G. A finite-element formulation of heating rate and skin friction on the basis of conservation laws. *Acta Mechanica Sinica*, 16:128–132, 2000. ISSN 05677718.

Dunn, M. G., Silver, F. H., and Swann, D. A. Mechanical analysis of hypertrophic scar tissue: structural basis for apparent increased rigidity. *The Journal of Investigative Dermatology*, 84(1):9–13, 1985. ISSN 0022-202X. doi: 10.1111/1523-1747.ep12274528.

Durian, D. J. The physics of foam. Technical report, UCLA Physics and Astronomics, Los Angeles, CA, 2002. URL http://boulder.research.yale.edu/Boulder-2002/Lectures/Durian/[1]introduction.pdf.

Egawa, M., Oguri, M., Hirao, T., Takahashi, M., and Miyakawa, M. The evaluation of skin friction using africtional feel analyzer. *Skin Research and Technology*, 8(1):41–51, feb 2002. ISSN 0909752X. doi: 10.1034/j.1600-0846.2002.080107.x. URL http://doi.wiley.com/10.1034/j.1600-0846.2002.080107.x.

Elbischger, P. J., Bischof, H., Regitnig, P., and Holzapfel, G. A. Automatic analysis of collagen fiber orientation in the outermost layer of human arteries. *Pattern Analysis and Applications*, 7(3):269–284, dec 2004. ISSN 1433-7541. doi: 10.1007/s10044-004-0224-3. URL http://link.springer.com/10.1007/s10044-004-0224-3.

Epstein, W. L. and Maibach, H. I. Cell Renewal in Human Epidermis. *Archives of Dermatology*, 92(4):462, oct 1965. ISSN 0003-987X. doi: 10.1001/archderm.1965.01600160118025. URL http://archderm.jamanetwork.com/article.aspx?doi=10.1001/archderm.1965.01600160118025.

Evans, N. D., Oreffo, R. O., Healy, E., Thurner, P. J., and Man, Y. H. Epithelial mechanobiology, skin wound healing, and the stem cell niche. *Journal of the Mechanical Behavior of Biomedical Materials*, 28:397–409, dec 2013. ISSN 17516161. doi: 10.1016/j.jmbbm.2013.04.023. URL http://linkinghub.elsevier.com/retrieve/pii/S1751616113001550.

Evans, S. On the implementation of a wrinkling, hyperelastic membrane model for skin and other materials. *Computer Methods in Biomechanics and Biomedical Engineering*, 12(3):319–332, jun 2009. ISSN 1025-5842. doi: 10.1080/10255840802546762. URL http://www.tandfonline.com/doi/abs/10.1080/10255840802546762.

Ferguson, B. Elastic Deformation Effects in Precision Measurement. *Microtecnic*, 11: 256–258, 1957.

Finocchietti, S., Mørch, C. D., Arendt-Nielsen, L., and Graven-Nielsen, T. Effects of Adipose Thickness and Muscle Hardness on Pressure Pain Sensitivity: Correction. *The Clinical Journal of Pain*, 27(8):735–745, 2011.

Flynn, C. Finite element models of wound closure. *Journal of Tissue Viability*, 19(4): 137–149, nov 2010. ISSN 0965206X. doi: 10.1016/j.jtv.2009.10.001. URL http://linkinghub.elsevier.com/retrieve/pii/S0965206X09000382.

Flynn, C. and McCormack, B. A. A simplified model of scar contraction. *Journal of Biomechanics*, 41(7):1582–1589, jan 2008a. ISSN 00219290. doi: 10.1016/j.jbiomech.2008.02.024. URL http://linkinghub.elsevier.com/retrieve/pii/S0021929008000821.

Flynn, C. and McCormack, B. A. Simulating the wrinkling and aging of skin with a multi-layer finite element model. *Journal of Biomechanics*, 43(3):442–448, feb 2010. ISSN 00219290. doi: 10.1016/j.jbiomech.2009.10.007. URL http://www.ncbi.nlm.nih.gov/pubmed/19889419http://linkinghub.elsevier.com/retrieve/pii/S0021929009005806.

Flynn, C. and McCormack, B. A. O. Finite element modelling of forearm skin wrinkling. *Skin Research and Technology*, 14(3):261–269, aug 2008b. ISSN 0909752X.

doi: 10.1111/j.1600-0846.2008.00289.x. URL http://doi.wiley.com/10.1111/j.1600-0846.2008.00289.x.

Flynn, C., Taberner, A. J., and Nielsen, P. M. F. Characterizing skin using a three-axis parallel drive force-sensitive micro-robot. In *2010 Annual International Conference of the IEEE Engineering in Medicine and Biology*, volume 2010, pages 6481–6484. IEEE, aug 2010. ISBN 978-1-4244-4123-5. doi: 10.1109/IEMBS.2010.5627357. URL http://www.ncbi.nlm.nih.gov/pubmed/21096723http://ieeexplore.ieee.org/lpdocs/epic03/wrapper.htm?arnumber=5627357.

Flynn, C., Rubin, M. B., and Nielsen, P. A model for the anisotropic response of fibrous soft tissues using six discrete fibre bundles. *International Journal for Numerical Methods in Biomedical Engineering*, 27(11):1793–1811, nov 2011a. ISSN 20407939. doi: 10.1002/cnm.1440. URL http://onlinelibrary.wiley.com/doi/10.1002/cnm.1440/fullhttp://doi.wiley.com/10.1002/cnm.1440.

Flynn, C., Taberner, A., and Nielsen, P. Measurement of the force-displacement response of in vivo human skin under a rich set of deformations. *Medical engineering & physics*, 33(5):610–9, jun 2011b. ISSN 1873-4030. doi: 10.1016/j.medengphy.2010.12.017. URL http://www.ncbi.nlm.nih.gov/pubmed/21242096.

Flynn, C., Taberner, A. J., Nielsen, P. M. F., and Fels, S. Simulating the three-dimensional deformation of in vivo facial skin. *Journal of the mechanical behavior of biomedical materials*, 28:484–94, dec 2013. ISSN 1878-0180. doi: 10.1016/j.jmbbm.2013.03.004. URL http://www.ncbi.nlm.nih.gov/pubmed/23566769.

Flynn, C., Stavness, I., Lloyd, J., and Fels, S. A finite element model of the face including an orthotropic skin model under in vivo tension. *Computer Methods in Biomechanics and Biomedical Engineering*, 18(6):571–582, 2015. doi: 10.1016/S0021-9290(12)70266-X.

Flynn, C. O. and McCormack, B. A. A three-layer model of skin and its application in simulating wrinkling. *Computer Methods in Biomechanics and Biomedical Engineering*, 12(2):125–134, apr 2009. ISSN 1025-5842. doi: 10.1080/10255840802529933. URL http://www.ncbi.nlm.nih.gov/pubmed/19016055http://www.tandfonline.com/doi/abs/10.1080/10255840802529933.

Fung, Y. *Biomechanics: mechanical properties of living tissues*. Springer-Verlag, New York, NY, 1981. ISBN 978-1-4757-2257-4.

Geerligs, M. *Skin layer mechanics*. PhD thesis, Technische Universiteit Eindhoven, 2010.

Geerligs, M., Peters, G., Ackermans, P., Oomens, C. W. J., and Baaijens, F. P. T. Linear viscoelastic behavior of subcutaneous adipose tissue. *Biorheology*, 45(6):677–688,

2008. doi: 10.3233/BIR-2008-0517. URL http://iospress.metapress.com/index/F7713285766R17JU.pdf.

Geerligs, M., Oomens, C., Ackermans, P., Baaijens, F., and Peters, G. Linear shear response of the upper skin layers. *Biorheology*, 48(3-4):229–45, jan 2011a. ISSN 1878-5034. doi: 10.3233/BIR-2011-0590. URL http://www.ncbi.nlm.nih.gov/pubmed/22156036.

Geerligs, M., van Breemen, L., Peters, G., Ackermans, P., Baaijens, F., and Oomens, C. In vitro indentation to determine the mechanical properties of epidermis. *Journal of Biomechanics*, 44(6):1176–1181, apr 2011b. ISSN 00219290. doi: 10.1016/j.jbiomech.2011.01.015. URL http://www.ncbi.nlm.nih.gov/pubmed/21296353http://linkinghub.elsevier.com/retrieve/pii/S0021929011000455.

Gefen, A. How do microclimate factors affect the risk for superficial pressure ulcers: A mathematical modeling study. *Journal of Tissue Viability*, 20(3):81–88, 2011. ISSN 0965206X. doi: 10.1016/j.jtv.2010.10.002. URL http://dx.doi.org/10.1016/j.jtv.2010.10.002.

Gerhardt, L.-C., Strässle, V., Lenz, a., Spencer, N. D., and Derler, S. Influence of epidermal hydration on the friction of human skin against textiles. *Journal of the Royal Society, Interface / the Royal Society*, 5(28):1317–28, nov 2008. ISSN 1742-5689. doi: 10.1098/rsif.2008.0034. URL http://www.pubmedcentral.nih.gov/articlerender.fcgi?artid=2607440{&}tool=pmcentrez{&}rendertype=abstract.

Gerhardt, L.-C., Lenz, A., Spencer, N. D., Münzer, T., and Derler, S. Skin-textile friction and skin elasticity in young and aged persons. *Skin Research and Technology*, 15(3):288–298, aug 2009a. ISSN 0909752X. doi: 10.1111/j.1600-0846.2009.00363.x. URL http://www.ncbi.nlm.nih.gov/pubmed/19624425http://doi.wiley.com/10.1111/j.1600-0846.2009.00363.x.

Gerhardt, L.-C., Schiller, a., Müller, B., Spencer, N. D., and Derler, S. Fabrication, Characterisation and Tribological Investigation of Artificial Skin Surface Lipid Films. *Tribology Letters*, 34(2):81–93, feb 2009b. ISSN 1023-8883. doi: 10.1007/s11249-009-9411-0. URL http://www.springerlink.com/index/10.1007/s11249-009-9411-0.

Giesekus, H. A simple constitutive equation for polymer fluids based on the concept of deformation-dependent tensorial mobility. *Journal of Non-Newtonian Fluid Mechanics*, 11(1-2):69–109, 1982. ISSN 03770257. doi: 10.1016/0377-0257(82)85016-7. URL http://www.sciencedirect.com/science/article/pii/0377025782850167.

Goldstein, B. and Sanders, J. Skin Response to Repetitive Mechanical Stress : a New Experimental Model in Pig. *Archives of Physical Medicine and Rehabilitation*, 79(3):265–272, 1998. doi: 10.1016/S0003-9993(98)90005-3.

Goldstein, E. B. *The Blackwell Handbook of Sensation and Perception*. Wiley-Blackwell, 2008. ISBN 9780470751992. URL http://www.myilibrary.com/?ID=132251.

Gopal, A. D. and Durian, D. J. Shear-Induced "Melting" of an Aqueous Foam. *Journal of Colloid and Interface Science*, 213:169–178, 1999.

Graebel, W. *Advanced Fluid Mechanics*. Academic Press, Burlington, US, 2007. ISBN 9780080549088. URL ProQuestebraryhttp://site.ebrary.com/lib/soton/detail.action?docID=10216796.

Graham, J. S., Vomund, A. N., Phillips, C. L., and Grandbois, M. Structural changes in human type I collagen fibrils investigated by force spectroscopy. *Experimental cell research*, 299(2):335–42, oct 2004. ISSN 0014-4827. doi: 10.1016/j.yexcr.2004.05.022. URL http://www.sciencedirect.com/science/article/pii/S0014482704003052.

Granick, S., Zhu, Y., and Lee, H. Slippery questions about complex fluids flowing past solids. *Nature Materials*, 2(4):221–227, apr 2003. ISSN 14761122. doi: 10.1038/nmat854. URL http://www.nature.com/doifinder/10.1038/nmat854.

Greenwood, J. a. and Tabor, D. The Friction of Hard Sliders on Lubricated Rubber: The Importance of Deformation Losses. *Proceedings of the Physical Society*, 71(6):989–1001, 1958. ISSN 0035-9475. doi: 10.5254/1.3542119.

Groves, R. B., Coulman, S. A., Birchall, J. C., and Evans, S. L. An anisotropic, hyperelastic model for skin: Experimental measurements, finite element modelling and identification of parameters for human and murine skin. *Journal of the Mechanical Behavior of Biomedical Materials*, 18:167–180, feb 2013. ISSN 17516161. doi: 10.1016/j.jmbbm.2012.10.021. URL http://linkinghub.elsevier.com/retrieve/pii/S1751616112002974.

Gu, Y., Li, J., Ren, X., Lake, M. J., and Zeng, Y. Heel skin stiffness effect on the hind foot biomechanics during heel strike. *Skin Research and Technology*, 16(3):291–6, apr 2010. ISSN 0909752X. doi: 10.1111/j.1600-0846.2010.00425.x. URL http://www.ncbi.nlm.nih.gov/pubmed/20636997http://doi.wiley.com/10.1111/j.1600-0846.2010.00425.x.

Guerra, C. and Schwartz, C. J. Development of a synthetic skin simulant platform for the investigation of dermal blistering mechanics. *Tribology Letters*, 44:223–228, 2011. ISSN 10238883. doi: 10.1007/s11249-011-9840-4.

Gunner, C. W., Hutton, W. C., and Burlin, T. E. The mechanical properties of skin in vivo–a portable hand-held extensometer. *The British Journal of Dermatology*, 100(2):161–163, 1979. ISSN 0007-0963. doi: 10.1111/j.1365-2133.1979.tb05555.x.

Gurtner, G. C., Dauskardt, R. H., Wong, V. W., Bhatt, K. A., Wu, K., Vial, I. N., Padois, K., Korman, J. M., and Longaker, M. T. Improving Cutaneous Scar Formation by Controlling the Mechanical Environment. *Annals of Surgery*, 254(2):217–225, aug 2011. ISSN 0003-4932. doi: 10.1097/SLA.0b013e318220b159. URL http://content.wkhealth.com/linkback/openurl?sid=WKPTLP:landingpage{&}an=00000658-201108000-00007.

Hale, J. F., McDonald, D. A., and Womersley, J. R. Velocity profiles of oscillating arterial flow, with some calculations of viscous drag and the Reynolds number. *The Journal of Physiology*, 128(3):629–640, jun 1955. ISSN 00223751. doi: 10.1113/jphysiol.1955.sp005330. URL http://doi.wiley.com/10.1113/jphysiol.1955.sp005330.

Harris, T. A. and Kotzalas, M. N. *Rolling bearing analysis. Essential concepts of bearing technology*. CRC/Taylor & Francis, Boca Raton; London, 5th edition, 2007. ISBN 9780849371837.

Hatzikiriakos, S. G. Slip mechanisms in complex fluid flows. *Soft Matter*, 11(40):7851–7856, 2015. ISSN 1744-683X. doi: 10.1039/C5SM01711D. URL http://xlink.rsc.org/?DOI=C5SM01711D.

Haynes, W. M. *CRC handbook of chemistry and physics: a ready-reference book of chemical and physical data*. CRC PRESS, Boca Raton, 95th edition, 2014. ISBN 9781482208672.

Hendriks, C. P. and Franklin, S. E. Influence of Surface Roughness, Material and Climate Conditions on the Friction of Human Skin. *Tribology Letters*, 37(2):361–373, oct 2010. ISSN 1023-8883. doi: 10.1007/s11249-009-9530-7. URL http://www.springerlink.com/index/N161UU88K8XR8627.pdfhttp://www.springerlink.com/index/10.1007/s11249-009-9530-7.

Hendriks, F. *Mechanical behaviour of human epidermal and dermal layers in vivo*. Doctoral thesis, Technische Universiteit Eindhoven, 2005. URL http://en.scientificcommons.org/17601300.

Hendriks, F., Brokken, D., Oomens, C., Bader, D., and Baaijens, F. The relative contributions of different skin layers to the mechanical behavior of human skin in vivo using suction experiments. *Medical Engineering & Physics*, 28(3):259–266, apr 2006. ISSN 13504533. doi: 10.1016/j.medengphy.2005.07.001. URL http://www.ncbi.nlm.nih.gov/pubmed/16099191http://linkinghub.elsevier.com/retrieve/pii/S1350453305001451.

Hendriks, F. M., Brokken, D., van Eemeren, J. T. W. M., Oomens, C. W. J., Baaijens, F. P. T., and Horsten, J. B. A. M. A numerical-experimental method to characterize the non-linear mechanical behaviour of human skin. *Skin Research and Technology*, 9(3):

274–283, aug 2003. ISSN 0909-752X. doi: 10.1034/j.1600-0846.2003.00019.x. URL http://doi.wiley.com/10.1034/j.1600-0846.2003.00019.x.

Hendriks, F. M., Brokken, D., Oomens, C. W. J., and Baaijens, F. P. T. Influence of hydration and experimental length scale on the mechanical response of human skin in vivo, using optical coherence tomography. *Skin Research and Technology*, 10(4): 231–241, nov 2004. ISSN 0909-752X. doi: 10.1111/j.1600-0846.2004.00077.x. URL http://www.ncbi.nlm.nih.gov/pubmed/15479446http://doi.wiley.com/10.1111/j.1600-0846.2004.00077.x.

Henry, C., Neto, C., Evans, D., Biggs, S., and Craig, V. The effect of surfactant adsorption on liquid boundary slippage. *Physica A: Statistical Mechanics and its Applications*, 339(1-2):60–65, aug 2004. ISSN 03784371. doi: 10.1016/j.physa.2004.03.044. URL http://www.sciencedirect.com/science/article/pii/S0378437104003577.

Heuzé, O. General form of the Mie-Grüneisen equation of state. *Comptes Rendus - Mecanique*, 340(10):679–687, 2012. ISSN 16310721. doi: 10.1016/j.crme.2012.10.044. URL http://dx.doi.org/10.1016/j.crme.2012.10.044.

Holt, R. G. Bubbles and acoustics in foam.

Holzapfel, G. A. *Nonlinear Solid Mechanics: A Continuum Approach for Engineering*. Wiley, Great Britain, 2004.

Holzapfel, G. A., Gasser, T. C., and Ogden, R. W. A New Constitutive Framework for Arterial Wall Mechanics and a Comparative Study of Material Models. *Journal of Elasticity*, 61(1/3):1–48, 2000. ISSN 03743535. doi: 10.1023/A:1010835316564. URL http://link.springer.com/10.1023/A:1010835316564.

Horgan, C. O. and Murphy, J. G. On the volumetric part of strain-energy functions used in the constitutive modeling of slightly compressible solid rubbers. *International Journal of Solids and Structures*, 46(16):3078–3085, 2009. ISSN 00207683. doi: 10.1016/j.ijsolstr.2009.04.007. URL http://linkinghub.elsevier.com/retrieve/pii/S0020768309001723.

Huang, Z., Zhou, D., and Ren, Q.-s. Nonlinear anisotropic composite biomechanical modeling of human skin. *Journal of Shanghai Jiaotong University (Science)*, 15(3): 363–367, may 2010. ISSN 1007-1172. doi: 10.1007/s12204-010-1017-z. URL http://www.springerlink.com/index/10.1007/s12204-010-1017-z.

Humbert, P., Viennet, C., Legagneux, K., Grandmottet, F., Robin, S., Oddos, T., and Muret, P. In the shadow of the wrinkle: theories. *Journal of cosmetic dermatology*, 11(1):72–8, mar 2012. ISSN 1473-2165. doi: 10.1111/j.1473-2165.2011.00602.x. URL http://www.ncbi.nlm.nih.gov/pubmed/22360338.

Hung, A., Mithraratne, K., and Sagar, M. Multilayer soft tissue continuum model: towards realistic simulation of facial expressions. *World Academy of Science,*, 54:134–138, 2009. URL http://www.waset.ac.nz/journals/waset/v54/v54-25.pdf.

Israelachvili, J. N. *Intermolecular and Surface Forces*. Elsevier Ltd, Santa Barbara, California, USA, second edi edition, 1991. ISBN 0-12-375181-0.

Jachowicz, J., Mcmullen, R., and Prettypaul, D. Indentometric analysis of in vivo skin and comparison with artificial skin models. *Skin Research and Technology*, 2(13): 299–309, 2007. doi: 10.1111/j.1600-0846.2007.00229.x.

Jee, T. and Komvopoulos, K. In vitro measurement of the mechanical properties of skin by nano/microindentation methods. *Journal of Biomechanics*, 47(5):1186–1192, 2014. ISSN 18732380. doi: 10.1016/j.jbiomech.2013.10.020. URL http://dx.doi.org/10.1016/j.jbiomech.2013.10.020.

Jemec, G. B. and Wulf, H. C. Correlation between the greasiness and the plasticizing effect of moisturizers. *Acta Dermato-Venereologica*, 79(2):115–7, mar 1999. ISSN 0001-5555. URL http://www.ncbi.nlm.nih.gov/pubmed/10228628.

Jemec, G. B. E. and Na, R. Hydration and plasticity following long-term use of a moisturizer: a single-blind study. *Acta Dermato-Venereologica*, 82(5):322–4, 2002. ISSN 0001-5555. URL http://www.medicaljournals.se/acta/content/download.php?doi=10.1080/000155502320624023http://www.ncbi.nlm.nih.gov/pubmed/12430728.

Johnson, K. L. *Contact Mechanics*. Cambridge University Press, Cambridge, UK., 1985. ISBN 0 521 34796 3.

Jor, J. W. Y., Parker, M. D., Taberner, A. J., Nash, M. P., and Nielsen, P. M. F. Computational and experimental characterization of skin mechanics: Identifying current challenges and future directions. *Wiley Interdisciplinary Reviews: Systems Biology and Medicine*, 5:539–556, 2013. ISSN 19395094. doi: 10.1002/wsbm.1228.

Kamenskiy, A. V., Dzenis, Y. A., Mactaggart, J. N., Desyatova, A. S., and Pipinos, I. I. In vivo three-dimensional blood velocity profile shapes in the human common, internal, and external carotid arteries. *Journal of vascular surgery*, 54(4):1011–20, oct 2011. ISSN 1097-6809. doi: 10.1016/j.jvs.2011.03.254. URL http://www.sciencedirect.com/science/article/pii/S0741521411007300.

Karduna, A. R., Halperin, H. R., and Yin, F. C. P. Experimental and numerical analyses of indentation in finite-sized isotropic and anisotropic rubber-like materials. *Annals of Biomedical Engineering*, 25(6):1009–1016, 1997. ISSN 00906964. doi: 10.1007/BF02684136.

Kareklas, K., Nettle, D., and Smulders, T. V. Water-induced finger wrinkles improve handling of wet objects. *Biology Letters*, 9(2):20120999–20120999, jan 2013. ISSN 1744-9561. doi: 10.1098/rsbl.2012.0999. URL http://rsbl.royalsocietypublishing.org/cgi/doi/10.1098/rsbl.2012.0999.

Katgert, G. *Flow of Foams*. Phd, University of Leiden, 2008.

Khan, S. A. Foam Rheology: III. Measurement of Shear Flow Properties. *Journal of Rheology*, 32(1):69, 1988. ISSN 01486055. doi: 10.1122/1.549964. URL http://scitation.aip.org/content/sor/journal/jor2/32/1/10.1122/1.549964.

Khatyr, F., Imberdis, C., Vescovo, P., Varchon, D., and Lagarde, J.-M. Model of the viscoelastic behaviour of skin in vivo and study of anisotropy. *Skin Research and Technology*, 10(2):96–103, 2004. URL http://onlinelibrary.wiley.com/doi/10.1111/j.1600-0846.2004.00057.x/full.

Khatyr, F., Imberdis, C., Varchon, D., Lagarde, J.-M., and Josse, G. Measurement of the mechanical properties of the skin using the suction test. *Skin Research and Technology*, 12(1):24–31, 2006. URL http://onlinelibrary.wiley.com/doi/10.1111/j.0909-725X.2006.00126.x/full.

Kirkham, S., Lam, S., Nester, C., and Hashmi, F. The effect of hydration on the risk of friction blister formation on the heel of the foot. *Skin Research and Technology*, pages 246–253, 2014. ISSN 0909752X. doi: 10.1111/srt.12136.

Kong, X. Q., Zhou, P., and Wu, C. W. Numerical simulation of microneedles' insertion into skin. *Computer Methods in Biomechanics and Biomedical Engineering*, 14(9):827–835, sep 2011. ISSN 1025-5842. doi: 10.1080/10255842.2010.497144. URL http://www.ncbi.nlm.nih.gov/pubmed/21480017http://www.tandfonline.com/doi/abs/10.1080/10255842.2010.497144.

Kottner, J., Dobos, G., and Blume-Peytavi, U. How does immobility affect the skin barrier? In *23rd Conference of the European Wound Management Association*, 2013.

Koudine, Barquins, Anthoine, Aubert, and Lévêque. Frictional properties of skin: proposal of a new approach. *International Journal of Cosmetic Science*, 22(1):11–20, feb 2000. ISSN 01425463. doi: 10.1046/j.1467-2494.2000.00006.x. URL http://doi.wiley.com/10.1046/j.1467-2494.2000.00006.x.

Kuhl, E., Garikipati, K., Arruda, E. M., and Grosh, K. Remodeling of biological tissue: Mechanically induced reorientation of a transversely isotropic chain network. *Journal of the Mechanics and Physics of Solids*, 53(7):1552–1573, jul 2005. ISSN 00225096. doi: 10.1016/j.jmps.2005.03.002. URL http://linkinghub.elsevier.com/retrieve/pii/S0022509605000578.

Kumagai, K., Koike, H., Kudo, Y., Nagaoka, R., Kubo, K., Kobayashi, K., and Saijo, Y. Imaging of sebaceous glands of human skin by three-dimensional ultrasound microscopy and its relation to elasticity. In *2011 Annual International Conference of the IEEE Engineering in Medicine and Biology Society*, volume 2011, pages 7199–7202. IEEE, aug 2011. ISBN 978-1-4577-1589-1. doi: 10.1109/IEMBS.2011.6091819. URL http://www.ncbi.nlm.nih.gov/pubmed/22255999http://ieeexplore.ieee.org/lpdocs/epic03/wrapper.htm?arnumber=6091819.

Kuwazuru, O., Saothong, J., and Yoshikawa, N. Mechanical approach to aging and wrinkling of human facial skin based on the multistage buckling theory. *Medical Engineering & Physics*, 30(4):516–522, may 2008. ISSN 13504533. doi: 10.1016/j.medengphy.2007.06.001. URL http://linkinghub.elsevier.com/retrieve/pii/S1350453307001154.

Kvistedal, Y. and Nielsen, P. Investigating stress-strain properties of in-vivo human skin using multiaxial loading experiments and finite element modeling. In *Engineering in Medicine and Biology Society, 2004. IEMBS'04. 26th Annual International Conference of the IEEE*, volume 2, pages 5096–5099. IEEE, 2004. ISBN 0780384393. URL http://ieeexplore.ieee.org/xpls/abs{_}all.jsp?arnumber=1404408.

Kwiatkowska, M., Franklin, S. E., Hendriks, C. P., and Kwiatkowski, K. Friction and deformation behaviour of human skin. *Wear*, 267(5-8):1264–1273, 2009. ISSN 00431648. doi: 10.1016/j.wear.2008.12.030.

Langer, K. Zur Anatomie und Physiologie der Haut. Über die Spaltbarkeit der Cutis, Sitzungsbericht der Mathematisch-naturwissenschaftlichen Classe der Wiener Kaiserlichen Academie der Wissenschaften Abt 44, 1861. URL http://www.zobodat.at/pdf/SBAWW{_}44{_}0019-0046.pdf.

Lanir, Y. and Fung, Y. Two-dimensional mechanical properties of rabbit skin-II. Experimental results. *Journal of Biomechanics*, 7(2):171–182, mar 1974. ISSN 00219290. doi: 10.1016/0021-9290(74)90058-X. URL http://linkinghub.elsevier.com/retrieve/pii/002192907490058X.

Lanir, Y., Sdekstein, Hartzshtark, A., and Manny, V. In-vivo indentation of human skin. *Journal of Biomechanical Engineering*, 112:63–69, 1990.

Lapeer, R. J., Gasson, P. D., and Karri, V. A Hyperelastic Finite-Element Model of Human Skin for Interactive Real-Time Surgical Simulation. *IEEE Transactions on Biomedical Engineering*, 58(4):1013–1022, apr 2011. ISSN 0018-9294. doi: 10.1109/TBME.2009.2038364. URL http://www.ncbi.nlm.nih.gov/pubmed/20172812http://ieeexplore.ieee.org/lpdocs/epic03/wrapper.htm?arnumber=5415594.

Larrabee, W. F. A finite element model of skin deformation. I. Biomechanics of skin and soft tissue: a review. *The Laryngoscope*, 96(4):399–405, 1986. ISSN 0023-852X. doi: 10.1288/00005537-198604000-00012.

Larrabee, W. F. and Galt, J. A. A finite element model of skin deformation. III. The finite element model. *The Laryngoscope*, 96(4):413–419, 1986a. ISSN 0023-852X. doi: 10.1288/00005537-198604000-00014.

Larrabee, W. F. and Galt, J. A. A finite element model for the design of local skin flaps. *Otolaryngologic clinics of North America*, 19(4):807–824, 1986b. ISSN 00306665.

Larrabee, W. F. and Sutton, D. A finite element model of skin deformation. II. An experimental model of skin deformation. *The Laryngoscope*, 96(4):406–412, 1986. ISSN 0023852X. doi: 10.1288/00005537-198604000-00012.

Lawler, J. V. Blade Skin Fluid Modeling. Technical report, The Gillette Company, Gillette Advanced Technology Center, US, 2001.

Leighton, T. Private communication, 2014.

Leighton, T. G., Meers, S. D., and White, P. R. Propagation through nonlinear time-dependent bubble clouds and the estimation of bubble populations from measured acoustic characteristics. *Proceedings of the Royal Society A: Mathematical, Physical and Engineering Sciences*, 460(2049):2521–2550, 2004. ISSN 1364-5021. doi: 10.1098/rspa.2004.1298. URL http://dx.doi.org/10.1098/rspa.2004.1298$\delimiter"026E30F$nhttp://rspa.royalsocietypublishing.org/cgi/doi/10.1098/rspa.2004.1298.

Lévêque, J. L. and Audoly, B. Influence of Stratum Corneum on the entire skin mechanical properties, as predicted by a computational skin model. *Skin Research and Technology*, 19(1):42–46, feb 2013. ISSN 0909752X. doi: 10.1111/j.1600-0846.2012.00664.x. URL http://www.ncbi.nlm.nih.gov/pubmed/22925192http://doi.wiley.com/10.1111/j.1600-0846.2012.00664.x.

Levi, K. and Dauskardt, R. H. Application of substrate curvature method to differentiate drying stresses in topical coatings and human stratum corneum. *International Journal of Cosmetic Science*, 32(4):294–298, 2010. ISSN 01425463. doi: 10.1111/j.1468-2494.2010.00568.x.

Levi, K., Kwan, A., Rhines, A., Gorcea, M., Moore, D., and Dauskardt, R. Emollient molecule effects on the drying stresses in human stratum corneum. *British Journal of Dermatology*, 163(4):695–703, jul 2010a. ISSN 00070963. doi: 10.1111/j.1365-2133.2010.09937.x. URL http://doi.wiley.com/10.1111/j.1365-2133.2010.09937.x.

Levi, K., Weber, R. J., Do, J. Q., and Dauskardt, R. H. Drying stress and damage processes in human stratum corneum. *International Journal of Cosmetic Science*, 32(4): 276–293, 2010b. ISSN 01425463. doi: 10.1111/j.1468-2494.2009.00557.x.

Levi, K., Kwan, A., Rhines, A. S., Gorcea, M., Moore, D. J., and Dauskardt, R. H. Effect of glycerin on drying stresses in human stratum corneum, 2011. ISSN 09231811.

Leyva-Mendivil, M. F., Page, A., Bressloff, N. W., and Limbert, G. A mechanistic insight into the mechanical role of the stratum corneum during stretching and compression of the skin. *Journal of the Mechanical Behavior of Biomedical Materials*, 49:197–219, 2015. ISSN 17516161. doi: 10.1016/j.jmbbm.2015.05.010. URL http://www.sciencedirect.com/science/article/pii/S1751616115001745.

Li, L., Buschmann, M., and Shirazi-Adl, A. A fibril reinforced nonhomogeneous poroelastic model for articular cartilage: inhomogeneous response in unconfined compression. *Journal of Biomechanics*, 33(12):1533–1541, dec 2000. ISSN 00219290. doi: 10.1016/S0021-9290(00)00153-6. URL http://linkinghub.elsevier.com/retrieve/pii/S0021929000001536.

Liang, X., Graf, B. W., and Boppart, S. a. In Vivo Multiphoton Microscopy for Investigating Biomechanical Properties of Human Skin. *Cellular and Molecular Bioengineering*, 4(2):231–238, nov 2010. ISSN 1865-5025. doi: 10.1007/s12195-010-0147-6. URL http://www.springerlink.com/index/10.1007/s12195-010-0147-6.

Limbert, G. A transversely isotropic viscohyperelastic materialApplication to the modeling of biological soft connective tissues. *International Journal of Solids and Structures*, 41(15):4237–4260, jul 2004. ISSN 00207683. doi: 10.1016/j.ijsolstr.2004.02.057. URL http://linkinghub.elsevier.com/retrieve/pii/S0020768304001118.

Limbert, G. A mesostructurally-based anisotropic continuum model for biological soft tissues–decoupled invariant formulation. *Journal of the mechanical behavior of biomedical materials*, 4(8):1637–57, nov 2011. ISSN 1878-0180. doi: 10.1016/j.jmbbm.2011.07.016. URL http://www.ncbi.nlm.nih.gov/pubmed/22098866.

Limbert, G. State-of-the-art constitutive models of skin biomechanics. In Querleux, B., editor, *Computational Biophysics of the Skin*, chapter 4, pages 95–131. Pan Stanford Publishing Pte. Ltd, Singapore, 2014.

Limbert, G. and Simms, C. Special issue on skin mechanobiology. *Journal of the Mechanical Behavior of Biomedical Materials*, 28:395–396, dec 2013. ISSN 17516161. doi: 10.1016/j.jmbbm.2013.10.001. URL http://linkinghub.elsevier.com/retrieve/pii/S1751616113003275.

Limbert, G. and Taylor, M. On the constitutive modeling of biological soft connective tissues. *International Journal of Solids and Structures*, 39(8):2343–2358, apr 2002.

ISSN 00207683. doi: 10.1016/S0020-7683(02)00084-7. URL http://linkinghub.elsevier.com/retrieve/pii/S0020768302000847.

Lipic, P. and Smith, E. Private communication, 2012.

Love, E. R. Compression of elastic bodies in contact, 1942.

Luboz, V., Petrizelli, M., Bucki, M., Diot, B., Vuillerme, N., and Payan, Y. Biomechanical modeling to prevent ischial pressure ulcers. *Journal of Biomechanics*, 47(10):2231–2236, jul 2014. ISSN 00219290. doi: 10.1016/j.jbiomech.2014.05.004. URL http://www.ncbi.nlm.nih.gov/pubmed/24873863http://linkinghub.elsevier.com/retrieve/pii/S0021929014002851.

Lundberg, G. Elastische Berührung zweier Halbräume. *Forschung auf dem Gebiete des Ingenieurwesens*, 10(5):201–211, sep 1939. ISSN 0015-7899. doi: 10.1007/BF02584950. URL http://link.springer.com/10.1007/BF02584950.

Luo, G., Houston, V. L., Garbarini, M. A., Beattie, A. C., and Thongpop, C. Finite element analysis of heel pad with insoles. *Journal of Biomechanics*, 44(8):1559–1565, may 2011. ISSN 00219290. doi: 10.1016/j.jbiomech.2011.02.083. URL http://www.ncbi.nlm.nih.gov/pubmed/21420682http://linkinghub.elsevier.com/retrieve/pii/S0021929011001758.

Macdougall, G. and Ockrent, C. Surface Energy Relations in Liquid/Solid Systems. I. The Adhesion of Liquids to Solids and a New Method of Determining the Surface Tension of Liquids. *Proceedings of the Royal Society A: Mathematical, Physical and Engineering Sciences*, 180(981):151–173, jun 1942. ISSN 1364-5021. doi: 10.1098/rspa.1942.0031. URL http://rspa.royalsocietypublishing.org/cgi/doi/10.1098/rspa.1942.0031.

Magnenat-Thalmann, N., Kalra, P., Luc Leveque, J., Bazin, R., Batisse, D., and Querleux, B. A computational skin model: fold and wrinkle formation. *IEEE Transactions on Information Technology in Biomedicine*, 6(4):317–323, dec 2002. ISSN 1089-7771. doi: 10.1109/TITB.2002.806097. URL http://www.ncbi.nlm.nih.gov/pubmed/15224846http://ieeexplore.ieee.org/lpdocs/epic03/wrapper.htm?arnumber=1146681.

Mainardi, F. *Fractional Calculus and Waves in Linear Viscoelasticity : An Introduction to Mathematical Models*. Imperial College Press, London, GB, 2010. URL http://site.ebrary.com/lib/soton/detail.action?docID=10422020.

Mak, A. F. T., Huang, L., and Wang, Q. A Biphasic Poroelastic Analysis of the Flow Dependent Subcutaneous Tissue Pressure and Compaction Due to Epidermal Loadings: Issues in Pressure Sore. *Journal of Biomechanical Engineering*, 116(4):421, 1994. ISSN 01480731. doi: 10.1115/1.2895793. URL http://biomechanical.asmedigitalcollection.asme.org/article.aspx?articleid=1399961.

Makhsous, M., Dohyung Lim, Hendrix, R., Bankard, J., Rymer, W., and Fang Lin. Finite Element Analysis for Evaluation of Pressure Ulcer on the Buttock: Development and Validation. *IEEE Transactions on Neural Systems and Rehabilitation Engineering*, 15(4):517–525, dec 2007. ISSN 1534-4320. doi: 10.1109/TNSRE.2007.906967. URL http://www.pubmedcentral.nih.gov/articlerender.fcgi?artid=2861146{&}tool=pmcentrez{&}rendertype=abstracthttp://ieeexplore.ieee.org/lpdocs/epic03/wrapper.htm?arnumber=4359226.

Marieb, E. N. and Hoehn, K. *Human Anatomy & Physiology*. Pearson International Edition, United States of America, 8th edition, 2010. ISBN 0-321-60261-7.

Marrington, R., Dafforn, T. R., Halsall, D. J., MacDonald, J. I., Hicks, M., and Rodger, A. Validation of new microvolume Couette flow linear dichroism cells. *The Analyst*, 130(12):1608–16, dec 2005. ISSN 0003-2654. doi: 10.1039/b506149k. URL http://www.ncbi.nlm.nih.gov/pubmed/16284659.

Masen, M. a. A systems based experimental approach to tactile friction. *Journal of the Mechanical Behavior of Biomedical Materials*, 4(8):1620–1626, 2011. ISSN 17516161. doi: 10.1016/j.jmbbm.2011.04.007. URL http://dx.doi.org/10.1016/j.jmbbm.2011.04.007.

Matts, P., Hendrix, S., Barton, P., and Vanoosthuyze, K. Stratum corneum protein and proinflammatory cytokine biomarkers as end points for understanding the effects of a high-efficacy body moisturizer containing niacinamide. *Journal of the American Academy of Dermatology*, 54, 2006.

Mavon, A., Zahouani, H., Redoules, D., Agache, P., Gall, Y., and Humbert, P. Sebum and stratum corneum lipids increase human skin surface free energy as determined from contact angle measurements: A study on two anatomical sites. *Colloids and Surfaces B: Biointerfaces*, 8(3):147–155, mar 1997. ISSN 09277765. doi: 10.1016/S0927-7765(96)01317-3. URL http://www.sciencedirect.com/science/article/pii/S0927776596013173.

McFeat, G. and Ertel, K. Blade Shaving. In Draelos, Z. D., editor, *Cosmetic Dermatology: Products and Procedures*, chapter 21. Wiley-Blackwell, Oxford, UK, 2010. ISBN 9781405186353. doi: 10.1002/9781444317657.ch21.

Meeten, G. H. Squeeze-flow and vane rheometry of a gasâĂŞliquid foam. *Rheologica Acta*, 47(8):883–894, apr 2008. ISSN 0035-4511. doi: 10.1007/s00397-008-0269-0. URL http://www.springerlink.com/index/10.1007/s00397-008-0269-0.

Moir, R. and Craig, A. Shave Prep Modelling, 2010.

Mujica, N. and Fauve, S. Sound velocity and absorption in a coarsening foam. *Physical Review E*, 66(2):1–14, aug 2002. ISSN 1063-651X. doi: 10.1103/PhysRevE.66.021404. URL http://link.aps.org/doi/10.1103/PhysRevE.66.021404.

Nakajima, K. and Narasaka, H. Evaluation of skin surface associated with morphology and coefficient of friction. *International Journal of Cosmetic Science*, 15(4):135–151, sep 2010. ISSN 01425463. doi: 10.1111/j.1468-2494.1993.tb00594.x. URL http://doi.wiley.com/10.1111/j.1468-2494.1993.tb00594.x.

Nakhatakyan, F. G. Precise solution of Hertz contact problem for circular cylinders with parallel axes. *Russian Engineering Research*, 31(3):193–196, 2011. ISSN 1068-798X. doi: 10.3103/S1068798X11030208.

Naylor, E. C., Watson, R. E. B., and Sherratt, M. J. Molecular aspects of skin ageing. *Maturitas*, 69(3):249–56, jul 2011. ISSN 1873-4111. doi: 10.1016/j.maturitas.2011.04.011. URL http://www.ncbi.nlm.nih.gov/pubmed/21612880.

Ní Annaidh, A., Bruyère, K., Destrade, M., Gilchrist, M. D., Maurini, C., Otténio, M., and Saccomandi, G. Automated Estimation of Collagen Fibre Dispersion in the Dermis and its Contribution to the Anisotropic Behaviour of Skin. *Annals of Biomedical Engineering*, 40(8):1666–1678, aug 2012a. ISSN 0090-6964. doi: 10.1007/s10439-012-0542-3. URL http://link.springer.com/10.1007/s10439-012-0542-3.

Ní Annaidh, A., Bruyère, K., Destrade, M., Gilchrist, M. D., and Otténio, M. Characterization of the anisotropic mechanical properties of excised human skin. *Journal of the Mechanical Behavior of Biomedical Materials*, 5(1):139–148, jan 2012b. ISSN 17516161. doi: 10.1016/j.jmbbm.2011.08.016. URL http://linkinghub.elsevier.com/retrieve/pii/S1751616111002219.

Norden, B. N. On the compression of a cylinder in contact with a plane surface. Technical report, Institute for Basic Standards, National Bureau of Standards, Washington, D. C., 1973.

O'Callaghan, D. J. and Cowley, K. D. Skin Modeling Methods and Systems, 2010.

Ogden, R. W. *Non-linear elastic deformations*. Ellis Horwood Ltd., West Sussex, England, 1984.

Oomens, C., Zenhorst, W., Broek, M., Hemmes, B., Poeze, M., Brink, P., and Bader, D. A numerical study to analyse the risk for pressure ulcer development on a spine board. *Clinical Biomechanics*, 28(7):736–742, aug 2013. ISSN 02680033. doi: 10.1016/j.clinbiomech.2013.07.005. URL http://www.ncbi.nlm.nih.gov/pubmed/23953331http://linkinghub.elsevier.com/retrieve/pii/S0268003313001617.

Oomens, C. W. J., van Campen, D. H., and Grootenboer, H. J. A Mixture Approach to the Mechanics of Skin. *Journal of Biomechanics*, 20(9):887–885, 1987. ISSN 00219290. doi: 10.1016/0021-9290(87)90147-3.

Pailler-Mattéi, C. and Zahouani, H. Study of adhesion forces and mechanical properties of human skin in vivo. *Journal of Adhesion Science and Technology*, 18(January 2015):1739–1758, 2004. ISSN 01694243. doi: 10.1163/1568561042708368. URL http://www.ingentaconnect.com/content/vsp/ast/2004/00000018/F0020015/art00005$\delimiter"026E30F$nhttp://www.ingentaselect.com/rpsv/cgi-bin/cgi?ini=xref{&}body=linker{&}reqdoi=10.1163/1568561042708368.

Pailler-Mattéi, C. and Zahouani, H. Analysis of adhesive behaviour of human skin in vivo by an indentation test. *Tribology International*, 39(1):12–21, jan 2006. ISSN 0301679X. doi: 10.1016/j.triboint.2004.11.003. URL http://linkinghub.elsevier.com/retrieve/pii/S0301679X04002373.

Pailler-Mattei, C., Pavan, S., Vargiolu, R., Pirot, F., Falson, F., and Zahouani, H. Contribution of stratum corneum in determining bio-tribological properties of the human skin. *Wear*, 263:1038–1043, 2007. ISSN 00431648. doi: 10.1016/j.wear.2007.01.128.

Pailler-Mattei, C., Bec, S., and Zahouani, H. In vivo measurements of the elastic mechanical properties of human skin by indentation tests. *Medical engineering & physics*, 30(5):599–606, jun 2008. ISSN 1350-4533. doi: 10.1016/j.medengphy.2007.06.011. URL http://www.ncbi.nlm.nih.gov/pubmed/17869160.

Pailler-Mattei, C., Guerret-Piécourt, C., Zahouani, H., and Nicoli, S. Interpretation of the human skin biotribological behaviour after tape stripping. *Journal of the Royal Society, Interface / the Royal Society*, 8(60):934–941, jul 2011. ISSN 1742-5689. doi: 10.1098/rsif.2010.0672. URL http://www.pubmedcentral.nih.gov/articlerender.fcgi?artid=3104339{&}tool=pmcentrez{&}rendertype=abstract.

Pannisset, F., Varchon, D., and Agache, P. Non invasive measurement of stratum corneum Young's modulus in vivo. In *XIVth Congress on Biomechanics*, 1994.

Panton, R. L. *Incompressible Flow*. John Wily & Sons, New Jersey, 4th editio edition, 2013. ISBN 9781118418451. URL http://site.ebrary.com/lib/soton/detail.action?docID=10731720.

Papir, Y. S., Hsu, K.-H., and Wildnauer, R. G. The mechanical properties of stratum corneum. I. The effect of water and ambient temperature on the tensile properties of newborn rat stratum corneum. *Biochimica et Biophysica acta*, 399(170-180), 1975.

Park, A. Rheology of stratum corneum. I. A molecular interpretation of the stress-strain curve. *Journal of the Society of Cosmetic Chemists*, 12, 1972. URL http://journal.scconline.org/abstracts/cc1972/cc023n01/p00003-p00012.html.

Park, S. and Durian, D. Viscous and elastic fingering instabilities in foam. *Physical review letters*, 72(21):3347–3350, may 1994. ISSN 1079-7114. URL http://www.ncbi.nlm.nih.gov/pubmed/10056175.

Pathak, H. S. Ansys user defined material implementation of van der Waals model. In Heinrich, G., Kaliske, M., Lion, A., and Reese, S., editors, *Constitutive Models for Rubber VI*, pages 33–38. CRC PRESS-Taylor & Francis Group, Dresden, GERMANY, 2010. ISBN 978-0-415-56327-7.

Payne, P. a. Measurement of properties and function of skin. *Clinical Physics and Physiological Measurement*, 12(2):105–29, may 1991. ISSN 0143-0815. URL http://www.ncbi.nlm.nih.gov/pubmed/1855358http://iopscience.iop.org/0143-0815/12/2/001.

Pedersen, L. and Jemec, G. B. E. Mechanical Properties and Barrier Function of Healthy Human Skin. *Acta Dermato-Venereologica*, 86(4):308–311, 2006. doi: 10.2340/00015555-0080.

Peña, A., Bolton, M., and Pickard, J. Cellular poroelasticity: a theoretical model for soft tissue mechanics. In *Biot Conference on Poromechanics*, pages 475–480, Louvain-la-Neuve, Belgium, 1998.

Persson, B. N. J. *Sliding Friction*. NanoScience and Technology. Springer Berlin Heidelberg, Berlin, Heidelberg, 2000. ISBN 978-3-642-08652-6. doi: 10.1007/978-3-662-04283-0. URL http://link.springer.com/10.1007/978-3-662-04283-0.

Piérard, G. E., Uhoda, I., and Piérard-Franchimont, C. From skin microrelief to wrinkles. An area ripe for investigation. *Journal of cosmetic dermatology*, 2(1):21–28, 2003. ISSN 1473-2165. doi: 10.1111/j.1473-2130.2003.00012.x.

Puttock, M. J. and Thwaite, E. G. Elastic Compression of Spheres and Cylinders at Point and Line Contact. *National Standards Laboratory Technical Paper*, 25(25), 1969.

Rausch, M. K. and Kuhl, E. On the effect of prestrain and residual stress in thin biological membranes. *Journal of the Mechanics and Physics of Solids*, 61(9):1955–1969, 2013. ISSN 00225096. doi: 10.1016/j.jmps.2013.04.005.

Rennels, D. C. and Hudson, H. M. *Pipe Flow: A Practical and comprehensive Guide*. John Wiley & Sons, Incorporated, first edit edition, 2012. ISBN 1118275241.

Rheosys LLC. A Basic Introduction to Viscometers & Viscometry, 2011. URL http://www.rheosys.com/intro.html.

Rim, J., Pinsky, P., and van Osdol, W. Finite element modeling of coupled diffusion with partitioning in transdermal drug delivery. *Annals of biomedical engineering*, 33(10):1422, 2005. ISSN 0090-6964. doi: 10.1007/s10439-005-5788-6. URL http://www.scopus.com/scopus/inward/record.url?eid=2-s2.0-27244450288{&}partnerID=40{&}rel=R6.5.0$\delimiter"026E30F$nhttp://link.springer.com/article/10.1007/s10439-005-5788-6.

Rouyer, F., Cohen-Addad, S., and Höhler, R. Is the yield stress of aqueous foam a well-defined quantity? *Colloids and Surfaces A: Physicochemical and Engineering Aspects*, 263(1-3):111–116, aug 2005. ISSN 09277757. doi: 10.1016/j.colsurfa.2005.01.025. URL http://linkinghub.elsevier.com/retrieve/pii/S0927775705000919.

Samani, A. and Plewes, D. A method to measure the hyperelastic parameters of ex vivo breast tissue samples. *Physics in Medicine and Biology*, 49(18):4395–4405, sep 2004. ISSN 0031-9155. doi: 10.1088/0031-9155/49/18/014. URL http://stacks.iop.org/0031-9155/49/i=18/a=014?key=crossref.4a8069c8c53067447eea388da01686c1.

Sánchez, M., Valencia, C., Franco, J., and Gallegos, C. Wall Slip Phenomena in Oil-in-Water Emulsions: Effect of Some Structural Parameters. *Journal of Colloid and Interface Science*, 241(1):226–232, sep 2001. ISSN 00219797. doi: 10.1006/jcis.2001.7732. URL http://www.sciencedirect.com/science/article/pii/S002197970197732X.

Schmatko, T., Hervet, H., and Leger, L. Friction and slip at simple fluid-solid interfaces: The roles of the molecular shape and the solid-liquid interaction. *Physical Review Letters*, 94(24):1–4, 2005. ISSN 00319007. doi: 10.1103/PhysRevLett.94.244501.

Serup, J., Jemec, G., and Grove, G. *Handbook of Non-Invasive Methods and the Skin*. Boca Raton FL: CRC Press, 1995.

Servais, C., Ravji, S., Sansonnens, C., and Bauwens, I. Oscillating Vane Geometry for Soft Solid Gels and Foams. *Journal of Texture Studies*, 33(6):487–504, dec 2002. ISSN 0022-4901. doi: 10.1111/j.1745-4603.2002.tb01363.x. URL http://onlinelibrary.wiley.com/doi/10.1111/j.1745-4603.2002.tb01363.x/abstracthttp://doi.wiley.com/10.1111/j.1745-4603.2002.tb01363.x.

Shai, A., Maibach, H. I., and Baran, R., editors. *Handbook of cosmetic skin care*. Informa UK Ltd, 2nd edition, 2009. ISBN 9781841845098. URL http://oa.lib.ksu.edu.tw/OA/handle/987654321/43270.

Shames, I. H. and Cozzarelli, F. A. *Elastic And Inelastic Stress Analysis*. CRC Press, Boca Raton, 1997. ISBN 10: 1560326867.

Shimizu, H. *Shimizu's Textbook of Dermatology*. Hokkaido University Press/Nakayama Shoten, Hokkaido, Japan, 1st edition, 2007. ISBN 4521679218.

Shpenkov, G. *Friction Surface Phenomena*. Elseiver Science, Amsterdam, The Netherlands, 1995. ISBN 0444816844.

Simo, J. C. and Hughes, T. J. *Computational Inelasticity*. Springer, Secaucus, NJ, USA, 1998.

Sivamani, R. K., Goodman, J., Gitis, N. V., and Maibach, H. I. Friction coefficient of skin in real-time. *Skin Research and Technology*, 9(3):235–9, aug 2003. ISSN 0909-752X. URL http://www.ncbi.nlm.nih.gov/pubmed/12877684.

Sobol', I. On the distribution of points in a cube and the approximate evaluation of integrals. *USSR Computational Mathematics and Mathematical Physics*, 7(4):86–112, jan 1967. ISSN 00415553. doi: 10.1016/0041-5553(67)90144-9. URL http://linkinghub.elsevier.com/retrieve/pii/0041555367901449.

Sochi, T. Slip at Fluid-Solid Interface. *Polymer Reviews*, 51(4):309–340, 2011. ISSN 1558-3724. doi: 10.1080/15583724.2011.615961. URL http://arxiv.org/abs/1101.4421.

Sokolov, I. and Woodworth, C. D. Loss of Elasticity of Ageing Epithelial Cells, and Its Possible Reversal. In *NSTI-Nanotech 2005*, volume 1, pages 63–66, 2005. ISBN 0976798506. URL http://www.nsti.org/Nanotech2005/showabstract.html?absno=1087.

Sommer, G., Eder, M., Kovacs, L., Pathak, H., Bonitz, L., Mueller, C., Regitnig, P., and Holzapfel, G. a. Multiaxial mechanical properties and constitutive modeling of human adipose tissue: A basis for preoperative simulations in plastic and reconstructive surgery. *Acta Biomaterialia*, 9(11):9036–9048, 2013. ISSN 17427061. doi: 10.1016/j.actbio.2013.06.011. URL http://dx.doi.org/10.1016/j.actbio.2013.06.011.

Sopher, R. and Gefen, A. Effects of skin wrinkles, age and wetness on mechanical loads in the stratum corneum as related to skin lesions. *Medical & Biological Engineering & Computing*, 49(1):97–105, jan 2011. ISSN 0140-0118. doi: 10.1007/s11517-010-0673-3. URL http://www.ncbi.nlm.nih.gov/pubmed/20717736http://www.ncbi.nlm.nih.gov/pubmed/9523777http://link.springer.com/10.1007/s11517-010-0673-3.

Stachowiak, G. and Batchelor, A. W. Engineering Tribology, 2013. URL http://www.myilibrary.com/?ID=518823.

Stupkiewicz, S., Lewandowski, M. J., and Lengiewicz, J. Micromechanical analysis of friction anisotropy in rough elastic contacts. *International Journal of Solids and Structures*, 51(23-24):3931–3943, 2014. ISSN 00207683. doi: 10.1016/j.ijsolstr.2014.07.013. URL http://www.scopus.com/inward/record.url?eid=2-s2.0-84921789550{&}partnerID=tZOtx3y1.

Suarez, E., Syed, F., Rasgado, T. a., Walmsley, A., Mandal, P., and Bayat, A. Skin equivalent tensional force alters keloid fibroblast behaviour and phenotype. *Wound repair and regeneration: official publication of the Wound Healing Society [and] the European Tissue Repair Society*, pages 1–38, 2014. ISSN 1524-475X. doi: 10.1111/wrr.12215. URL http://www.ncbi.nlm.nih.gov/pubmed/25046655.

Takizawa, K., Tezduyar, T. E., Mochizuki, H., Hattori, H., Mei, S., Pan, L., and Montel, K. SpaceâĂŞtime VMS method for flow computations with slip interfaces (ST-SI). *Mathematical Models and Methods in Applied Sciences*, 25(12):2377–2406, nov 2015. ISSN 0218-2025. doi: 10.1142/S0218202515400126. URL http://www.worldscientific.com/doi/10.1142/S0218202515400126.

Tang, W. and Bhushan, B. Adhesion, friction and wear characterization of skin and skin cream using atomic force microscope. *Colloids and surfaces. B, Biointerfaces*, 76(1):1–15, 2010. ISSN 1873-4367. doi: 10.1016/j.colsurfb.2009.09.039. URL http://www.sciencedirect.com/science/article/pii/S092777650900472X.

Taylor, R. L. and Zienkiewicz, O. C. *Finite Element Method for Solid and Structural Mechanics*. Butterworth-Heinemann, Jordan Hill, GBR, 6th edition, 2005.

Tepole, A. B. and Kuhl, E. Computational modeling of chemo-bio-mechanical coupling: a systems-biology approach toward wound healing. *Computer Methods in Biomechanics and Biomedical Engineering*, pages 1–18, nov 2014. ISSN 1025-5842. doi: 10.1080/10255842.2014.980821. URL http://www.tandfonline.com/doi/full/10.1080/10255842.2014.980821.

Tepole, A. B., Gart, M., Gosain, A. K., and Kuhl, E. Characterization of living skin using multi-view stereo and isogeometric analysis, 2014a. ISSN 17427061.

Tepole, A. B., Gosain, A. K., and Kuhl, E. Computational modeling of skin: Using stress profiles as predictor for tissue necrosis in reconstructive surgery. *Computers and Structures*, 143:32–39, 2014b. ISSN 00457949. doi: 10.1016/j.compstruc.2014.07.004.

Thomas, H. R. and Hoersch, V. A. Stresses due to the pressure of one elastic solid upon another with special reference to railroad rails : a report, 1930. URL http://hdl.handle.net/2142/4409.

Tomonaga, G., Mitake, H., Hoki, N., and Kajiya, F. Measurement of point velocity in the canine coronary artery by laser Doppler velocimeter with optical fiber. *The Japanese Journal of Surgery*, 11(4):226–231, jul 1981. ISSN 0047-1909. doi: 10.1007/BF02468760. URL http://link.springer.com/10.1007/BF02468760.

Tonge, T. K., Atlan, L. S., Voo, L. M., and Nguyen, T. D. Full-field bulge test for planar anisotropic tissues: Part I-Experimental methods applied to human skin tissue. *Acta Biomaterialia*, 9(4):5913–5925, 2013a. ISSN 17427061. doi: 10.1016/j.actbio.2012.11.035.

Tonge, T. K., Voo, L. M., and Nguyen, T. D. Full-field bulge test for planar anisotropic tissues: Part II-A thin shell method for determining material parameters and comparison of two distributed fiber modeling approaches. *Acta Biomaterialia*, 9(4):5926–5942, 2013b. ISSN 17427061. doi: 10.1016/j.actbio.2012.11.034.

Tran, H. V., Charleux, F., Ehrlacher, A., and Ho Ba Tho, M. Propriétés mécaniques multicouches de la peau humain in vivo, modèle numérique anatomique. In *Proceedings du Septième Colloque National en Calcul des Structures de Giens*, pages 101–106, 2005.

Tran, H. V., Charleux, F., Rachik, M., Ehrlacher, A., and Ho Ba Tho, M. C. In vivo characterization of the mechanical properties of human skin derived from MRI and indentation techniques. *Computer Methods in Biomechanics and Biomedical Engineering*, 10(6):401–407, dec 2007. ISSN 1025-5842. doi: 10.1080/10255840701550287. URL http://www.ncbi.nlm.nih.gov/pubmed/17891674http://www.tandfonline.com/doi/abs/10.1080/10255840701550287.

Vad, S., Eskinazi, A., Corbett, T., McGloughlin, T., and Vande Geest, J. P. Determination of Coefficient of Friction for Self-Expanding Stent-Grafts. *Journal of Biomechanical Engineering*, 132(12):121007, dec 2010. ISSN 01480731. doi: 10.1115/1.4002798. URL http://www.ncbi.nlm.nih.gov/pubmed/21142321http://biomechanical.asmedigitalcollection.asme.org/article.aspx?articleid=1427723.

Van der Heide, E., Zeng, X., and Masen, M. A. Skin tribology: Science friction? *Friction*, 1(2):130–142, 2013. doi: 10.1007/s40544-013-0015-1.

van Kuilenburg, J., Masen, M., and van der Heide, E. The role of the skin microrelief in the contact behaviour of human skin: Contact between the human finger and regular surface textures. *Tribology International*, 65:81–90, sep 2013a. ISSN 0301679X. doi: 10.1016/j.triboint.2012.11.024. URL http://linkinghub.elsevier.com/retrieve/pii/S0301679X12003945.

van Kuilenburg, J., Masen, M. A., and van der Heide, E. Contact modelling of human skin: What value to use for the modulus of elasticity? *Proceedings of the Institution of Mechanical Engineers, Part J: Journal of Engineering Tribology*, 227(4):349–361, apr 2013b. ISSN 1350-6501. doi: 10.1177/1350650112463307. URL http://pij.sagepub.com/lookup/doi/10.1177/1350650112463307.

Veijgen, N. K. *Skin Friction: A novel approach to measuring in vivo human skin*. PhD thesis, Universiteit Twente, 2013. URL http://doc.utwente.nl/84303/.

Veijgen, N. K., Masen, M. a., and van der Heide, E. Relating Friction on the Human Skin to the Hydration and Temperature of the Skin. *Tribology Letters*, 49(1):251–262, jan 2013a. ISSN 1023-8883. doi: 10.1007/s11249-012-0062-1. URL http://link.springer.com/10.1007/s11249-012-0062-1.

Veijgen, N. K., Masen, M. A., and van der Heide, E. Variables influencing the frictional behaviour of in vivo human skin. *Journal of the Mechanical Behavior of Biomedical Materials*, 28:448–461, 2013b. ISSN 17516161. doi: 10.1016/j.jmbbm.2013.02.009.

Veijgen, N. K., van der Heide, E., and Masen, M. a. A multivariable model for predicting the frictional behaviour and hydration of the human skin. *Skin Research and Technology*, 19(3):330–338, aug 2013c. ISSN 0909752X. doi: 10.1111/srt.12053. URL http://www.ncbi.nlm.nih.gov/pubmed/23441726http://doi.wiley.com/10.1111/srt.12053.

Verruijt, A. *Theory and Problems of Poroelasticity*. Delft, The Netherlands, 2015.

Vexler, A., Polyansky, I., and Gorodetsky, R. Evaluation of skin viscoelasticity and anisotropy by measurement of speed of shear wave propagation with viscoelasticity skin analyzer. *The Journal of Investigative Dermatology*, 113(5):732–9, nov 1999. ISSN 0022-202X. doi: 10.1046/j.1523-1747.1999.00751.x. URL http://www.ncbi.nlm.nih.gov/pubmed/10571727.

Vodovotz, Y. Translational systems biology of inflammation and healing. *Wound Repair and Regeneration*, 18(1):3–7, jan 2010. ISSN 10671927. doi: 10.1111/j.1524-475X.2009.00566.x. URL http://doi.wiley.com/10.1111/j.1524-475X.2009.00566.x.

Wagner, M. B., Gerling, M. G. J., and Scanlon, J. Validation of a 3-D Finite Element Human Fingerpad Model Composed of Anatomically Accurate Tissue Layers. In *2008 Symposium on Haptic Interfaces for Virtual Environment and Teleoperator Systems*, pages 101–105. IEEE, mar 2008. ISBN 978-1-4244-2005-6. doi: 10.1109/HAPTICS.2008.4479922. URL http://ieeexplore.ieee.org/xpls/abs{_}all.jsp?arnumber=4479922http://ieeexplore.ieee.org/lpdocs/epic03/wrapper.htm?arnumber=4479922.

Waller, J. M. and Maibach, H. I. Age and skin structure and function, a quantitative approach (I): Blood flow, pH, thickness, and ultrasound echogenicity, 2005. ISSN 0909752X.

Waller, J. M. and Maibach, H. I. Age and skin structure and function, a quantitative approach (II): Protein, glycosaminoglycan, water, and lipid content and structure, 2006. ISSN 0909752X.

Wan Abas, W. and Barbenel, J. Uniaxial tension test of human skin in vivo. *Journal of Biomedical Engineering*, 4(1):65–71, jan 1982. ISSN 01415425. doi: 10.1016/0141-5425(82)90029-2. URL http://linkinghub.elsevier.com/retrieve/pii/0141542582900292.

Warner, R. R., Stone, K. J., and Boissy, Y. L. Hydration disrupts human stratum corneum ultrastructure. *Journal of Investigative Dermatology*, 120(2):275–284, 2003. ISSN 0022202X. doi: 10.1046/j.1523-1747.2003.12046.x.

Weiss, J., Maker, B., and Schauer, D. Treatment of initial stress in hyperelastic finite element models of soft tissues. In *ASME Conference BED*, 1995.

Weiss, J. A., Maker, B. N., and Govindjee, S. Finite element implementation of incompressible, transversely isotropic hyperelasticity. *Computer Methods in Applied Mechanics and Engineering*, 135(1-2):107–128, aug 1996. ISSN 00457825. doi: 10.1016/0045-7825(96)01035-3. URL http://linkinghub.elsevier.com/retrieve/pii/0045782596010353.

Wilhelm, K.-P. Skin Aging. *Archives of Dermatology*, 127(12):1806, dec 1991. ISSN 0003-987X. doi: 10.1001/archderm.1991.04520010052006. URL http://archderm.jamanetwork.com/article.aspx?doi=10.1001/archderm.1991.04520010052006.

Winger, M., de Vries, A. H., and van Gunsteren, W. F. Force-field dependence of the conformational properties of α,ω-dimethoxypolyethylene glycol. *Molecular Physics*, 107(13):1313–1321, jul 2009. ISSN 0026-8976. doi: 10.1080/00268970902794826. URL http://www.tandfonline.com/doi/abs/10.1080/00268970902794826.

Wolfram, L. J. Friction of Skin. *Journal of the Society of Cosmetic Chemists*, 34 (December):465–476, 1983.

Wolfram Research. Wolfram Mathematica 10.0 Manual., 2014.

Wong, V. W., Levi, K., Akaishi, S., Schultz, G., and Dauskardt, R. H. Scar Zones: Region-Specific Differences in Skin Tension May Determine Incisional Scar Formation. *Plastic and Reconstructive Surgery*, 129(6):1272, 2012. ISSN 1529-4242. doi: 10.1097/PRS.0b013e31824eca79. URL http://journals.lww.com/plasreconsurg/Fulltext/2012/06000/Scar{_}Zones{_}{_}{_}Region{_}Specific{_}Differences{_}in{_}Skin.9.aspx$\delimiter"026E30F$npapers2://publication/doi/10.1097/PRS.0b013e31824eca79.

Wu, J., Dong, R., Schopper, A., and Smutz, W. Analysis of Skin Deformation Profiles During Sinusoidal Vibration of Fingerpad. *Annals of Biomedical Engineering*, 31(7): 867–878, 2003.

Wu, K. *Mechanical behavior of human stratum corneum: relationship to tissue structure and condition*. Doctor of philosophy, Standford University, 2006. URL http://adsabs.harvard.edu/abs/2006PhDT.....73W.

Wu, K., van Osdol, W. W., and Dauskardt, R. H. Mechanical and microstructural properties of stratum corneum. In *Materials Research Society Symposium - Proceedings*, volume 724, pages 27–33. DTIC Document, 2002. URL http://oai.dtic.mil/oai/oai?verb=getRecord{&}metadataPrefix=html{&}identifier=ADP014395.

Wu, K. S., Stefik, M. M., Ananthapadmanabhan, K. P., and Dauskardt, R. H. Graded delamination behavior of human stratum corneum. *Biomaterials*, 27(34):5861–70,

dec 2006a. ISSN 0142-9612. doi: 10.1016/j.biomaterials.2006.08.008. URL http://www.sciencedirect.com/science/article/pii/S0142961206006958http://www.ncbi.nlm.nih.gov/pubmed/16934326.

Wu, K. S., van Osdol, W. W., and Dauskardt, R. H. Mechanical properties of human stratum corneum: effects of temperature, hydration, and chemical treatment. *Biomaterials*, 27(5):785–95, feb 2006b. ISSN 0142-9612. doi: 10.1016/j.biomaterials.2005.06.019. URL http://www.sciencedirect.com/science/article/pii/S0142961205005867http://www.ncbi.nlm.nih.gov/pubmed/16095683.

Xing Liang and Boppart, S. Biomechanical Properties of In Vivo Human Skin From Dynamic Optical Coherence Elastography. *IEEE Transactions on Biomedical Engineering*, 57(4):953–959, apr 2010. ISSN 0018-9294. doi: 10.1109/TBME.2009.2033464. URL http://www.ncbi.nlm.nih.gov/pubmed/19822464http://ieeexplore.ieee.org/lpdocs/epic03/wrapper.htm?arnumber=5282637.

Zacharias, E. M. J. and Parnell, R. A. J. Solid Measurements in Beverages, Sauces, and Syrups Using Sound Velocimetry. *Journal of the Acoustical Society of America*, 51 (4A):1198–1201, 1972.

Zahouani, H., Boyer, G., Pailler-Mattei, C., Ben Tkaya, M., and Vargiolu, R. Effect of human ageing on skin rheology and tribology. *Wear*, 271(9-10):2364–2369, jul 2011. ISSN 00431648. doi: 10.1016/j.wear.2011.02.024. URL http://linkinghub.elsevier.com/retrieve/pii/S004316481100278X.

Zhai, H. and Maibach, H. I. Occlusion vs. skin barrier function. *Skin Research and technology*, 8(1):1–6, 2002. URL http://onlinelibrary.wiley.com/doi/10.1046/j.0909-752x.2001.10311.x/abstract.

Zhong, W., Xing, M. M. Q., Pan, N., and Maibach, H. I. Textiles and Human Skin, Microclimate, Cutaneous Reactions: An Overview. *Cutaneous and Ocular Toxicology*, 25 (1):23–39, jan 2006. ISSN 1556-9527. doi: 10.1080/15569520500536600. URL http://www.tandfonline.com/doi/full/10.1080/15569520500536600.

Zöllner, A. M., Holland, M. A., Honda, K. S., Gosain, A. K., and Kuhl, E. Growth on demand: Reviewing the mechanobiology of stretched skin. *Journal of the Mechanical Behavior of Biomedical Materials*, 28:495–509, 2013. ISSN 17516161. doi: 10.1016/j.jmbbm.2013.03.018.